

**QUANTUM MANY-BODY DYNAMICS OF ULTRACOLD  
BOSONS IN ONE-DIMENSIONAL OPTICAL LATTICES:  
THEORETICAL ASPECTS, SIMULATION METHODS,  
AND SOLITON FORMATION AND STABILITY**

by

Ryan V. Mishmash

A thesis submitted to the Faculty and the Board of Trustees of the Colorado School of Mines in partial fulfillment of the requirements for the degree of Master of Science (Applied Physics).

Golden, Colorado

Date \_\_\_\_\_

Signed: \_\_\_\_\_  
Ryan V. Mishmash

Approved: \_\_\_\_\_  
Dr. Lincoln D. Carr  
Assistant Professor of Physics  
Thesis Advisor

Golden, Colorado

Date \_\_\_\_\_

\_\_\_\_\_  
Dr. Thomas E. Furtak  
Professor and Head  
Department of Physics

## ABSTRACT

We study complex quantum many-body dynamics of ultracold bosons in one-dimensional optical lattice potentials. Until recently, reliable time-dependent simulation of these systems was limited due to exponential growth of the Hilbert space with the size of the quantum system. However, in 2003-2004, G. Vidal devised the time-evolving block decimation algorithm: a time-adaptive density matrix renormalization group routine with roots in quantum information theory that allows efficient quasi-exact classical simulation of one-dimensional quantum many-body systems exhibiting a limited amount of entanglement. We apply these algorithms to the Bose-Hubbard Hamiltonian, a truncation of the full many-body Hamiltonian in second quantization that accurately describes the physics of ultracold bosons in deep optical lattices.

Specifically, we study dark solitons, self-sustaining nonlinear waves that are observed throughout nature and are an emergent property of Bose-Einstein condensates in the mean-field limit; we treat solitons in the fully quantum many-body setting of ultracold atoms on a Bose-Hubbard lattice. We consider two types of initial conditions for subsequent soliton propagation. In the first method, we build quantum analogs to the dark soliton solutions of the discrete nonlinear Schrödinger (DNLS) equation, a mean-field approximation of the Bose-Hubbard Hamiltonian; in the second method, we use density and phase engineering techniques to quantum engineer dark soliton initial conditions directly. We show that for both types of initial conditions, quantum fluctuations cause standing dark solitons to fill in at times on the order of tens of tunneling times. The static Bogoliubov spectrum is calculated for the dark soliton state of the discrete nonlinear Schrödinger equation, and we show

that such a treatment is inadequate to fully describe the filling-in of the soliton. We also show that quantum many-body effects can effectively induce an inelasticity in a collision between two solitons. Both of these results are in strong contrast to the predictions of pure mean-field theory.

Finally, we present a preliminary study of spin-1 bosons on an optical lattice undergoing a symmetry-breaking dynamical quantum phase transition. Using a mean-field vector DNLS approach, we show that the scaling properties of the system with respect to the rate of the phase transition should be describable by the Kibble-Zurek mechanism, an effect originally proposed to predict string and monopole formation during the evolution of the early Universe. Comparisons are made to previous mean-field studies in continuous geometries, and we make suggestions regarding how to investigate quantum many-body effects on this phase transition by simulating it using the aforementioned time-evolving block decimation method.

# TABLE OF CONTENTS

ABSTRACT . . . . .	iii
LIST OF FIGURES . . . . .	viii
ACKNOWLEDGMENT . . . . .	x
Chapter 1 INTRODUCTION . . . . .	1
1.1 Ultracold Atoms and Bose-Einstein Condensation . . . . .	1
1.2 Ultracold Atoms in Optical Lattices . . . . .	4
1.3 Simulation Techniques, Solitons, and a Spin-1 Phase Transition . . . .	7
1.4 Thesis Overview . . . . .	11
Chapter 2 BACKGROUND: FUNDAMENTALS OF ULTRACOLD QUANTUM GASES AND THEORETICAL CONNECTIONS BETWEEN MODELS . . . . .	13
2.1 Bose-Einstein Condensation . . . . .	14
2.1.1 Non-Interacting Systems . . . . .	14
2.1.2 Interacting Systems . . . . .	17
2.2 Optical Lattices . . . . .	19
2.3 Governing Models for Scalar Bosons . . . . .	23
2.3.1 Basic Quantum Many-Body Theory . . . . .	23
2.3.2 Continuous Gross-Pitaevskii Equation . . . . .	24
2.3.3 Bose-Hubbard Hamiltonian . . . . .	28
2.3.4 Connections to Discrete Nonlinear Schrödinger Equation . . . .	35
2.3.5 The Bogoliubov Approximation . . . . .	40
2.4 Complexity, Integrability, and Connections to Solitons . . . . .	42
2.5 The Hyperfine Degree of Freedom and Spin-1 Bosons . . . . .	45
2.5.1 Hyperfine Degree of Freedom . . . . .	45
2.5.2 Spin-1 Bose-Hubbard Hamiltonian . . . . .	46
2.5.3 Spin-1 Vector Discrete Nonlinear Schrödinger Equation . . . .	49
2.5.4 Dynamical Phase Transition and Kibble-Zurek Mechanism . . .	51

Chapter 3	SIMULATION METHODS: MEAN FIELD AND QUANTUM FIELD	53
3.1	Mean-Field Simulation: Finite Difference Methods . . . . .	53
3.1.1	Formulation of Problem . . . . .	54
3.1.2	Methods . . . . .	56
3.1.3	Implementation . . . . .	58
3.2	Quantum Many-Body Simulation: Time-Evolving Block Decimation .	58
3.2.1	Schmidt Decomposition . . . . .	60
3.2.2	Vidal's Decomposition . . . . .	63
3.2.3	Two-Site Operation . . . . .	66
3.2.4	Suzuki-Trotter Expansion and Time Evolution . . . . .	69
3.2.5	Calculation of Observables . . . . .	71
3.2.6	Application to Bose-Hubbard Hamiltonian . . . . .	74
3.2.7	Implementation of Spin-1 Bose-Hubbard Hamiltonian . . . . .	76
3.2.8	Use of Conserved Quantities . . . . .	78
Chapter 4	QUANTUM EVOLUTION OF MEAN-FIELD SOLITONS . . . . .	79
4.1	Characterization Measures . . . . .	79
4.1.1	Average Particle Number . . . . .	80
4.1.2	Normalized Particle Number Variance . . . . .	80
4.1.3	The Order Parameter . . . . .	81
4.1.4	Pegg-Barnett Hermitian Phase Operator . . . . .	81
4.1.5	Quantum Depletion . . . . .	82
4.1.6	Quantum Entanglement . . . . .	85
4.2	Truncated Coherent States . . . . .	88
4.3	Standing Solitons . . . . .	89
4.3.1	Fundamental Dark Soliton Solutions . . . . .	90
4.3.2	Characteristic Simulation . . . . .	92
4.3.3	Soliton Lifetimes . . . . .	101
4.3.4	Comparison to Experiment and to Finite-Temperature Effects	104
4.3.5	Bogoliubov Analysis . . . . .	106
4.4	Soliton-Soliton Collisions . . . . .	110
4.4.1	Density and Phase Engineering Dark Soliton-Soliton Collisions	111
4.4.2	Characteristic Simulation . . . . .	113
4.4.3	Quantum-Induced Inelasticity . . . . .	119
4.5	Summary . . . . .	120
Chapter 5	QUANTUM SOLITON ENGINEERING . . . . .	122
5.1	Methods for Density and Phase Engineering . . . . .	123
5.2	Standing Solitons . . . . .	124

5.2.1	Density and Phase Engineering of Standing Solitons . . . . .	124
5.2.2	Characteristic Simulation . . . . .	126
5.2.3	Soliton Lifetimes . . . . .	132
5.3	Soliton-Soliton Collisions and Quantum-Induced Inelasticity . . . . .	134
5.4	Summary . . . . .	136
Chapter 6	PRELIMINARY STUDY OF KIBBLE-ZUREK MECHANISM IN OPTICAL LATTICE OF SPIN-1 BOSONS . . . . .	138
6.1	Formulation of Problem and Methods Used . . . . .	138
6.2	Characteristic Simulation . . . . .	142
6.3	Calculation of Time Scaling Exponent . . . . .	147
6.4	Summary and Suggestions for Future Work . . . . .	149
Chapter 7	CONCLUSIONS AND OUTLOOK . . . . .	152
REFERENCES	. . . . .	158
APPENDIX A	VIDAL DECOMPOSITION EXAMPLES . . . . .	171
A.1	Product States . . . . .	171
A.2	GHZ State . . . . .	174
A.3	W State . . . . .	175
APPENDIX B	ACCURACY AND CONVERGENCE OF TIME-EVOLVING BLOCK DECIMATION SIMULATIONS . . . . .	178
B.1	Error in Schmidt Truncation Procedure . . . . .	178
B.1.1	Mean-Field Soliton Initial Conditions . . . . .	179
B.1.2	Quantum Engineered Soliton Initial Conditions . . . . .	180
B.2	Other Sources of Error . . . . .	187
APPENDIX C	MEAN-FIELD SIMULATION CODE . . . . .	188
C.1	scalarDNLS_RTP.m . . . . .	188
C.2	vectorDNLS_RTP.m . . . . .	191
C.3	BogModes.m . . . . .	195
APPENDIX D	TIME-EVOLVING BLOCK DECIMATION CODE . . . . .	197
D.1	spin1_module.f90 . . . . .	197
DVD	. . . . .	Pocket

## LIST OF FIGURES

2.1	Schematic of 3D optical lattice . . . . .	22
2.2	Bose-Hubbard parameters calculated from single-particle orbitals . . .	32
2.3	Schematic of 1D optical lattice and Bose-Hubbard Hamiltonian . . .	34
4.1	Coherent state truncation error . . . . .	90
4.2	Fundamental dark soliton solution of DNLS . . . . .	92
4.3	DNLS soliton propagation . . . . .	94
4.4	Density and phase measures during quantum evolution of a standing mean-field soliton . . . . .	95
4.5	Natural orbital dynamics during quantum evolution of a standing mean- field soliton . . . . .	98
4.6	Quantum measures during quantum evolution of a standing mean-field soliton . . . . .	100
4.7	Growth times of quantum effects and correlation to soliton lifetime .	103
4.8	Anomalous Bogoliubov mode: Density profile, comparison to first de- pleted mode, and frequency . . . . .	107
4.9	Low frequency Bogoliubov modes: Ground and first excited state of DNLS . . . . .	109
4.10	Dark soliton engineering in DNLS . . . . .	112
4.11	DNLS soliton-soliton collision . . . . .	114
4.12	Density and phase measures for quantum evolution of a mean-field soliton-soliton collision . . . . .	116
4.13	Natural orbital dynamics during quantum evolution of a mean-field soliton-soliton collision . . . . .	117



4.14	Quantum measures for quantum evolution of a mean-field soliton-soliton collision . . . . .	118
4.15	Inelastic soliton-soliton collision induced by quantum fluctuations . .	119
5.1	Schematic of density and phase engineering a standing soliton . . . .	125
5.2	Standing soliton engineering in DNLS . . . . .	127
5.3	Engineered standing soliton propagation in DNLS . . . . .	128
5.4	Density and natural orbital dynamics for engineered standing quantum soliton . . . . .	129
5.5	Quantum measures for engineered standing quantum soliton . . . . .	130
5.6	Engineered dark soliton decay times . . . . .	133
5.7	Quantum-induced inelasticity for quantum engineered dark solitons .	135
6.1	Comparison of dynamic and equilibrium quantum phase transition . .	143
6.2	Time evolution of transverse spin components . . . . .	145
6.3	Snapshot of formed magnetic domains . . . . .	146
6.4	Calculation of power law scaling exponent in time . . . . .	148
B.1	Dependence of observables on $\chi$ for quantum evolution of a standing mean-field soliton . . . . .	181
B.2	Relative error of observables with different $\chi$ for quantum evolution of a standing mean-field soliton . . . . .	182
B.3	Truncation error and conservation of good quantum numbers for quantum evolution of a standing mean-field soliton . . . . .	183
B.4	Dependence of observables on $\chi$ for engineered standing quantum soliton	184
B.5	Relative error of observables with different $\chi$ for engineered standing quantum soliton . . . . .	185
B.6	Truncation error and conservation of good quantum numbers for engineered standing quantum soliton . . . . .	186

## ACKNOWLEDGMENT

Looking back on my physics education over the last five years, there are many people with whom I am grateful to have interacted. Here, I would like to acknowledge those who have encouraged and inspired me.

I would like to first and foremost thank my advisor, Lincoln Carr. I started doing research with Dr. Carr during my junior year. In fact, at that time, I knew very little about quantum mechanics and was then enrolled in an undergraduate quantum class. Directly applying the concepts learned in class to a research problem was quite enjoyable and really accelerated my understanding of the material. I am thankful that Dr. Carr is so willing to take on undergraduates and expose them to cutting-edge research so early on in their physics lives. I know that the opportunity he gave me to do undergraduate research and pursue a Master's degree will be invaluable as I continue on in my career. Not only am I thankful to Dr. Carr for spilling onto me his knowledge of physics, but I also appreciate the advice he gives on *how* to practice physics. I admire the strong belief he has in his work and the importance he places on presenting work. Finally, his strong criticisms, e.g., on my papers and this thesis, are always appreciated because I know that he knows what is best.

However, I must say that Dr. Carr is only the second most critical person to have ever critiqued my work: Richard Ransome, my high school English taker, wins in that regard. I believe that Mr. Ransome's class is that which is most responsible for the mental strength that I now have, a strength necessary to pursue a physics career. I also must acknowledge Pat Mara, my high school math teacher, for giving me what is arguably the most solid mathematics foundation possible at that level.

I would of course like to thank all the professors I had while at Colorado School of Mines. Chris Kelso and David Flammer, my first physics professors, inspired me to major in physics in the first place. I am grateful to Mark Coffey and David Wood for serving as members on my thesis committee. The classes that I took from John Scales (undergrad quantum), Jim Bernard (undergrad stat. mech.), Mark Coffey (quantum computing), Lincoln Carr (graduate quantum), and David Wood (solid state) were especially important for my understanding of the basic foundations of the problems considered in this thesis. I must also thank Barbara Pratt-Johnson for being *so* helpful as secretary in our CSM physics department.

My experience at NIST, Gaithersburg, in Summer of 2007 was necessary for much of the material in this thesis. I am very grateful to Charles Clark for giving me the opportunity to work in his group at NIST. The penetrating insight into my work by both Charles and Ippei Danshita were instrumental in me understanding the physics of the projects contained herein. I also must thank Ippei and Jamie Williams for their many, many hours spent on TEBD code development. Without Ippei's help, my understanding of the TEBD algorithm would be nowhere near where it is now.

When I first started this project, I worked with Roger Brown and Dustin McIntosh. To this day, I still bounce ideas off of them. Dimitri Dounas-Frazier taught me the definition of *good work*. I constantly use his work as a measuring stick for my own, but I never quite measure up. I also thank Daniel Schirmer for sharing his computer expertise and Michael Wall for sharing his deep knowledge of quantum theory.

Last, but certainly not least, I would like to thank my parents for, well, everything. Their support and encouragement have been unwavering at every step of the way. Without them, I would not be nearly the person I am today. I simply could not have asked for better parents.

I was born not knowing and have had only a little time to change that here and there.

-Richard P. Feynman

## Chapter 1

### INTRODUCTION

This introductory chapter gives a thorough review of the main theories and experiments pertaining to Bose-Einstein condensation and ultracold atoms in optical lattices. We discuss the history of simulation techniques used for many-body quantum lattice systems and also review the theories and experimental studies of solitons and dynamical phase transitions in spinor condensates. The chapter concludes with a short overview of the entire thesis.

#### 1.1 Ultracold Atoms and Bose-Einstein Condensation

Low-temperature phenomena have been at or near the forefront of modern physics for a large part of the past century. Among early advances, Einstein in 1925, inspired by the work of Bose on photon statistics a year earlier [1], predicted a phase transition of non-interacting bosons when cooled below a critical temperature [2]. This phase transition is characterized by macroscopic occupation, i.e., condensation, of the particles into the lowest-lying single-particle quantum state. Known today as Bose-Einstein condensation (BEC), this phenomenon now allows scientists to study, test, and apply the microscopic theory of quantum mechanics in macroscopic settings. However, for typical dilute Bose gases, the onset of BEC occurs at *ultracold* temperatures ( $\sim 100$  nanokelvin), and it wasn't until 70 years after Einstein's prediction that BEC was first observed in the laboratory. Combining laser cooling techniques pioneered by Chu, Cohen-Tannoudji, and Phillips (1997 Nobel Prize) with the technique

of evaporative cooling, groups at Colorado, MIT, and Rice were able to experimentally create BEC in dilute atomic vapors of rubidium [3], sodium [4], and lithium [5], respectively. The 2001 Nobel Prize recognized the achievements of the former two.

Ever since the experimental birth of BEC 13 years ago, theoretical and experimental research in ultracold atomic gases has progressed at an astonishing rate. This excitement can mainly be attributed to the following characteristics of systems of ultracold atoms: (i) precise control of external fields which leads to precise knowledge of system parameters; (ii) the ability to probe the properties of the system in unprecedented detail; and (iii) knowledge of a detailed description of the system's microscopic properties. These characteristics make systems of ultracold atoms not only a perfect testbed for the fundamentals of quantum theory in macroscopic systems, but they also open up exciting possibilities for applications of quantum theory. Examples of the former case include studies of ultracold collisional properties of atoms and molecules [6] and the experimental demonstration of matter-wave coherence of Bose-Einstein condensates via observation of interference between two initially separated Bose condensed clouds [7]. Examples of applications of BEC-related systems include the creation of atom lasers with Bose-condensed atoms [8], measurement of the deviation of Newtonian gravity at small length scales [9], and proposals to build a quantum computer via controlled manipulations of ultracold atoms [10].

Einstein's original prediction of Bose condensation was for the case of non-interacting particles. A natural question arises: how do interactions affect the occurrence of BEC? Penrose and Onsager formally defined BEC in interacting systems by noting that off-diagonal long-range order in the system's single-particle density matrix is closely related to the onset of BEC; in this formalism, the condensate wave function and condensate fraction can be calculated via an eigen-decomposition of

the single-particle density matrix [11]. Strong interactions may prevent the formation of BEC altogether. However, the zero-temperature statics and dynamics of a weakly interacting dilute Bose gas in the mean-field limit is, somewhat surprisingly, well-described by the so-called nonlinear Schrödinger (NLS) or Gross-Pitaevskii (GP) equation [12]. This equation is equivalent to the usual linear Schrödinger equation in quantum mechanics with the addition of a nonlinear term representing the effective potential of the condensate's mean field on the condensate wave function. In this treatment, it is still assumed that all particles occupy only one single-particle state which, up to normalization, corresponds to the condensate wave function; the effects of interactions are taken into account by a two-body contact interaction that leads to a relatively simple and intuitive, yet nonlinear, equation describing the condensate. The NLS is ubiquitous and has been studied extensively in many fields outside of ultracold atomic gases including nonlinear optics [13] and integrable nonlinear equations [14]. In the BEC context, the NLS has proven an excellent model for experiments in harmonic traps [12, 15, 16, 17]. However, for the lattice geometries discussed in the next section, one must usually go beyond mean-field theory and use a more complete quantum many-body description, as we will demonstrate in this thesis. Perturbations of pure mean-field (NLS) theory usually begin with the original prescription of Bogoliubov in which quasiparticle amplitudes are added onto a stationary condensate wave function resulting in a linearization of the GP equation [18]. Other formalisms that go beyond GP theory include the Hartree-Fock and Popov [19] approximations which can be used to describe elementary excitations due to thermal or quantum fluctuations [20].

## 1.2 Ultracold Atoms in Optical Lattices

Systems of ultracold atoms in optical lattice potentials may presently be the most versatile BEC-related system both for studies of fundamental quantum many-body phenomena as well as for potential applications of ultracold atoms. Mainly due to experimental convenience, BEC was originally achieved in harmonic trap geometries; however, counter-propagating laser beams can be used to produce a standing light field and hence a periodic *optical* potential for the atoms. In 1998, Anderson and Kasevich performed the first experiment of Bose-Einstein condensates in an optical lattice [21]. The unprecedented control of system parameters mentioned in the previous section especially holds in optical lattice systems where experimentalists can rather trivially adjust the height of the lattice by changing the intensity of the laser field used to create it. The height of the lattice can be used to control the strength of atom-atom interactions, but it should be noted that interaction strength, symmetry, and sign (repulsive versus attractive) can be varied independent of the lattice height via use of a Feshbach resonance [22]. In these systems, experimentalists presently also have control over the lattice site filling factor, lattice geometry and dimensionality, as well as species type (bosons versus fermions). The importance of using ultracold atoms here is not necessarily to achieve BEC. In fact, BEC-like many-body states in optical lattices are not energetically favorable if the lattice height is too great. Instead, ultracold temperatures are necessary so that the thermal energy of the atoms does not exceed the lattice height energy and the atoms remain confined in the lattice. Also, ultracold temperatures allow for the study of purely quantum mechanical phenomena without the intervention of finite-temperature effects.

Ultracold atoms in optical lattices behave very much like electrons in periodic crystals. Instead of feeling the Coulomb potential of ionized atoms, the atoms interact



with the periodic laser light through the AC-Stark effect, creating an effective periodic potential. However, optical lattice systems are experimentally and theoretically (except for non-uniformity and finite-size corrections) much cleaner than their solid state counterparts: first, there are no impurities present, as is unavoidable in real solid state systems; and second, the lattice sites remain stationary, so there are no atom-phonon interactions as there are electron-phonon interactions in naturally-occurring crystals. For these reasons, along with the advantages mentioned above, ultracold atoms in optical lattices can be used to effectively design condensed matter systems. In fact, as was shown in the seminal paper of Jaksch *et al.*, an optical lattice containing ultracold bosons is an almost perfect realization of the Bose-Hubbard Hamiltonian [23], a model introduced in 1989 by M. P. A. Fisher *et al.* to describe short-range interacting bosons on a lattice [24]. Similarly, an optical lattice containing ultracold fermions is an excellent realization of the well-known Hubbard Hamiltonian introduced by J. Hubbard in 1963 [25] and solved analytically in one spatial dimension by Lieb and Wu in 1968 [26]. If the fermions are allowed to couple to a bosonic molecular state, then one arrives at a Fermi-Bose-Hubbard Hamiltonian which may eventually be used to fully describe the Bardeen-Cooper-Schrieffer to Bose-Einstein condensation (BCS-BEC) crossover in an atomic Fermi gas trapped on a lattice [27, 28, 29, 30, 31].

Traditionally, theoretical investigations of condensed matter Hamiltonians, e.g., the Hubbard and Bose-Hubbard models, have focused almost exclusively on the static ground state properties of the system. The reason is that crystals in solid state are not easily moved far from equilibrium. One cannot alter the potential on the electrons due to the ionized atoms in a nontrivial way. Nor can one alter the electron-electron interaction. The system parameters are set by nature, and the initial task of the physicist is to determine the system's ground state. However, the control permitted

by ultracold atoms and optical lattices gives the physicist an ideal setting for studying far-from-equilibrium quantum many-body dynamics. Examples include the celebrated Greiner experiment of the non-adiabatic transition across the Mott-superfluid boundary [32, 33], numerous experiments designed to study quantum transport phenomena [34, 35] including the experimental observation of Bloch oscillations [36, 37], and recent theoretical works investigating relaxation properties of the system after a quantum quench [38, 39].

When working with a lattice geometry, unlike in simpler geometries such as the harmonic trap, pure mean-field theory and its perturbations are not always a satisfactory description of the many-body physics. In fact, at a critical value of the lattice height, a system of ultracold bosons on an optical lattice undergoes a *quantum phase transition* from a superfluid to a Mott insulator, an effect that pure mean-field theory, i.e., the GP equation, will completely fail to describe. Generally speaking, a quantum phase transition is characterized by a fundamental change in some macroscopic order parameter as the system is swept through a critical point; the transition is driven by quantum, not thermal, fluctuations and thus occurs even at zero temperature. The superfluid-Mott insulator quantum phase transition in the Bose-Hubbard model was first predicted in the condensed matter context by Fisher *et al.* [24]. In 1998, Jaksch *et al.* demonstrated that the same quantum phase transition should be realizable in an optical lattice [23]; this prediction was proven correct by the experimental work of Greiner *et al.* four years later [32]. If the kinetic energy of the atoms dominates the atom-atom interaction energy, i.e., for a sufficiently weak lattice potential, then one has a superfluid-like many-body ground state. The condensate fraction is large and there is long-range phase coherence in the system due to macroscopic occupation of a delocalized single-particle orbital. But, as the

lattice height is raised, the energetically preferable single-particle states are localized about each site, so that the many-body ground state is a Mott insulator. In this case, one has entered the strongly correlated regime. Then, a full quantum many-body description of the problem is necessary. Experimentally, the phase transition is observed by taking absorption images of the matter wave interference pattern in time of flight (see Figure 2 in [32]). Although certain mean-field theories can give insight into nature of this phase transition [23], a full solution of the Bose-Hubbard Hamiltonian is required for accurate calculations.

### 1.3 Simulation Techniques, Solitons, and a Spin-1 Phase Transition

Simulating an  $N$ -body quantum system is a notoriously difficult task due to exponential growth of the Hilbert space dimension with system size. For concreteness, consider a single-band lattice problem containing  $M$  lattice sites. If we restrict each site to contain at most  $d - 1$  bosons, then the Hilbert space containing all pure states of this many-body quantum system is  $d^M$ -dimensional. This space is prohibitively large, especially if one wants to perform exact diagonalization of the governing Hamiltonian. However, there do exist well-established numerical methods, such as quantum Monte Carlo [40] and density matrix renormalization group (DMRG) [41], that can accurately calculate the system's ground state. Recently, G. Vidal developed the time-evolving block decimation (TEBD) algorithm: a time-adaptive DMRG (t-DMRG) routine rooted in quantum information theory that allows efficient classical simulation of slightly entangled one-dimensional quantum many-body systems [42, 43]. Specifically, given that the amount of entanglement is not too large, one can accurately simulate time-dependent quantum many-body phenomena in such a way that the simulation scales *linearly* with the number of lattice sites. The simulation

protocol requires specification of an entanglement cutoff parameter, which we denote as  $\chi$ , that should be chosen close to the system's Schmidt number [44] for accurate results [42]. Although Vidal's original papers were in the context of quantum computation and quantum simulation, Daley *et al.* [45] and White and Feiguin [46] soon translated the algorithm into the more familiar DMRG language. The important difference between TEBD and early attempts at time-dependent DMRG lies in TEBD's ability to *adapt* the truncated Hilbert space so as to most accurately represent the time-evolving quantum state [47]. In this thesis, we employ the TEBD algorithm to simulate quantum many-body dynamics in the Bose-Hubbard Hamiltonian.

In particular, for the scalar Bose-Hubbard model, we consider the quantum evolution of *solitons*. Solitons are robust nonlinear waves that appear throughout nature. Regardless of the physical system in which they occur, solitons are characterized by stable, non-dispersing propagation of either a minima (dark solitons) or a maxima (bright solitons) of the physically relevant dependent variable, e.g., electric field intensity or particle number density. Solitons have been observed in many places in nature including, but not limited to, fiber optics, plasmas, DNA, and water: an example of a soliton in the last case is a tsunami. It has been well-known for decades, since the seminal papers of Zakharov and Shabat on the inverse scattering transform [48, 49], that solitons exist as solutions to the NLS. However, the success of the NLS as a model to describe the ultracold atomic Bose gas, as well as the observation of solitons in systems such as photonic crystals and nonlinear waveguide arrays, excited a new interest in solitons in the last decade. Both dark [15, 16, 50, 51] and bright [52, 53] solitons have been observed experimentally in systems of ultracold atoms. On the theoretical side, solitons in Bose-Einstein condensates have been studied extensively using the mean-field NLS approach both in the free continuum [54, 55] and

on the periodic lattice [56]; in the latter case, the lattice soliton solutions of the NLS have been mapped out in detail [57, 58]. Discretization of the continuous NLS on a lattice using a lowest Bloch band tight-binding approximation results in the *discrete* nonlinear Schrödinger equation (DNLS) [59]. However, the DNLS is more perspicuously obtained as a mean-field approximation of the quantum Bose-Hubbard Hamiltonian [60]. Solitons in fundamentally discrete models, e.g., the DNLS and the Ablowitz-Ladik equation [61], have been given much attention both in purely mathematical [62, 63] and in BEC-related [59, 64] contexts. A large portion of this thesis is devoted to addressing how *quantum* effects such as fluctuations and entanglement affect the stability of dark solitons on a lattice, thereby providing a quantitative measure of the applicability of mean-field theory. To this end, we study analogs of the dark soliton solutions of the DNLS in a quantum Bose-Hubbard setting. Using Bogoliubov-based methods and few-mode approximations, Dziarmaga and Sacha characterized the effects of quantum fluctuations on excited condensates, e.g., soliton-like states, in continuous geometries [65, 66, 67, 68, 69]. Using related methods, Law studied the dynamical depletion of dark solitons created via phase imprinting [70]. An early study of quantum *lattice* solitons is presented in [71]; a quantum theory of solitons in optical fibers was developed by Lai and Haus [72]. Here, we present the first full entangled dynamical quantum many-body treatment of dark solitons formed by ultracold atoms in optical lattices.

The final component of this thesis involves a dynamical phase transition involving bosons with a contributing internal degree of freedom, namely the hyperfine degree of freedom. This degree of freedom arises from the interaction of the nuclear spin with the outer electronic spin which results in a splitting of atomic energy levels. In the presence of a magnetic field, the energy levels are further split by the Zeeman

effect leading to different possible hyperfine sublevels labeled by the projection of the atomic spin in the direction of the field [20, 73]. The hyperfine degree of freedom ultimately manifests itself in the dynamics of an ultracold Bose gas through spin-dependent scattering process between atoms. In traditional BEC experiments in magnetic traps, the spin degree of freedom plays no role because the trap selects only a single hyperfine species so that there exist no spin-conserving collisional processes to change the hyperfine levels of the atoms. The atoms in such experiments are referred to as spinless or *scalar* bosons. In 2006, an experiment was performed at Berkeley involving a dynamical phase transition in a system of  $^{87}\text{Rb}$  atoms in an optical trap [74]. In optical traps, unlike in magnetic traps, it is possible to simultaneously hold atoms with different magnetic sublevels, so that the hyperfine degree of freedom does in general contribute to the physics. This was demonstrated in the first spinor BEC experiments performed at MIT in the late 1990s [75, 76]. In the Berkeley experiment, through the quadratic Zeeman effect, a strong uniform magnetic field (not a magnetic trap) was used to create a polar condensate with all atoms in the zero hyperfine level. Because  $^{87}\text{Rb}$  atoms interact with a ferromagnetic sign, there is an energy competition between the quadratic Zeeman and spin-dependent interaction terms in the governing Hamiltonian: the former prefers a ground state phase with zero net magnetization, whereas the latter prefers a ferromagnetic broken-symmetry phase. When quenching the applied magnetic field below the critical value that separates these two phases, a spontaneous symmetry breaking occurs. Such a quench was performed in the Berkeley experiment, and the subsequent evolution revealed formation of spin textures, magnetic domains, and topological spin polar core vortices. If instead of an instantaneous quench, the magnetic field is decreased adiabatically but still fast enough to produce macroscopic excitations, it has been shown [77, 78, 79] that scaling

properties of the system can be described by the Kibble-Zurek mechanism, a theory that predicts topological defect formation during nonequilibrium phase transitions. The Kibble-Zurek mechanism was originally proposed by Kibble in the context of nonequilibrium evolution in the early Universe [80, 81] and later shown by Zurek to be applicable in tabletop condensed matter experiments [82, 83]. Numerous studies have thus far been performed on the aforementioned spinor condensate phase transition investigating both the instantaneous [84, 85] and finite-rate [77, 79, 78] quench; on the other hand, symmetry restoration dynamics can be achieved by quenching in the opposite direction from the broken-symmetry to the polar phase [86]. Investigations of Kibble-Zurek mechanism in the quantum Ising [87] and Landau-Zener [88] models suggest a quantum version of the mechanism. Using TEBD, we eventually hope to simulate a fully quantum Kibble-Zurek mechanism in a system of ultracold spin-1 bosons on an optical lattice. In Chapter 6, we present a numerical analysis of the dynamical quantum phase transition using the corresponding discrete mean-field theory, i.e., a DNLS with a three-component vector order parameter. These calculations are inspired by the recent work of Damski and Zurek in which the authors investigate the Kibble-Zurek mechanism in a system of spin-1 ferromagnetic Bose condensates in a continuous 1D box [78].

#### 1.4 Thesis Overview

The remainder of the thesis is organized as follows. Chapter 2 provides the reader a background on some fundamental aspects of ultracold quantum gases. In particular, we discuss Bose-Einstein condensation for both non-interacting and interacting systems, the atomic and optical physics governing how optical potentials influence atoms, and the pertinent models we use to describe both scalar and spin-1 bosons on

optical lattices. Chapter 3 is devoted to the numerical methods we employ to simulate the system both in the mean-field and quantum pictures. For the latter case, we explain the important aspects of the TEBD routine and our implementation of it. In Chapter 4, we consider the quantum many-body evolution according to the Bose-Hubbard Hamiltonian of mean-field dark soliton initial states. We also perform a static Bogoliubov calculation for a dark soliton. The beginning of the chapter focuses on the measures that we employ to characterize the system during quantum evolution. In Chapter 5, we propose a scheme to quantum engineer dark solitons using density and phase manipulation techniques. Both standing solitons and soliton-soliton collisions are studied in Chapters 4 and 5. We show that quantum many-body effects cause stationary dark solitons to fill in and can induce an inelasticity in a collision between two solitons. In Chapter 6, we present preliminary mean-field results of a Kibble-Zurek phase transition for spin-1 bosons in the presence of a lattice; the direction of future quantum many-body studies is suggested. Finally, in Chapter 7, we summarize our results and present an outlook on where this work may head in the future. In Appendix A, we derive Vidal decompositions for simple but important states. Discussion of the accuracy and convergence of our results obtained via TEBD can be found in Appendix B. Appendices C and D contain important pieces of code used for mean-field and TEBD calculations, respectively.



## Chapter 2

### BACKGROUND: FUNDAMENTALS OF ULTRACOLD QUANTUM GASES AND THEORETICAL CONNECTIONS BETWEEN MODELS

The purpose of this chapter is to review the fundamental principles of the theory of BEC and optical lattices, as well as to derive and connect the pertinent models describing ultracold atomic gases on optical lattices. First, a general discussion of Bose-Einstein condensation is given. This includes derivations of the critical temperature and condensate fraction for the non-interacting Bose gas in simple harmonic trap geometries as well as consideration of the effects of interactions on Bose condensation. We then formally discuss the basic atomic physics governing optical lattice potentials including a derivation of the AC-Stark effect. Next, the continuous Gross-Pitaevskii or nonlinear Schrödinger equation is derived from the full continuous Hamiltonian in second quantization, and the Bose-Hubbard Hamiltonian is obtained as a discretization of the second-quantized continuous Hamiltonian for the case of an optical lattice potential. Then, connections are made between the continuous Gross-Pitaevskii equation, the Bose-Hubbard Hamiltonian, and the *discrete* nonlinear Schrödinger equation. Finally, we discuss the hyperfine degree of freedom and derive the spin-1 Bose-Hubbard Hamiltonian and vector discrete nonlinear Schrödinger equation which describe a system of spin-1 bosons on a lattice.

## 2.1 Bose-Einstein Condensation

In this section, we discuss the concepts and mathematics behind Bose-Einstein condensation for both non-interacting and interacting systems.

### 2.1.1 Non-Interacting Systems

For the case of a uniform, non-interacting gas of spinless bosons, the formal mathematics behind BEC is a standard topic in textbooks on statistical physics. For example, see Reference [89]. Here, we summarize those results and formally derive the critical temperature for condensation and the condensate fraction. The derivations are based explicitly on discussion presented in Chapter 2 of Reference [20]. To begin, the statistical distribution function for non-interacting bosons in thermal equilibrium at temperature  $T$  is

$$f_{\text{BE}}(\epsilon_\nu, \mu, T) = \frac{1}{e^{(\epsilon_\nu - \mu)/k_B T} - 1}, \quad (2.1)$$

where  $\epsilon_\nu$  is the energy of the single-particle state  $|\nu\rangle$ ,  $\mu$  is the chemical potential, and  $k_B$  is Boltzmann's constant. The function  $f_{\text{BE}} \equiv \langle \nu | \hat{n} | \nu \rangle$  is the mean occupation of the single-particle state  $|\nu\rangle$ . The chemical potential appears as a Lagrange multiplier that ensures the total number of particles  $N$  is conserved; it is defined implicitly by requiring  $N = \int d\epsilon g(\epsilon) f_{\text{BE}}(\epsilon, \mu, T)$ , where  $g(\epsilon)$  is the energy density of states that is used to convert sums over discrete sets of states to integrals over energy. The dimensionless quantity  $g(\epsilon)d\epsilon$  is the number of allowed energy states in the region of the energy spectrum from  $\epsilon$  to  $\epsilon + d\epsilon$ . For concreteness, we consider a density of states of the form

$$g_\alpha(\epsilon) = C_\alpha \epsilon^{\alpha-1}, \quad (2.2)$$

which appears in many contexts, e.g., free, boxed, and harmonically trapped particles in  $d = 1, 2$ , or  $3$  dimensions [20].  $C_\alpha$  and  $\alpha$  are constants that depend on the specific potential.

To calculate the condensation critical temperature and condensate fraction, we note that if the number of particles  $N$  is sufficiently large, the zero-point energy of the atoms may be neglected, and we are allowed to set the minimum of energy to zero. The number of particles in *excited states* is therefore given by

$$N_{\text{ex}} = \int_0^\infty d\epsilon g_\alpha(\epsilon) f_{\text{BE}}(\epsilon, \mu, T), \quad (2.3)$$

which is maximized for  $\mu = 0$ . The critical temperature  $T_c$  is defined as the temperature at which all  $N$  particles reside in excited states for  $\mu = 0$ :

$$N = N_{\text{ex}} = \int_0^\infty d\epsilon g_\alpha(\epsilon) f_{\text{BE}}(\epsilon, \mu = 0, T_c). \quad (2.4)$$

Thus, the critical temperature for BEC can be viewed as the temperature below which additional particles added to the system can only enter the ground state, in equilibrium. The integral in Equation (2.4) can be evaluated analytically to obtain an expression for  $T_c$  with the result being

$$k_B T_c = \frac{N^{1/\alpha}}{[C_\alpha \Gamma(\alpha) \zeta(\alpha)]^{1/\alpha}}, \quad (2.5)$$

where  $\Gamma(\alpha)$  and  $\zeta(\alpha)$  are the gamma and Riemann zeta functions evaluated at  $\alpha > 1$ . Below  $T_c$ , we may compute the total occupation of excited states as before:

$$N_{\text{ex}} = \int_0^\infty d\epsilon g_\alpha(\epsilon) f_{\text{BE}}(\epsilon, \mu = 0, T) = C_\alpha \Gamma(\alpha) \zeta(\alpha) (k_B T)^\alpha = N \left( \frac{T}{T_c} \right)^\alpha, \quad (2.6)$$

where the last equality makes use of (2.5). The *condensate fraction* at temperature  $T$  is thus given by

$$\frac{N_0}{N} = \frac{N - N_{\text{ex}}}{N} = \left[ 1 - \left( \frac{T}{T_c} \right)^\alpha \right]. \quad (2.7)$$

*Bose-Einstein condensation* refers to the macroscopic population of the lowest-lying state ( $N_0/N \sim 1$ ) for temperatures  $T < T_c$ , although the term can be generalized to include macroscopic occupation of any single-particle state, a point we address in the next section.

Now, we briefly consider the effect of reduced dimensionality on BEC. Consider the three-dimensional (3D) harmonic oscillator potential in which case  $\alpha = 3$  and  $C_3 = (2\hbar^3 \omega_x \omega_y \omega_z)^{-1}$ , with  $\omega_i$  being the trapping frequency in direction  $i$ . From (2.5), we have for the critical temperature

$$k_B T_{c,3D} = \left[ \frac{N}{\zeta(3)} \right]^{1/3} \hbar \bar{\omega}_{3D} \approx 0.94 N^{1/3} \hbar \bar{\omega}_{3D} \approx 4.5 \left( \frac{\bar{\omega}_{3D}}{2\pi \cdot 100 \text{ Hz}} \right) N^{1/3} \text{ nK} \cdot k_B, \quad (2.8)$$

where  $\bar{\omega}_{3D} \equiv (\omega_x \omega_y \omega_z)^{1/3}$  is the geometrical mean of the three trapping frequencies [20]. A two-dimensional (2D) BEC can be obtained in the  $x$ - $y$  plane in a harmonic trap geometry given

$$\hbar \omega_z > k_B T_{c,2D} \gg \hbar \bar{\omega}_{2D}, \quad (2.9)$$

where  $\bar{\omega}_{2D} \equiv (\omega_x \omega_y)^{1/2}$  and the critical temperature can be computed using (2.5) with  $\alpha = 2$  resulting in

$$k_B T_{c,2D} = \left[ \frac{N}{\zeta(2)} \right]^{1/2} \hbar \bar{\omega}_{2D} \approx 0.78 N^{1/2} \hbar \bar{\omega}_{2D} \approx 3.7 \left( \frac{\bar{\omega}_{2D}}{2\pi \cdot 100 \text{ Hz}} \right) N^{1/2} \text{ nK} \cdot k_B. \quad (2.10)$$

The one-dimensional (1D) case is of special importance, since all new results in this thesis pertain to 1D models. For a 1D harmonic trap,  $\alpha = 1$ , and the integral

(2.4) defining the critical temperature diverges. Hence, BEC does not occur in 1D in the thermodynamic limit; however, given the one-dimensionality condition

$$\omega_y, \omega_z \gg \omega_x, \quad (2.11)$$

macroscopic occupation of the lowest-lying state can still occur in a *finite* one-dimensional system aligned in the  $x$ -direction. BEC is thus not restricted to 3D systems. In fact, it has been observed experimentally in 2D and 1D as well [90].

### 2.1.2 Interacting Systems

In 1956, Penrose and Onsager elaborated on an earlier work by Penrose [91] and developed an extremely useful criterion for defining the onset of BEC for the case of interacting particles [11]. Their work was originally in the context of liquid helium, but it applies equally well to any system of Bose particles, liquid or gas. The basic idea is as follows. For a non-interacting ideal Bose gas, we know from above that below the critical temperature a finite fraction of the particles occupy the lowest single-particle *energy level* of the system's single-particle Hamiltonian. However, when interactions are added into the picture, macroscopic occupation of the lowest single-particle energy eigenstate will not necessarily occur. The contribution of Penrose and Onsager was to (1) consider the von Neumann statistical operator [92], i.e., the density matrix  $\hat{\rho}$ , in a basis of the real-space coordinates of the  $N$  particles that constitute the many-body system, (2) perform a partial trace over all but one of the  $N$  particles resulting in the *single-particle density matrix* denoted  $\hat{\rho}_{\text{sp}} \equiv N \text{Tr}_{2\dots N}(\hat{\rho})$ , (3) diagonalize the (Hermitian) single-particle density matrix, and (4) note that the eigenstates of the single-particle density matrix are the system's single-particle *natural orbitals* with occupation numbers given by the corresponding eigenvalues. This is conceptually

equivalent to diagonalization of a general density matrix describing a mixed quantum system:

$$\hat{\rho} = \sum_{\alpha} w_{\alpha} |\psi_{\alpha}\rangle \langle \psi_{\alpha}| \rightarrow \sum_n p_n |n\rangle \langle n|, \quad (2.12)$$

where  $|n\rangle$  are the eigenstates of  $\hat{\rho}$  with eigenvalues  $p_n$ . The usual interpretation is that the mixed quantum system described by  $\hat{\rho}$  will be found in the pure state  $|n\rangle$  with probability  $p_n$ . Note, however, this is only a convenient interpretation since the density matrix does not *uniquely* specify the ensemble of quantum states present.

The single-particle density matrix is the reduced density matrix that describes a *single particle* which is, in general, in a mixed state due to it being part of a larger quantum system containing  $N > 1$  particles. We can say that if a particle's reduced density matrix, i.e., the single-particle density matrix, has more than one nonzero eigenvalue, then it is *entangled* with at least one of the remaining  $N - 1$  particles. In general, this will be the case because the particles are interacting [93]. One rather trivial difference between the general density matrix given in (2.12) and  $\hat{\rho}_{\text{sp}}$  is that we take the eigenvalues of  $\hat{\rho}_{\text{sp}}$  to be actual occupation numbers and not occupation probabilities, hence  $\text{Tr}(\hat{\rho}_{\text{sp}}) = N$ . The main point made by Penrose and Onsager is that the system can be said to be Bose-condensed if the largest eigenvalue  $N_0$  of  $\hat{\rho}_{\text{sp}}$  remains on the order  $N$  while the other eigenvalues remain finite in the thermodynamic limit.

In practice, the matrix elements of the single-particle density matrix are calculated as two-point correlation functions between points  $\mathbf{r}$  and  $\mathbf{r}'$  [20, 73]. That is,

$$\rho_{\text{sp}}(\mathbf{r}, \mathbf{r}') \equiv \langle \mathbf{r} | \hat{\rho}_{\text{sp}} | \mathbf{r}' \rangle = \langle \hat{\Psi}^{\dagger}(\mathbf{r}') \hat{\Psi}(\mathbf{r}) \rangle, \quad (2.13)$$

where  $\hat{\Psi}(\mathbf{r})$  and  $\hat{\Psi}^{\dagger}(\mathbf{r})$  are the bosonic destruction and creation operators, respectively,

which destroy and create a boson in a given internal atomic state at position  $\mathbf{r}$ , and the expectation value is taken with respect to the state  $|\Psi\rangle$  of the many-body system. Thus,  $\rho_{\text{sp}}(\mathbf{r}, \mathbf{r}')$  is the amplitude for creating a particle at position  $\mathbf{r}'$  while destroying one at position  $\mathbf{r}$ . Diagonalization of the single-particle density matrix in position representation yields

$$\rho_{\text{sp}}(\mathbf{r}, \mathbf{r}') = \sum_j N_j \chi_j^*(\mathbf{r}') \chi_j(\mathbf{r}), \quad (2.14)$$

where  $\chi_j$  are the many-body system's single-particle *natural orbitals* with occupation numbers  $N_j$ . Since off-diagonal long-range order is required for a macroscopic eigenvalue of  $\rho_{\text{sp}}(\mathbf{r}, \mathbf{r}')$ , it is clear that BEC is directly related to off-diagonal long-range order [11, 94]. In fact, the presence of BEC *implies* off-diagonal long-range order, while its connection to superfluidity is less direct [95, 96, 97].

For systems of finite size, one cannot rigorously employ the criterion of Penrose and Onsager because it assumes the thermodynamic limit, i.e., the number of particles  $N$  and the system size  $L$  both tend to infinity while the ratio  $N/L$  remains constant. Specifically, we cannot strictly determine the *absence* of BEC for finite-size systems because the single-particle density matrix will always have an eigenvalue  $N_i \gtrsim a/L$  for finite  $L$ , where  $a$  is some natural length scale of the system [97]. However, this is just a formal complication, and we will still use the Penrose-Onsager prescription for calculating natural orbitals and the condensate fraction.

## 2.2 Optical Lattices

As discussed in Chapter 1, systems of ultracold atoms in optical lattices offer an enormous wealth of interesting physics. Such systems are useful both as ideal testbeds for quantum many-body dynamics as well as for exciting new applications of quantum theory. In this section, we discuss from an atomic and optical perspective

how individual atoms interact with laser light to create an effective optical lattice potential. The basic mechanism is the interaction of the electric field with the dipole moment of the atom that leads to an effective potential proportional to the intensity of the laser field.

For simplicity, consider a single-mode laser of frequency  $\omega_L$  and an atom with a ground state  $|g\rangle$  and excited state  $|e\rangle$  differing in energy by amount  $\hbar\omega_{eg}$ . We use the dipole approximation to describe the interaction between the atom and the electric field. The resulting Hamiltonian is

$$H_{\text{dip}} = -\mathbf{d} \cdot \mathbf{E}(\mathbf{r}, t), \quad (2.15)$$

where  $\mathbf{d}$  is the electric dipole moment of the atom and  $\mathbf{E}(\mathbf{r}, t)$  is the electric field. The standing light field created by two identical single-mode laser beams counter-propagating along the  $x$ -direction polarized in the  $\epsilon$ -direction with electric fields  $\mathbf{E}_{\pm}(x, t) = \epsilon E_0 e^{i(\pm kx - \omega_L t)}$  is given by

$$\mathbf{E}(x, t) = \mathbf{E}_+(x, t) + \mathbf{E}_-(x, t) = \epsilon 2E_0 \cos(kx) e^{-i\omega_L t} \rightarrow \epsilon 2E_0 \cos(kx) \cos(\omega_L t), \quad (2.16)$$

where  $k = \omega_L/c$  is the magnitude of the laser's wave vector. If the laser light only couples the ground state  $|g\rangle$  to the single excited state  $|e\rangle$ , then basic perturbation theory can be used to calculate the shift in the ground state energy due to the presence of the electric field [20]. The first nonzero term in perturbation theory is of second order and is referred to as the *AC-Stark shift*:

$$\Delta E_g(x) = -\frac{1}{2} \alpha < E^2(x, t) >, \quad (2.17)$$



where the angular brackets denote a time average and  $\alpha$  is the atomic polarizability. Taking only the term in  $\alpha$  with the smallest energy denominator, we find [20]

$$\alpha \approx -\frac{|\langle e|\mathbf{d} \cdot \boldsymbol{\epsilon}|g\rangle|^2}{\hbar \delta}, \quad (2.18)$$

where  $\delta \equiv \omega_L - \omega_{eg}$  is the *detuning*. The time average of the squared electric field can be calculated from Equation (2.16) from which, after a shift of the origin, we can write the *optical lattice potential* as

$$V_{\text{lat}}(x) \equiv \Delta E_g(x) = V_0 \sin^2(kx), \quad (2.19)$$

where the lattice height  $V_0 \equiv -\alpha E_0^2$  is proportional to the laser intensity. Note that the sign of the potential depends on whether we have blue detuning ( $\delta > 0$  and  $V_0 > 0$ ) or red detuning ( $\delta < 0$  and  $V_0 < 0$ ). We have made the following assumptions when deriving Equation (2.17) and hence Equation (2.19): (1) the excited state  $|e\rangle$  has an infinite lifetime, i.e., we have neglected the spontaneous emission of photons, and (2) the laser frequency is close to resonance so that the electric field couples the ground state  $|g\rangle$  to only a single excited state, namely  $|e\rangle$ . Succinctly, the validity of Equation (2.17), assuming no spontaneous emission, is  $\Omega_R(x) \ll |\delta|$ , where  $\Omega_R(x)$  is the position-dependent Rabi frequency that drives transitions between  $|g\rangle$  and  $|e\rangle$  [20, 98, 99].

To obtain a full 3D periodic potential landscape, two additional pairs of orthogonally polarized counter-propagating laser beams can be added to give

$$V_{\text{lat}}(\mathbf{r}) = V_{0x} \sin^2(k_x x) + V_{0y} \sin^2(k_y y) + V_{0z} \sin^2(k_z z). \quad (2.20)$$

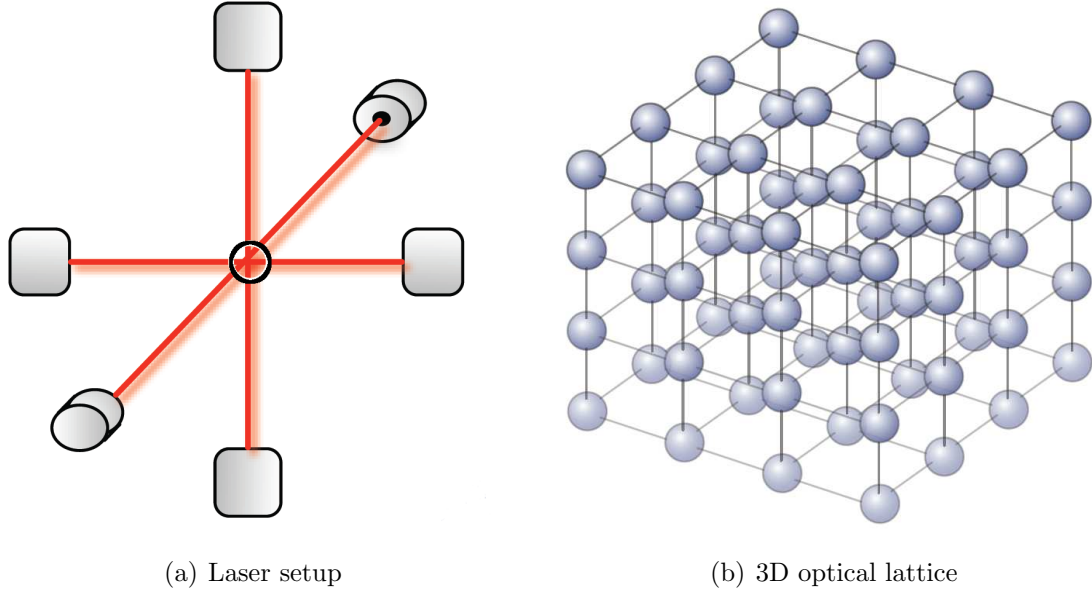


Figure 2.1. *Schematic of 3D optical lattice.* (a) Three pairs of counter-propagating laser beams add to give (b) a 3D optical lattice potential. The black circle at the intersection of the three pairs of laser beams in (a) indicates the array of lattice sites shown in (b). As explained in Section 2.3.3, ramping up the lattice height in one direction creates a stack of parallel 2D lattices, whereas ramping up the lattice height in two directions creates an array of parallel 1D lattices, i.e., an *array of 1D tubes* with a sinusoidal potential in the longitudinal direction. The latter situation gives rise to the 1D optical lattice depicted in in Figure 2.3.

The subscripts  $x, y, z$  on the factors  $V_0$  and  $k$  are needed to indicate that, if desired, the lattice heights and wave vectors can be altered in each direction independently. Experimentally, this tunability can be used to change the effective dimensionality of the system and/or create exotic lattice geometries. The geometry can also be altered by using beams not orthogonal to one another in which case interference terms appear in Equation (2.20) [100]. In Figure 2.1, we depict a schematic of a 3D optical lattice and the counter-propagating laser beams used to create it.

## 2.3 Governing Models for Scalar Bosons

In this section, we derive the models that we employ to study the behavior of scalar bosons at zero temperature both in the free continuum (full second-quantized Hamiltonian and Gross-Pitaevskii equation) and on the periodic lattice (Bose-Hubbard Hamiltonian and discrete nonlinear Schrödinger equation) and elucidate the connections between them.

### 2.3.1 Basic Quantum Many-Body Theory

Neglecting interaction processes involving three or more particles, the Hamiltonian of a system of  $N$  interacting spinless particles of mass  $m$  with positions  $\{\mathbf{r}_1, \mathbf{r}_2, \dots, \mathbf{r}_N\}$  and momenta  $\{\mathbf{p}_1, \mathbf{p}_2, \dots, \mathbf{p}_N\}$  is given in first quantization by

$$H = \sum_{i=1}^N \left[ \frac{\mathbf{p}_i^2}{2m} + V(\mathbf{r}_i) \right] + \frac{1}{2} \sum_{i \neq j} V_{\text{int}}(\mathbf{r}_i - \mathbf{r}_j), \quad (2.21)$$

where  $V(\mathbf{r})$  is an external potential and  $V_{\text{int}}(\mathbf{r}_i - \mathbf{r}_j)$  is the interaction potential between particles  $i$  and  $j$ ; the factor of  $1/2$  avoids double-counting interactions. In principle, the problem amounts to diagonalization of Equation (2.21) in the  $N$  coordinates  $\{\mathbf{r}_1, \mathbf{r}_2, \dots, \mathbf{r}_N\}$  while imposing a symmetry condition (symmetrical or antisymmetrical) on the wave function under any two-particle interchange to reflect the particles' quantum statistics (Bose-Einstein or Fermi-Dirac). For the general  $N$ -body problem, this is a task of hopeless difficulty.

It is more convenient to work in *second quantization* in which the corresponding Hamiltonian describing a system of interacting bosons at zero temperature is given

by [101]

$$\begin{aligned} \hat{H} = & \int d\mathbf{r} \hat{\Psi}^\dagger(\mathbf{r}) \left[ -\frac{\hbar^2}{2m} \nabla^2 + V(\mathbf{r}) \right] \hat{\Psi}(\mathbf{r}) \\ & + \frac{1}{2} \int d\mathbf{r} \int d\mathbf{r}' \hat{\Psi}^\dagger(\mathbf{r}) \hat{\Psi}^\dagger(\mathbf{r}') V_{\text{int}}(\mathbf{r} - \mathbf{r}') \hat{\Psi}(\mathbf{r}') \hat{\Psi}(\mathbf{r}). \end{aligned} \quad (2.22)$$

The field operators  $\hat{\Psi}$  and  $\hat{\Psi}^\dagger$  obey the canonical commutation relations:

$$[\hat{\Psi}(\mathbf{r}), \hat{\Psi}^\dagger(\mathbf{r}')] = \delta(\mathbf{r} - \mathbf{r}'), \quad (2.23)$$

$$[\hat{\Psi}(\mathbf{r}), \hat{\Psi}(\mathbf{r}')] = 0, \quad (2.24)$$

$$[\hat{\Psi}^\dagger(\mathbf{r}), \hat{\Psi}^\dagger(\mathbf{r}')] = 0, \quad (2.25)$$

where  $\delta(\mathbf{r} - \mathbf{r}')$  is the Dirac delta function. For completeness, we note that in the case of Fermi statistics, Equation (2.22) still holds except the commutation relations (2.23)–(2.25) are replaced by anti-commutation relations.

### 2.3.2 Continuous Gross-Pitaevskii Equation

The Gross-Pitaevskii (GP) equation can be used to accurately describe the zero-temperature statics and dynamics of a dilute, weakly interacting Bose gas. One can derive the GP equation in first quantization as follows [20]: first, assume a fully-condensed state so that the many-body wave function  $\Psi$  takes the form of a simple product  $\Psi(\mathbf{r}_1, \mathbf{r}_2, \dots, \mathbf{r}_N) = \prod_{i=1}^N \chi_0(\mathbf{r}_i)$ , where  $\chi_0$  is the single-particle state into which all particles are condensed; second, calculate the energy functional for this state using Equation (2.21) with a contact interaction for  $V_{\text{int}}$  [see Equation (2.31) below]; finally, minimize the energy functional with respect to variations of the condensate wave function and its complex conjugate under the constraint of fixed total particle

number to obtain the time-independent GP equation. Generalization to the time-dependent version is straightforward.

In the following, we derive the GP equation using the second quantization formalism. First, we evolve the bosonic field operator forward in time in the Heisenberg picture to obtain its evolution equation:

$$i\hbar \frac{\partial}{\partial t} \hat{\Psi} = [\hat{\Psi}, \hat{H}], \quad (2.26)$$

where  $\hat{\Psi} = \hat{\Psi}(\mathbf{r}, t)$  is a function of both position and time. On the right-hand side, the first two terms due to the kinetic energy and external potential are straightforward to evaluate. For the kinetic energy term, we have

$$[\hat{\Psi}(\mathbf{r}), \int d\mathbf{r}' \hat{\Psi}^\dagger(\mathbf{r}') \left( -\frac{\hbar^2}{2m} \nabla'^2 \right) \hat{\Psi}(\mathbf{r}')] = -\frac{\hbar^2}{2m} \nabla^2 \hat{\Psi}(\mathbf{r}), \quad (2.27)$$

where we have used the commutation relations in Equations (2.23)–(2.25) and suppressed writing explicitly the time dependence of  $\hat{\Psi}$ . Similarly, for the external potential term, we find

$$[\hat{\Psi}(\mathbf{r}), \int d\mathbf{r}' \hat{\Psi}^\dagger(\mathbf{r}') V(\mathbf{r}') \hat{\Psi}(\mathbf{r}')] = V(\mathbf{r}) \hat{\Psi}(\mathbf{r}). \quad (2.28)$$

To evaluate the interaction term, we note

$$\begin{aligned} & [\hat{\Psi}(\mathbf{r}), \hat{\Psi}^\dagger(\mathbf{r}') \hat{\Psi}^\dagger(\mathbf{r}'') V_{\text{int}}(\mathbf{r}' - \mathbf{r}'') \hat{\Psi}(\mathbf{r}'') \hat{\Psi}(\mathbf{r}')] \\ &= 2\delta(\mathbf{r}'' - \mathbf{r}') \hat{\Psi}^\dagger(\mathbf{r}'') V_{\text{int}}(\mathbf{r} - \mathbf{r}') \hat{\Psi}(\mathbf{r}'') \hat{\Psi}(\mathbf{r}), \end{aligned} \quad (2.29)$$

so, finally, we find

$$\begin{aligned} i\hbar \frac{\partial}{\partial t} \hat{\Psi}(\mathbf{r}, t) &= [\hat{\Psi}, \hat{H}] \\ &= \left[ -\frac{\hbar^2}{2m} \nabla^2 + V(\mathbf{r}) + \int d\mathbf{r}' \hat{\Psi}^\dagger(\mathbf{r}', t) V_{\text{int}}(\mathbf{r} - \mathbf{r}') \hat{\Psi}(\mathbf{r}', t) \right] \hat{\Psi}(\mathbf{r}, t). \end{aligned} \quad (2.30)$$

For a cold and dilute Bose gas, we can describe the interatomic potential by considering only binary contact collisions characterized by a single parameter  $a_s$ , the three-dimensional  $s$ -wave scattering length [12]. Specifically,

$$V_{\text{int}}(\mathbf{r} - \mathbf{r}') = g \delta(\mathbf{r} - \mathbf{r}'), \quad (2.31)$$

where

$$g \equiv \frac{4\pi\hbar^2 a_s}{m} \quad (2.32)$$

is proportional to the scattering length and thus parameterizes the interaction strength. Equation (2.31) is valid for low energies when all other relevant length scales of the system, i.e., the de Broglie wavelength of the atoms and the average interatomic spacing, are much larger than the range of the two-body scattering potential  $V_{\text{int}}$ . Throughout this thesis, we consider repulsively interacting atoms so that  $g > 0$ .

After inserting (2.31) into (2.30) and replacing the field operator  $\hat{\Psi}$  with the classical c-number  $\Phi \equiv N^{1/2} \chi_0$ , where  $\chi_0$  is the condensed *single-particle* state from above, we obtain the well-known Gross-Pitaevskii [102, 103] or nonlinear Schrödinger (NLS) equation:

$$i\hbar \frac{\partial}{\partial t} \Phi(\mathbf{r}, t) = \left[ -\frac{\hbar^2}{2m} \nabla^2 + V(\mathbf{r}) + g |\Phi(\mathbf{r}, t)|^2 \right] \Phi(\mathbf{r}, t). \quad (2.33)$$

The function  $\Phi(\mathbf{r}, t)$ , which we normalize to the number of particles  $N = \int d\mathbf{r} |\Phi(\mathbf{r}, t)|^2$ ,

is known as the condensate order parameter or condensate wave function, and, up to normalization, corresponds directly to the single-particle wave function into which we have Bose-Einstein condensation [73]. Note, however, that A. Leggett, the author of Reference [73], disagrees with defining the order parameter as the expectation value of the (non-Hermitian) field operator. For this definition to be valid, we fundamentally must have a non-conservation of total particle number and a broken Bose symmetry [104].

The derivation of Equation (2.33) assumed three spatial dimensions, although it is also valid in the quasi-1D and quasi-2D regimes where the gas is tightly confined in the transverse directions by means of a harmonic trap. To obtain the lower-dimensional equations one assumes separability of the condensate wave function in its transverse coordinates and projects onto the mean-field ground state in the transverse directions [105, 106, 107]. Then,  $\nabla^2$  becomes the appropriate  $d$ -dimensional Laplacian, and the coupling constant  $g$  becomes dependent on the transverse confinement. Specifically, in  $d$ -dimensions, we find the following for  $g \rightarrow g^{(d)}$ :

$$g^{(1)} = 2\hbar\omega_{\perp}a_s, \quad g^{(2)} = \sqrt{\frac{8\pi\hbar^3\omega_z}{m}}a_s, \quad \text{and} \quad g^{(3)} = \frac{4\pi\hbar^2a_s}{m}, \quad (2.34)$$

where  $g^{(3)}$  is included for completeness and  $\omega_{\perp}$  and  $\omega_z$  are the transverse trapping frequencies for 1D and 2D, respectively. The quasi-1D (-2D) regime is obtained if (1) the transverse confinement length  $\ell_{\perp} \equiv \sqrt{\hbar/m\omega_{\perp}}$  ( $\ell_z \equiv \sqrt{\hbar/m\omega_z}$ ) is on the order of the condensate healing length  $\xi \equiv 1/\sqrt{8\pi\bar{n}_0a_s}$ , where  $\bar{n}_0$  is the mean particle density, and (2) the trapping is sufficiently strong in the transverse directions so that  $\omega_{\perp} \gg \omega_x$  ( $\omega_z \gg \omega_x, \omega_y$ ), where we have assigned  $x$  the longitudinal direction in 1D and the  $x$ - $y$  plane the 2D plane for 2D. The term *quasi* is used to describe the lower dimensionality because even though excitations only occur along the longitudinal

direction, the underlying scattering process is still three-dimensional so long as the transverse confinement length is much greater than the scattering length. For systems in which the confinement length is comparable to the interaction length or to the actual atomic size, a completely different treatment becomes necessary [108, 109].

Some discussion is in order as to what allows one to replace the field operator  $\hat{\Psi}$  with a scalar quantity  $\Phi$  in obtaining Equation (2.33). The Bogoliubov prescription is to split the field operator into a condensate term and a fluctuation term. That is,

$$\hat{\Psi}(\mathbf{r}, t) = \Phi(\mathbf{r}, t) + \hat{\zeta}(\mathbf{r}, t), \quad (2.35)$$

where  $\Phi(\mathbf{r}, t) \equiv \langle \hat{\Psi}(\mathbf{r}, t) \rangle$  is termed the *condensate mean field* whose square modulus corresponds to the condensate density  $n_0(\mathbf{r}, t) \equiv |\Phi(\mathbf{r}, t)|^2$  and  $\hat{\zeta}(\mathbf{r}, t)$  is an operator representing fluctuations away from the mean field. Hence, when taking the expectation value of each side of Equation (2.30) to obtain Equation (2.33), we are assuming vanishing moments for the fluctuation operator when evaluating the right-hand side, i.e.,  $\langle \hat{\zeta} \rangle = \langle \hat{\zeta} \hat{\zeta} \rangle = \langle \hat{\zeta}^\dagger \hat{\zeta} \rangle = \langle \hat{\zeta}^\dagger \hat{\zeta} \hat{\zeta} \rangle = 0$ , where the vanishing second and third moment conditions are required for the interaction term. Perturbations to pure mean-field theory involve retaining terms up to a given order in the fluctuation operator. For example, the Bogoliubov theory retains terms up to first-order in  $\hat{\zeta}$ , while its variants, e.g., Hartree-Fock-Bogoliubov and Hartree-Fock-Bogoliubov-Popov, retain terms up to second order.

### 2.3.3 Bose-Hubbard Hamiltonian

The Bose-Hubbard Hamiltonian is an approximation of the continuous many-body Hamiltonian (2.22) appropriate for a system of ultracold bosons in a strong periodic potential. It is an approximation in the sense that the full quantum many-



body Hamiltonian of Equation (2.22) is *truncated* on physical grounds. However, the model is still a quantum many-body Hamiltonian; no semiclassical approximations are present. To derive the Bose-Hubbard model, we first split the potential into a term pertaining to the lattice potential plus an arbitrary external potential:

$$V(\mathbf{r}) = V_{\text{lat}}(\mathbf{r}) + V_{\text{ext}}(\mathbf{r}). \quad (2.36)$$

As above, we assume that the only contributing interatomic interactions are two-body contact interactions so that we can insert Equation (2.31) into Equation (2.22). Next, we expand the field operators in a basis of localized Wannier functions [23]:

$$\hat{\Psi}(\mathbf{r}) = \sum_{i;m} \hat{b}_i^{(m)} w^{(m)}(\mathbf{r} - \mathbf{r}_i). \quad (2.37)$$

The operator  $\hat{b}_i^{(m)}$  ( $\hat{b}_i^{(m)\dagger}$ ) annihilates (creates) a boson in the  $m^{\text{th}}$  Bloch band Wannier state  $w^{(m)}(\mathbf{r} - \mathbf{r}_i)$  localized at site  $i$  with  $\mathbf{r}_i$  being the primitive translation vectors of the lattice. Hence, subscripts are site indices, while superscripts are band indices. Insertion of Equation (2.37) into Equation (2.22) yields

$$\hat{H} = - \sum_{i,j;m,n} J_{ij}^{mn} \hat{b}_i^{(m)\dagger} \hat{b}_j^{(n)} + \sum_{i,j,k,\ell;m,n,p,q} \frac{U_{ijkl}^{mnpq}}{2} \hat{b}_i^{(m)\dagger} \hat{b}_j^{(n)\dagger} \hat{b}_k^{(p)} \hat{b}_\ell^{(q)} + \sum_{i,j;m,n} \epsilon_{ij}^{mn} \hat{b}_i^{(m)\dagger} \hat{b}_n^{(n)}, \quad (2.38)$$

where

$$J_{ij}^{mn} \equiv - \int d\mathbf{r} w^{(m)*}(\mathbf{r} - \mathbf{r}_i) \left[ -\frac{\hbar^2}{2m} \nabla^2 + V_{\text{lat}}(\mathbf{r}) \right] w^{(n)}(\mathbf{r} - \mathbf{r}_j), \quad (2.39)$$

$$U_{ijkl}^{mnpq} \equiv g \int d\mathbf{r} w^{(m)*}(\mathbf{r} - \mathbf{r}_i) w^{(n)*}(\mathbf{r} - \mathbf{r}_j) w^{(p)}(\mathbf{r} - \mathbf{r}_k) w^{(q)}(\mathbf{r} - \mathbf{r}_\ell), \quad (2.40)$$

$$\epsilon_{ij}^{mn} \equiv \int d\mathbf{r} w^{(m)*}(\mathbf{r} - \mathbf{r}_i) V_{\text{ext}}(\mathbf{r}) w^{(n)}(\mathbf{r} - \mathbf{r}_j). \quad (2.41)$$

Up to this point, we have been completely general regarding dimensionality, number of allowed bands, and range of coupling between sites. The only approximation we have made thus far is the contact interaction approximation (2.31). If we only allow particles to occupy the lowest Bloch band and invoke the tight-binding approximation so that only nearest-neighbor tunneling and on-site interactions contribute to the energy, we recover the usual BHH:

$$\hat{H} = -J \sum_{\langle i,j \rangle} \hat{b}_i^\dagger \hat{b}_j + \frac{U}{2} \sum_i \hat{b}_i^\dagger \hat{b}_i^\dagger \hat{b}_i \hat{b}_i + \sum_i \epsilon_i \hat{b}_i^\dagger \hat{b}_i, \quad (2.42)$$

where  $\hat{b}_i \equiv \hat{b}_i^{(0)}$  annihilates a boson in the lowest vibrational Wannier state of the  $i^{\text{th}}$  lattice site and  $\langle i, j \rangle$  denotes a summation over nearest neighbors.

From Section 2.2, a general optical lattice potential in 3D can be written as

$$V_{\text{lat}}(\mathbf{r}) = V_{0x} \sin^2(k_x x) + V_{0y} \sin^2(k_y y) + V_{0z} \sin^2(k_z z), \quad (2.43)$$

where  $V_{0i}$  and  $k_i$  are the lattice height and wave vector in direction  $i$ . Parallel 2D lattices in the  $x$ - $y$  plane can be made by imposing the condition  $V_{0x}, V_{0y} \ll V_{0z}$ . Similarly, parallel 1D lattices in the  $x$ -direction require  $V_{0x} \ll V_{0y}, V_{0z}$ . These conditions suppress tunneling in the transverse directions. We will work strictly with 1D lattices from here on. In this limit, with  $V_{0\perp} \equiv V_{0y} = V_{0z}$  and  $k_{\perp} \equiv k_y = k_z$ , we can expand the transverse part of  $V_{\text{lat}}(\mathbf{r})$  in a Taylor series:

$$V_{\perp}(y, z) = V_{0\perp} [\sin^2(k_{\perp} y) + \sin^2(k_{\perp} z)] \approx \frac{1}{2} m \omega_{\perp}^2 r_{\perp}^2, \quad \text{where } \omega_{\perp}^2 \equiv \frac{4V_{0\perp} E_{R\perp}}{\hbar^2} \quad (2.44)$$

and  $r_{\perp}^2 \equiv y^2 + z^2$ ;  $E_{R\perp} \equiv \hbar^2 k_{\perp}^2 / 2m$  is the transverse recoil energy. We denote the

longitudinal part of the lattice potential as

$$V_{\text{lat}}(x) = V_0 \sin^2(kx) \equiv V_{0x} \sin^2(k_x x). \quad (2.45)$$

For the 1D lattice with spatial period  $a = \pi/k$  containing  $M$  sites and assuming box boundary conditions, Equation (2.42) can be written as

$$\hat{H} = -J \sum_{i=1}^{M-1} (\hat{b}_{i+1}^\dagger \hat{b}_i + \text{h.c.}) + \frac{U}{2} \sum_{i=1}^M \hat{n}_i (\hat{n}_i - \hat{\mathbb{1}}) + \sum_{i=1}^M \epsilon_i \hat{n}_i, \quad (2.46)$$

where we have introduced the number operator  $\hat{n}_i \equiv \hat{b}_i^\dagger \hat{b}_i$  which counts the number of bosons at site  $i$ . We can write the parameters of the 1D Bose-Hubbard model in terms of overlap integrals involving single-particle Wannier wave functions and the external potentials:

$$J \equiv - \int_{-\infty}^{\infty} dx w^{(0)*}(x) \left[ -\frac{\hbar^2}{2m} \frac{d^2}{dx^2} + V_{\text{lat}}(x) \right] w^{(0)}(x-a), \quad (2.47)$$

$$U \equiv g^{(1)} \int_{-\infty}^{\infty} dx |w^{(0)}(x)|^4, \quad (2.48)$$

$$\epsilon_i \equiv \int_{-\infty}^{\infty} V_{\text{ext}}(x) |w^{(0)}(x-x_i)|^2 \approx V_{\text{ext}}(x_i), \quad (2.49)$$

where we have shifted the zero of energy such that  $J_{ii}^{00} \equiv 0$ , cf. Equation (2.39), and  $g^{(1)}$  is given by (2.34) using (2.44) for  $\omega_\perp$ . The last relationship regarding an external potential aside from the lattice potential assumes  $V_{\text{ext}}(x)$  varies sufficiently slowly over the spatial extent of a single lattice site so that it can be pulled out of the integral as a constant. Strictly speaking, a correct usage of box boundary conditions would account for the change in form of the localized wave functions near the boundary, cf. the butadiene molecule in elementary quantum chemistry [110], and change the

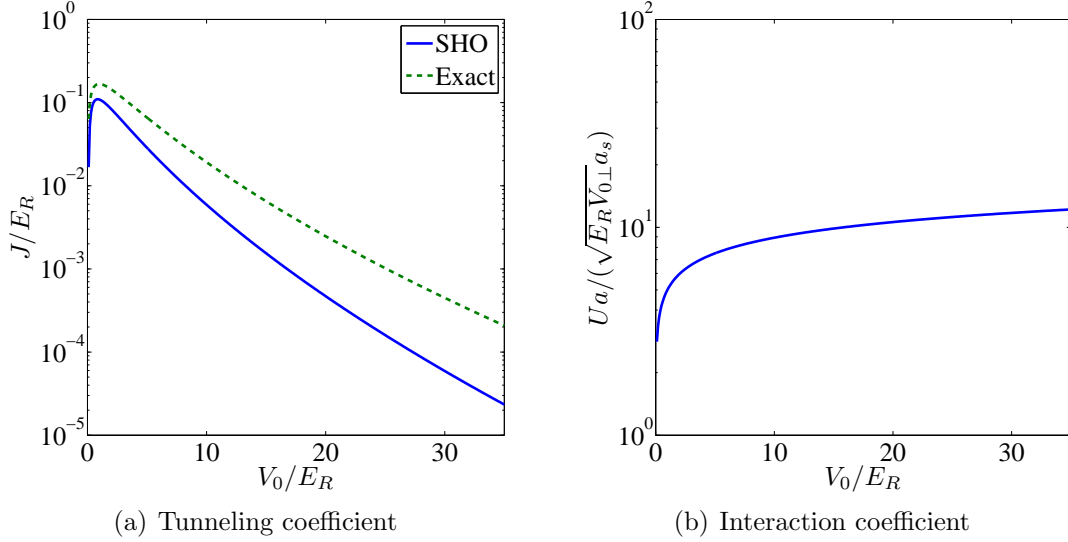


Figure 2.2. *Bose-Hubbard parameters calculated from overlap integrals of Wannier orbitals.* (a)  $J$  and (b)  $U$  are plotted versus  $V_0$  scaled to the recoil energy  $E_R$ . In (a), we see that the simple harmonic oscillator (SHO) approximation underestimates the tunneling coefficient by about an order of magnitude, while in (b), the SHO approximation can be considered exact for calculation of the interaction parameter as in Reference [111].

tunneling and interaction parameters for those sites accordingly. However, since we are not greatly concerned with the behavior of the system near the boundary, we assume identical Wannier functions at all  $M$  sites so that our model contains only a single tunneling parameter  $J$  and a single interaction parameter  $U$ .

The Bose-Hubbard parameters  $J$  and  $U$  can be expressed in terms of the lattice heights and recoil energy, both experimentally tunable parameters. Next, we discuss this calculation for the case of a 1D lattice. Approximating the Wannier functions with the ground state of the simple harmonic oscillator, we have

$$w^{(0)}(x) \approx \ell_{\text{ho}}^{-1/2} \pi^{-1/4} \exp(-x^2/2\ell_{\text{ho}}^2), \quad (2.50)$$

where  $\ell_{\text{ho}} \equiv \sqrt{\hbar/m\omega}$  is the oscillator length and  $\omega \equiv \sqrt{4V_0 E_R}/\hbar$  is the effective trapping frequency. After evaluating the integrals (2.47) and (2.48) using (2.50) for the Wannier orbitals and (2.45) for the lattice potential and simplifying, we find

$$\frac{J}{E_R} \approx \frac{V_0}{2E_R} \exp\left(\frac{-\pi^2}{4} \sqrt{\frac{V_0}{E_R}}\right) \left[ \frac{\pi^2 - 2}{2} - \sqrt{\frac{E_R}{V_0}} - \exp\left(-\sqrt{\frac{E_R}{V_0}}\right) \right], \quad (2.51)$$

$$\frac{U}{E_R} \approx 4\sqrt{2\pi} \left(\frac{a_s}{\lambda}\right) \left(\frac{V_{0\perp}}{E_R}\right)^{1/2} \left(\frac{V_0}{E_R}\right)^{1/4}, \quad (2.52)$$

where  $\lambda = 2a$  is the wavelength of the laser used to create the lattice. This approximation is insufficient for the tunneling coefficient as it completely ignores any oscillatory behavior in the tails of the Wannier wave function. A better expression can be found in References [111, 100] obtained by Fourier transforming Mathieu functions which are exact solutions of the single-particle Schrödinger equation for a sinusoidal potential, calculating the overlap integral (2.47) for different lattice heights, and performing a numerical fit to the data. The resulting expression, which for most purposes can be considered exact, is quoted as

$$\frac{J}{E_R} \approx A \left(\frac{V_0}{E_R}\right)^B \exp\left(-C \sqrt{\frac{V_0}{E_R}}\right), \quad (2.53)$$

where  $A \equiv 1.397$ ,  $B \equiv 1.051$ , and  $C \equiv 2.121$ . On the other hand, Equation (2.52) for the interaction parameter derived in the Gaussian approximation is adequate [111]. See Figure 2.2 for plots of  $J$  and  $U$  versus the lattice height  $V_0$  and Figure 2.3 for a schematic of the 1D Bose-Hubbard model with Gaussian wave functions shown to approximate the real Wannier functions.

Let us now discuss precisely the conditions under which Equation (2.46) is an accurate description of the physical system:

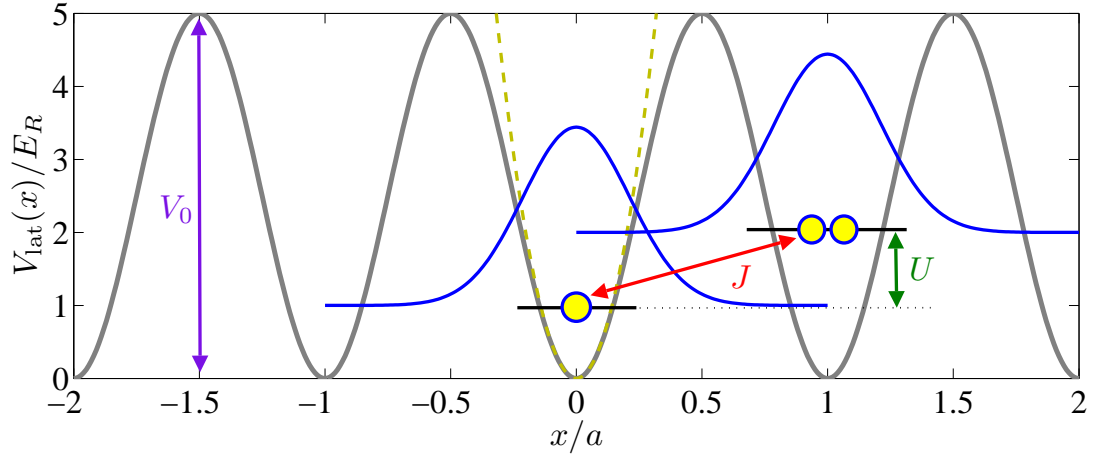


Figure 2.3. *Schematic of 1D optical lattice and Bose-Hubbard Hamiltonian.* The lattice potential  $V_{\text{lat}}(x) = V_0 \sin^2(kx)$  is plotted (solid gray curve) in units of the recoil energy  $E_R$  versus position  $x$  in units of the lattice constant  $a = \pi/k$ . The simple harmonic oscillator approximation (dashed gold curve) was used to generate approximations of the Wannier functions (solid blue curves) for the case  $V_0 = 5E_R$ . The tunneling and interaction processes are indicated by their corresponding energy scales  $J$  and  $U$ , respectively. In the latter case, the localized Wannier function is shown higher up on the graph to indicate that there is an energy cost  $\sim U$  for the case of two particles simultaneously occupying the same on-site Wannier state. Let it be clear that both particles at the site centered at  $x = a$  occupy the same *single-particle* Wannier function shown.

1. The tight-binding approximation must be valid; this assumes second-order effects such as nearest-neighbor interactions and next-nearest-neighbor tunneling can be neglected. In the former case, we find the nearest-neighbor interaction parameter to be  $V = U \exp(-a^2/2\ell_{\text{ho}}^2)$ , which for a relatively shallow lattice of height  $V_0 = E_R$  is only  $V \approx 0.01 U$ . Of course,  $V$  decreases as the lattice height is increased, so  $V \lesssim 0.01 U$ .
2. Contributions from the second band of the lattice must be negligible. This assumes that the temperature, tunneling, interaction energies are smaller than the band spacing  $\hbar\omega$ . That is,  $k_B T, J, \nu^2 U \lesssim \hbar\omega$ , where  $\nu$  is the average lattice

site filling factor [99]. The latter two conditions are generally satisfied if  $V_0 \gtrsim E_R$  for reasonable scattering lengths  $a_s$  and transverse lattice heights  $V_{0\perp}$ . Note that for  $V_0 \lesssim E_R$  the tunneling coefficient in Figure 2.2(a) decreases as the lattice height is decreased, thus clearly indicating a breakdown of the model at that point.

3. The entire model is based on single-particle physics, so the interactions must be small enough so that the condensate mean field does not distort the single-particle wave functions. Specifically, we must have  $\nu^2 U \lesssim \hbar\omega$ . This condition is not independent of the second condition above, and if it is not met, a completely different treatment is necessary. An example of such a treatment is the time-dependent multiconfigurational Hartree-Fock theory, a method which has heretofore only been applied successfully to two-well systems [112, 113, 114].

#### 2.3.4 Connections to Discrete Nonlinear Schrödinger Equation

The discrete nonlinear Schrödinger equation (DNLS) describing ultracold atoms on a discrete lattice can be obtained as either a discretization of the continuous Gross-Pitaevskii equation or as a semiclassical approximation of the Bose-Hubbard Hamiltonian. In the latter case, the derivation is more physically intuitive because the Bose-Hubbard Hamiltonian is a more complete quantum description of the problem and occupation of a single natural orbital is not assumed until the end. We note that DNLS is not the only route to discretization for the continuous NLS. For example, another sensible discretization results in the integrable Ablowitz-Ladik equation [61]; however, quantum mechanics motivates DNLS over Ablowitz-Ladik.

Let us first consider the simplest discretization of the continuous GP equation. The first step is to expand the condensate wave function in a basis of localized wave

functions  $\phi(\mathbf{r} - \mathbf{r}_i)$  in the lowest Bloch band of the lattice:

$$\Phi(\mathbf{r}, t) = \sum_i \psi_i(t) \phi(\mathbf{r} - \mathbf{r}_i). \quad (2.54)$$

The coefficients  $\psi_i(t) \equiv \sqrt{\rho_i(t)} e^{i\theta_i(t)}$  are dimensionless c-numbers that weight the localized wave functions at sites  $i$ , with  $\rho_i$  and  $\theta_i$  being the average particle number occupation and phase, respectively, associated with site  $i$ . Next, we insert (2.54) into (2.33), multiply by the complex conjugate of another member of the set of localized condensate wave functions, integrate over all space, and invoke the tight-binding approximation [59]. The result is the DNLS in the following form:

$$i\hbar\dot{\psi}_k = -J \sum_{j \in \Omega_k} \psi_j + U|\psi_k|^2\psi_k + \epsilon_k\psi_k, \quad (2.55)$$

where  $\Omega_k$  is the set of site  $k$ 's nearest neighbors and the coefficients are defined as

$$J \equiv - \int d\mathbf{r} \phi^*(\mathbf{r}) \left[ -\frac{\hbar^2}{2m} \nabla^2 + V_{\text{lat}}(\mathbf{r}) \right] \phi(\mathbf{r} - \mathbf{a}), \quad (2.56)$$

$$U \equiv g \int d\mathbf{r} |\phi(\mathbf{r})|^4, \quad (2.57)$$

$$\epsilon_k \equiv \int d\mathbf{r} V_{\text{ext}}(\mathbf{r}) |\phi(\mathbf{r} - \mathbf{r}_k)|^2 \approx V_{\text{ext}}(\mathbf{r}_k), \quad (2.58)$$

with  $\mathbf{a} \equiv \mathbf{r}_{k+1} - \mathbf{r}_k$  being a primitive translation vector of the assumed cubic lattice. The tight-binding approximation assumes that the  $\phi(\mathbf{r} - \mathbf{r}_i)$  are sufficiently localized on-site so that

$$\int d\mathbf{r} \phi^*(\mathbf{r} - \mathbf{r}_i) \phi(\mathbf{r} - \mathbf{r}_{i+j}) \approx 0, \quad (2.59)$$

$$\int d\mathbf{r} \phi^*(\mathbf{r} - \mathbf{r}_i) \left[ -\frac{\hbar^2}{2m} \nabla^2 + V_{\text{lat}}(\mathbf{r}) \right] \phi(\mathbf{r} - \mathbf{r}_{i+k}) \approx 0, \quad (2.60)$$



for  $|j| \geq 1$ ,  $|k| \geq 2$  or  $k = 0$  with  $j$  and  $k$  integers. The restriction of Equations (2.55)–(2.58) to the 1D lattice is straightforward:

$$i\hbar\dot{\psi}_k = -J(\psi_{k+1} + \psi_{k-1}) + U|\psi_k|^2\psi_k + \epsilon_k\psi_k, \quad (2.61)$$

where

$$J \equiv - \int_{-\infty}^{\infty} dx \phi^*(x) \left[ -\frac{\hbar^2}{2m} \frac{d^2}{dx^2} + V_{\text{lat}}(x) \right] \phi(x-a), \quad (2.62)$$

$$U \equiv g^{(1)} \int_{-\infty}^{\infty} dx |\phi(x)|^4, \quad (2.63)$$

$$\epsilon_k \equiv \int_{-\infty}^{\infty} dx V_{\text{ext}}(x) |\phi(x-x_k)|^2 \approx V_{\text{ext}}(x_k). \quad (2.64)$$

For a 1D lattice of  $M$  lattice sites, the site index takes on values  $k \in \{1, 2, \dots, M\}$ . The approximations made here are very similar to the single-band tight-binding approximation used to derive the Bose-Hubbard Hamiltonian in Section 2.3.3 except that in that case the localized wave functions were actual single-particle Wannier functions, whereas here they are a set of yet unspecified localized condensate wave functions with which we have chosen to expand the full condensate wave function.

Alternatively, the DNLS can be obtained as a mean-field approximation of the quantum Bose-Hubbard Hamiltonian. This derivation can be done in at least two ways, each of which assume the many-body state to be in the form of a product of Glauber coherent states. We discuss both methods in the following. In the first method, we evolve the bosonic destruction operator  $\hat{b}_k$  forward in time in the Heisenberg picture according to the Bose-Hubbard Hamiltonian [Equation (2.46)]. That is,

$$i\hbar \frac{d}{dt} \hat{b}_k = [\hat{b}_k, \hat{H}]. \quad (2.65)$$

Then we can use the commutation relations

$$[\hat{b}_i, \hat{b}_j^\dagger] = \delta_{i,j} \quad \text{and} \quad [\hat{b}_i, \hat{b}_j] = [\hat{b}_i^\dagger, \hat{b}_j^\dagger] = 0 \quad (2.66)$$

to obtain the following evolution equation for the on-site destruction operator:

$$i\hbar \frac{d}{dt} \hat{b}_k = -J(\hat{b}_{k+1} + \hat{b}_{k-1}) + U \hat{b}_k \hat{b}_k^\dagger \hat{b}_k + \epsilon_k \hat{b}_k. \quad (2.67)$$

We can then take the expectation value of Equation (2.67) to obtain an equation of motion for the order parameter  $\langle \hat{b}_k \rangle$ . The DNLS is recovered exactly if the expectation value is taken with respect to a product of atom-number Glauber coherent states. Hence, for states of the form

$$|\Psi\rangle = \bigotimes_{k=1}^M |z_k\rangle, \quad \text{where} \quad |z_k\rangle \equiv e^{-\frac{|z_k|^2}{2}} \sum_{n=0}^{\infty} \frac{(z_k)^n}{\sqrt{n!}} |n\rangle, \quad (2.68)$$

we obtain the DNLS for the equation of motion governing the coherent state amplitudes  $z_k = \langle \hat{b}_k \rangle \equiv \psi_k$ :

$$i\hbar \dot{\psi}_k = -J(\psi_{k+1} + \psi_{k-1}) + U|\psi_k|^2 \psi_k + \epsilon_k \psi_k. \quad (2.69)$$

For an extensive review of coherent states and their properties, see Reference [115].

The DNLS can also be derived from the Bose-Hubbard model within the time-dependent variational principle [60]. In this case, we take as a trial state

$$|\Psi\rangle = e^{iS/\hbar} |Z\rangle, \quad \text{where} \quad |Z\rangle \equiv \bigotimes_{k=1}^M |z_k\rangle. \quad (2.70)$$

Thus, the trial state is a product of coherent states multiplied by the exponential of

an effective action  $S = S(t)$ . If the time evolution is constrained to obey a weaker form of the time-dependent Schrödinger equation  $\langle \Psi | (i\hbar\partial_t - \hat{H}) | \Psi \rangle = 0$ , then we obtain for the action

$$\dot{S} = i\hbar \langle Z | \partial_t | Z \rangle - \langle Z | \hat{H} | Z \rangle. \quad (2.71)$$

Upon integration and evaluation of  $\langle Z | \partial_t | Z \rangle$ , Equation (2.71) becomes

$$S = \int dt \left[ i\hbar \sum_i \frac{1}{2} (\dot{z}_i z_i^* - \dot{z}_i^* z_i) - \mathcal{H}(Z) \right] \equiv \int dt \mathcal{L}, \quad (2.72)$$

where  $\mathcal{H}(Z) \equiv \langle Z | \hat{H} | Z \rangle$  takes the place of a semiclassical Hamiltonian. Invoking the Lagrange equation of motion

$$\frac{\partial \mathcal{L}}{\partial z_k^*} = \frac{d}{dt} \frac{\partial \mathcal{L}}{\partial \dot{z}_k^*} \quad (2.73)$$

and simplifying, one obtains exactly the DNLS given in Equation (2.69) with  $\psi_k \equiv z_k$ . In each derivation of the DNLS from the Bose-Hubbard Hamiltonian, a different answer is obtained if one uses  $\hat{n}_i(\hat{n}_i - \hat{1})$  instead of  $\hat{b}_i^\dagger \hat{b}_i^\dagger \hat{b}_i \hat{b}_i$  for the interaction term. Of course, these two forms are equivalent in the quantum picture. The only difference in the semiclassical DNLS is a constant shift in energy which has for simplicity been set to zero in Equation (2.69).

The coherent states of Equation (2.68) are known to well describe the ground state of the Bose-Hubbard Hamiltonian for  $J \gg U$  in the limit of an infinite number of sites  $M$  and particles  $N$  at fixed filling  $N/M$  [116]. It is in this regime that quantum depletion can be safely neglected and Equation (2.69) is an accurate description of the system. However, the lattice must be deep enough so that the single-band tight-binding approximation is still valid. In Chapter 4, we use *truncated* coherent states discussed later in Section 4.2 to create nonequilibrium initial quantum states in the Bose-Hubbard Hamiltonian that are analogs to the dark soliton solutions of

the discrete nonlinear Schrödinger equation.

### 2.3.5 The Bogoliubov Approximation

One can perform linear stability analysis on any stationary state of the DNLS by employing the Bogoliubov prescription [18, 20]. The result is the spectrum of elementary excitations about the condensate's mean field. Let us assume a stationary state of the DNLS so that the amplitude at each site  $k$  evolves according to  $\xi_k e^{-i\mu t/\hbar}$ , where  $\xi_k$  is not a function of time  $t$ . We then perturb this initial condition and look for solutions to the DNLS of the form

$$\psi_k = \psi_k(t) = [\xi_k + u_k e^{-i\omega t} + v_k^* e^{i\omega^* t}] e^{-i\mu t/\hbar}, \quad (2.74)$$

where  $u_k$  and  $v_k$  are quasiparticle amplitudes with frequency  $\omega$  and  $\mu$  is the chemical potential of the stationary state  $\xi_k$  as given in Equation (4.24). With  $\xi_k$  and  $\mu$  assumed known, insertion of Equation (2.74) into the DNLS results in the following coupled linear system for the amplitudes  $u_k$  and  $v_k$ :

$$\begin{cases} -J(u_{k+1} + u_{k-1}) + 2U|\xi_k|^2 u_k - \mu u_k + \epsilon_k u_k + U\xi_k^2 v_k &= \hbar\omega u_k, \\ J(v_{k+1} + v_{k-1}) - 2U|\xi_k|^2 v_k + \mu v_k - \epsilon_k v_k - U(\xi_k^*)^2 u_k &= \hbar\omega v_k. \end{cases} \quad (2.75)$$

Hence, the Bogoliubov transformation of Equation (2.74) acts as a linearization of the DNLS around a stationary solution. An alternative route to Bogoliubov analysis for a lattice potential is to start from the quantum picture, i.e., the Bose-Hubbard Hamiltonian, and include small quantum fluctuations by assuming the lowering operator takes the form  $\hat{b}_k = (z_k + \hat{\delta}_k) e^{-i\mu t/\hbar}$  [cf. Equation (2.35)] as explained, for instance, in References [117, 118].

In practice, we solve the system (2.75) by defining the vectors  $(\mathbf{u})_k \equiv u_k$  and

$(\mathbf{v})_k \equiv v_k$  and their concatenation  $\mathbf{w} \equiv (\mathbf{u}, \mathbf{v})^T$  so that (2.75) can be written in the form  $G\mathbf{w} = \hbar\omega\mathbf{w}$ , where, as usual, the site index  $k \in \{1, 2, \dots, M\}$ . The matrix  $G$  represents the left-hand side of the equations in (2.75) and is given by

$$G \equiv \begin{pmatrix} G_{1,1} & G_{1,2} \\ G_{2,1} & G_{2,2} \end{pmatrix}, \quad (2.76)$$

where

$$G_{1,1} \equiv \begin{pmatrix} -\mu + \epsilon_1 + 2U|\xi_1|^2 & -J & 0 & \cdots & 0 \\ -J & -\mu + \epsilon_2 + 2U|\xi_2|^2 & -J & \ddots & \vdots \\ 0 & -J & \ddots & \ddots & 0 \\ \vdots & \ddots & \ddots & \ddots & -J \\ 0 & \cdots & 0 & -J & -\mu + \epsilon_M + 2U|\xi_M|^2 \end{pmatrix}, \quad (2.77)$$

$$G_{1,2} \equiv \begin{pmatrix} U\xi_1^2 & 0 & \cdots & \cdots & 0 \\ 0 & U\xi_2^2 & \ddots & \ddots & \vdots \\ \vdots & \ddots & \ddots & \ddots & \vdots \\ \vdots & \ddots & \ddots & \ddots & 0 \\ 0 & \cdots & \cdots & 0 & U\xi_M^2 \end{pmatrix}, \quad (2.78)$$

$G_{2,2} \equiv -G_{1,1}$ , and  $G_{2,1} \equiv -G_{1,2}^*$ . Note that the terms  $U\xi_k^2 v_k$  and  $-U(\xi_k^*)^2 u_k$  are accounted for on the diagonals of the upper-right and lower-left blocks of  $G$ , respectively. Hence, the problem amounts to diagonalizing  $G$  to solve for the eigenvectors  $\mathbf{w}$  and corresponding eigenvalues  $\hbar\omega$ . The diagonalization routine results in  $2M$  eigenvectors with eigenvalues, but the only relevant modes are those  $j_{\max} \leq M$  modes with

positive norm:

$$\sum_{k=1}^M \left[ |u_k^{(j)}|^2 - |v_k^{(j)}|^2 \right] > 0, \quad (2.79)$$

where  $j \in \{1, 2, \dots, j_{\max}\}$  is a mode index. The frequency associated with mode  $j$  is denoted  $\omega_j$ , and the frequencies are ordered such that  $\omega_1 \leq \omega_2 \leq \dots \leq \omega_{j_{\max}}$ . The density of a given mode  $j$  at site  $k$  is defined as  $|u_k^{(j)}|^2 - |v_k^{(j)}|^2$  and we renormalize the amplitudes so that

$$\sum_{k=1}^M \left[ |u_k^{(j)}|^2 - |v_k^{(j)}|^2 \right] = 1. \quad (2.80)$$

The MATLAB code we use to calculate the Bogoliubov spectrum for a given DNLS stationary state can be found in Appendix C under the name `BogModes.m`.

If for a given mode the frequency  $\omega_j$  is complex, the DNLS solution  $\xi_k$  is said to be *dynamically unstable*, whereas if  $\omega_j$  is negative, the mode is said to be *anomalous* and the stationary DNLS solution is *energetically unstable* [119, 120]. That is, an anomalous mode is one with negative frequency but positive norm. In Chapters 4 and 5, we apply the above methods to analyze the stability of dark soliton solutions of the DNLS and make direct comparisons to full many-body TEBD simulations.

## 2.4 Complexity, Integrability, and Connections to Solitons

In deriving the Gross-Pitaevskii equation from the full continuous quantum many-body Hamiltonian in Section 2.3.2, we have replaced a linear  $N$ -body problem of nondeterministic polynomial (NP) complexity with a much more tractable, albeit nonlinear, partial differential equation. The presence of a Bose condensate allows one to effectively replace the  $N$ -body problem with a one-body problem in which the interactions between atoms are accounted for in the nonlinear term which represents the condensate mean field. To demonstrate the NP complexity of the many-body

problem, consider the Bose-Hubbard model derived above in Section 2.3.3. For a number-conserving Fock space with  $N$  particles and  $M$  lattice sites, a full solution of the model requires knowledge of

$$\Omega_{\text{NC}} = \binom{N+M-1}{N} \equiv \frac{(N+M-1)!}{N!(M-1)!} \quad (2.81)$$

coefficients of the many-body quantum state ket  $|\Psi\rangle$ . By Stirling's approximation, the multiplicity  $\Omega_{\text{NC}}$  scales as  $N^{M-1}$  for large  $N$ . If the Fock space does not conserve particle number and instead one allows up to  $d-1$  bosons per site, then the multiplicity becomes

$$\Omega_{\text{NNC}} = d^M. \quad (2.82)$$

In both cases, the size of the Hilbert space scales exponentially with the system size  $M$ , so the problem is said to be an NP problem. However, we can still study the fundamental physics of the model by considering systems of sufficiently small size or by applying specialized approximative techniques for such many-body problems. Examples of the latter include quantum Monte Carlo [40] and the density matrix renormalization group [41].

*Integrability* of a given model refers to the existence of an infinite number of conserved quantities or integrals of motion. Usually, this means that the solution to the model can be written down in terms of elementary and/or special functions. Hence, an NP problem can be solved exactly if the governing model is integrable. In quantum many-body theory, this amounts to being able to exactly diagonalize the governing Hamiltonian analytically. However, analytic exact diagonalization is usually not possible, in which case the model is said to be non-integrable. Exceptions are usually limited to one spatial dimension; they include the well-known Bethe ansatz

originally developed to solve the Heisenberg model with antiferromagnetic interactions [121], the gas of hard-core bosons both in the continuum [122, 123] and on the lattice [124, 125], and the attractive Fermi-Hubbard model describing fermions on a lattice [26]. The Bose-Hubbard model is integrable only in special cases, e.g., for the case of hard-core interacting bosons where exact studies can be performed by mapping the problem onto one of noninteracting fermions via the Jordan-Wigner transformation [124]. On the other hand, the mean-field GP equation is an integrable model as has been known since the invention of the inverse scattering transform [48, 49]. Other related integrable nonlinear equations include the Korteweg-de Vries [126] and sine-Gordon equations [127].

*Solitons* exist as solutions to each of these nonlinear partial differential equations. Such solutions are characterized by non-dispersing propagation of a density maximum or minimum. A bright soliton is a density maxima made stable by a focusing nonlinearity. A dark soliton, on the other hand, is a density minima made stable by the countering forces of a defocusing nonlinearity and steep phase gradient across the density notch. Solitons are also characterized by their ability to survive mutual collisions, i.e., a collision between two solitons is completely elastic. In contrast, stably propagating nonlinear waves that do not survive collisions are termed *solitary waves*. In a mathematically rigorous sense, solitons are defined as localized solutions to integrable partial differential equations such as the NLS. However, discretization of continuous integrable models often breaks the integrability. For example, the DNLS, a discretization of the NLS, is known to be non-integrable, whereas the closely related Ablowitz-Ladik equation is in fact integrable [61]. Even though the DNLS is non-integrable, it still possesses solutions that closely resemble the bright and dark solitons of the continuous GP equation, although the discretization does introduce



novel effects [62]. For instance, discreteness has been shown to affect the stability of dark solitons [63, 128] and the collisional properties of bright solitons [129]. Even though these structures are not rigorous solutions of an integrable system, we still refer to such solutions as solitons. In Chapter 4, we consider the quantum evolution of mean-field DNLS dark solitons in the Bose-Hubbard model; in Chapter (5), we study the dynamics of density and phase engineered dark solitons on a Bose-Hubbard lattice. Collectively, we refer to all soliton-like solutions in the Bose-Hubbard model as *quantum solitons*. These are by no means soliton solutions of an integrable quantum system—in fact, the corresponding mean-field and quantum models are both non-integrable—but are instead quantum analogs to the dark soliton solutions encountered in discrete mean-field theory.

## 2.5 The Hyperfine Degree of Freedom and Spin-1 Bosons

Up to this point, we have considered a system of scalar bosons, i.e., bosons with no contributing hyperfine degree of freedom. In this section, we briefly discuss the effects of this internal degree of freedom on the physics with emphasis placed on the pertaining models for spin-1 bosons on optical lattices. For more extensive discussions of the hyperfine degree of freedom and its consequences, see, for instance, References [20, 73].

### 2.5.1 Hyperfine Degree of Freedom

When we refer to a system of *scalar bosons*, we mean that the hyperfine degree of freedom has been frozen out so that it plays no role in the system dynamics. The individual atoms, of course, still have finite total spin. To clarify this point, consider neutral  $^{87}\text{Rb}$  which, having an even number of neutrons, is an effective boson. The

total nuclear spin of  $^{87}\text{Rb}$  is  $I = 3/2$ , as is the case for  $^{23}\text{Na}$ , the other most commonly used alkali atom in BEC experiments. Like all alkali atoms, for  $^{87}\text{Rb}$  there is only one electron in an outer shell, namely the  $s$  orbital, so the total electronic angular momentum is  $J = S = 1/2$ . Hence, the total spin can be either  $F = 1$  or  $2$ . In the absence of an external magnetic field, the atomic levels will be split by the hyperfine interaction between the nuclear and electronic spins resulting in different *hyperfine manifolds* labeled by the total spin quantum number  $F$  [20]. However, the atoms can be subject to a magnetic trapping potential which selects only a single hyperfine species, e.g., the “maximally stretched” states  $|F = 1, m_F = -1\rangle$  or  $|F = 2, m_F = 2\rangle$  [73], where  $m_F$  is the projection of the spin in the direction of the applied field. With all atoms in such a hyperfine state, the internal degree of freedom is irrelevant, i.e., there will be no two-body collision processes which alter the hyperfine levels of the colliding atoms, and the atoms behave as scalar bosons. However, optical traps can hold multiple hyperfine components at once in which case the hyperfine degree of freedom can give rise to interesting physics. In this thesis, we consider a system of atoms all from the same hyperfine manifold  $F = 1$  loaded into an optical lattice where all hyperfine sublevels  $m_F \in \{1, 0, -1\}$  are in general present.

### 2.5.2 Spin-1 Bose-Hubbard Hamiltonian

As in Section 2.3.3 for the case of scalar bosons on a tight optical lattice, one can truncate a full continuous many-body Hamiltonian and obtain a spin-1 Bose-Hubbard model [130, 131]. For the case of spin-1, all components come from the same hyperfine manifold and the number of parameters in the model is reduced substantially. In contrast, see the two-component Bose-Hubbard model as in [132] which models a two-state bosonic system created either by forbidding a single hyperfine state of the

$F = 1$  manifold or by taking two components from different manifolds. The final result for the spin-1 case is

$$\begin{aligned} \hat{H} = & -J \sum_{i=1}^{M-1} \sum_{\alpha=-1}^1 (\hat{b}_{i+1,\alpha}^\dagger \hat{b}_{i,\alpha} + \text{h.c.}) + \frac{U_0}{2} \sum_{i=1}^M \hat{n}_i (\hat{n}_i - \hat{\mathbb{1}}) \\ & + \frac{U_2}{2} \sum_{i=1}^M (\hat{\mathbf{S}}_i^2 - 2\hat{n}_i) + \sum_{i=1}^M \sum_{\alpha=-1}^1 \epsilon_{i,\alpha} \hat{n}_{i,\alpha}, \end{aligned} \quad (2.83)$$

where  $\hat{b}_{i,\alpha}$ ,  $\hat{b}_{i,\alpha}^\dagger$ , and  $\hat{n}_{i,\alpha} \equiv \hat{b}_{i,\alpha}^\dagger \hat{b}_{i,\alpha}$  are the destruction, creation, and number operators for an atom in the hyperfine state  $|F = 1, m_F = \alpha\rangle$ ,  $\alpha \in \{1, 0, -1\}$ , in a Wannier function localized at site  $i$  in the lowest Bloch band of the lattice. In Equation (2.83), we are neglecting small differences in the atomic polarizability of the three spin components; this means that each spin component feels approximately the same effective potential from the lattice via the AC-Stark effect. One implication of this assumption is that the model includes only a single hopping parameter  $J$  which is the same for each spin component. The on-site total number and spin operators  $\hat{n}_i$  and  $\hat{\mathbf{S}}_i^2$  can be written in terms of the more primitive operators  $\hat{b}_{i,\alpha}$ ,  $\hat{b}_{i,\alpha}^\dagger$ , and  $\hat{n}_{i,\alpha}$  as follows:

$$\hat{n}_i \equiv \sum_{\alpha=-1}^1 \hat{n}_{i,\alpha}, \quad (2.84)$$

$$\begin{aligned} \hat{\mathbf{S}}_i^2 & \equiv \left( \sum_{\alpha,\beta=-1}^1 \hat{b}_{i,\alpha}^\dagger \mathbf{F}_{\alpha\beta} \hat{b}_{i,\beta} \right)^2 \\ & = 2\hat{n}_{i,1}\hat{n}_{i,0} + 2\hat{n}_{i,0}\hat{n}_{i,-1} + \hat{n}_{i,1} + 2\hat{n}_{i,0} + \hat{n}_{i,-1} \\ & \quad + \hat{n}_{i,1}^2 - 2\hat{n}_{i,1}\hat{n}_{i,-1} + \hat{n}_{i,-1}^2 + 2\hat{b}_{i,1}^\dagger \hat{b}_{i,-1}^\dagger \hat{b}_{i,0}^2 + 2(\hat{b}_{i,0}^\dagger)^2 \hat{b}_{i,1} \hat{b}_{i,-1}. \end{aligned} \quad (2.85)$$

The  $\mathbf{F}_{\alpha\beta}$  are elements of the usual spin-1 matrices:

$$F_x = \frac{1}{\sqrt{2}} \begin{pmatrix} 0 & 1 & 0 \\ 1 & 0 & 1 \\ 0 & 1 & 0 \end{pmatrix}, \quad F_y = \frac{i}{\sqrt{2}} \begin{pmatrix} 0 & -1 & 0 \\ 1 & 0 & -1 \\ 0 & 1 & 0 \end{pmatrix}, \quad F_z = \begin{pmatrix} 1 & 0 & 0 \\ 0 & 0 & 0 \\ 0 & 0 & -1 \end{pmatrix}, \quad (2.86)$$

where the selected basis orders the hyperfine states in decreasing value of  $\alpha, \beta = 1, 0, -1$ .

As in the Bose-Hubbard Hamiltonian for scalar bosons, the parameters  $J$ ,  $U_0$ , and  $U_2$  can be written in terms of overlap integrals of single-particle Wannier orbitals, where for the quasi-1D case we obtain

$$J \equiv - \int_{-\infty}^{\infty} dx w^{(0)*}(x) \left[ -\frac{\hbar^2}{2m} \frac{d^2}{dx^2} + V_{\text{lat}}(x) \right] w^{(0)}(x-a), \quad (2.87)$$

$$U_F \equiv c_F^{(1)} \int_{-\infty}^{\infty} dx |w^{(0)}(x)|^4, \quad F \in \{0, 2\}. \quad (2.88)$$

In 3D, we have for the coupling factors

$$c_0^{(3)} = \frac{g_0^{(3)} + 2g_2^{(3)}}{3} \quad \text{and} \quad c_2^{(3)} = \frac{g_2^{(3)} - g_0^{(3)}}{3}, \quad (2.89)$$

where

$$g_F^{(3)} \equiv \frac{4\pi\hbar^2 a_F}{m} \quad (2.90)$$

and  $a_F$  is the  $s$ -wave scattering length for two atoms scattering in a channel with total spin  $F$ . The  $c_F^{(1)}$  in (2.88) are 1D coupling constants obtained by projecting onto the mean-field ground state in the transverse directions as in Equation (2.34).

Specifically, we have

$$c_0^{(1)} = \frac{g_0^{(1)} + 2g_2^{(1)}}{3} \quad \text{and} \quad c_2^{(1)} = \frac{g_2^{(1)} - g_0^{(1)}}{3}, \quad (2.91)$$

where

$$g_F^{(1)} \equiv 2\hbar\omega_\perp a_F. \quad (2.92)$$

Also,  $\epsilon_{i,\alpha}$  is an external potential aside from the lattice potential acting on hyperfine state  $\alpha$  at site  $i$ :

$$\epsilon_{i,\alpha} \equiv \int_{-\infty}^{\infty} dx V_{\text{ext},\alpha}(x) |w^{(0)}(x - x_i)|^2 \approx V_{\text{ext},\alpha}(x_i). \quad (2.93)$$

The second term in Equation (2.83) accounts for spin-independent interactions, whereas the third term accounts for spin-dependent interactions [131]. For anti-ferromagnetic interactions as in  $^{23}\text{Na}$ ,  $a_2 > a_0$  so  $U_2 > 0$ , while for ferromagnetic interactions as in  $^{87}\text{Rb}$ ,  $a_2 < a_0$  so  $U_2 < 0$ . We concern ourselves with the latter case. Although the individual scattering lengths  $a_F$  can be tuned independently via Feshbach resonance, typical values of non-Feshbach-tuned scattering lengths give values of  $U_2$  one to two orders of magnitude less than  $U_0$  [131]. We neglect magnetic dipole-dipole interactions which are an order of magnitude smaller than spin-dependent interactions [133].

### 2.5.3 Spin-1 Vector Discrete Nonlinear Schrödinger Equation

An analog to the DNLS for a spin-1 system results in a *vector DNLS*. This model can be obtained from the spin-1 Bose-Hubbard Hamiltonian introduced in the previous section by applying the time-dependent variational principle used in Section 2.3.4 for the scalar case. Specifically, we assume a trial state in form of a multi-mode

coherent state

$$|\Psi\rangle = e^{iS/\hbar}|Z\rangle, \quad \text{where } |Z\rangle \equiv \bigotimes_{k=1}^M \bigotimes_{\alpha=-1}^1 |z_{\alpha,k}\rangle \quad (2.94)$$

and the  $|z_{\alpha,k}\rangle$  are usual Glauber coherent states with amplitudes  $z_{\alpha,k}$  at sites indexed  $k$  and for hyperfine states indexed  $\alpha$ . Applying to Equation (2.83) an identical procedure to that used in Section 2.3.4 by constraining the dynamics to a weaker form of the time-dependent Schrödinger equation and invoking Lagrange's equations of motion applied to the classical action  $S = S(t)$ , we arrive at the spin-1 *vector DNLS* for the amplitudes  $\psi_{\alpha,k} \equiv z_{\alpha,k}$ :

$$\begin{aligned} i\hbar\dot{\psi}_{\pm 1,k} = & -J(\psi_{\pm 1,k+1} + \psi_{\pm 1,k-1}) + \left( \epsilon_{\pm 1,k} + U_0 \sum_{\alpha=-1}^1 |\psi_{\alpha,k}|^2 \right) \psi_{\pm 1,k} \\ & + U_2 \left( \frac{1}{\sqrt{2}} f_{\mp,k} \psi_{0,k} \pm f_{z,k} \psi_{\pm 1,k} \right), \end{aligned} \quad (2.95)$$

$$\begin{aligned} i\hbar\dot{\psi}_{0,k} = & -J(\psi_{0,k+1} + \psi_{0,k-1}) + \left( \epsilon_{0,k} + \frac{U_2}{2} + U_0 \sum_{\alpha=-1}^1 |\psi_{\alpha,k}|^2 \right) \psi_{0,k} \\ & + U_2 (f_{+,k} \psi_{+1,k} \pm f_{-,k} \psi_{-1,k}), \end{aligned} \quad (2.96)$$

where

$$f_{z,k} \equiv |\psi_{+1,k}|^2 - |\psi_{-1,k}|^2, \quad (2.97)$$

$$f_{+,k} \equiv \sqrt{2} (\psi_{+1,k}^* \psi_{0,k} + \psi_{0,k}^* \psi_{-1,k}) = f_{-,k}^* \quad (2.98)$$

are derived from the spin-1 matrices [79]. The matrix representation of the vector DNLS given in Equations (2.95)–(2.96) can be found in Section 3.1.1. Note that there is an additional energy in the amount  $U_2/2$  on the  $\alpha = 0$  component in Equation (2.96) which comes from the factor of 2 multiplying  $\hat{n}_{i,0}$  in Equation (2.85). This additional term is not present in the continuous version of Equations (2.95)–(2.96) presented in

Reference [79]. However, for our particular calculation, this point does not matter as we explain in the next section. In Chapter 6, we present numerical simulation of the vector DNLS discussed above in the context of the dynamical phase transition in a ferromagnetic spin-1 condensate studied in References [79, 78] for the continuous case.

#### 2.5.4 Dynamical Phase Transition and Kibble-Zurek Mechanism

Through the quadratic Zeeman effect, application of a magnetic field  $\mathbf{B}$  in the  $z$ -direction has the effect of adding a potential

$$\epsilon_{\pm,k} = Q \equiv \frac{\mu_B^2 B^2}{4E_{\text{hf}}} \quad (2.99)$$

to the  $\alpha = \pm 1$  hyperfine components, where  $\mu_B$  is the Bohr magneton and  $E_{\text{hf}} > 0$  is the hyperfine splitting between manifolds  $F = 1$  and  $F = 2$  [79]. We ignore the linear Zeeman effect by assuming that in spin space we are in a frame rotating at the Larmor frequency. For ferromagnetic interactions with  $U_2 < 0$  as in  $^{87}\text{Rb}$ , we expect a quantum phase transition at a critical value of  $Q$  so that above the critical value we find a polar phase and below the critical value a broken-symmetry phase. In the polar phase, all atoms are in the  $m_F = 0$  hyperfine level, while the broken-symmetry phase is characterized by magnetization in a direction perpendicular to the magnetic field, i.e., finite transverse magnetization. For the discrete 1D box that we consider in Chapter 6, we do not derive an analytic expression for the critical value but numerically observe its existence by propagating the spin-1 vector DNLS in imaginary time to calculate the equilibrium state; this derivation will be done in future work. For a similar derivation without the lattice present, see Reference [79]. In Chapter 6, we show that generalization of this continuum prediction holds in the

discrete lattice up to a few percent for the lattice sizes we consider. That is, the critical quadratic Zeeman strength is

$$Q_c \approx 2\nu|U_2|, \quad (2.100)$$

where  $\nu$  is the filling factor. Also, the extra  $U_2/2$  term in Equation (2.96) can be eliminated by changing the zero of energy since the potential  $Q$  only affects the  $\alpha = \pm 1$  components. For consistency with previous work [78, 79], we thus ignore the  $U_2/2$  term in the vector DNLS calculations done in Chapter 6. The energy shift on the  $\alpha = 0$  component would just change the critical point  $Q_c$  by an amount  $U_2/2$ .

As described in Section 1.3, in a beautiful experiment performed by the Stamper-Kurn group at Berkeley [74], a Bose-Einstein condensate of  $^{87}\text{Rb}$  was prepared in the polar phase so that (almost) all atoms were in the state  $|F = 1, m_F = 0\rangle$ . The magnetic field used to create the polar phase was then quenched below the critical value and transverse magnetization appeared in the  $x$ - $y$  plane, thus breaking the axisymmetry in spin space. Topological spin textures and ferromagnetic domains were observed to form when the system was driven across the critical point. A number of recent theoretical works have investigated this dynamical phase transition [79, 78, 84, 77, 85]. These studies have mainly focused on topological defect formation and have revealed that the scaling properties of the dynamical phase transition can be explained by the Kibble-Zurek mechanism, e.g., the rate of growth of transverse magnetization and the size of post-transition defects are simple power laws of the transition rate [78]; however, this has yet to be clearly observed in experiment. In Chapter 6, we numerically investigate this dynamical phase transition in the presence of a lattice by using the vector DNLS as defined in Equations (2.96)–(2.96). The finite difference methods we use to simulate Equations (2.96)–(2.96) are described in Section 3.1.



## Chapter 3

### SIMULATION METHODS: MEAN FIELD AND QUANTUM FIELD

The majority of the results presented in this thesis are numerical in nature. The purpose of this chapter is to describe the methods we use to numerically simulate systems of ultracold bosons on one-dimensional optical lattices. The chapter has two sections. The first section focuses on the finite difference methods, e.g., Crank-Nicolson and Runge-Kutta, that we use to simulate the relevant discrete mean-field theories, i.e., the discrete nonlinear Schrödinger equation for both scalar and spin-1 bosons. The second section describes the time-evolving block decimation algorithm, an advanced and recently developed routine, which we employ to simulate the full quantum many-body Bose-Hubbard Hamiltonian.

#### 3.1 Mean-Field Simulation: Finite Difference Methods

From a numerical standpoint, it is important to note that discretization of the continuum NLS to obtain the DNLS as derived in Section 2.3.4 can be thought of as application of the *finite element method*. That is, we take the full condensate wave function  $\Phi(\mathbf{r}, t)$  and expand it in a basis of localized condensate wave functions  $\phi_i(\mathbf{r}) \equiv \phi(\mathbf{r} - \mathbf{r}_i)$  with complex, time-dependent weighting coefficients  $\psi_i(t)$ . In the language of finite element analysis, the functions  $\phi_i(\mathbf{r})$  are termed *finite elements*. By selecting this basis of functions, we have discretized the problem in space and kept the time variable  $t$  continuous. This approach is known as the *method of lines*. It replaces a continuous partial differential equation with a set of coupled ordinary

differential equations (ODEs). For scalar bosons, we obtain the  $M$  coupled ODEs given in Equation (2.61), and for spin-1 bosons, we obtain the  $3M$  coupled ODEs given in Equations (2.95)–(2.96). We then solve these systems of ODEs numerically using *finite difference methods*. In this section, we discuss the Crank-Nicolson and Runge-Kutta methods as applied to the DNLS for both scalar and spin-1 bosons.

### 3.1.1 Formulation of Problem

We first consider the scalar boson DNLS. The system of  $M$  coupled ODEs in Equation (2.61) can be written in matrix-vector form as

$$i\hbar\dot{\vec{\psi}}(t) = H[\vec{\psi}(t), t]\vec{\psi}(t), \quad (3.1)$$

where  $\vec{\psi}(t)$  is an  $M$ -dimensional vector with elements  $[\vec{\psi}(t)]_k \equiv \psi_k(t)$  and  $H[\vec{\psi}(t), t]$  is an  $M \times M$  matrix:

$$H \equiv \begin{pmatrix} U|\psi_1|^2 + \epsilon_1 & -J & 0 & \cdots & 0 \\ -J & U|\psi_2|^2 + \epsilon_2 & -J & \ddots & \vdots \\ 0 & -J & \ddots & \ddots & 0 \\ \vdots & \ddots & \ddots & \ddots & -J \\ 0 & \cdots & 0 & -J & U|\psi_M|^2 + \epsilon_M \end{pmatrix}. \quad (3.2)$$

In general,  $H$  is explicitly dependent both on the state  $\vec{\psi}(t)$  and on time  $t$  since the external potential  $\epsilon_k$  is allowed to be time-dependent. Equation (3.2) assumes box boundary conditions so that  $\psi_0 = \psi_{M+1} \equiv 0$ .

The spin-1 vector DNLS of Equations (2.95)–(2.96) can also be written in the form (3.1). In this case,  $\vec{\psi}(t)$  is taken as a concatenation of  $M$ -dimensional vectors

for each spin component:  $\vec{\psi}(t) = [\vec{\psi}_{+1}(t), \vec{\psi}_0(t), \vec{\psi}_{-1}(t)]^T$ , where  $[\vec{\psi}_\alpha(t)]_k \equiv \psi_{\alpha,k}(t)$ ,  $\alpha \in \{1, 0, -1\}$ . In this case,  $H[\vec{\psi}(t), t]$  is a  $3M \times 3M$  matrix that splits up into nine  $M \times M$  submatrices as follows:

$$H \equiv \begin{pmatrix} H_{+1,+1} & H_{+1,0} & H_{+1,-1} \\ H_{0,+1} & H_{0,0} & H_{0,-1} \\ H_{-1,+1} & H_{-1,0} & H_{-1,-1} \end{pmatrix}. \quad (3.3)$$

The submatrices are defined as

$$H_{\pm 1, \pm 1} \equiv \begin{pmatrix} V_{\pm 1,1} \pm U_2 f_{z,1} & -J & 0 & \cdots & 0 \\ -J & V_{\pm 1,2} \pm U_2 f_{z,2} & -J & \ddots & \vdots \\ 0 & -J & \ddots & \ddots & 0 \\ \vdots & \ddots & \ddots & \ddots & -J \\ 0 & \cdots & 0 & -J & V_{\pm 1,M} \pm U_2 f_{z,M} \end{pmatrix}, \quad (3.4)$$

$$H_{0,0} \equiv \begin{pmatrix} V_{0,1} & -J & 0 & \cdots & 0 \\ -J & V_{0,2} & -J & \ddots & \vdots \\ 0 & -J & \ddots & \ddots & 0 \\ \vdots & \ddots & \ddots & \ddots & -J \\ 0 & \cdots & 0 & -J & V_{0,M} \end{pmatrix}, \quad (3.5)$$

$$H_{+1,0} \equiv \begin{pmatrix} \frac{U_2}{\sqrt{2}} f_{-,1} & 0 & \cdots & \cdots & 0 \\ 0 & \frac{U_2}{\sqrt{2}} f_{-,2} & \ddots & \ddots & \vdots \\ \vdots & \ddots & \ddots & \ddots & \vdots \\ \vdots & \ddots & \ddots & \ddots & 0 \\ 0 & \cdots & \cdots & 0 & \frac{U_2}{\sqrt{2}} f_{-,M} \end{pmatrix} = H_{0,-1} = H_{0,+1}^\dagger = H_{0,-1}^\dagger, \quad (3.6)$$

$$H_{\pm 1, \mp 1} \equiv 0, \quad (3.7)$$

where  $V_{\alpha,k} \equiv \epsilon_{\alpha,k} + \sum_{\alpha'=-1}^1 |\psi_{\alpha',k}|^2$  and  $f_{\pm,k}$ ,  $f_{z,k}$  are defined in Equations (2.97)–(2.98).

### 3.1.2 Methods

We have established that the scalar and vector DNLS can both be written in matrix-vector form as in Equation (3.1). Such a set of first-order ODEs can be solved using standard methods. We consider the Crank-Nicolson and Runge-Kutta methods.

**Crank-Nicolson** The Crank-Nicolson method [134, 135] considers propagation forward and backward one-half time step  $\delta t/2$  according to the Euler method:

$$\vec{\psi}(t \pm \delta t/2) \approx \left\{ I \pm \frac{i\delta t}{2\hbar} H[\vec{\psi}(t), t] \right\} \vec{\psi}(t), \quad (3.8)$$

where  $I$  is the identity matrix of appropriate dimensionality. From the backward time step, we have

$$\vec{\psi}(t) \approx \frac{\vec{\psi}(t - \delta t/2)}{I + \frac{i\delta t}{2\hbar} H[\vec{\psi}(t), t]}, \quad (3.9)$$

which in combination with the forward time step allows us to write

$$\vec{\psi}(t + \delta t/2) \approx \frac{I - \frac{i\delta t}{2\hbar} H[\vec{\psi}(t), t]}{I + \frac{i\delta t}{2\hbar} H[\vec{\psi}(t), t]} \vec{\psi}(t - \delta t/2). \quad (3.10)$$

The matrices in denominators indicates matrix inversion which we perform in practice with the MATLAB “slash” operator. A shift in time by  $\delta t/2$  gives us a formula for propagation forward in time by one full time step  $\delta t$  according to the Crank-Nicolson method:

$$\vec{\psi}(t + \delta t) \approx \frac{I - \frac{i\delta t}{2\hbar} H[\vec{\psi}(t + \delta t/2), t + \delta t/2]}{I + \frac{i\delta t}{2\hbar} H[\vec{\psi}(t + \delta t/2), t + \delta t/2]} \vec{\psi}(t). \quad (3.11)$$

The vector  $\vec{\psi}(t+\delta t/2)$  can be approximated with the Euler method applied over a half time step starting from  $\vec{\psi}(t)$ . Starting with an initial configuration  $\vec{\psi}(0)$ , Equation (3.11) can be applied iteratively to obtain approximate solutions of the DNLS at times  $t = 0, \delta t, 2\delta t, \dots, t_f$ . It can be shown that the error of the Crank-Nicolson method at each time step is  $\mathcal{O}(\delta t^3)$ , i.e., it is a second-order method.

The Crank-Nicolson method as outlined above is equivalent to the Cayley transformation in the limit of the linear Schrödinger equation. The Cayley transformation is appealing for numerical simulations of the Schrödinger equation because it preserves unitarity, whereas a method like Runge-Kutta does not. However, for nonlinear equations such as the DNLS, Crank-Nicolson does not necessarily preserve unitarity and is thus not always the most preferable method to use.

**Runge-Kutta** The fourth-order Runge-Kutta method [136] is a commonly used explicit scheme. First, we rewrite Equation (3.1) as

$$\dot{\vec{\psi}}(t) = F[\vec{\psi}(t), t]\vec{\psi}(t), \quad (3.12)$$

where  $F[\vec{\psi}(t), t] \equiv H[\vec{\psi}(t), t]/i\hbar$ . The Runge-Kutta prescription is to first calculate the following intermediate vectors at time  $t$ :

$$\vec{k}_1(t) = F[\vec{\psi}(t), t]\vec{\psi}(t), \quad (3.13)$$

$$\vec{k}_2(t) = F[\vec{\psi}(t), t] \left\{ \vec{\psi}(t) + \frac{\delta t}{2} \vec{k}_1(t) \right\}, \quad (3.14)$$

$$\vec{k}_3(t) = F[\vec{\psi}(t), t] \left\{ \vec{\psi}(t) + \frac{\delta t}{2} \vec{k}_2(t) \right\}, \quad (3.15)$$

$$\vec{k}_4(t) = F[\vec{\psi}(t), t] \left\{ \vec{\psi}(t) + \delta t \vec{k}_3(t) \right\}. \quad (3.16)$$

Then, the approximate solution at time  $t + \delta t$  reads

$$\vec{\psi}(t + \delta t) \approx \vec{\psi}(t) + \frac{\delta t}{6} \left[ \vec{k}_1(t) + 2\vec{k}_2(t) + 2\vec{k}_3(t) + \vec{k}_4(t) \right]. \quad (3.17)$$

As with Crank-Nicolson, we can iteratively apply Equation (3.17) to propagate an initial condition forward in time in steps of size  $\delta t$  for total duration  $t_f$ . The error associated with each time step can be shown to be  $\mathcal{O}(\delta t^5)$ . For all mean-field results in this thesis, we use the fourth-order Runge-Kutta method with time steps of size  $\delta t = 0.001 \hbar/J$  to obtain converged results.

### 3.1.3 Implementation

We implement the above routines in a MATLAB code. The core real time propagation functions for scalar and spin-1 vector DNLS can be found in Appendix C under the names `scalarDNLS_RTP.m` and `vectorDNLS_RTP.m`, respectively. The functions take the method as an input argument; the forward Euler method is also included as an option. Imaginary time propagation can trivially be implemented by taking  $\tau \equiv it$  and renormalizing the solution to the desired value at each time step. The functions used for imaginary time are not included in Appendix C.

## 3.2 Quantum Many-Body Simulation: Time-Evolving Block Decimation

Efficient numerical simulation of quantum many-body phenomena is currently one of the most sought-after challenges in theoretical physics. The main difficulty lies in the exponential growth of the full many-body Hilbert space with the size of the system, thus rendering exact diagonalization of the governing Hamiltonian intractable for large systems. Over the past 20 years, well-proven methods such as quantum Monte Carlo and density matrix renormalization group (DMRG) have

been developed which allow accurate calculation of ground state properties of many-body systems in one spatial dimension without knowledge of all coefficients of the full many-body state ket. However, within the past five years, generalization of the latter method to time-dependent phenomena received a major boost from a rather unexpected corner: quantum information theory.

In 2003 and 2004, G. Vidal developed the now well-established time-evolving block decimation (TEBD) routine for accurate time-dependent simulation of quantum many-body lattice systems [42, 43]. Unlike exact diagonalization methods which scale exponentially in the spatial extent of the system, TEBD scales linearly with the system size, hence allowing numerical investigation of rather large systems. In its original form, this method is restricted to 1D systems governed by Hamiltonians that only link nearest-neighbor sites. However, so-called swapping routines [137] can be used to map multi-legged systems [138] and/or systems with non-nearest-neighbor interactions to a more TEBD-friendly 1D nearest-neighbor interaction system. The accuracy of the routine depends explicitly on the amount of entanglement present. This is due to the fact that the number of basis sets required to exactly represent the quantum state for a given bipartite splitting of the system is in itself a measure of entanglement. The TEBD method retains a number of basis sets less than that required for exact representation, and hence the method is more accurate provided the number of required basis sets is small. This idea of a reduction of the Hilbert space to its most important states, namely the eigenstates of bipartite reduced matrices, is central to DMRG, a method originally invented by White in 1992 [139]. In fact, attempts at time-dependent DMRG occurred well before Vidal (see [45] and references therein). In these early attempts at time-dependent DMRG, the manner in which the Hilbert space is truncated remains constant throughout time evolution. However,

as established in References [45, 46], the ideas set forth by Vidal can be cast very nicely into the original DMRG language, and TEBD is actually equivalent to a time-*adaptive* DMRG routine. That is, at each time step the truncation adapts itself in the way that most accurately represents the evolving state. Hence, TEBD allows for the quasi-exact integration of the time-dependent Schrödinger equation for relatively large 1D quantum many-body systems with nearest-neighbor coupling. Note that the ground state of such systems can also be determined using TEBD by propagation in imaginary time.

In this section, we discuss in detail the most important aspects of TEBD, its application to simulation of the Bose-Hubbard Hamiltonian for both scalar and spin-1 bosons, as well as specific aspects of our implementation of the algorithm. Our actual code can be found in Appendix D. A complete version of the code is included in the attached thesis DVD under the name `AppD:TEBDcode.pdf`.

### 3.2.1 Schmidt Decomposition

Perhaps the most important concept in TEBD is that of the Schmidt decomposition of a vector in a bipartite tensor product space, an idea developed in 1906 [140]. Consider a general state in a Hilbert generated by a tensor product of  $M$  subsystem Hilbert spaces each of dimension  $d$ . Then, any pure state of the full Hilbert space  $\mathcal{H} = \mathcal{H}_d^{\otimes M}$  can be written as

$$|\Psi\rangle = \sum_{i_1, i_2, \dots, i_M=1}^d c_{i_1 i_2 \dots i_M} |i_1\rangle \otimes |i_2\rangle \otimes \dots \otimes |i_M\rangle \in \mathcal{H}, \quad (3.18)$$

where  $i_k$  indexes the states for subsystem  $k$ . Clearly the dimension of the space is exponential in  $M$ , i.e.,  $\dim(\mathcal{H}) = d^M$ . For the case of bosons on a lattice, we can take  $i_k \rightarrow n_k \in \{0, 1, \dots, d-1\}$  so that the state index corresponds directly to particle



occupation number at the subsystem site  $k$ . However, the  $i_k$  need not necessarily denote occupation numbers; they are general labels for the states of each subsystem. Also, note that the subsystems need not necessarily be sites. For example, in a system of bosons and fermions on a lattice, one can choose to describe the occupation of bosonic and fermionic fields on the same site as different subsystems; in this case,  $M$  would be twice the number of lattice sites.

If we partition the full system into two subsystems  $A$  and  $B$  containing subsystems  $[1 \cdots \ell]$  and  $[\ell + 1 \cdots M]$ , respectively, then the Schmidt decomposition guarantees

$$|\Psi\rangle = \sum_{\alpha_\ell=1}^{\chi_\ell} \lambda_{\alpha_\ell}^{[\ell]} |\Phi_{\alpha_\ell}^{[A]}\rangle \otimes |\Phi_{\alpha_\ell}^{[B]}\rangle, \quad (3.19)$$

where the coefficients are ordered such that  $\lambda_1^{[\ell]} \geq \lambda_2^{[\ell]} \geq \cdots \geq \lambda_{\chi_\ell}^{[\ell]} \geq 0$ . Upon tracing over either subsystem  $A$  or  $B$  in the full density matrix  $\hat{\rho} \equiv |\Psi\rangle\langle\Psi|$ , it is clear that the  $|\Phi_{\alpha_\ell}^{[A]}\rangle$  ( $|\Phi_{\alpha_\ell}^{[B]}\rangle$ ) are the eigenkets of the reduced density matrix  $\hat{\rho}_A$  ( $\hat{\rho}_B$ ) for describing subsystem  $A$  ( $B$ ). Hence, each subsystem's reduced density matrix has the same spectrum of eigenvalues  $(\lambda_{\alpha_\ell}^{[\ell]})^2$  which satisfy the normalization

$$\sum_{\alpha_\ell} (\lambda_{\alpha_\ell}^{[\ell]})^2 = 1. \quad (3.20)$$

Also, the number of eigenvalues  $\chi_\ell$  is bounded from above by the dimension of the smaller subsystem, i.e.,  $1 \leq \chi_\ell \leq \min[\dim(A), \dim(B)]$ . However,  $\chi_\ell$  is often much less than its upper bound. This point is central to the functioning of the TEBD algorithm.

When  $\chi_\ell = 1$ , then  $|\Psi\rangle$  is a product state with respect to subsystems  $A$  and  $B$ , and we have maximal knowledge of each subsystem. We say that the two subsystems are *separable* or completely unentangled from one another. More coefficients (larger

$\chi_\ell$ ) needed in the expansion (3.19) implies more eigenvalues of each reduced density matrix  $\hat{\rho}_A$  and  $\hat{\rho}_B$ , from which it follows that each subsystem is in a more mixed state. The integer  $\chi_\ell$  is thus naturally a measure of entanglement between subsystems  $A$  and  $B$ . If we consider all possible bipartite splittings, then the *Schmidt number*

$$\chi_S \equiv \max_{\ell}(\chi_\ell), \quad \ell \in \{1, 2, \dots, M-1\}, \quad (3.21)$$

is a global measure of entanglement in the system. Vidal points out that the related measure  $\log_d(\chi_S)$  satisfies a number of desirable properties for use as an entanglement quantifier, e.g., it is an entanglement monotone and is additive under tensor products [42]. We stress that the TEBD algorithm uses an entanglement cutoff parameter  $\chi \leq \chi_S$  to truncate the Schmidt decomposition at each link of the lattice. It is in this sense that TEBD works for states with a limited amount of entanglement: the lower the Schmidt number  $\chi_S$ , the fewer retained Schmidt basis vectors  $\chi$  are required for accurate representation of the state. In Section 3.2.3, we discuss the exact manner that  $\chi$  enters into the inner workings of the algorithm.

The Schmidt decomposition of a vector as in Equation (3.19) is guaranteed by the singular value decomposition of a matrix [44]. Let  $i$  ( $j$ ) denote collectively the states of subsystem  $A$  ( $B$ ) so that we can write

$$|\Psi\rangle = \sum_{i,j} c_{ij} |ij\rangle. \quad (3.22)$$

By the singular value decomposition, we can write the matrix of coefficients as

$$c_{ij} = \sum_k u_{ik} d_{kk} v_{kj}. \quad (3.23)$$

Then, the  $d_{kk}$  are the singular values corresponding to Schmidt coefficients  $\lambda_{\alpha_\ell}^{[\ell]}$ , and the elements of the unitary matrices  $u$  and  $v$  are the Fock space coefficients of the Schmidt vectors  $|\Phi_{\alpha_\ell}^{[A]}\rangle$  and  $|\Phi_{\alpha_\ell}^{[B]}\rangle$ . Specifically, in our original notation, we can write

$$\lambda_{\alpha_\ell}^{[\ell]} = d_{\alpha_\ell, \alpha_\ell}, \quad (3.24)$$

$$|\Phi_{\alpha_\ell}^{[A]}\rangle = \sum_i u_{i, \alpha_\ell} |i\rangle, \quad (3.25)$$

$$|\Phi_{\alpha_\ell}^{[B]}\rangle = \sum_j v_{\alpha_\ell, j} |j\rangle, \quad (3.26)$$

where the states  $|i\rangle$  ( $|j\rangle$ ) are identified with subsystem  $A$  ( $B$ ).

### 3.2.2 Vidal's Decomposition

The starting point for TEBD is to express the coefficients in Equation (3.18) as a product of  $M$  tensors  $\{\Gamma^{[\ell]}\}$  and  $M - 1$  vectors  $\{\lambda^{[\ell]}\}$ :

$$c_{i_1 i_2 \dots i_M} = \sum_{\alpha_1, \dots, \alpha_{M-1}=1}^{\chi_S} \Gamma_{\alpha_1}^{[1]i_1} \lambda_{\alpha_1}^{[1]} \Gamma_{\alpha_1 \alpha_2}^{[2]i_2} \lambda_{\alpha_2}^{[2]} \Gamma_{\alpha_2 \alpha_3}^{[3]i_3} \dots \Gamma_{\alpha_{M-1}}^{[M]i_M}. \quad (3.27)$$

This representation of the state can be thought of as a *matrix product decomposition* (MPD) [45, 46], an idea used since near the inception of DMRG [141]. Referring to the subsystems associated with the indices  $i_k$  as “sites,” it is useful to associate the  $\Gamma$ s with sites and the  $\lambda$ s with links between sites. The  $\lambda_{\alpha_\ell}^{[\ell]}$  are the Schmidt coefficients obtained when a bipartite splitting is made at link  $\ell$ . On the other hand, elements of the  $\Gamma$  tensors are related to the elements of the Schmidt vectors. The indices  $i_k \in \{1, 2, \dots, d\}$  label the states of subsystem  $k$ , whereas the indices  $\alpha_\ell \in \{1, 2, \dots, \chi_S\}$  label the Schmidt coefficients and vectors at link  $\ell$ . In writing Equation 3.27,  $d^M$

coefficients have been replaced by

$$\Omega_{\text{TEBD}} \approx (d\chi_s^2 + \chi_s)M \quad (3.28)$$

coefficients, where the change in structure of the  $\Gamma$ s at the boundaries of our 1D box require us to use an approximate equality. We note that  $\Omega_{\text{TEBD}}$  is linear in  $M$ , but for general states, the Schmidt number  $\chi_s$  scales as  $\mathcal{O}[\exp(M)]$ , so that the decomposition (3.27) by itself is not useful. However, if  $\chi_s$  scales as  $\mathcal{O}[\text{poly}(M)]$ , approximate exponential speedup will occur. This is the case for many states of physical interest.

The procedure for determining the  $\Gamma$ s and  $\lambda$ s from known coefficients  $c_{i_1 i_2 \dots i_M}$  is only of theoretical importance because for arbitrary states in which  $\chi_s$  scales exponentially with  $M$  we cannot practically expect to know all  $d^M$  coefficients. However, we outline this procedure here because it is useful in connecting the Vidal representation (3.27) to the Schmidt decomposition of the state at each bipartite splitting of the system. For examples of decompositions of important low- $\chi_s$  states using rather *ad hoc* yet intuitive methods, see Appendix A.

The general procedure for calculation of  $\Gamma$ s and  $\lambda$ s from the  $c_{i_1 i_2 \dots i_M}$  can be effectively illustrated by considering, for simplicity, a system of  $M = 4$  subsystems. In this case, according to (3.27), we have

$$c_{i_1 i_2 i_3 i_4} = \sum_{\alpha_1, \alpha_2, \alpha_3=1}^{\chi_s} \Gamma_{\alpha_1}^{[1]i_1} \lambda_{\alpha_1}^{[1]} \Gamma_{\alpha_1 \alpha_2}^{[2]i_2} \lambda_{\alpha_2}^{[2]} \Gamma_{\alpha_2 \alpha_3}^{[3]i_3} \lambda_{\alpha_3}^{[3]} \Gamma_{\alpha_3}^{[4]i_4}. \quad (3.29)$$

The elements of  $\Gamma^{[1]}$  and  $\lambda^{[1]}$  come directly from the Schmidt decomposition obtained

by splitting after subsystem 1 as follows:

$$|\Psi\rangle = \sum_{\alpha_1=1}^{\chi_S} \lambda_{\alpha_1}^{[1]} |\Phi_{\alpha_1}^{[1]}\rangle \otimes |\Phi_{\alpha_1}^{[234]}\rangle = \sum_{\alpha_1; i_1, i_2, i_3, i_4} \lambda_{\alpha_1}^{[1]} \Gamma_{\alpha_1}^{[1]i_1} |i_1\rangle \otimes \Gamma_{\alpha_1}^{[234]i_2 i_3 i_4} |i_2 i_3 i_4\rangle, \quad (3.30)$$

where the tensor product symbol has been suppressed. We have defined a new tensor  $\Gamma^{[234]}$  with only a single index  $\alpha_1$  whose elements are the coefficients of the Schmidt vector  $|\Phi_{\alpha_1}^{[234]}\rangle$  in the original Fock space spanned by the vectors  $\{|i_2 i_3 i_4\rangle\}$  for the subsystem  $[234]$ . We then identify from Equation (3.29) that

$$\Gamma_{\alpha_1}^{[234]i_2 i_3 i_4} = \sum_{\alpha_2, \alpha_3} \Gamma_{\alpha_1 \alpha_2}^{[2]i_2} \lambda_{\alpha_2}^{[2]} \Gamma_{\alpha_2 \alpha_3}^{[3]i_3} \lambda_{\alpha_3}^{[3]} \Gamma_{\alpha_3}^{[4]i_4}. \quad (3.31)$$

Another Schmidt decomposition needs to be performed before we can solve for the  $\Gamma_{\alpha_1 \alpha_2}^{[2]i_2}$ . Splitting after subsystem 2, we obtain for the Schmidt decomposition

$$|\Psi\rangle = \sum_{\alpha_2=1}^{\chi_S} \lambda_{\alpha_2}^{[2]} |\Phi_{\alpha_2}^{[12]}\rangle \otimes |\Phi_{\alpha_2}^{[34]}\rangle = \sum_{\alpha_2; i_1, i_2, i_3, i_4} \lambda_{\alpha_2}^{[2]} \Gamma_{\alpha_2}^{[12]i_1 i_2} |i_1 i_2\rangle \otimes \Gamma_{\alpha_2}^{[34]i_3 i_4} |i_3 i_4\rangle. \quad (3.32)$$

Once again we can inspect (3.29) to write

$$\Gamma_{\alpha_2}^{[34]i_3 i_4} = \sum_{\alpha_3} \Gamma_{\alpha_2 \alpha_3}^{[3]i_3} \lambda_{\alpha_3}^{[3]} \Gamma_{\alpha_3}^{[4]i_4}, \quad (3.33)$$

so it must be that

$$\Gamma_{\alpha_2}^{[12]i_1 i_2} = \sum_{\alpha_1} \Gamma_{\alpha_1}^{[1]i_1} \lambda_{\alpha_1}^{[1]} \Gamma_{\alpha_1 \alpha_2}^{[2]i_2}, \quad (3.34)$$

but the numbers  $\Gamma_{\alpha_2}^{[12]i_1 i_2}$  on the left-hand side are just the coefficients in Fock space of the Schmidt vector  $|\Phi_{\alpha_2}^{[12]}\rangle$ . We have already calculated the  $\Gamma_{\alpha_1}^{[1]i_1}$  and  $\lambda_{\alpha_1}^{[1]}$ , so we can solve for the  $\Gamma_{\alpha_1 \alpha_2}^{[2]i_2}$  on the right-hand side of (3.34) algebraically. Similarly, we

can split the system after subsystem 3 and again inspect (3.29) to find

$$\Gamma_{\alpha_2}^{[34]i_3i_4} = \sum_{\alpha_3} \Gamma_{\alpha_2\alpha_3}^{[3]i_3} \lambda_{\alpha_3}^{[3]} \Gamma_{\alpha_3}^{[4]i_4}, \quad (3.35)$$

from which we can solve for the  $\Gamma_{\alpha_2\alpha_3}^{[3]i_3}$  algebraically after computing the  $\Gamma_{\alpha_3}^{[4]i_4}$  via Schmidt decomposition. In practice, as discussed in the previous section, all Schmidt decompositions are easily calculated via the singular value decomposition. Note that the elements of all  $\lambda$ s can be calculated directly via a Schmidt decomposition at each splitting as in Equation (3.19). No algebraic solving using previously calculated quantities is necessary for the  $\lambda$ s as it is for the  $\Gamma$ s.

### 3.2.3 Two-Site Operation

To see why the Vidal decomposition (3.27) is useful, let us consider a two-site unitary operation

$$\hat{V} = \sum_{i_\ell, i_{\ell+1}; i'_\ell, i'_{\ell+1}} V_{i'_\ell i'_{\ell+1}}^{i_\ell i_{\ell+1}} |i_\ell i_{\ell+1}\rangle \langle i'_\ell i'_{\ell+1}| \quad (3.36)$$

acting on sites  $\ell$  and  $\ell+1$ . By *sites* we of course mean the two subsystems associated with indices  $i_\ell$  and  $i_{\ell+1}$  that may or may not correspond to actual *physical* sites as explained in Section 3.2.1. First, we write  $|\Psi\rangle$  in terms of Schmidt vectors for the subsystems  $[1 \cdots \ell-1]$  and  $[\ell+2 \cdots M]$  spanned by the Hilbert spaces on the left and right of the cut at link  $\ell$ . That is,

$$\begin{aligned} |\Psi\rangle &= \sum_{\alpha_{\ell-1}, \alpha_\ell, \alpha_{\ell+1}; i_\ell, i_{\ell+1}} \lambda_{\alpha_{\ell-1}}^{[\ell-1]} \Gamma_{\alpha_{\ell-1}\alpha_\ell}^{[\ell]i_\ell} \lambda_{\alpha_\ell}^{[\ell]} \Gamma_{\alpha_\ell\alpha_{\ell+1}}^{[\ell+1]i_{\ell+1}} |\Phi_{\alpha_{\ell-1}}^{[1 \cdots \ell-1]}\rangle \otimes |i_\ell i_{\ell+1}\rangle \otimes |\Phi_{\alpha_{\ell+1}}^{[\ell+2 \cdots M]}\rangle \\ &= \sum_{\alpha_{\ell-1}, \alpha_{\ell+1}; i_\ell, i_{\ell+1}} \Theta_{\alpha_{\ell-1}\alpha_{\ell+1}}^{i_\ell i_{\ell+1}} |\Phi_{\alpha_{\ell-1}}^{[1 \cdots \ell-1]}\rangle \otimes |i_\ell i_{\ell+1}\rangle \otimes |\Phi_{\alpha_{\ell+1}}^{[\ell+2 \cdots M]}\rangle \end{aligned} \quad (3.37)$$

by invoking Equations (13) and (14) of [42], where

$$\Theta_{\alpha_{\ell-1}\alpha_{\ell+1}}^{i_{\ell}i_{\ell+1}} \equiv \sum_{\alpha_{\ell}} \lambda_{\alpha_{\ell-1}}^{[\ell-1]} \Gamma_{\alpha_{\ell-1}\alpha_{\ell}}^{[\ell]i_{\ell}} \lambda_{\alpha_{\ell}}^{[\ell]} \Gamma_{\alpha_{\ell}\alpha_{\ell+1}}^{[\ell+1]i_{\ell+1}} \lambda_{\alpha_{\ell+1}}^{[\ell+1]}. \quad (3.38)$$

Note that this definition of the tensor  $\Theta$  differs from an analogous construct in [42] which is also denoted  $\Theta$  in that work. Up to this point, we have assumed that we know the decomposition (3.27) of  $|\Psi\rangle$ , and hence we also know all elements of  $\Theta$ . However, by writing  $|\Psi\rangle$  in the form of Equation (3.37) we can easily write the updated state after the application of  $\hat{V}$  as

$$\hat{V}|\Psi\rangle = \sum_{\alpha_{\ell-1}, \alpha_{\ell+1}; i_{\ell}, i_{\ell+1}} \tilde{\Theta}_{\alpha_{\ell-1}\alpha_{\ell+1}}^{i_{\ell}i_{\ell+1}} |\Phi_{\alpha_{\ell-1}}^{[1\cdots\ell-1]}\rangle \otimes |i_{\ell}i_{\ell+1}\rangle \otimes |\Phi_{\alpha_{\ell+1}}^{[\ell+2\cdots M]}\rangle, \quad (3.39)$$

where  $\tilde{\Theta}$  can be written in terms of the updated tensors  $\tilde{\Gamma}^{[\ell]}$  and  $\tilde{\Gamma}^{[\ell+1]}$  and the updated vector  $\tilde{\lambda}^{[\ell]}$ :

$$\tilde{\Theta}_{\alpha_{\ell-1}\alpha_{\ell+1}}^{i_{\ell}i_{\ell+1}} = \sum_{i'_{\ell}, i'_{\ell+1}} V_{i'_{\ell}i'_{\ell+1}}^{i_{\ell}i_{\ell+1}} \Theta_{\alpha_{\ell-1}\alpha_{\ell+1}}^{i'_{\ell}i'_{\ell+1}} = \sum_{\tilde{\alpha}_{\ell}} \lambda_{\alpha_{\ell-1}}^{[\ell-1]} \tilde{\Gamma}_{\alpha_{\ell-1}\tilde{\alpha}_{\ell}}^{[\ell]i_{\ell}} \tilde{\lambda}_{\tilde{\alpha}_{\ell}}^{[\ell]} \tilde{\Gamma}_{\tilde{\alpha}_{\ell}\alpha_{\ell+1}}^{[\ell+1]i_{\ell+1}} \lambda_{\alpha_{\ell+1}}^{[\ell+1]}. \quad (3.40)$$

In the above discussion,  $\alpha_{\ell} \in \{1, 2, \dots, \chi\}$ , where  $\chi \leq \chi_s$  is the number of retained reduced density matrix eigenvalues associated with a splitting at link  $\ell$ . The closer  $\chi$  is to the Schmidt number  $\chi_s$  of the state after the application of  $\hat{V}$ , the more faithful is this method of applying the two-site operation.

In practice, a given two-site operation is performed as follows: (1) form  $\Theta$  from current  $\Gamma$ s and  $\lambda$ s [Equation (3.38)]; (2) update  $\Theta$  by applying  $\hat{V}$  to obtain  $\tilde{\Theta}$  [Equation (3.40)]; (3) reshape  $\tilde{\Theta}$  from a 4-tensor to a  $(\chi d) \times (\chi d)$  matrix; (4) perform a singular value decomposition on this matrix, retaining only the largest  $\chi$  singular values  $\tilde{\lambda}_{\alpha_{\ell}}^{[\ell]}$ ; and (5) divide out the previous values of  $\lambda^{[\ell-1]}$  and  $\lambda^{[\ell+1]}$  in order to

compute  $\tilde{\Gamma}^{[\ell]}$  and  $\tilde{\Gamma}^{[\ell+1]}$  from the matrix elements obtained via the singular value decomposition. Note that for simplicity we retain  $\chi$  singular values regardless of the size of the subsystems on the left and right of the cut at site  $\ell$ . Slight computational speedup could be achieved if near the ends of the system we selected  $\chi$  so as not to exceed its upper bound of  $\min[\dim(A), \dim(B)]$ . The most expensive computational steps are (1), the formation of  $\Theta$ , and (2), the update of  $\Theta$  after the application of  $\hat{V}$ . The former requires  $\mathcal{O}(d^2\chi^3)$  elementary operations, whereas the latter requires  $\mathcal{O}(d^4\chi^2)$  elementary operations; hence, our overall two-site operation scales as  $\mathcal{O}[\max(d^2\chi^3, d^4\chi^2)]$ . We stress that in step (4) we discard the smallest  $\chi(d-1)$  eigenvalues of the  $(\chi d) \times (\chi d)$  matrix obtained by reshaping  $\tilde{\Theta}$ . It is in this sense that we have approximated the two-site operation  $\hat{V}$  and truncated the full Hilbert space. Owing to the normalization of the Schmidt coefficients as in Equation (3.20), the validity of this truncation can be quantified by computing the Schmidt truncation error associated with application of  $\hat{V}$ :

$$\tau_\ell^S \equiv 1 - \sum_{\alpha_\ell=1}^{\chi} (\lambda_{\alpha_\ell}^{[\ell]})^2. \quad (3.41)$$

It is important to note that the accuracy of the method depends explicitly on the amount of entanglement created by applying the two-site operation. However, this method *optimally* truncates the Hilbert space as the truncation itself is determined by the present state. Hence, TEBD is a *time-adaptive* routine. TEBD is also termed *quasi-exact* because the accuracy of the routine is strictly controlled by the Schmidt truncation error, a quantity itself controlled by the tunable numerical parameter  $\chi$ .



### 3.2.4 Suzuki-Trotter Expansion and Time Evolution

We have thus far established that any two-site operation can be performed in such a manner that is low-order polynomial in both  $\chi$ , the number of basis sets retained, and  $d$ , the local Hilbert space dimension. The ultimate goal is to be able to perform time-dependent simulation of a given many-body Hamiltonian in 1D. To this end, we need a way to write the time evolution operator  $e^{-i\hat{H}\delta t/\hbar}$  over small time steps  $\delta t$  as a product of one- and two-site unitary operations. One-site operations are much less computationally costly than their two-site counterparts and only require updating the  $\Gamma$  associated with the site being operated upon [42]. This procedure scales as  $\mathcal{O}(d\chi^2)$ . All but the most trivial of many-body Hamiltonians consist of multi-site operations. If the Hamiltonian consists only of one- and two-site operations that link only nearest neighbors, then it is convenient to decompose the Hamiltonian  $\hat{H} = \sum_{\ell} \hat{H}_{\ell}$  as

$$\hat{H} = \hat{H}_{\text{odd}} + \hat{H}_{\text{even}}, \text{ where } \hat{H}_{\text{odd}} \equiv \sum_{\text{odd } \ell} \hat{H}_{\ell} \text{ and } \hat{H}_{\text{even}} \equiv \sum_{\text{even } \ell} \hat{H}_{\ell}, \quad (3.42)$$

where  $\ell$  is best thought of as a link index so that  $\hat{H}_{\ell}$  operates only on sites connected to link  $\ell$ , i.e., sites  $\ell$  and  $\ell + 1$ . Note that any one-site operations in  $\hat{H}$  can be written as two-site operations by appropriate tensor products with the identity operator  $\hat{\mathbb{1}}$ . Although  $\hat{H}_{\text{odd}}$  and  $\hat{H}_{\text{even}}$  do not commute with each other, i.e.,  $[\hat{H}_{\text{even}}, \hat{H}_{\text{odd}}] \neq 0$ , each term within both  $\hat{H}_{\text{odd}}$  and  $\hat{H}_{\text{even}}$  commute because  $\hat{H}$  consists of terms that only couple nearest-neighbor sites, i.e.,  $[\hat{H}_{\ell}, \hat{H}_{\ell+j}] = 0$  for  $|j| \geq 2$ . The natural way to proceed is to then employ a Suzuki-Trotter expansion [142] of the time evolution operator. In our implementation, we use the second-order expansion:

$$e^{-i\hat{H}\delta t/\hbar} = e^{-i\hat{H}_{\text{odd}}\delta t/2\hbar} e^{-i\hat{H}_{\text{even}}\delta t/\hbar} e^{-i\hat{H}_{\text{odd}}\delta t/2\hbar} + \mathcal{O}(\delta t^3). \quad (3.43)$$

Because all terms within both  $\hat{H}_{\text{odd}}$  and  $\hat{H}_{\text{even}}$  commute, we have

$$e^{-i\hat{H}_{\text{odd}}\delta t/2\hbar} = \prod_{\text{odd } \ell} e^{-i\hat{H}_{\ell}\delta t/2\hbar}, \quad (3.44)$$

$$e^{-i\hat{H}_{\text{even}}\delta t/\hbar} = \prod_{\text{even } \ell} e^{-i\hat{H}_{\ell}\delta t/\hbar}. \quad (3.45)$$

So, by (3.43)–(3.45), we can in practice approximate  $|\Psi(t + \delta t)\rangle = e^{-i\hat{H}\delta t/\hbar}|\Psi(t)\rangle$ , the evolution of the full many-body state over a small time step  $\delta t$ , by (1) propagating all odd links forward in time one-half time step, (2) propagating all even links forward in time one full time step, and (3) again propagating all odd links forward one-half time step. The exact details of this procedure depend on the specific order of the Suzuki-Trotter expansion being utilized, where the above prescription is for the second-order expansion of Equation (3.43). It is important to note that evolving the state of the entire system forward at each time step involves only  $\mathcal{O}(M)$  two-site operations. For evolution over a total time interval of size  $t_f$ , the overall algorithm scales as  $\mathcal{O}[M \frac{t_f}{\delta t} \max(d^2\chi^3, d^4\chi^2)]$ , a quantity linear in the system size  $M$ . There are two sources of error inherent in the algorithm: (1) the retention of only the largest  $\chi$  singular values of the tensor  $\tilde{\Theta}$  in Equation (3.40) and (2) the Suzuki-Trotter representation of the time evolution operator as in Equation (3.43). We can monitor the former error by computing, for a given time step, the total Schmidt truncation error, which we denote  $\tau^S$ , defined as the sum of the Schmidt truncation errors  $\tau_{\ell}^S$  [see Equation (3.41)] associated with all two-site operations required to evolve the full system forward in time by amount  $\delta t$ . The more entanglement generated by application of  $e^{-i\hat{H}\delta t/\hbar}$ , the greater is the total Schmidt truncation error over that time step; hence,  $\int_0^t \tau^S(t') dt'$  serves as a global measure of spatial entanglement present in the system at time  $t$ . Plots of  $\tau^S$  over time for our particular applications of the

algorithm can be found in Appendix B. Regarding the latter source of error, we find that using time steps of size  $\delta t = 0.01 \hbar/J$  is sufficient to obtain converged results for simulating the Bose-Hubbard Hamiltonian.

Real time evolution on some initial configuration  $|\Psi(t=0)\rangle$  decomposed according to the Vidal form of Equation (3.27) can be performed by the procedure described above. A faithful ground state can also be obtained by starting with some initial state with finite overlap of the true ground state and performing imaginary time evolution. That is, we let  $\tau \equiv it$  and renormalize the state at each time step according to Equation (3.20). This renormalization is also done in real time to help preserve the unitarity of the evolution. We can succinctly write the ground state as

$$|\Psi_{\text{ground}}\rangle = \lim_{\tau \rightarrow \infty} \frac{e^{-\hat{H}\tau/\hbar}|\Psi_0\rangle}{\|e^{-\hat{H}\tau/\hbar}|\Psi_0\rangle\|}, \quad (3.46)$$

where, in practice,  $|\Psi_0\rangle$  is often taken as the completely uniform product state with  $c_{i_1 i_2 \dots i_M} = \frac{1}{\sqrt{d^M}}$ . It is common to take as the initial condition for real time evolution some perturbed state of the system's ground state. It is also straightforward to simulate many-body dynamics after a quantum quench by performing real time evolution according to Hamiltonian  $\hat{H}_B$  on a ground state configuration of a different Hamiltonian  $\hat{H}_A$ . In Chapter 5, we use this type of approach to density and phase engineer dark quantum solitons on a Bose-Hubbard lattice. In Chapter 4, we perform real time evolution according to the Bose-Hubbard Hamiltonian on initial product states resembling discrete dark solitons in the corresponding mean-field theory.

### 3.2.5 Calculation of Observables

Of course, in order to understand the physical properties of the system, it is necessary to be able to calculate expectation values of relevant physical observables.

For definitions of the observables we use, see Section 4.1. To calculate expectation values, we first compute the reduced density matrix of the subsystem of interest. Then, the expectation value of any observable associated with that subsystem is easily computable. The main observables we are concerned with are single-site observables such as  $\langle \hat{n}_k \rangle$ , the expectation value of the number operator at site  $k$  (see Section 4.1.1), and two-site observables such as  $\langle \hat{b}_j^\dagger \hat{b}_i \rangle$ , the elements of the single-particle density matrix (see Section 4.1.5).

For a general single-site observable  $\hat{A}$ , we calculate its expectation value at site  $k$  as

$$\langle \hat{A}_k \rangle = \text{Tr}(\hat{\rho}_k \hat{A}), \quad (3.47)$$

where  $\hat{\rho}_k$ , the reduced density matrix of site  $k$ , is calculated as follows. The density matrix of the full system in terms of Fock space coefficients is

$$\hat{\rho} = |\Psi\rangle\langle\Psi| = \sum_{i_1, \dots, i_M; i'_1, \dots, i'_M} c_{i_1 \dots i_M} c_{i'_1 \dots i'_M}^* |i_1 \dots i_M\rangle \langle i'_1 \dots i'_M|. \quad (3.48)$$

Tracing over all sites but site  $k$  results in

$$\hat{\rho}_k = \text{Tr}_{j \neq k}(\hat{\rho}) = \sum_{i_k, i'_k} \left( \sum_{i_1, \dots, i_{k-1}, i_{k+1}, \dots, i_M} c_{i_1 \dots i_{k-1} i_{k+1} \dots i_M}^* c_{i_1 \dots i_{k-1} i_{k+1} \dots i_M} \right) |i_k\rangle \langle i'_k|, \quad (3.49)$$

so the elements of the  $d \times d$  matrix  $\hat{\rho}_k$  are

$$(\hat{\rho}_k)_{i'_k i_k} = \sum_{i_1, \dots, i_{k-1}, i_{k+1}, \dots, i_M} c_{i_1 \dots i_{k-1} i_{k+1} \dots i_M}^* c_{i_1 \dots i_{k-1} i_{k+1} \dots i_M}. \quad (3.50)$$

The same partial trace can easily be performed in terms of the Vidal decomposition

of  $\Gamma$ s and  $\lambda$ s if the state is written as

$$|\Psi\rangle = \sum_{i_k; \alpha_{k-1}, \alpha_k} |\Phi_{\alpha_{k-1}}^{[1 \dots k-1]}\rangle \otimes \lambda_{\alpha_k}^{[k]} \Gamma_{\alpha_{k-1} \alpha_k}^{[k] i_k} \lambda_{\alpha_k}^{[k]} |i_k\rangle \otimes |\Phi_{\alpha_k}^{[k+1 \dots M]}\rangle. \quad (3.51)$$

The end result is

$$(\hat{\rho}_k)_{i_k i'_k} = \sum_{\alpha_{k-1}, \alpha_k} \lambda_{\alpha_{k-1}}^{[k-1]} \left( \Gamma_{\alpha_{k-1} \alpha_k}^{[k] i'_k} \right)^* \lambda_{\alpha_k}^{[k]} \lambda_{\alpha_{k-1}}^{[k-1]} \Gamma_{\alpha_{k-1} \alpha_k}^{[k] i_k} \lambda_{\alpha_k}^{[k]}. \quad (3.52)$$

At the boundaries, we get a slightly different result owing to the change in form of  $\Gamma^{[1]}$  and  $\Gamma^{[M]}$ :

$$(\hat{\rho}_1)_{i_1 i'_1} = \sum_{\alpha_1} \left( \Gamma_{\alpha_1}^{[1] i'_1} \right)^* \lambda_{\alpha_1}^{[1]} \Gamma_{\alpha_1}^{[1] i_1} \lambda_{\alpha_1}^{[1]}, \quad (3.53)$$

$$(\hat{\rho}_M)_{i_M i'_M} = \sum_{\alpha_{M-1}} \lambda_{\alpha_{M-1}}^{[M-1]} \left( \Gamma_{\alpha_{M-1}}^{[M] i'_M} \right)^* \lambda_{\alpha_{M-1}}^{[M-1]} \Gamma_{\alpha_{M-1}}^{[M] i_M}. \quad (3.54)$$

Calculation of a given single-site density matrix thus requires  $\mathcal{O}(d^2 \chi^2)$  elementary operations, and, of course, the small matrix multiplication and trace required to evaluate the actual expectation value in Equation (3.47) can be performed with  $\mathcal{O}(d^2)$  elementary operations.

Now, suppose we want to compute the expectation value of a two-site operator  $\hat{B}$  at sites  $k$  and  $\ell$ . As before, we must compute a reduced density matrix, this time for sites  $k$  and  $\ell$ . Then, similar to Equation (3.47), the expectation value of  $\hat{B}$  is

$$\langle \hat{B}_{k\ell} \rangle = \text{Tr}(\hat{\rho}_{k\ell} \hat{B}). \quad (3.55)$$

For instance, to calculate the correlation function  $\langle \hat{b}_k^\dagger \hat{b}_\ell \rangle$ , we take  $\hat{B} = \hat{b}^\dagger \otimes \hat{b}$  in (3.55). The bookkeeping required for actual calculation of  $\hat{\rho}_{k\ell}$  is rather cumbersome,

especially if  $k$  and  $\ell$  are not near one another in the indexing of sites. Here, we just quote the final result as

$$\begin{aligned}
 (\hat{\rho}_{k\ell})_{i_k i_\ell; i'_k i'_\ell} = & \sum_{i_{k+1}, \dots, i_{\ell-1}} \sum_{\alpha_{k-1}, \alpha_\ell} \sum_{\alpha_k, \dots, \alpha_{\ell-1}} \sum_{\alpha'_k, \dots, \alpha'_{\ell-1}} \\
 & \times \left[ \lambda_{\alpha_{k-1}}^{[k-1]} \Gamma_{\alpha_{k-1} \alpha_k}^{[k] i_k} \lambda_{\alpha_k}^{[k]} \Gamma_{\alpha_k \alpha_{k+1}}^{[k+1] i_{k+1}} \lambda_{\alpha_{k+1}}^{[k+1]} \dots \lambda_{\alpha_{\ell-2}}^{[\ell-2]} \Gamma_{\alpha_{\ell-2} \alpha_{\ell-1}}^{[\ell-1] i_{\ell-1}} \lambda_{\alpha_{\ell-1}}^{[\ell-1]} \Gamma_{\alpha_{\ell-1} \alpha_\ell}^{[\ell] i_\ell} \lambda_{\alpha_\ell}^{[\ell]} \right] \\
 & \times \left[ \lambda_{\alpha_{k-1}}^{[k-1]} \left( \Gamma_{\alpha_{k-1} \alpha'_k}^{[k] i'_k} \right)^* \lambda_{\alpha'_k}^{[k]} \left( \Gamma_{\alpha'_k \alpha'_{k+1}}^{[k+1] i'_{k+1}} \right)^* \dots \left( \Gamma_{\alpha'_{\ell-2} \alpha'_{\ell-1}}^{[\ell-1] i'_{\ell-1}} \right)^* \lambda_{\alpha'_{\ell-1}}^{[\ell-1]} \left( \Gamma_{\alpha'_{\ell-1} \alpha'_\ell}^{[\ell] i'_\ell} \right)^* \lambda_{\alpha'_\ell}^{[\ell]} \right],
 \end{aligned} \tag{3.56}$$

where for simplicity and without loss of generality we have assumed  $k < \ell$ . Clearly, the number of elementary operations required to calculate a given two-site density matrix depends on how close  $k$  and  $\ell$  are in the indexing; however, this is not a limiting step because we only record data at a relatively small fraction of time steps throughout the evolution. Actual implementation of the calculation in Equation (3.56) by employing convenient kernels for data storage can be found in subroutines `ThetaKernel`, `ThetaNext`, and `TwoSiteRho` of the module named `observables_module.f90` in the Fortran code.

Alternatively, one can compute the expectation value of any one-site observable or any two-site correlation function by first performing one-site operations on the ket on the right-hand side of the expectation value and then taking an inner product with the bra on the left-hand side [143]. The above procedure of first calculating reduced density matrices, however, is more robust and applies to any class of operators. It is also easily generalizable to operators acting on more than two sites.

### 3.2.6 Application to Bose-Hubbard Hamiltonian

The Bose-Hubbard Hamiltonian of Equation (2.46) is a perfect testbed for the TEBD algorithm as it is a one-dimensional many-body lattice model involving only

nearest-neighbor coupling. Splitting the Hamiltonian into two terms

$$\hat{H}_{\text{odd}} \equiv -J \sum_{i \text{ odd}} (\hat{b}_{i+1}^\dagger \hat{b}_i + \text{h.c.}) + \sum_{i \text{ odd}} \left[ \frac{U}{2} \hat{n}_i (\hat{n}_i - \hat{\mathbb{1}}) + \epsilon_i \hat{n}_i \right], \quad (3.57)$$

$$\hat{H}_{\text{even}} \equiv -J \sum_{i \text{ even}} (\hat{b}_{i+1}^\dagger \hat{b}_i + \text{h.c.}) + \sum_{i \text{ even}} \left[ \frac{U}{2} \hat{n}_i (\hat{n}_i - \hat{\mathbb{1}}) + \epsilon_i \hat{n}_i \right] \quad (3.58)$$

so that  $\hat{H} = \hat{H}_{\text{odd}} + \hat{H}_{\text{even}}$  as in Equation (3.42), allows us to use the Suzuki-Trotter time-stepping routine explained in Section 3.2.4 since each term within both  $\hat{H}_{\text{odd}}$  and  $\hat{H}_{\text{even}}$  commute. In practice, we build matrix representations of each term in the Hamiltonian in a two-site basis, i.e., the matrices we construct are of dimension  $d^2 \times d^2$ . Each term multiplying  $J$  is already a two-site operator, so building these terms amounts to computing  $\hat{b}^\dagger \otimes \hat{b}$  and  $\hat{b} \otimes \hat{b}^\dagger$ . Even though the terms involving only  $\hat{n}$  are one-site operations, we still treat them as two-site operations by appropriate tensor products with the identity operator. Namely, we must compute  $\hat{n} \otimes \hat{\mathbb{1}}$ ,  $\hat{\mathbb{1}} \otimes \hat{n}$ ,  $\hat{n}^2 \otimes \hat{\mathbb{1}}$ , and  $\hat{\mathbb{1}} \otimes \hat{n}^2$  in order to use two-site operations that only act on a single site. Careful consideration must be taken to not doubly apply these one-site operations. Also, the boundary terms must be taken into account separately. Building matrix representations of the required operators in Fock space is rather trivial because the on-site state index  $i_k \in \{1, 2, \dots, d\}$  can be mapped in an unambiguous way to the particle occupation number  $n_k$  for a given on-site state, i.e.,  $i_k \rightarrow n_k + 1$  because we only allow up to  $d - 1$  bosons per site. The destruction, creation, and number operators for a localized Wannier function are easily obtained in this number basis (see Sections 4.1.3 and 4.1.1). The tensor product operation is the usual Kronecker tensor product.

In our code, actual construction of the Bose-Hubbard Hamiltonian takes place in the subroutine `HamiltonianBoseHubbard`. The exponentiation of the Hamiltonian

terms [see Equations (3.44) and (3.45)] is performed in the subroutine `ConstructPropagators`. Both of these subroutines are in the module `MPDtools_module.f90`. The second-order Suzuki-Trotter time propagation procedure is performed by the subroutine `TrotterStep2ndOrder` located in `propagation_module.f90`. `TrotterStep2ndOrder` uses the two-site operation subroutine `TwoSiteOp` which is located in `local_operations_module.f90` and performs the tasks described in Section 3.2.3.

In Chapters 4 and 5, we use our Bose-Hubbard implementation of TEBD to simulate quantum many-body dynamics of dark solitons formed by ultracold atoms in optical lattices. In Appendix B, we discuss the accuracy associated with using the Vidal-truncated Hilbert space as well as convergence of the results presented in Chapters 4 and 5.

### 3.2.7 Implementation of Spin-1 Bose-Hubbard Hamiltonian

The inner workings of the TEBD algorithm do not depend on the exact choice of Hamiltonian so long as it fits into the TEBD framework. Consider the one-dimensional spin-1 Bose-Hubbard Hamiltonian for a lattice of  $M$  sites as presented in Section 2.5.2. Each site, i.e., each localized Wannier function, can now hold atoms with three different hyperfine states, namely  $m_F = 1, 0, -1$ . If we restrict each site to contain at most  $n_{\max}$  bosons regardless of their spin, then the size of the local Hilbert space dimension is

$$d = \sum_{n=0}^{n_{\max}} \frac{(n+2)(n+1)}{2} = \frac{(n_{\max}+3)(n_{\max}+2)(n_{\max}+1)}{6}, \quad (3.59)$$

where this expression can be derived by considering the number of ways of arranging  $n \in \{0, 1, \dots, n_{\max}\}$  particles among three spin states and summing the individual multiplicities. The multiplicity for each given  $n$  can be computed from Equation (2.81)



with  $M = 3$  and  $N = n$ . For  $n_{\max} = 1, 2, 3, 4$ , we have  $d = 4, 10, 20, 35$ , respectively. The low-order polynomial scaling of TEBD with local dimension  $d$  thus restricts us to take  $n_{\max} = 1$  or  $2$  in our current spin-1 code which is not yet optimized with number and spin conservation as discussed next in Section 3.2.8. Then, simulation of the spin-1 Bose-Hubbard Hamiltonian amounts to selecting an ordering of the  $d$  on-site states and building matrix representations of all one- and two-site operators in Equations (2.83)–(2.85) under this ordering. The procedure is conceptually equivalent to that explained above in Section 3.2.6 for the scalar boson Bose-Hubbard model except that the matrix representations are not quite as trivial to compute, although that aspect is still rather straightforward. All necessary subroutines for implementation of the spin-1 Bose-Hubbard model in TEBD are included in the module `spin1_module.f90` of the Fortran package; this module is included in Appendix D.

We note that the spin-1 Bose-Hubbard Hamiltonian of Equation (2.83) can easily be mapped onto a three-legged ladder model by considering each on-site spin state a different leg of the ladder. Then, the three-legged ladder can be flattened onto a one-legged ladder and the different “sites” can be brought together using the swap gate [137] as in [138] in order to apply the local operations of the Hamiltonian as explained in Section 3.2.4. This would be computationally beneficial because the local dimension for each spin state is much lower than the on-site local dimension as discussed in the previous paragraph. That is, we would incur a substantial speedup by tripling the number of sites and having a local dimension on the order of 3 to 5, say. However, the two spin-exchange terms  $2\hat{b}_{i,1}^\dagger \hat{b}_{i,-1}^\dagger \hat{b}_{i,0}^2$  and  $2(\hat{b}_{i,0}^\dagger)^2 \hat{b}_{i,1} \hat{b}_{i,-1}$  in the  $\hat{\mathbf{S}}_i^2$  part of the spin-1 Bose-Hubbard Hamiltonian [see Equations (2.83)–(2.85)] are three-site operations within the framework of this approach. To date, there does not exist a three-site operation routine for the TEBD algorithm, and hence we must specify a

physical site local dimension  $n_{\max}$  as described above.

### 3.2.8 Use of Conserved Quantities

As demonstrated in References [45, 46], the ideas of TEBD fit nicely into the framework of the already well-established DMRG methods. One of the reasons for the success of DMRG lies in its ability to take into account good quantum numbers to improve efficiency. By *good quantum numbers*, we mean some quantity conserved by the Hamiltonian during time evolution, e.g., total particle number in the scalar Bose-Hubbard Hamiltonian and total particle number and total spin in the spin-1 Bose-Hubbard Hamiltonian. Not surprisingly, use of good quantum numbers can be used to enhance the efficiency of TEBD as well [143]. Ippei Danshita at NIST, Gaithersburg, has implemented such a procedure in our Fortran code to conserve total particle number during time evolution according to the Bose-Hubbard Hamiltonian. We find that employing number conservation speeds up the method by about one order of magnitude for typical simulation parameters. In the future, we will add spin conservation capabilities to our code for use with the spin-1 Bose-Hubbard Hamiltonian.

## Chapter 4

### QUANTUM EVOLUTION OF MEAN-FIELD SOLITONS

In this chapter, we investigate how quantum many-body phenomena, e.g., quantum fluctuations and quantum entanglement, affect the behavior of mean-field dark solitons formed by ultracold atoms loaded into one-dimensional optical lattices. We first give a list of measures used to characterize the system. These include purely quantum measures of quantum depletion, spatial entanglement, and number fluctuations. We consider both stationary dark solitons and soliton-soliton collisions.

#### 4.1 Characterization Measures

For a lattice containing  $M$  sites, a full quantum description of the problem involves knowledge of the pure state  $|\Psi\rangle$  of the many-body system. In an occupation number basis, i.e., a Fock basis, of localized Wannier states, we can write

$$|\Psi\rangle = \sum_{n_1, n_2, \dots, n_M=0}^{d-1} c_{n_1 n_2 \dots n_M} |n_1 n_2 \dots n_M\rangle, \quad (4.1)$$

where  $n_k$  is the number of particles occupying the Wannier state localized at site  $k$ ,  $c_{n_1 n_2 \dots n_M}$  are the coefficients weighting the individual Fock states, and we've suppressed writing the tensor product symbol between on-site states. The occupancy of a given site is restricted to  $d-1$  bosons so that the local Hilbert space is of dimension  $d$ . That is,  $n_k \in \{0, 1, \dots, d-1\}$ . The multiplicity of the full Hilbert space is then  $\Omega_{\text{NNC}} = d^M$ . Knowledge of the state ket in Fock space, either in full form or in the

Vidal-truncated form of Section 3.2.2, is necessary, but by itself ultimately useless. The bulk measures by which we use to characterize the full Hilbert space are outlined below. These measures are what allow us to probe the physical properties of the system.

#### 4.1.1 Average Particle Number

The number operator is an on-site observable whose expectation value is the *average particle number* which corresponds directly to the particle density observed in experiment average over many runs. Being an on-site observable, the number operator

$$\hat{n} = \sum_{n=0}^{d-1} n |n\rangle \langle n| \quad (4.2)$$

is diagonal in the on-site occupation basis. As with any local observable, we can compute the expectation value of the number operator at site  $k$  by first calculating  $\hat{\rho}_k = \text{Tr}_{j \neq k} |\Psi\rangle \langle \Psi|$ , the reduced density matrix for site  $k$ , and then using  $\langle \hat{n}_k \rangle = \text{Tr}(\hat{\rho}_k \hat{n})$  as explained in Section 3.2.5.

#### 4.1.2 Normalized Particle Number Variance

Another number related observable is the *normalized particle number variance* defined as

$$\eta \equiv \frac{\langle (\Delta n)^2 \rangle}{\langle \hat{n} \rangle} \equiv \frac{\langle \hat{n}^2 \rangle - \langle \hat{n} \rangle^2}{\langle \hat{n} \rangle}. \quad (4.3)$$

This measure characterizes the deviation of on-site number statistics away from the classical Poissonian limit. Specifically,  $\eta = 1$  for atom-number Glauber coherent states which obey Poissonian number statistics,  $\eta < 1$  for a *number-squeezed* state,  $\eta > 1$  for a *phase-squeezed* state, and  $\eta = 0$  for a single Fock state of definite

occupancy. Calculation of the normalized number variance on-site simply amounts to calculating  $\langle \hat{n}_k \rangle$ , the expectation value of the number operator, and  $\langle \hat{n}_k^2 \rangle$ , the expectation value of the number operator squared, at a given site.

#### 4.1.3 The Order Parameter

In a dynamical mean-field theory in which one assumes the many-body state is for all times a direct product of atom-number Glauber coherent states [60, 144], the condensate *order parameter* is accurately defined as  $\langle \hat{b}_k \rangle$ , the expectation value of the on-site destruction operator. The destruction operator can be written in the number basis as

$$\hat{b} = \sum_{n=1}^{d-1} \sqrt{n} |n-1\rangle \langle n|. \quad (4.4)$$

Such a definition of the order parameter fundamentally requires that the Hilbert space not conserve total particle number because the average of the destruction operator will obviously yield zero for a number-conserving space. Note that this definition of the order parameter is just a discrete version of defining the condensate wave function as the expectation value of the field operator when deriving the continuous GP equation in Section 2.3.2. In practice, the on-site order parameter is calculated just as any other local observable:  $\langle \hat{b}_k \rangle = \text{Tr}(\hat{\rho}_k \hat{b})$ . In the following sections of this chapter, we use this observable to streamline the mapping from solitons obtained in the semiclassical picture (DNLS) to those in the quantum picture (Bose-Hubbard Hamiltonian).

#### 4.1.4 Pegg-Barnett Hermitian Phase Operator

For an infinite-dimensional Fock space, one cannot define states of definite phase for obvious normalization reasons. However, following the prescription of Pegg and

Barnett [145, 146], we can define such states for a Fock space of dimension  $d < \infty$ :

$$|\theta\rangle \equiv \frac{1}{\sqrt{d}} \sum_{n=0}^{d-1} \exp(in\theta) |n\rangle, \quad (4.5)$$

where  $\theta$  is the phase and  $i = \sqrt{-1}$ . We point out that such a phase state describes a given mode, e.g., a localized Wannier state, and should not be confused with states of definite quasimomentum that describe single particles, not modes. States of the form (4.5) differing in phase  $\theta$  by integer multiples of  $2\pi/d$  can be shown to be orthogonal. There are  $d$  such states in the window  $\theta_0 \leq \theta < \theta_0 + 2\pi$  that can be used as an eigenbasis to define a Hermitian *phase operator*. In the number basis, the result is

$$\hat{\theta} \equiv \theta_0 + \frac{(d-1)\pi}{d} + \frac{2\pi}{d} \sum_{n \neq n'} \frac{\exp[i(n' - n)\theta_0]}{\exp[i(n' - n)2\pi/d] - 1} |n'\rangle \langle n|, \quad (4.6)$$

where  $\theta_0$  is a reference phase that can be set to  $\theta_0 = 0$  for convenience. The matrix elements of the phase operator in the number basis, i.e.,  $\langle n' | \hat{\theta} | n \rangle$ , can be gleaned directly from Equation (4.6). We use  $\langle \hat{\theta}_k \rangle = \text{Tr}(\hat{\rho}_k \hat{\theta})$ , the expectation value of the on-site phase operator, as a quantum measure of relative phase between lattice sites in characterizing quantum solitons.

#### 4.1.5 Quantum Depletion

In Section 2.1.2, it was established that the condensate wave function and condensate fraction can be calculated via a diagonalization of the single-particle density matrix:

$$\rho_{\text{sp}}(x, x') = \langle \hat{\Psi}^\dagger(x') \hat{\Psi}(x) \rangle \rightarrow \sum_{j=0}^{M-1} N_j \chi_j^*(x') \chi_j(x), \quad (4.7)$$

where 1D has been assumed for simplicity and the summation limits have been stated explicitly with  $M$  being the number of allowed single-particle modes in the system. For a single-band Bose-Hubbard model of  $M$  lattices in which there are  $M$  allowed Wannier functions, the number of allowed single-particle modes is simply equal to the number of lattice sites. When deriving the Bose-Hubbard Hamiltonian in Section 2.3.3, we expanded the field operator in a basis of Wannier functions:  $\hat{\Psi}(x) = \sum_i \hat{b}_i w(x - x_i)$ , where  $w(x) \equiv w^{(0)}(x)$  is the lowest-band Wannier function. Thus the single-particle density matrix can be represented fully by a discrete matrix  $\rho_{\text{sp}}^{\text{lat}}$  as

$$\rho_{\text{sp}}(x, x') = \sum_{i,j=1}^M (\rho_{\text{sp}}^{\text{lat}})_{ij} w^*(x - x_j) w(x' - x_i), \quad (4.8)$$

where

$$(\rho_{\text{sp}}^{\text{lat}})_{ij} \equiv \langle \hat{b}_j^\dagger \hat{b}_i \rangle \quad (4.9)$$

is an  $M \times M$  matrix that can be diagonalized using standard methods. The single-particle *natural orbitals* [cf. Equation (2.14)] can then be written as

$$\chi_j(x) = \sum_{i=1}^M \phi_i^{(j)} w(x - x_i), \quad (4.10)$$

where now  $j \in \{0, 1, \dots, M-1\}$  is an index of the natural orbitals with  $j = 0$  ( $M-1$ ) denoting the most (least) highly occupied natural orbital. The quantity  $\phi_i^{(j)}$  is the coefficient of the  $(j+1)^{\text{th}}$  most highly occupied natural orbital associated with the Wannier function localized at site  $i$ . That is,  $\phi_i^{(j)}$  is the  $i^{\text{th}}$  component of the  $(j+1)^{\text{th}}$  largest eigenvector of the matrix  $\rho_{\text{sp}}^{\text{lat}}$ . The eigenvalues of  $\rho_{\text{sp}}^{\text{lat}}$  are the occupation numbers of the natural orbitals and are denoted  $N_j$  with  $N_0 \geq N_1 \geq \dots \geq N_{M-1}$ . Note that we assume eigenvectors normalized to unity:  $\sum_{i=1}^M |\phi_i^{(j)}|^2 = 1$ .

The *condensate wave function* is the system's most highly occupied natural orbital:

$$\chi_0(x) = \sum_{i=1}^M \phi_i^{(0)} w(x - x_i), \quad (4.11)$$

a function that is completely specified by the components  $\phi_i^{(0)}$  of the largest eigenvector of  $\rho_{\text{sp}}^{\text{lat}}$ . From Section 2.1, the *condensate fraction* is simply  $N_0/N$  with  $N_0$  the largest eigenvalue of  $\rho_{\text{sp}}^{\text{lat}}$  and  $N = \text{Tr}(\rho_{\text{sp}}^{\text{lat}})$  the total number of particles. Correspondingly, we define *quantum depletion* as the proportion of particles *not* in the condensed mode:

$$D \equiv 1 - \frac{N_0}{N}. \quad (4.12)$$

When working at zero temperature, finite quantum depletion ( $D \neq 0$ ) is due entirely to interactions between particles and is commonly referred to as *quantum fluctuations*. In continuous geometries such as the harmonic trap, one can show that  $D \sim (a_s/\bar{r})^{3/2}$ , where  $a_s$  is the  $s$ -wave scattering length and  $\bar{r}$  is the average interparticle spacing [20]. For typical BEC experiments in harmonic traps, this quantity is on the order of one percent or less. This is the main reason for the success of mean-field theory in describing the ground state properties of condensates in simple geometries. However, when working with excited condensates, e.g., solitons, and/or more exotic geometries, e.g., optical lattices, quantum fluctuations cannot be neglected, and a more complete quantum treatment of the problem becomes necessary. In the latter case of optical lattices, quantum depletion can actually be used to generate a ground state phase diagram of the Bose-Hubbard Hamiltonian and accurately predict the location of the Mott-superfluid border [147].



#### 4.1.6 Quantum Entanglement

Quantum entanglement is one of the most fascinating predictions of quantum theory and has puzzled physicists ever since the seminal paper of Einstein, Podolsky, and Rosen (EPR) in 1935 [93]. The idea is quite basic, but its consequences are profound. Simply put, two subsystems of a larger quantum system are said to be *entangled* if in order to describe one of the subsystems, we must reference the other. That is, the two subsystems are entangled when it is not possible to write down a pure quantum state for one of the subsystems. To describe each subsystem, we must resort to the reduced density matrix formalism. We consider two types of entanglement in characterizing a system of atoms on a Bose-Hubbard lattice: entanglement of modes and entanglement of particles. In the former case, we can think of each localized Wannier function as a quantum system that is, in general, entangled with the other  $M - 1$  Wannier functions. Because different Wannier functions are spatially distinct, we can refer to entanglement between Wannier modes as *spatial entanglement* or *entanglement between sites*. On the other hand, the particles themselves are interacting with one another so that the state of a given particle is, in general, entangled with the remaining  $N - 1$  particles [93]. We refer to this type of entanglement as *particle entanglement*.

**Spatial Entanglement** The *purity* of a quantum state described by the density matrix  $\hat{\rho}$  in a Hilbert space of dimension  $d$  is given by

$$\text{Tr}(\hat{\rho}^2) \in \left[ \frac{1}{d}, 1 \right]. \quad (4.13)$$

For a pure state, the matrix elements of  $\hat{\rho}$  in a diagonal basis are  $(\hat{\rho})_{ij} = \delta_{i,j}\delta_{i,0}$ , whereas for a maximally mixed state,  $(\hat{\rho})_{ij} = \frac{\delta_{i,j}}{d}$ . Hence, the upper (lower) bound

of the purity corresponds to a pure (maximally mixed) state. Based on this idea, we define the *average local impurity* as

$$Q_{\text{modes}} \equiv \frac{d}{d-1} \left[ 1 - \frac{1}{M} \sum_{k=1}^M \text{Tr}(\hat{\rho}_k^2) \right] \in [0, 1], \quad (4.14)$$

where  $d$  is the local Hilbert space dimension,  $M$  is the number of lattice sites, and  $\hat{\rho}_k$  is the reduced density matrix for site  $k$ . In Equation (4.14),  $\hat{\rho}_k$  is the reduced density matrix for a single lattice site and should not be confused with the single-particle density matrix  $\hat{\rho}_{\text{sp}}$ . In the former case, the partial trace is over all *lattice sites* except site  $k$ , whereas in the latter case, the partial trace is over all *particles* except one. We generalize this measure to entanglement between particles below. The normalization factor  $d/(d-1)$  in Equation (4.14) ensures  $Q_{\text{modes}} \leq 1$ . The average local impurity is maximal if each site is maximally mixed and is minimal for a direct product of on-site pure states. The measure  $Q_{\text{modes}}$  quantifies multipartite entanglement in the sense that it averages the bipartite entanglement between each site and the remaining sites. A related measure was originally introduced by Meyer and Wallach [148] and later put into more useable form by Brennen [149] for the purpose of quantifying multipartite entanglement as a function of pure states, i.e., for a system of qubits collectively in a pure state. We note that the average local impurity is equally well described as the average local mixedness, the generalized entropy [150, 151, 152], or a local average quantum Tsallis entropy [153].

We now turn to discussion of the localized von Neumann entropy. It can be shown that Shannon's definition of information entropy,

$$S \equiv - \sum_{i=1}^n p_i \log(p_i), \quad (4.15)$$

where the  $p_i$  are probabilities of events labeled  $i$ , is the unique function of the probability distribution  $\{p_i\}$  that is (1) a continuous function of the  $p_i$ , (2) a monotonically increasing function of  $n$  for a uniform probability distribution  $p_i = \frac{1}{n}$ , and (3) independent of the grouping of the events [154]. It is an extremely useful measure for quantifying the amount of information lost due to a given probability distribution. The quantum generalization is known as the *von Neumann entropy* which we define for a single site  $k$  as

$$S_{\text{vN},k} \equiv -\text{Tr} [\hat{\rho}_k \log_d(\hat{\rho}_k)] \in [0, 1], \quad (4.16)$$

resulting in the *local von Neumann entropy* where the base  $d$  logarithm is taken to ensure  $S_{\text{vN},k} \leq 1$ . We use both the average local impurity and the local von Neumann entropy to quantify the deviation of the system away from the semiclassical mean-field limit in which spatial entanglement between lattice sites is neglected completely.

**Particle Entanglement** Entanglement between particles is also neglected in pure mean-field theory because it is assumed that each particle occupies the same single-particle wave function. Thus, each particle can be described by a pure state, and, by definition, there is zero entanglement between each particle and the remaining  $N - 1$  particles. However, if a single particle is in an ensemble of different pure states, then there will be a finite amount of entanglement between particles. The particle entanglement measures that we employ are functions of the single-particle density matrix  $\hat{\rho}_{\text{sp}}$ . Generalizing the notions of impurity and von Neumann entropy to  $\hat{\rho}_{\text{sp}}$ , the reduced density matrix for a single particle, we define the *single-particle impurity* as

$$Q_{\text{particles}} \equiv \frac{M}{M-1} \left[ 1 - \frac{1}{N^2} \text{Tr}(\hat{\rho}_{\text{sp}}^2) \right] \in [0, 1], \quad (4.17)$$

and the *single-particle von Neumann entropy* as

$$S_{\text{vN, particles}} \equiv -\text{Tr} \left[ \frac{\hat{\rho}_{\text{sp}}}{N} \log_M \left( \frac{\hat{\rho}_{\text{sp}}}{N} \right) \right] \in [0, 1], \quad (4.18)$$

where the factors of total particle number  $N$  are necessary since  $\text{Tr}(\hat{\rho}_{\text{sp}}) = N$ . In a space of single-particle wave functions, the number of modes  $M$  takes the role of local dimension, hence the factor of  $M/(M-1)$  appearing in (4.17) and the base- $M$  logarithm appearing in (4.18). Owing to the indistinguishability of the particles, the single-particle impurity and single-particle entropy are in a sense bulk measures that characterize the system globally. Similarly, the average local impurity of Equation (4.14) is also a global entanglement measure, but it measures entanglement between spatially distinct modes.

## 4.2 Truncated Coherent States

We demonstrated in Section 2.3.4 that if the system is in a many-body state in the form of a direct product of Glauber coherent states, then the Bose-Hubbard Hamiltonian maps directly onto the discrete nonlinear Schrödinger equation. Within a truncated Fock space in which we retain only the first  $d$  number states, we must work with a product of *truncated coherent states*:

$$|\Psi\rangle = \bigotimes_{k=1}^M |z_k\rangle, \quad \text{where } |z_k\rangle \equiv \mathcal{N}_d e^{-\frac{|z_k|^2}{2}} \sum_{n=0}^{d-1} \frac{z_k^n}{\sqrt{n!}} |n\rangle, \quad (4.19)$$

where  $\mathcal{N}_d$  is a normalization factor that ensures  $\langle z_k | z_k \rangle = \langle \Psi | \Psi \rangle = 1$ .

The truncation error is defined as the amount of probability lost due to truncation

at  $d$  number states. If we define an unnormalized truncated coherent state

$$|z^{(d)}\rangle \equiv e^{-\frac{|z_k|^2}{2}} \sum_{n=0}^{d-1} \frac{z_k^n}{\sqrt{n!}} |n\rangle, \quad (4.20)$$

then the coherent state *truncation error* can be written as

$$\Delta(d, z) \equiv 1 - \langle z^{(d)} | z^{(d)} \rangle = 1 - e^{-|z|^2} \sum_{n=0}^{d-1} \frac{|z|^{2n}}{n!}. \quad (4.21)$$

In Figure 4.1, the coherent state truncation error is plotted for a relevant range of values of  $d$  and  $|z|^2$ . The modulus of the coherent state amplitude and the average particle number are equivalent for infinite-dimensional coherent states and are approximately equivalent for truncated coherent states, i.e.,  $|z_k|^2 \approx \langle \hat{n}_k \rangle$ . Hence, the truncation becomes less faithful for larger filling factors. However, we see that even for unit filling ( $|z|^2 = 1$ ), we only need  $d = 5, 6, 7$ , corresponding to  $\Delta \approx 10^{-2.4}, 10^{-3.2}, 10^{-4.0}$ , in order for truncated coherent states to well-represent true coherent states. We take  $d = 7$  for all simulations that follow.

### 4.3 Standing Solitons

Even though discretization of the GP equation breaks integrability, the first excited state of the DNLS can be considered its fundamental dark soliton solution. Due to the non-integrability, this solution must be found numerically. Such a solution is, by construction, a stationary state of the DNLS. In this section, we ask how such a solution evolves in time according to the corresponding quantum equations of motion. To this end, we use the TEBD routine to simulate the Bose-Hubbard Hamiltonian, taking as initial configurations the dark soliton solutions of the DNLS obtained via truncated coherent states. It is demonstrated that even deep in the

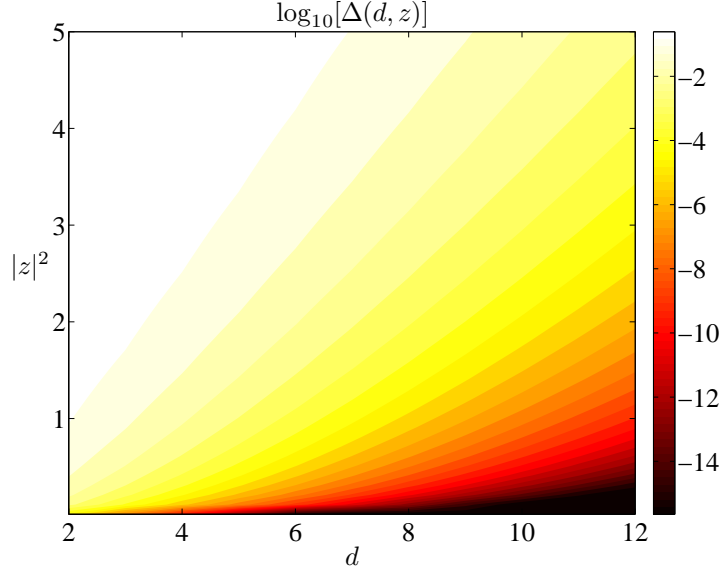


Figure 4.1. *Coherent state truncation error.* The logarithm of the coherent state truncation error, as defined in Equation (4.21), is plotted versus local dimension  $d$  and filling  $|z|^2$ . For the low filling factors that we consider in this thesis ( $|z|^2 \leq 1$ ), truncation at  $d = 7$  number states corresponding to  $\Delta \sim 10^{-4}$  is sufficient to accurately approximate infinite-dimensional coherent states. We investigate higher filling factors in a future work [155].

superfluid regime of the Bose-Hubbard phase diagram there is always a time scale at which the soliton fills in, indicating a breakdown of mean-field theory. For the parameters we consider, this time scale is on the order of tens of tunneling times and should thus be very observable in experiments. After displaying a characteristic simulation of the “graying” of the soliton, i.e., filling in of the density notch, we plot soliton decay times for different interaction strengths and filling factors.

#### 4.3.1 Fundamental Dark Soliton Solutions

The fundamental dark soliton solution of the DNLS is obtained by performing constrained imaginary time relaxation on Equation (2.61) using the Runge-Kutta method as described in Section 3.1. Specifically, we begin the imaginary time proce-

ture with a linear function through the center of the lattice:

$$\psi_k(\tau = 0) = \beta x_k, \quad (4.22)$$

where the slope  $\beta$  is arbitrary and

$$\frac{x_k}{a} = k - \frac{M+1}{2}, \quad k \in \{1, 2, \dots, M\}, \quad (4.23)$$

is the position of the  $k^{\text{th}}$  lattice site assuming the lattice is centered at  $x = 0$  with  $a$  the lattice constant and  $M$  the number of sites. Propagation of (4.22) in imaginary time according to the DNLS results in a node in the center of the lattice across which there is a  $\pi$  phase drop. The solution heals to  $\psi_k = 0$  on a length scale  $\xi \sim a/\sqrt{\nu U/J}$  analogous to the healing length in continuum mean-field theory;  $\nu$  is the average local density. Such a solution is the fundamental dark soliton of the DNLS. For the parameters used in Section 4.3.2 below, Figure 4.2(a) depicts the evolution of the solution in imaginary time, while Figure 4.2(b) shows the resulting soliton profile. Note the vanishing density notch at  $x = 0$  and the  $\pi$  phase drop across the notch.

The dark soliton solution of the DNLS is then carried over to the quantum picture by mapping the value of the mean-field condensate order parameter to the corresponding on-site coherent state amplitude, i.e.,  $\psi_k \rightarrow z_k$ . We then use the truncated coherent states of Equation (4.19) to initialize the system in a soliton-like state in which the quantum theory is approximately (due only to our truncation; see Figure 4.1) equivalent to the corresponding discrete mean-field theory.

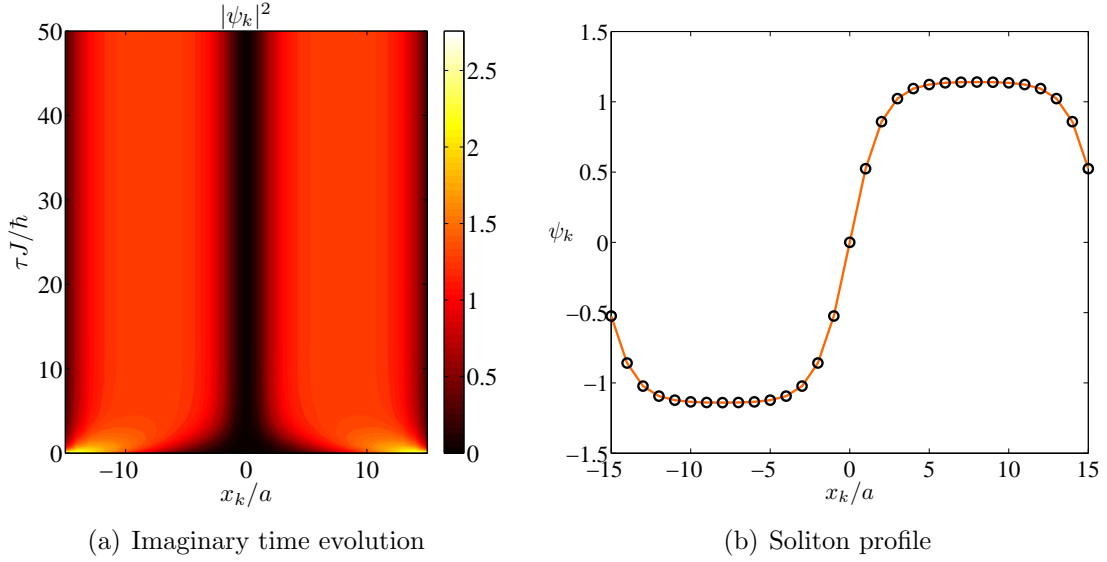


Figure 4.2. *Fundamental dark soliton solution of DNLS.* (a) Imaginary time evolution of an initial configuration  $\psi_k = \beta x_k$ , where  $\beta = 1/a$ , results in (b) the fundamental dark soliton solution of the DNLS. The solution vanishes identically at the origin because we have selected an odd number of lattice sites.

### 4.3.2 Characteristic Simulation

For definitiveness, we now focus on a single simulation displaying the system's characteristic behavior. In the following, we analyze the real time evolution of the fundamental dark soliton configuration calculated in Figure 4.2 according to both the mean-field and quantum equations of motion. Relevant parameters for the mean-field evolution are  $\nu J/U = 0.35$  at filling  $\nu \equiv N_{\text{DNLS}}/M = 1$  for  $M = 31$  lattice sites. As a brief aside, we report that the qualitative picture of the results presented below for both mean-field and quantum evolution is the same for an even number of lattice sites, e.g.,  $M = 30$ . The DNLS solution is normalized to  $N_{\text{DNLS}} \equiv \sum_{k=1}^M |\psi_k|^2$  at each step of imaginary time in Figure 4.2(a). We refer to  $\nu U/J$  as the *effective interaction strength* because it accounts for both the atom density  $\nu$  and the interaction energy



$U$ , all scaled to the tunneling coefficient  $J$ . Of course, formation of a dark soliton requires repulsive interactions so that  $U > 0$ . In Figure 4.3, we show the density and phase during real time evolution according to the DNLS. Of course, the initial configuration is a stationary solution of the DNLS, so the density does not change in time and the phase changes linearly at a rate  $\mu/\hbar$ , where

$$\mu = -J \left( \frac{\psi_{k+1} + \psi_{k-1}}{\psi_k} \right) + U|\psi_k|^2, \quad k \in \{1, 2, \dots, M\}, \quad (4.24)$$

is the chemical potential of the mean-field solution which, by definition, does not depend on the site index  $k$  for an eigenstate  $\psi_k$ . The argument of the order parameter is depicted in the window  $\pi \leq \arg(\psi_k) < \pi$ , and we assume box boundary conditions so that  $\psi_0 = \psi_{M+1} \equiv 0$ . The steep phase gradient across the notch is necessary for stable dark soliton propagation. Physically, this is because for a dark soliton state with repulsive interactions ( $U > 0$ ) the mean-field potential  $U|\psi_k|^2$  is minimal in the regions of the density notch and does not by itself support a density minima. The step function  $\pi$  phase drop across the density notch directly balances this effect creating a stable dark soliton as in Figure 4.3.

We now turn to the quantum picture and consider the evolution of the fundamental dark soliton solution of the DNLS according to the Bose-Hubbard Hamiltonian derived in Section 2.3.3. The solution of Figure 4.2(b) is carried over to an approximate Fock space representation using a direct product of truncated coherent states with  $d = 7$  number states. Specifically, we take  $\psi_k \rightarrow z_k$  in Equation (4.19). The Vidal decomposition of a product state  $|\Psi\rangle = \bigotimes_{k=1}^M \left( \sum_{n_k=0}^{d-1} c_{n_k}^{(k)} |n_k\rangle \right)$  is trivial to compute:

$$\lambda_{\alpha_\ell}^{[\ell]} = \delta_{\alpha_\ell, 1} \quad \text{and} \quad \Gamma_{\alpha_{\ell-1}\alpha_\ell}^{[\ell]n_\ell} = c_{n_\ell}^{(\ell)} \delta_{\alpha_{\ell-1}, 1} \delta_{\alpha_\ell, 1}, \quad (4.25)$$

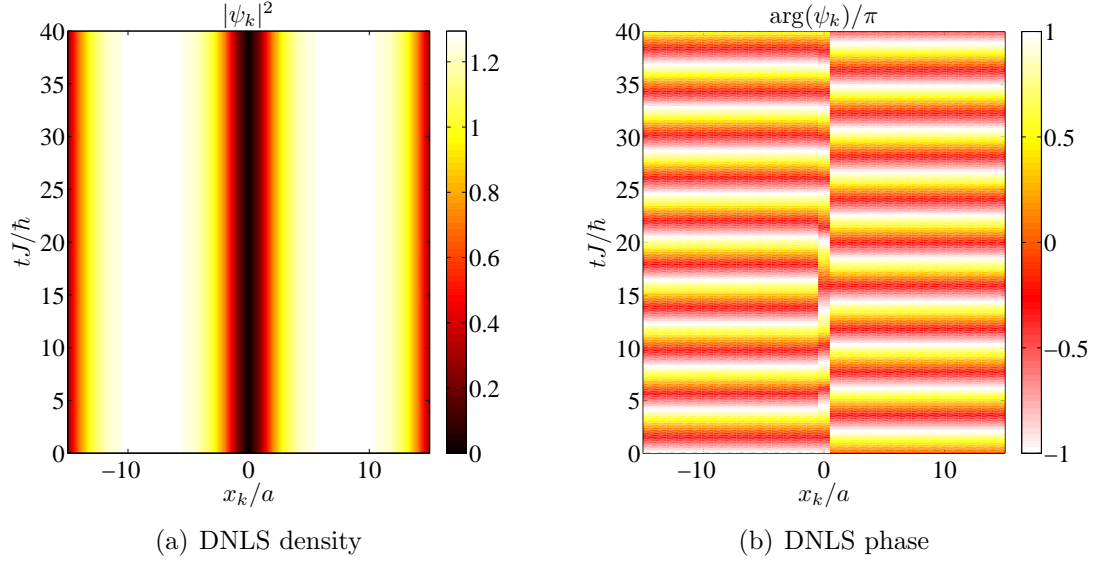


Figure 4.3. *DNLs soliton propagation.* The initial condition created in Figure 4.2 is an eigenstate of the DNLs, so the evolution of the (a) density and (b) phase is trivial. The nonlinearity is in a regime where discreteness-induced instability [63] does not destroy the soliton stability over the time scales that we consider.

where for truncated coherent states  $c_{n_k}^{(k)} = \mathcal{N}_d e^{-\frac{|z_k|^2}{2}} \frac{z_k^n}{\sqrt{n!}}$ . Equation (4.25) is derived in Appendix A.1. After carrying out the mapping from mean-field DNLs to Fock space, we propagate in time according to the Bose-Hubbard Hamiltonian using TEBD retaining basis sets of size  $\chi = 50$  throughout the procedure. The results are shown in Figures 4.4–4.6.

The density and phase dynamics during quantum evolution is shown in Figure 4.4. The expected particle number on site [Figure 4.4(a)] is the average number density measured in experiment. Hence, quantum evolution of a mean-field dark soliton state causes the soliton to fill in, or gray, over time. Eventually, the soliton is no longer visible in the density profile. Because we work with a system of finite size, exact quantum revivals will occur. However, these revivals occur on a time scale

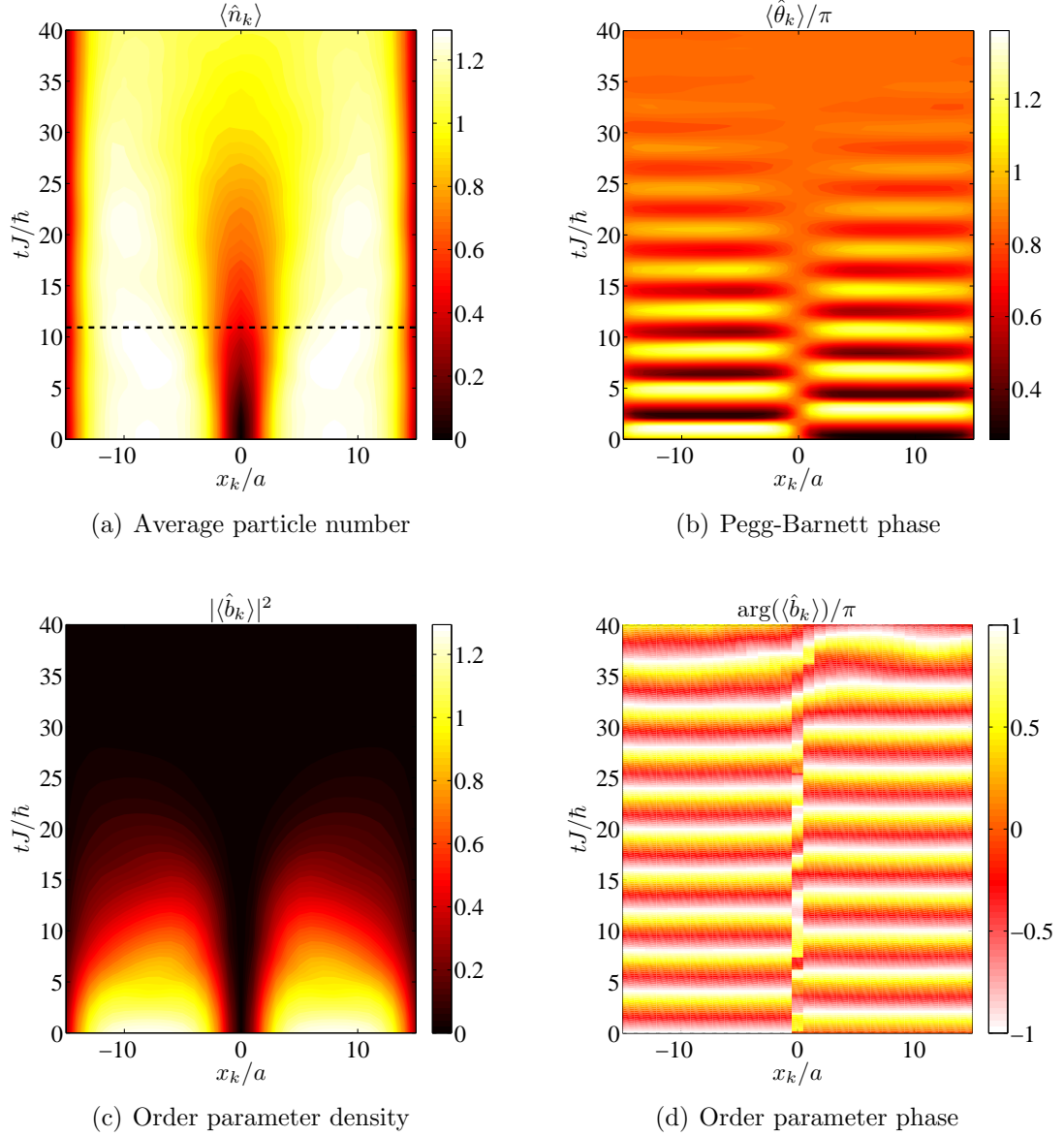


Figure 4.4. *Density and phase measures during quantum evolution of a standing mean-field soliton.* The expectation value of (a) the number operator and (b) the Pegg-Barnett phase operator during quantum evolution of a mean-field dark soliton. The density notch fills in with depleted atoms over time. (c) The order parameter density is initially approximately equivalent to the number density but decays over time as the system loses overall phase coherence, while (d) the order parameter phase maintains a  $\pi$  phase drop across  $x = 0$  for all times. The horizontal dashed line in (a) indicates the time at which  $N_b$  drops to  $1/e$  of its initial value.

much longer than can be accurately simulated using TEBD and, hence, they are never observed. For a discussion of when and how the TEBD algorithm breaks down, please see Appendix B.

During quantum evolution, the condensate order parameter, calculated as the expectation value of the lowering operator, has a time-dependent norm  $N_b \equiv \sum_{k=1}^M |\langle \hat{b}_k \rangle|^2$  that measures the overall system coherence [104, 156, 157]. The density and phase of  $\langle \hat{b}_k \rangle$  are shown in Figure 4.4(c)–(d). The decay of  $N_b$  is clearly observable and is correlated with the soliton fill-in time (see Figure 4.7). The phase, as measured by both the argument of the order parameter [Figure 4.4(d)] and the expectation value of the Pegg-Barnett phase operator [Figure 4.4(b)], initially drops by an amount  $\pi$  across the soliton notch and oscillates at the same rate as the DNLS phase [Figure 4.3(b)]. The phase operator does not retain the  $\pi$  drop over time, and for points in space-time where the order parameter density becomes negligible ( $tJ/\hbar \gtrsim 25$ ), the argument of the order parameter is meaningless. Decay in the phase drop according to the Pegg-Barnett definition does correlate with a filling-in of the soliton notch. One should expect this behavior because in mean-field theory the steep  $\pi$  phase gradient across the notch is what counters the repulsive mean-field interaction and leads to stable dark soliton propagation. However, a full quantum many-body calculation as we have presented here predicts depletion of particles out of the initial antisymmetric soliton mode into higher order modes of both even and odd symmetry (see Figure 4.5 and discussion in the following paragraphs). This has the effect of decreasing the Pegg-Barnett phase drop across the notch. We note that for times  $t > 0$  when multiple single-particle orbitals are occupied, the phase of the system in the single-particle wave function sense is ill-defined even though the Pegg-Barnett definition remains valid. Let it be stressed that, like all results we present, this is an effect observed over

many measurements.

The mean-field DNLS assumes all bosons occupy the same single-particle wave function. When creating quantum many-body states in the form of truncated coherent states obtained via the DNLS, we have effectively placed all bosons in the same configuration. However, the Bose-Hubbard Hamiltonian does not restrict bosons from depleting into other single-particle orbitals if it is energetically favorable. In pure mean-field theory, e.g., DNLS, the symmetry of the initial condition is preserved throughout time evolution in a manner very similar to that of the single-particle Schrödinger equation. Hence, for an initial configuration in the form of a soliton, the antisymmetry of the condensate wave function is preserved during mean-field evolution. But, a full quantum treatment such as simulation of the Bose-Hubbard model predicts depletion into modes with nonzero density in the center of the lattice. Because derivation of the Bose-Hubbard Hamiltonian takes into account only two-body scattering processes, it must be these processes that are responsible for depletion into non-solitonic orbitals. The symmetry of the many-body wave function is preserved regardless of the model chosen. Therefore, the mechanism most responsible for soliton graying should involve two atoms depleting from the antisymmetric condensate wave function into symmetric modes, the lowest energy of which has significant density in the region of the soliton notch. The other main scattering process involves two atoms previously depleted into a symmetric mode scattering into an antisymmetric mode of higher order than the soliton mode. Both of these processes retain the symmetry of the many-body wave function. A similar conclusion is reached in [65] where the authors use a three-mode approximation to model the antisymmetric to symmetric depletion of a soliton in a continuous trap geometry. Our treatment has the advantage in that bosons are allowed to occupy any of the  $M$  allowable natural modes of

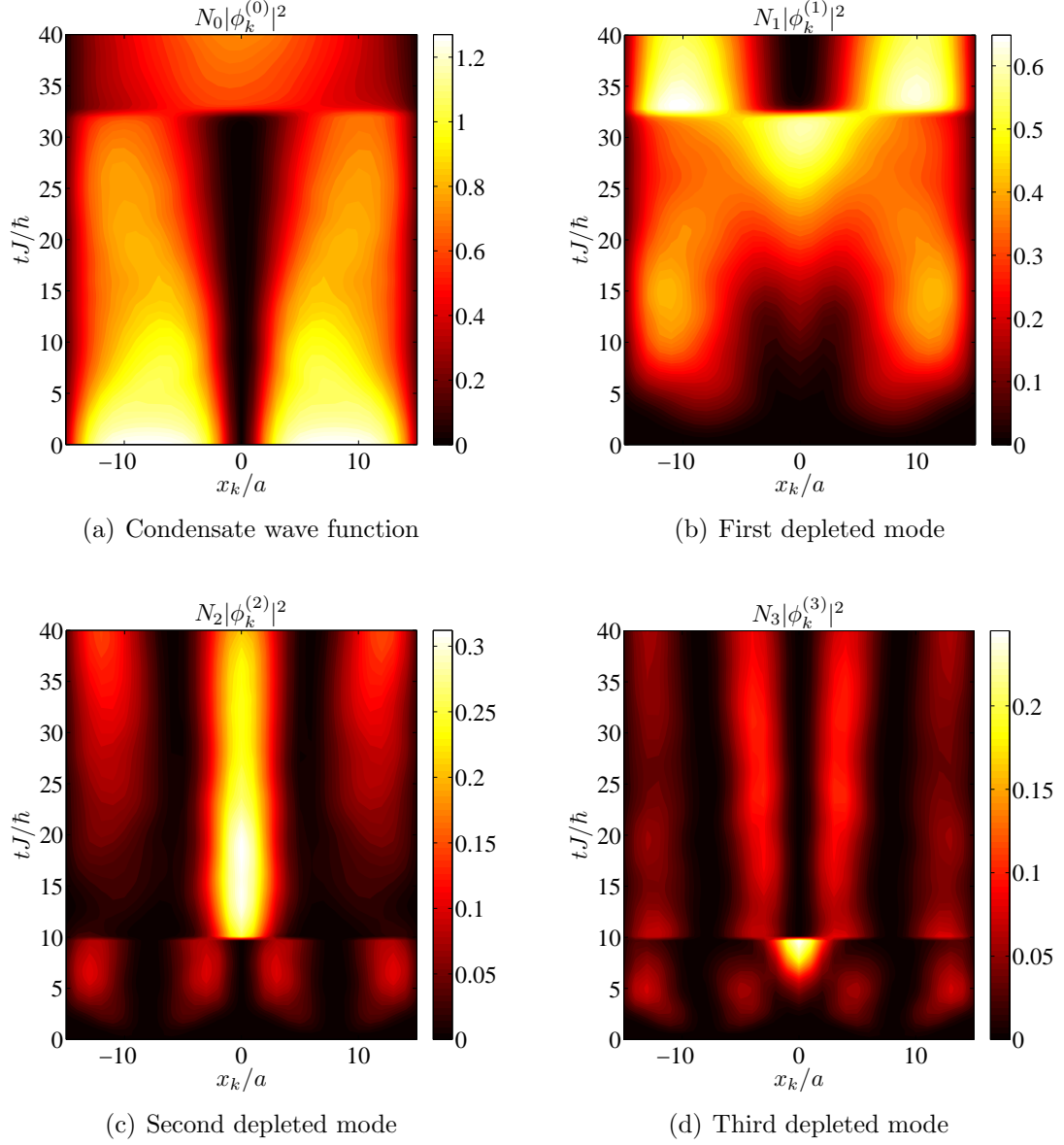


Figure 4.5. *Natural orbital dynamics during quantum evolution of a standing mean-field soliton.* (a) The condensate wave function and the (b) second, (c) third, and (d) fourth most highly occupied natural orbitals during quantum evolution of a mean-field dark soliton. Note the different color bars in each case. As explained in the text, the discontinuities are due to a swapping of natural orbital occupation numbers at specific times during the evolution.

the lattice so that both depletion processes can occur. Our method also allows us to directly probe the quantum many-body nature of the system using entanglement measures and number fluctuations as depicted in Figure 4.6.

The dynamics of the four most highly occupied natural orbitals, as calculated by diagonalization of the single-particle density matrix, are displayed in Figure 4.5. At the initial time, there is negligible depletion out of the soliton orbital ( $D \approx 0.1\%$ ). This mode is occupied by all but  $DN_{\text{ave}}$  bosons, where  $N_{\text{ave}} \equiv \sum_{k=1}^M \langle \hat{n}_k \rangle \approx N_{\text{DNLS}}$  is the total average number, a conserved quantity according to the Bose-Hubbard Hamiltonian. As explained above, quantum evolution causes an increase in occupation of non-solitonic orbitals, giving the soliton a finite lifetime. At the final time shown, approximately 48% of the bosons reside in the lowest-lying depleted symmetric mode, whereas the soliton mode is occupied by only 33% of the bosons. The other 19% can be accounted for in higher order orbitals. The discontinuities in the surface plots of Figure 4.5 are due to the fact that the natural orbitals are ordered such that  $\chi_j$  denotes the  $(j+1)^{\text{th}}$  most highly occupied natural orbital [see Equation (4.10)], and at certain times, the occupation numbers cross. In fact, for the simulation considered here, the first depleted symmetric mode gains higher occupation than the soliton mode at time  $tJ/\hbar \approx 32.5$  and becomes the system's official condensate wave function. Similarly,  $\chi_2$  and  $\chi_3$  cross in occupation at  $tJ/\hbar \approx 10$ . During the early stages of time evolution  $\chi_0$  and  $\chi_2$  are symmetric modes, whereas  $\chi_1$  and  $\chi_3$  are antisymmetric. The time dependence of the *phase* of the natural orbitals is difficult to show graphically because at each time step an independent diagonalization of the single-particle density matrix is performed, and the diagonalization routine arbitrarily assigns a global phase to the eigenvectors. However, the symmetry of the natural orbitals can still easily be discerned from these plots regardless of their unsightliness.

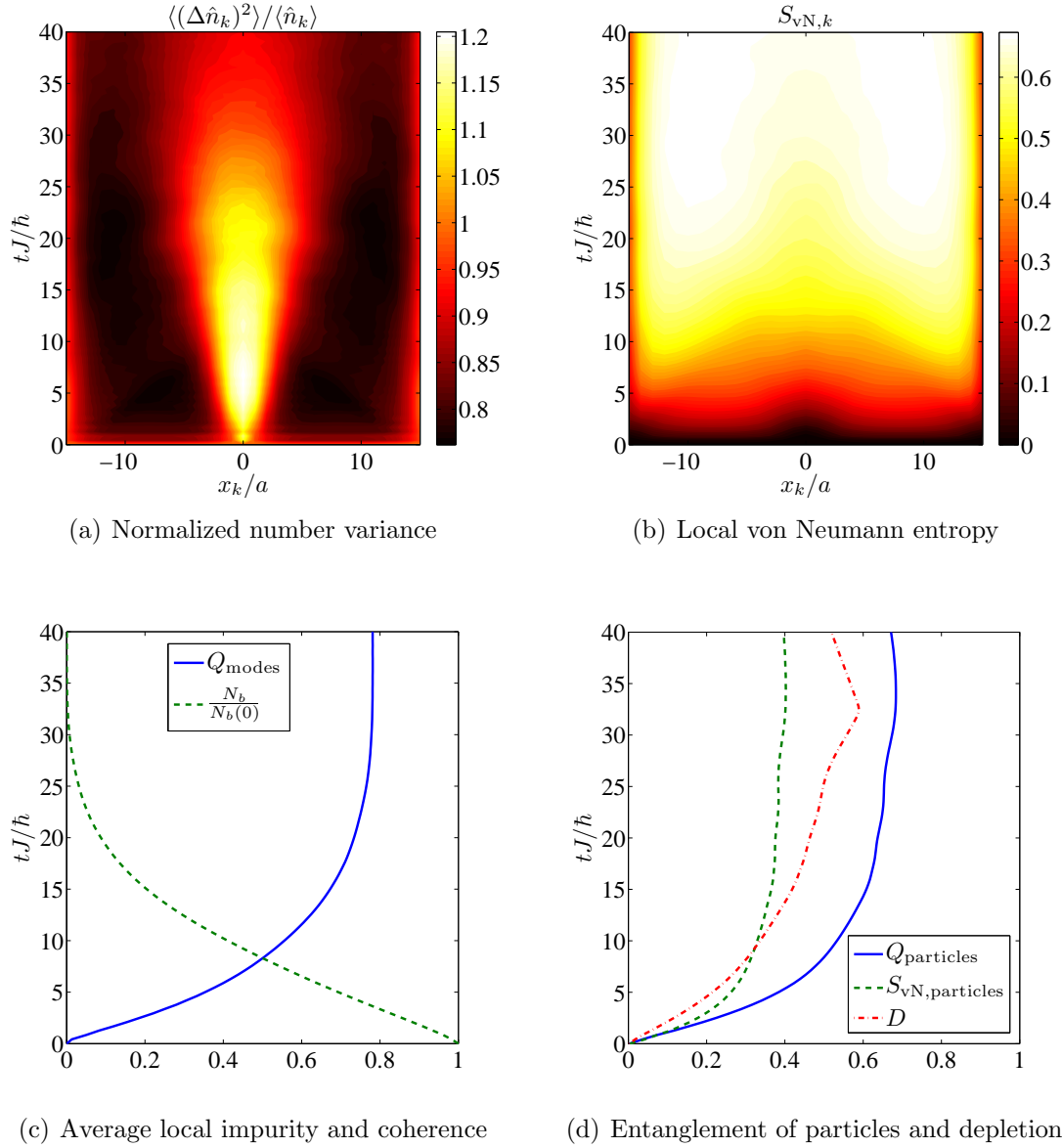


Figure 4.6. *Quantum measures during quantum evolution of a standing mean-field soliton.* (a) The normalized variance is initially unity at all sites due to on-site coherent states, but the system becomes phase-squeezed inside the density notch and number-squeezed outside until it begins to approach Poissonian number statistics at long times. (b) At  $t = 0$ , we have maximal knowledge about the state of each site, so the on-site entropy vanishes; however, the system becomes entangled spatially over time. (c) The average local impurity (order parameter norm) grows (decays) approximately exponentially in time (see Section 4.3.3). (d) Single-particle entanglement measures plateau approximately exponentially in time, and the peak in depletion coincides with condensate fragmentation [cf. the discontinuity in Figure 4.5(a)–(b)].



The semiclassical DNLS assumes that the system remains in product of Glauber coherent states for all times. However, unitary evolution according to the Bose-Hubbard Hamiltonian of a solitonic mean-field initial state causes quantum effects to crop up. Such effects are not describable by pure mean-field theory. Specifically, the DNLS assumes the following: (1) Poissonian on-site number statistics due to each site being in a coherent state, (2) zero entanglement between lattice sites due to the many-body state being a direct product of on-site states, and (3) zero entanglement between particles due to complete occupation of one single-particle wave function. The violation of these assumptions is depicted in Figure 4.6 where we display the time dependence of the normalized number variance, the local von Neumann entropy, the average local impurity, the order parameter norm, the single-particle impurity, the single-particle entropy, and the quantum depletion. All of these measures are discussed above in Section 4.1, and they are all related to the quantum many-body nature of the system. The relative number variance is maximal in regions of space-time where the soliton is filling in, thus indicating large fluctuations of the density away from its average value as particles deplete into the density notch. Also, we observe a growth in spatial entanglement between lattice sites as measured locally by the local von Neumann entropy and globally by the average local impurity. The particle entanglement also grows over time, as evidenced by an increase in both the single-particle impurity and single-particle von Neumann entropy.

### 4.3.3 Soliton Lifetimes

In the previous section, we analyzed a single instance of quantum propagation of a mean-field dark soliton. The observed behavior is observed consistently in all numerical simulations except that the soliton lifetime and growth times of quantum

effects change for different parameters. For brevity, we consider the average local impurity  $Q_{\text{modes}}$  and the order parameter norm  $N_b$  in determining the growth rate of quantum many-body effects. These quantities, being averages over local observables, are very stable numerically in the TEBD routine. Other quantities, e.g., growth in the first depleted mode  $\chi_1$ , are used to calculate these characteristic time scales in Chapter 5 where we consider the stability of density and phase engineered solitons in the Bose-Hubbard model.

Using the nonlinear fitting routine `FindFit` in *Mathematica*, we fit the order parameter norm to

$$\frac{N_b}{N_b(t=0)} \approx e^{-t/\tau_b}. \quad (4.26)$$

and the average local impurity to

$$Q_{\text{modes}} \approx Q_0 (1 - e^{-t/\tau_Q}) \quad (4.27)$$

In Figure 4.7(a)–(b) the time scales  $\tau_b$  and  $\tau_Q$  are plotted over a range of effective interaction strengths  $\nu U/J$ , all of which reside deep in the superfluid regime of the Bose-Hubbard ground state phase diagram, at three separate filling factors  $\nu = 0.1, 0.5, 1$ . As expected, the growth rates of decoherence and spatial entanglement increase monotonically (the characteristic time scales decrease) for increased interaction strength. Also, except for at very low interaction strengths, the growth rates decrease for increased filling. For a given filling factor, there is a positive correlation between the lifetime of the soliton and the time scales  $\tau_b$  and  $\tau_Q$ . To define the soliton lifetime, we fit the average number in the center site, i.e., the number of

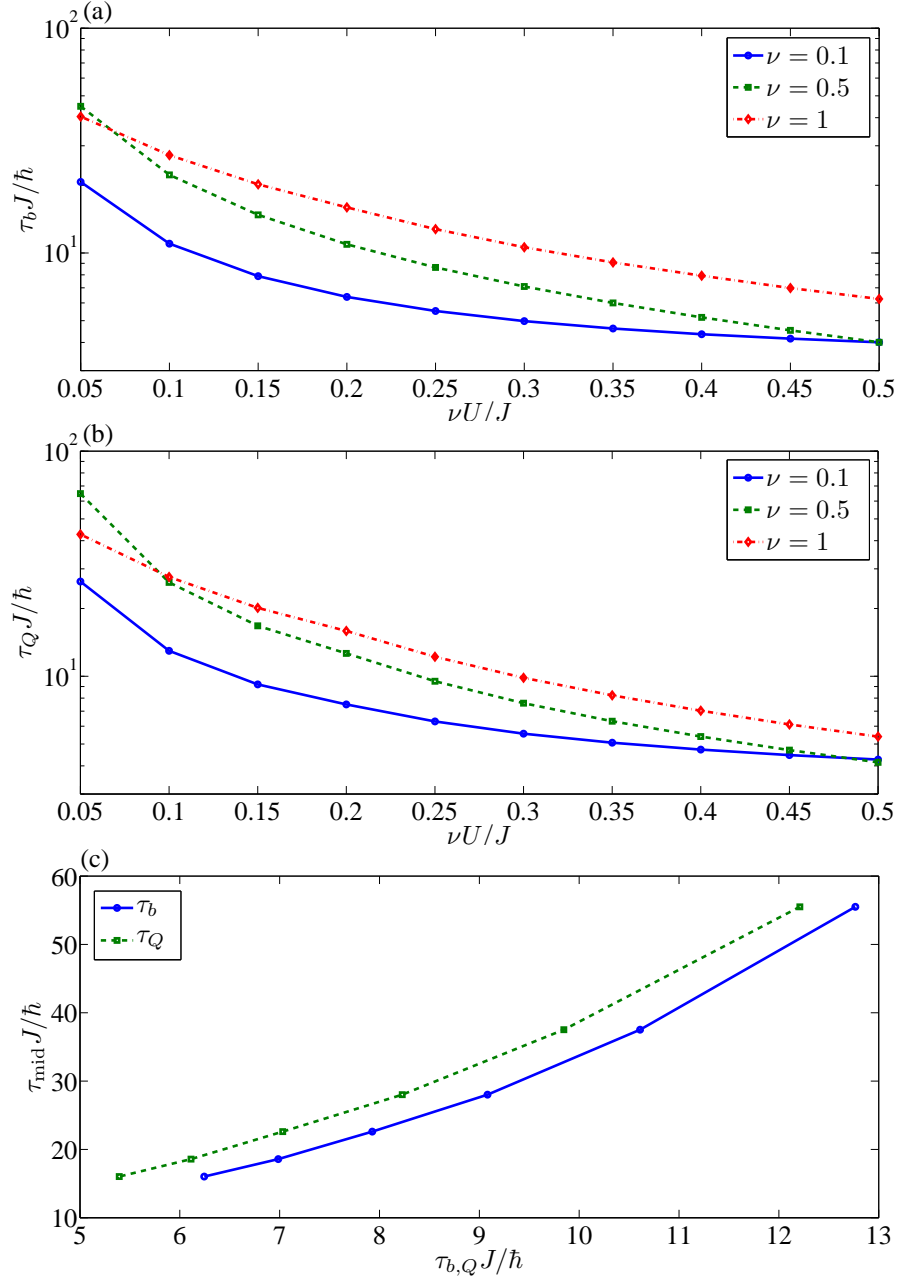


Figure 4.7. *Growth times of quantum effects and correlation to soliton lifetime.* The characteristic time scales of (a) decay in  $N_b$  and (b) growth in  $Q_{\text{modes}}$  are on the order of tens of tunneling times for the parameter regimes considered. Hence, there is always a very observable time scale at which quantum effects become significant no matter what the parameters. (c) The soliton fill-in time  $\tau_{\text{mid}}$  is plotted versus  $\tau_b$  and  $\tau_Q$  for the  $\nu = 1$  data showing a positive correlation. In all cases, the curves are a guide to the eye.

particles in the notch, to

$$\langle \hat{n}_{\text{mid}} \rangle \approx n_0 (1 - e^{-t/\tau_{\text{mid}}}). \quad (4.28)$$

Due to a poor reduced  $\chi^2$  value, we find this fit to not be valid for interaction strengths  $\nu U/J \leq 0.20$ . Figure 4.7(c) shows the positive correlation between  $\tau_b, \tau_Q$  and  $\tau_{\text{mid}}$  for the  $\nu = 1$  data points with  $\nu U/J > 0.20$ .

#### 4.3.4 Comparison to Experiment and to Finite-Temperature Effects

We use the definitions of the tunneling coefficient  $J$  and the interaction coefficient  $U$  in terms of overlap integrals involving Wannier orbitals (see Figure 2.2). We estimate that the simulation discussed at length in Section 4.3.2 and its associated data point in Figure 4.7 correspond experimentally to  $^{87}\text{Rb}$  atoms tuned via Feshbach resonance to a scattering length of  $a_s = 1.0$  nm loaded into an optical lattice created with lasers of wavelength  $\lambda = 850$  nm with lattice heights  $V_0 = E_R$  and  $V_{0\perp} = 25 E_R$  in the longitudinal and transverse directions, respectively, where  $E_R$  is the recoil energy. Using these quantities, the relevant time scales are

$$\tau_b \approx 9.1 (\hbar/J) \approx 2.8 \text{ ms}, \quad (4.29)$$

$$\tau_Q \approx 8.2 (\hbar/J) \approx 2.5 \text{ ms}, \quad (4.30)$$

$$\tau_{\text{mid}} \approx 28 (\hbar/J) \approx 8.5 \text{ ms}. \quad (4.31)$$

In the original Hannover experiment in which solitons were engineered using phase engineering methods in a highly elongated trapped Bose-Einstein condensate, interaction of the soliton with the thermal cloud caused the soliton contrast to decay to 50% on a time scale of 10 ms [15]. Note that our  $\tau_{\text{mid}}$  is a  $1/e$  decay time and is thus

a longer time scale than a 50% decay time. We stress that we are comparing two very different experiments here, one is in a harmonic trap and the other is in an optical lattice; the optical lattice experiment we are simulating has never been performed.

To make a concrete comparison to finite-temperature effects, we use the recent work of Jackson *et al.* [158] in which dark soliton decay due to thermal effects was studied numerically using the mean-field Zaremba-Nikuni-Griffin (ZNG) formalism [159]. In [158], the lowest velocity solitons for temperatures  $0.25 T_c \lesssim T \lesssim 0.5 T_c$ , where  $T_c$  is the condensation critical temperature defined in Equation (2.5), have 50% decay times  $\tau_{1/2}$  on the order of tens of longitudinal trap times. Using the  $\omega_\perp/\omega_x = 250$  trap frequency ratio as in [158], we can convert to our units using Equation (2.44) for  $\omega_\perp$  with the result for the soliton fill-in time being

$$\tau_{1/2} \gtrsim 10 (4.2 \hbar/J) \approx 13 \text{ ms.} \quad (4.32)$$

Hence, as a rough estimate, we estimate soliton decay due to thermal effects in a harmonic trap to occur on a time scale approximately 2 to 10 times slower than quantum effects in an optical lattice. Even though the parameters for the two cases are completed different, it is still useful to make comparisons in real experimental units. For truly stationary solitons such as the ones we consider, interaction with a thermal cloud, pushed out to the sides of the trap (or box) by the condensate mean field, would be minimal and the time scale of thermal effects should be much longer.

The parameters used in the simulation analyzed above are so deep in the superfluid regime of the Bose-Hubbard phase diagram that keeping  $V_0 \gtrsim E_R$  (we take  $V_0 = E_R$ ) requires the scattering length tuned down by approximately a factor of five. Yet, the solitons still have a very observable decay time, thus clearly demonstrating the inadequacy of mean-field theory for describing solitons on a lattice with just a

few atoms per site. The use of one band is justified by a quick calculation as follows. For  $V_0 = E_R$ , we have  $J \approx 0.17 E_R$  by Equation (2.53); and for  $\nu U/J = 0.35$  with  $\nu = 1$ , we have  $U \approx 0.06 E_R$ . But the band spacing is  $\hbar\omega = \sqrt{4V_0 E_R} = 2E_R$ , so in fact  $J, U \lesssim \hbar\omega$ .

#### 4.3.5 Bogoliubov Analysis

We now turn to the Bogoliubov method described in Section 2.3.5. We take the values of stationary dark solutions such as that shown in Figure 4.2(b) as the  $\xi_k$  in Equation (2.75). For the case of a harmonic trap geometry, it can be shown that the Bogoliubov quasiparticle spectrum for the dark soliton solution of the continuous GP equation contains a negative frequency mode with finite density in the region of the soliton notch [66, 67]. The frequency of this mode is  $-1/\sqrt{2}$  times the longitudinal trapping frequency  $\omega_x$  [160, 66]. For effective interaction strengths  $\nu U/J \lesssim 0.70$  on a tight-binding lattice, we observe in our calculations an anomalous mode with small negative frequency  $0 > \omega_1 \gtrsim -0.1 J/\hbar$  that is characterized by a density maxima concentrated in the soliton region. In Figure 4.8(a), we show the density of this mode for  $\nu U/J \in \{0, 0.05, 0.20, 0.35\}$ . Figure 4.8(b) depicts the density of the even natural orbital with highest occupation at times  $tJ/\hbar \approx 25, 30, 35, 40$  for the simulation presented in Section 4.4.2 for  $\nu U/J = 0.35$  and  $\nu = 1$  [see Figure 4.5(a)–(b)]. Formally speaking, this mode is  $\chi_1$  for  $tJ/\hbar \lesssim 32.5$  and  $\chi_0$  for  $tJ/\hbar \gtrsim 32.5$ . It is clear that for the parameter regimes considered here the symmetric natural orbital in Figure 4.8(b), the natural orbital most responsible for the soliton decay, is not equivalent to the negative frequency mode of the Bogoliubov theory. Also, as can be seen in Figure 4.13(c)–(d), there is significant contribution from natural orbitals of higher order, i.e.,  $\chi_2, \chi_3$ , etc., to the filling-in effect.

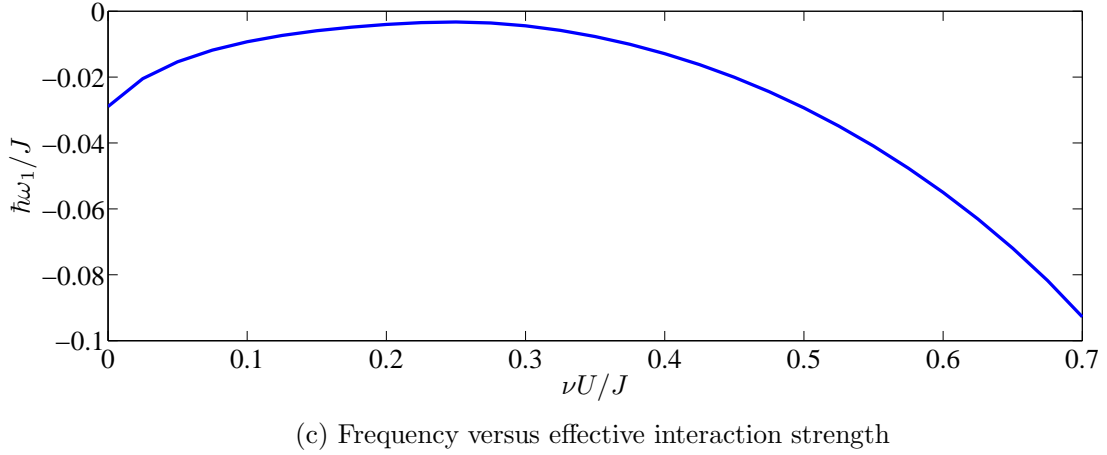
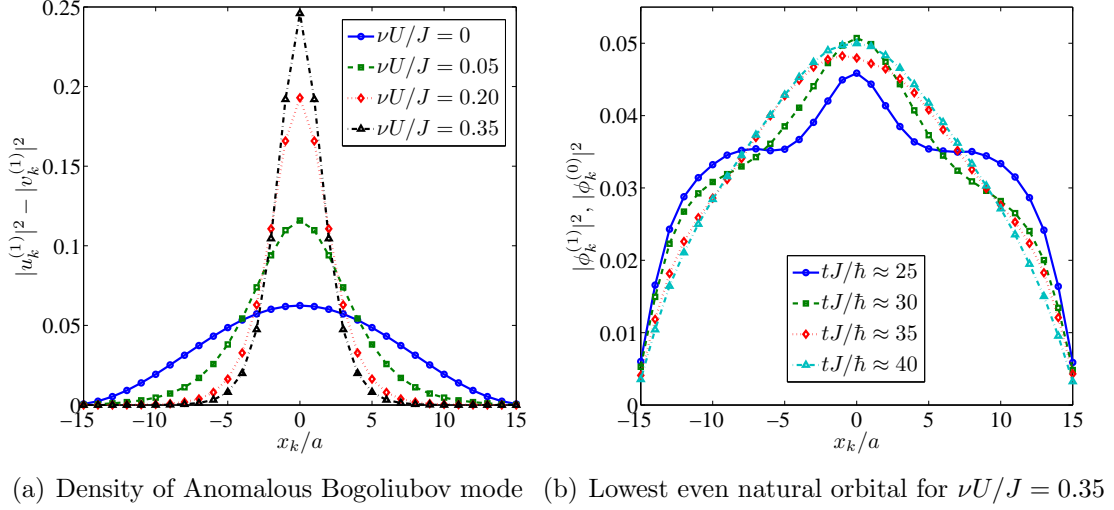


Figure 4.8. *Anomalous Bogoliubov mode: Density profile, comparison to first depleted mode, and frequency.* (a) The density of the anomalous (negative frequency) mode of the Bogoliubov excitation spectrum is plotted versus space for effective interactions  $\nu U/J = 0, 0.05, 0.20, 0.35$ . (b) For the latter case of  $\nu U/J$ , we show the time evolution at time steps  $tJ/\hbar \approx 25, 30, 35, 40$  of the depleted natural orbital most responsible for the decay of the dark soliton as shown in Figure 4.4(a). We see that the Bogoliubov mode in (a) for  $\nu U/J = 0.35$  does not resemble the evolving symmetric mode shown in (b). (c) The frequency  $\omega_1$  of the anomalous mode is plotted for different values of nonlinearity  $\nu U/J$ .

In the continuous setting, Bogoliubov modes such as those shown in Figure 4.8(a) are *anomalous*, i.e., have negative frequency, only in the presence of a harmonic trap [160, 66]. On a tight-binding lattice with no harmonic trap and box boundary conditions, we show in Figure 4.8(c) the dependence of the frequency of the anomalous mode for different values of  $\nu U/J$ . For  $\nu U/J \gtrsim 0.70$ , the anomalous mode does not appear in the Bogoliubov spectrum at all. When we add a harmonic trap on top of the lattice, as predicted in Reference [160] for the continuous case, we observe the frequency of the anomalous mode to change at a rate approximately proportional to minus the trapping frequency. This serves as a check on the validity of our calculation. It is also known for a continuous 1D box that the Bogoliubov spectrum for the soliton solution of the GP equation contains two *zero* modes, i.e., modes with vanishing frequency and vanishing norm. These two modes correspond to degeneracies in the soliton energy associated with the global phase of the wave function and the position of the soliton in the box [69]. Even though the magnitudes of the negative frequency modes obtained in our calculations are relatively small, they are surely nonzero. Before normalization to unity, the norms of the solutions are also nonzero ( $\sim 0.1$ ). Thus, we do believe that an anomalous mode indeed exists in the Bogoliubov theory, but, as shown in Figure 4.8(a)–(b), this mode is not identical to the first depleted mode observed during quantum evolution. Finally, we report that anomalous modes such as in Figure 4.8(a) fail to appear at all in the Bogoliubov theory for systems with an even number of lattice sites at interaction strengths  $\nu U/J \gtrsim 0.25$ . However, quantum many-body evolution of dark solitons in such systems is qualitatively identical to the behavior observed in Section 4.3.2 in which an odd number of sites was assumed.

In Figure 4.9, we show the Bogoliubov modes of lowest frequency for both the ground state and first excited (dark soliton) state of the DNLS. For the latter case,



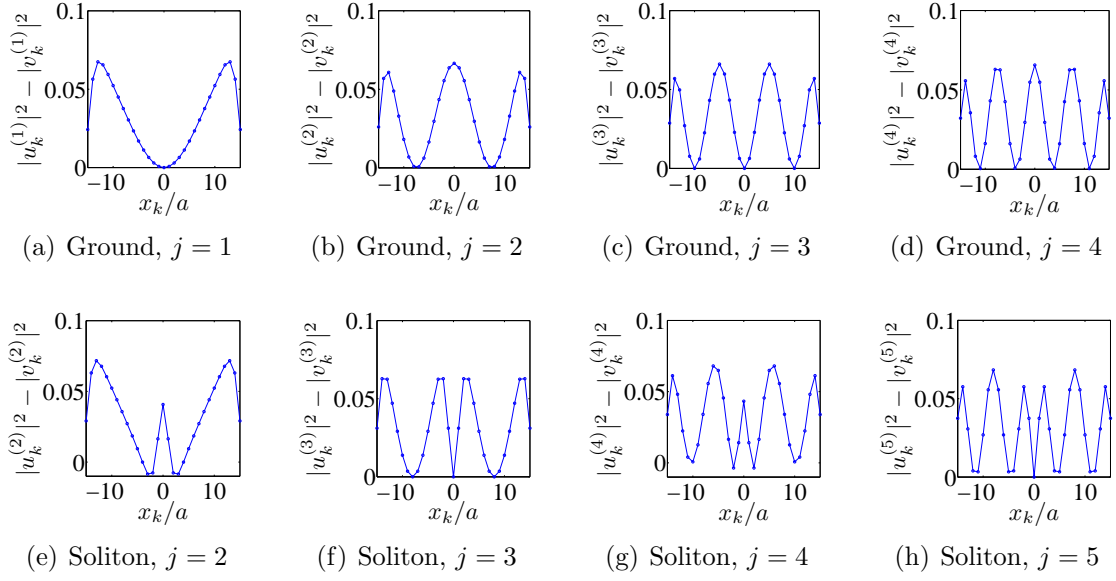


Figure 4.9. *Low frequency Bogoliubov modes: Ground and first excited state of DNLS.* For  $\nu U/J = 0.35$ , the densities of the lowest-lying Bogoliubov modes for (a)–(d) the ground state and (e)–(h) the dark soliton state of the DNLS are plotted versus spatial coordinate. In the latter case, we leave out the anomalous mode corresponding to  $j = 1$  because it is shown in Figure 4.8(a).

we omit the anomalous mode because it is shown in Figure 4.8(a). The effective non-linearity is chosen to be  $\nu U/J = 0.35$ . We see that modes of the ground state corresponding to odd (even)  $j$  are zero (maximal) at  $x = 0$ . The modes that appear in the ground state spectrum also appear in the spectrum for the dark soliton except that the modes with zero (maximal) density at  $x = 0$  develop a peak (dip) in the region of the soliton. These results are reminiscent of those in Reference [70] where time-dependent numerical Bogoliubov calculations were done to model quantum dynamics during dark soliton generation via phase imprinting in a harmonic trap. In our calculations, the lowest natural orbitals obtained using TEBD do not match the low energy Bogoliubov modes for the dark soliton state [compare Figure 4.5(b)–(d) to Figure 4.8(a) and Figure 4.9(e)–(f)]. The second and third depleted natural or-

bital, i.e.,  $\chi_1$  and  $\chi_2$ , compare more favorably to the second and third lowest energy Bogoliubov modes of the DNLS *ground state* [compare Figure 4.5(c)–(d) to Figure 4.9(b)–(d)]. Direct comparison is made difficult because the natural orbitals themselves are time-dependent. Exactly how the density of noncondensed atoms depends on the static Bogoliubov modes is unclear. The main point to be made is that a static Bogoliubov calculation as we have presented here gives some insight into the nature of quantum fluctuations but is ultimately inadequate for fully describing the dark soliton decay observed in Section 4.3.2. Another point to be made is that Bogoliubov analysis assumes the modes are completely decoupled. Our full quantum calculation clearly shows this not to be the case.

#### 4.4 Soliton-Soliton Collisions

We now turn to the case of a collision of two mean-field dark solitons in the Bose-Hubbard Hamiltonian. The initial conditions are generated in a very similar fashion to the stationary dark solitons discussed in the previous section in that we perform a mapping from the DNLS to the Bose-Hubbard model via truncated coherent states. However, instead of computing a fundamental dark soliton solution of the DNLS, we instead use the techniques of density and phase engineering to arrive at an initial condition resembling two dark solitons moving toward one another to the center of the lattice at finite velocity. We show that, unlike in pure mean-field theory, a collision between two solitons can become inelastic if the time scale of quantum fluctuations is less than or on the order of the time at which the solitons collide. This phenomenon can be understood by considering two-body scattering processes that deplete atoms into an antisymmetric mode that effectively increases the duration time of the collision.

#### 4.4.1 Density and Phase Engineering Dark Soliton-Soliton Collisions

The initial conditions are obtained by performing imaginary time relaxation in the DNLS on a constant initial condition  $\psi_k(\tau = 0) = 1$  in the presence of an external potential in the form of two Gaussians of height  $V_2$  and width  $\sigma_{V_2}$  displaced a distance  $b$  from the center of the lattice. This potential takes the form

$$\epsilon_k = V_2 \left\{ \exp \left[ -\frac{(x_k + b)^2}{2\sigma_{V_2}^2} \right] + \exp \left[ -\frac{(x_k - b)^2}{2\sigma_{V_2}^2} \right] \right\}, \quad (4.33)$$

which has the effect of creating two identical density notches at positions  $x = \pm b$  with depths and widths controlled by  $V_2$  and  $\sigma_{V_2}$ , respectively. We then imprint an instantaneous phase of the form

$$\theta_k = \Delta\theta_2 \left\{ -\frac{1}{2} \tanh \left[ \frac{2(x_k + b)}{\sigma_{\theta_2}} \right] + \frac{1}{2} \tanh \left[ \frac{2(x_k - b)}{\sigma_{\theta_2}} \right] + 1 \right\} \quad (4.34)$$

by multiplying the local condensate wave function  $\psi_k$  by the phase factor  $e^{i\theta_k}$ . Application of this phase profile gives the solitons equal-and-opposite initial velocities toward the center of the lattice. The speed of the solitons is controlled by the phase drop  $\Delta\theta_2$ , and phonon generation is minimized by appropriately tuning the width  $\sigma_{\theta_2}$  of the phase profiles to the soliton depth as determined by  $V_2$  in the density engineering stage. In Figure 4.10, we show the imaginary time evolution of the DNLS wave function and the final solution after phase imprinting; this solution is in turn used in Section 4.4.2 as an initial condition to analyze quantum evolution of a soliton-soliton collision.

The Gaussian potentials used for density engineering model two tightly-focused, blue-detuned laser beams shined at positions  $x = \pm b$  on the lattice. Blue detuning is required so that the Gaussian intensity profiles of the lasers produce a positive

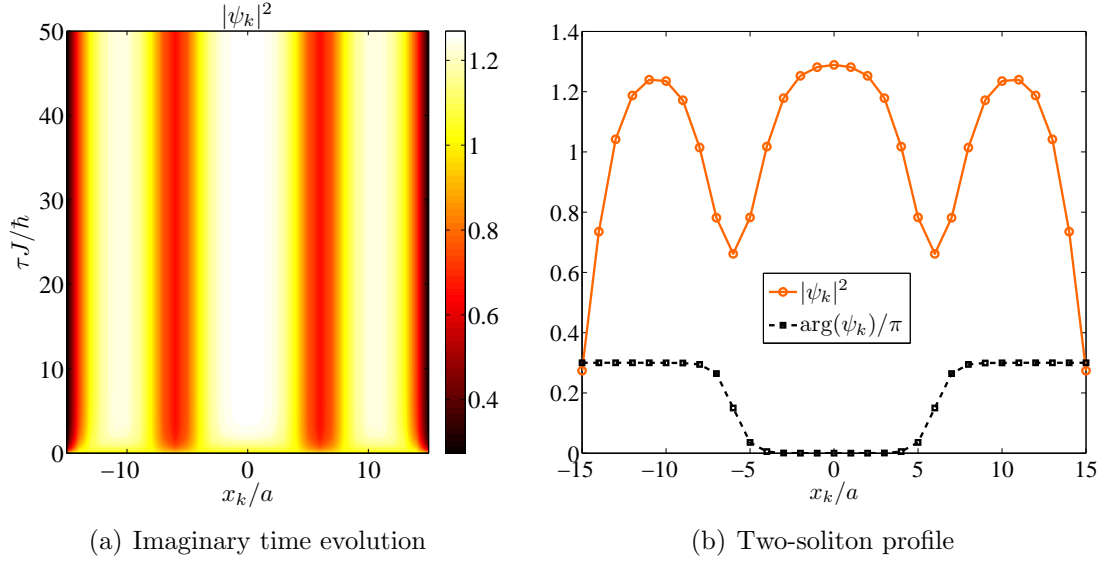


Figure 4.10. *Dark soliton engineering in DNLS.* (a) The DNLS is propagated forward in imaginary time with an external potential in the form of Equation (4.33), resulting in two symmetric density notches. An instantaneous phase given by Equation (4.34) is then imprinted on the wave function resulting in the solution shown in (b). This solution is used as an initial condition for the simulation analyzed in Section 4.4.2 where the relevant parameters are given.

potential for the atoms. Phase engineering can be realized experimentally by shining far-detuned laser pulses on the left and right ends of the lattice for a short, but specific, amount of time  $t_{\text{pulse}}$  so that a local potential  $\epsilon_k = -\theta_k \hbar / t_{\text{pulse}}$  is felt by the atoms at sites  $k$  with  $\theta_k$  given by Equation (4.34). Since all atoms are in phase, as assumed by the DNLS, this procedure has the effect of altering the on-site phase by amount  $\theta_k$  according to the time-dependent Schrödinger equation for a single particle. In order to ensure that the density is unaltered during phase engineering, we require  $t_{\text{pulse}}$  be much less than the correlation time  $\hbar/\mu$ , where  $\mu$  is the chemical potential. This assumption is what allows us to apply the phase instantaneously in simulations. It should be noted that the atoms interact with the laser light used for density and phase

engineering in the exact same way as they do with the optical lattice (see Section 2.2 for details). Such a density and phase engineering method is closely modelled after that presented in References [54, 55] for creating solitons in Bose-Einstein condensates in continuous geometries. The method of phase engineering alone was used to generate solitons experimentally in harmonic traps [15, 50]. For an array of 1D optical lattices, each 1D tube is density and phase engineered simultaneously. The present discussion concerns soliton engineering in the DNLS for the purpose of creating theoretically pleasing mean-field initial conditions for subsequent propagation according to the Bose-Hubbard Hamiltonian. In Chapter 5, we perform more experimentally relevant simulations by generalizing the procedure to the quantum picture and engineering solitons directly in the Bose-Hubbard Hamiltonian using TEBD.

#### 4.4.2 Characteristic Simulation

We now evolve the DNLS configuration calculated in Figure 4.10 in real time according to the both the DNLS and Bose-Hubbard Hamiltonian. As in Section 4.3.2, we take  $\nu U/J = 0.35$  at filling  $\nu = 1$  on a lattice of  $M = 31$  sites. The parameters used for the density and phase engineering are  $V_2/J = 0.4$ ,  $\sigma_{V2}/a = 1$ ,  $b/a = 6$ ,  $\Delta\theta_2 = 0.3\pi$ , and  $\sigma_{\theta2}/a = 2$ , where  $a$  is the lattice constant. Figure 4.11 depicts the mean-field DNLS evolution of the initial condensate wave function shown in Figure 4.10(b). The collision is very elastic as the speeds of the solitons are unchanged as a result of the collision. The forward in time (backward in space) trajectory shifts of the solitons due to the collision are barely noticeable by eye.

We now turn to the quantum picture and build the same initial condition in Fock space via a product of truncated coherent states as we did previously for standing solitons in Section 4.3.2, i.e., we take  $\psi_k \rightarrow z_k$  in Equation (4.19). The coherent states

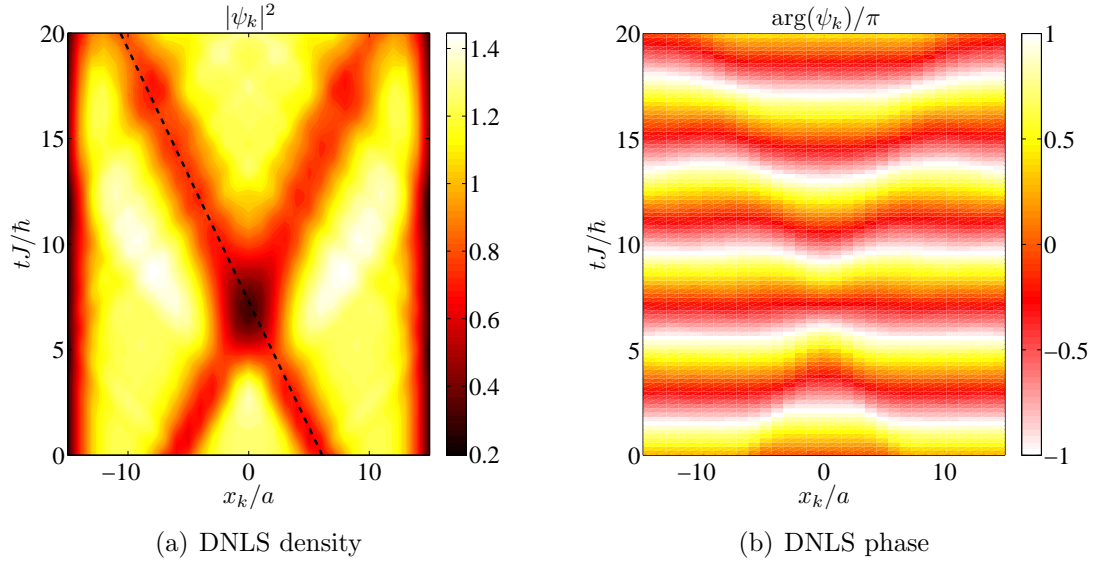


Figure 4.11. *DNLS soliton-soliton collision*. The density and phase engineered initial condition of Figure 4.10 is propagated forward in real time according to the DNLS. The dashed line in (a) is the trajectory of the soliton before collision. The space-time shift associated with the collision is very small. The phase drop across the solitons is maintained throughout evolution as can be seen in (b).

are truncated at  $d = 7$  number states. As before, we perform a Vidal decomposition on this initial condition for input into the TEBD routine which we employ for real time quantum evolution, keeping  $\chi = 50$  basis sets as before. The results are depicted in Figures 4.12–4.14.

We first focus on density and phase measures. The average particle number density [Figure 4.12(a)] closely follows the DNLS density [Figure 4.11(a)] before and during the collision because the decoherence time, as indicated by the dashed line in Figure 4.12(a), occurs just after the collision. As expected, the Pegg-Barnett phase operator exhibits a phase drop across the notch for short times. However, after the decoherence time, this drop is less pronounced. As in the standing soliton case,  $|\langle \hat{b}_k \rangle|^2$ , the square modulus of the order parameter, decays over time. Its phase

$\arg(\langle \hat{b}_k \rangle)$  rotates at the same rate as both the expectation value of the Pegg-Barnett phase operator and the phase of the DNLS wave function, although  $\arg(\langle \hat{b}_k \rangle)$  does lose meaning in the regions of space-time for which  $|\langle \hat{b}_k \rangle|^2$  vanishes.

The initial condition exhibits negligible quantum depletion, i.e., all atoms occupy the even single-particle mode proportional to that shown in Figure 4.10(b). However, as occurs for the standing soliton analyzed in Section 4.3.2, there exist two-body scattering processes which deplete the system and give rise to entangled quantum dynamics. The depletion processes which preserve the overall symmetry of the many-body function include two atoms scattering from an even mode into an odd mode and two atoms scattering from an even mode into another even mode of higher order. Since odd modes must vanish at  $x = 0$ , occupation of such modes will obviously effect a collision of two solitons that occurs at the center of the lattice. We show the densities of the four natural orbital with highest occupation. As in Figure 4.5, the discontinuities are due to the ordering of natural orbital occupation numbers at each time step shown. For times  $tJ/\hbar \gtrsim 3$ , we see that the second most highly occupied natural orbital  $\chi_1$  is indeed an antisymmetric mode similar to a standing soliton. However, for this particular simulation, such depletion processes do not have a drastic effect on the collision because they occur on a slightly longer time scale than the time it takes the solitons to collide. In the next section, we show that if the depletion time scale is tuned to occur at or before the time at which the two solitons collide, then an inelasticity is effectively induced in the collision.

In Figure 4.14, we show, for the soliton-soliton collision discussed above, the time evolution of the same quantum measures as in Figure 4.6 for the standing case. Figure 4.14(a) shows a normalized number variance less than unity, i.e., sub-Poissonian or number-squeezed number statistics, for all times  $t > 0$ . However, the relative

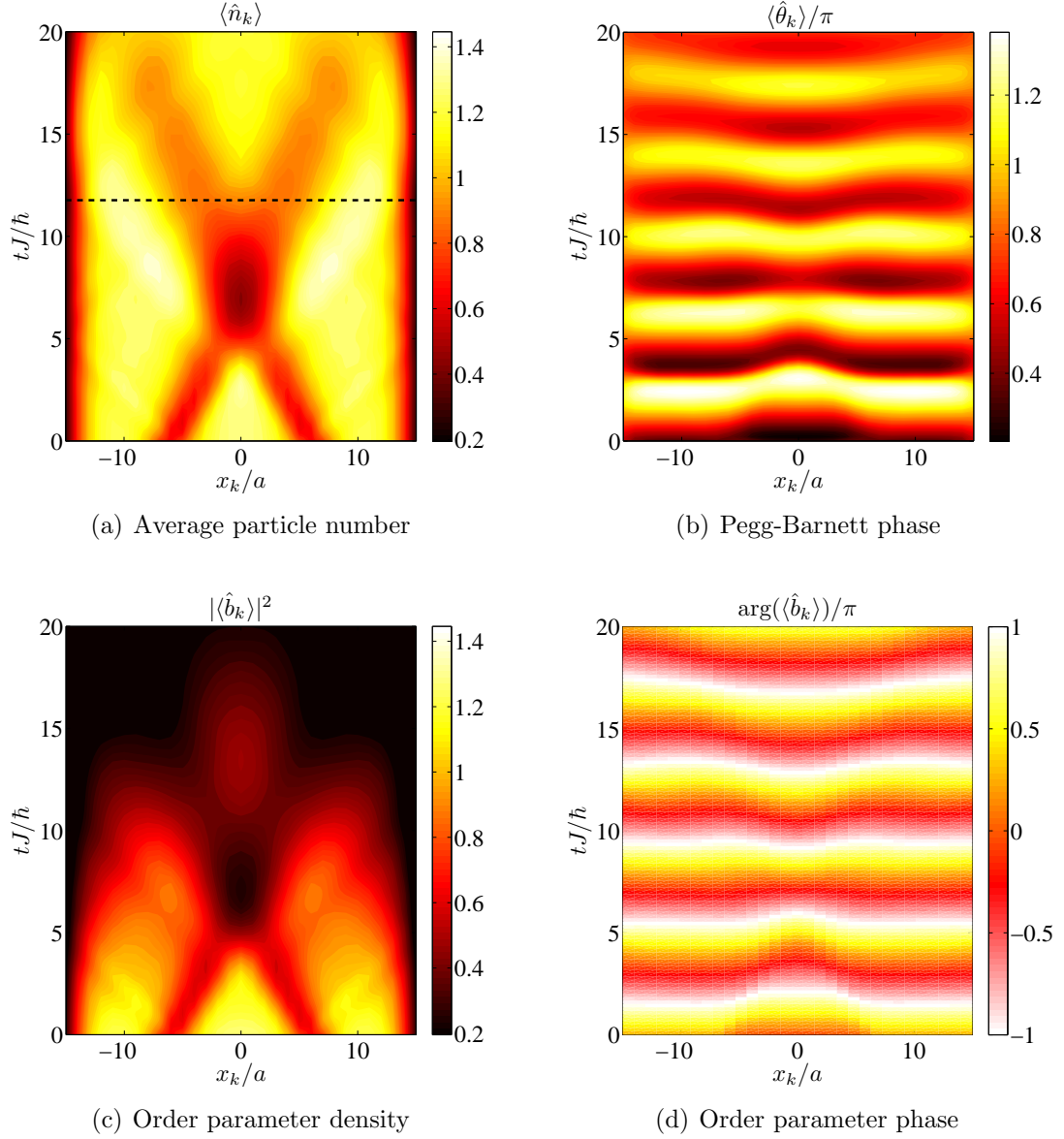


Figure 4.12. *Density and phase measures for quantum evolution of a mean-field soliton-soliton collision.* The expectation value of (a) the number operator and (b) the Pegg-Barnett phase operator during quantum evolution of a collision between two mean-field solitons. The collision is mean-field-like since it occurs before the decoherence time which is indicated by the dashed line in (a). The order parameter (c) density and (d) phase are shown for the same simulation.



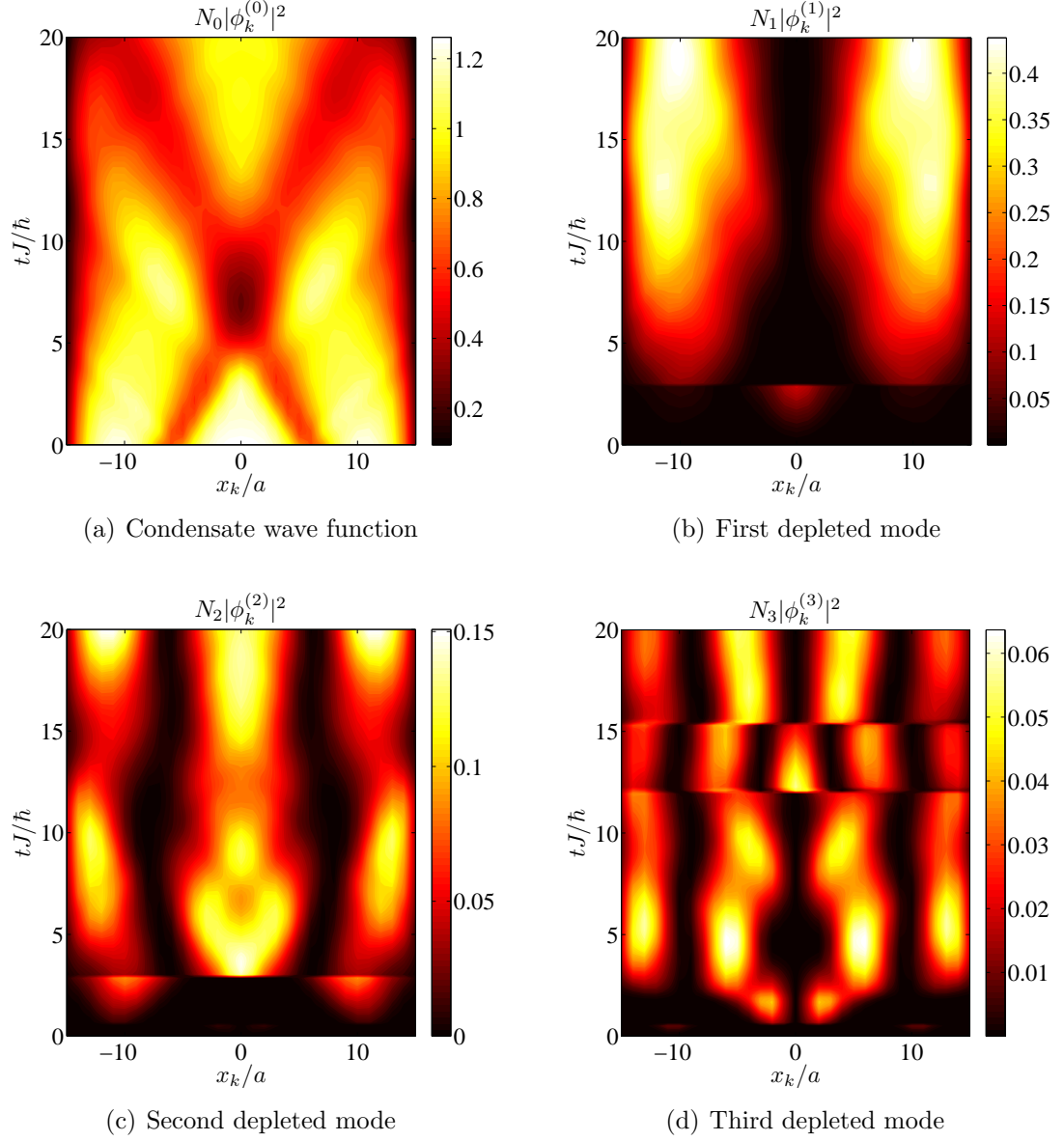


Figure 4.13. *Natural orbital dynamics during quantum evolution of a mean-field soliton-soliton collision.* (a) The condensate wave function and the (b) second, (c) third, and (d) fourth most highly occupied natural orbitals during quantum evolution of a collision between two mean-field solitons. Even though depletion is significant ( $D \approx 40\%$  at the final time), the collision is still quite elastic as the time scale for quantum fluctuations is slightly longer than the time of collision.

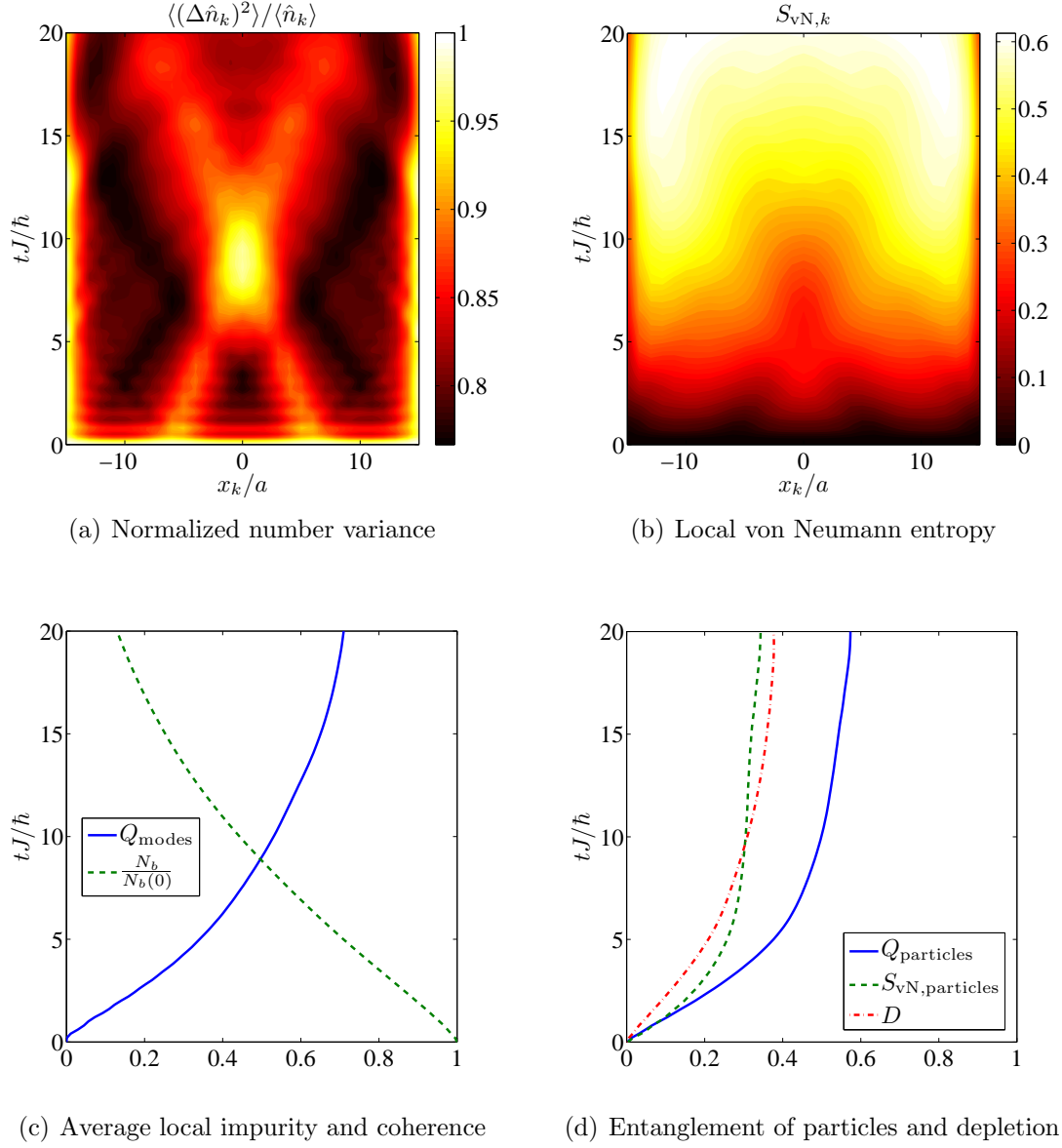


Figure 4.14. *Quantum measures for quantum evolution of a mean-field soliton-soliton collision.* The same measures as in Figure 4.6 are shown but for the case of a soliton-soliton collision. The behavior of the measures in (b)–(d) is generally similar to that observed in Figure 4.6. On the other hand, the normalized number variance in (a) displays number-squeezed number statistics for all times  $t > 0$ , whereas both number- and phase-squeezed statistics occur in the standing soliton simulation.

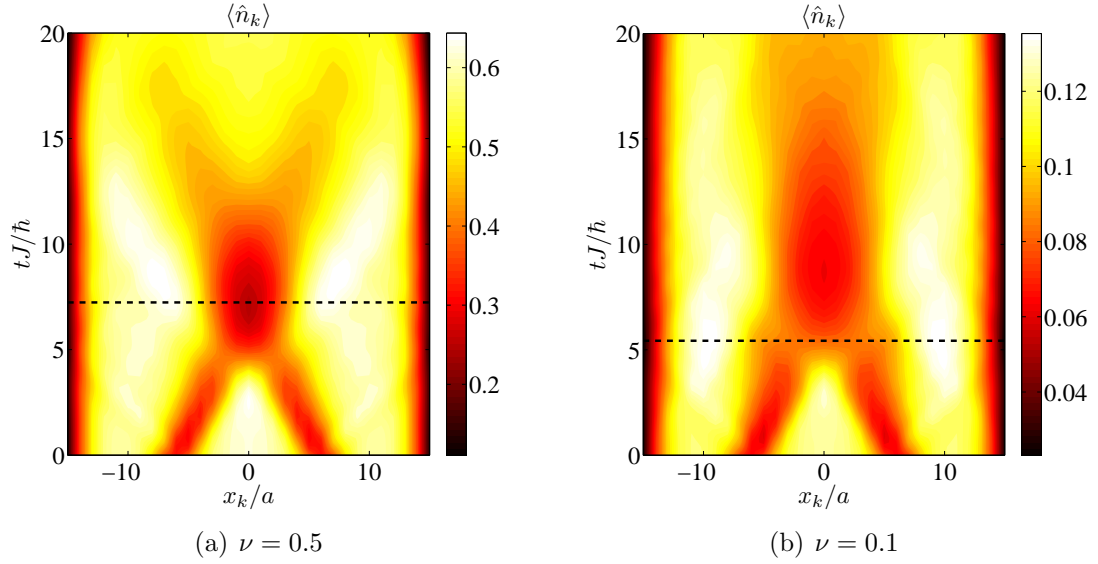


Figure 4.15. *Inelastic soliton-soliton collision induced by quantum fluctuations.* The average number density is plotted versus position and time for the exact same parameters as in Section 4.4.2, including the effective interaction strength  $\nu U/J = 0.35$  but with filling factors (a)  $\nu = 0.5$  and (b)  $\nu = 0.1$ . We see that when the decoherence time lies at or near the collision time, the collision elasticity decreases.

number variance is greatest during the soliton collision. Of course, the local von Neumann entropy shown in Figure 4.14(b) is initially zero since the initial condition is a full product state. As expected, quantum evolution causes a build-up in spatial entanglement as evidenced by nonzero values of both  $S_{\text{vN},k}$ , the local von Neumann entropy, and  $Q_{\text{modes}}$ , the average local impurity, as shown in Figure 4.14(c). Growth in entanglement between particles is shown in Figure 4.14(d).

#### 4.4.3 Quantum-Induced Inelasticity

For a fixed value of the effective nonlinearity  $\nu U/J$ , we can tune the growth rate of quantum fluctuations by changing the filling without altering the initial density-phase profile of the initial condition. Specifically, according to Figure 4.7, we can

increase this growth rate by decreasing the filling. When this occurs, support from the many-body wave function is lessened and the depletion processes occur at a faster rate. Depletion into an antisymmetric mode like that in Figure 4.13(b) is thus more pronounced. The final result on the dynamics is that the soliton-soliton collision becomes more inelastic, i.e., the solitons interact or “stick together” for a longer time. Subsequent filling in of the notch after collision can be explained by depletion into higher order natural orbitals, e.g.,  $\chi_2$ ,  $\chi_3$ , etc. This point is demonstrated in Figure 4.15 in which we show the number density for identical simulations to the one analyzed in detail in Section 4.4.2 except with filling factors  $\nu = 0.5, 0.1$ . The effective interaction is still taken to be  $\nu U/J = 0.35$ . As before, the dashed lines indicate the  $1/e$  decay time of the order parameter norm  $N_b$ .

## 4.5 Summary

In summary, we have presented a quasi-exact numerical analysis of quantum many-body effects on mean-field dark solitons in 1D optical lattice potentials. This was achieved by using the TEBD routine to simulate quantum many-body dynamics in the Bose-Hubbard Hamiltonian of initial dark soliton states based on a product of Glauber coherent states obtained via the discrete nonlinear Schrödinger equation. We showed that quantum depletion (1) causes standing solitons to have a finite lifetime that should be very observable in experiment and (2) induces an inelasticity in soliton-soliton collisions. For a 1D optical lattice, even deep in the superfluid region of the ground state phase diagram, discrete mean-field theory, i.e., the DNLS, is an inadequate description of dark solitons, at least for the parameter regimes that we explore. We also calculated the Bogoliubov spectrum for a discrete dark soliton state in the tight-binding limit. For low enough interaction strengths, we observe an

anomalous mode in the Bogoliubov spectrum with a density maximum in the soliton notch. However, this mode is different from the first depleted natural orbital in our TEBD calculations. All in all, the static Bogoliubov treatment leaves out a wealth of physics accessible with a full many-body treatment.

For a discussion of the convergence and accuracy of the results obtained using TEBD, see Appendix B. Because we are most interested in the short-time behavior of the system which is initially in a low-energy, spatially unentangled state, TEBD serves as an ideal numerical tool. However, our method for this particular problem could be improved by adapting  $\chi$ , the number of retained basis sets, in simulation time to the amount of entanglement currently present. We note that number-conserving methods can fundamentally not be used for the types of simulations presented in this chapter. The reason is that the initial conditions, products of truncated coherent states, are themselves a superposition of states that do not conserve total number. In the next chapter, we generate dark solitons in the Bose-Hubbard model in a manner that exactly replicates how it would be done in experiment. For such studies, we do in fact employ number conservation.

## Chapter 5

### QUANTUM SOLITON ENGINEERING

In the previous chapter, we investigated quantum many-body effects on dark solitons in an optical lattice by using the Bose-Hubbard Hamiltonian, a quantum many-body theory, to simulate initial conditions obtained directly from solitons obtained in the DNLS, the corresponding mean-field theory. From a theoretical perspective, this method has the advantage in that it provides a quantitative measure of the applicability of mean-field theory. Namely, we have shown that there is always a very observable time scale at which quantum effects cause mean-field theory to break down. However, from an experimental perspective, the initial conditions used in Chapter 4 are not easily created. That is, a direct product of Glauber coherent states is not close to the ground state of the Bose-Hubbard Hamiltonian unless one assumes (1) the thermodynamic limit, i.e.,  $M, N \rightarrow \infty$  at fixed filling  $N/M$ , and (2) a hopping parameter much greater than the interaction parameter, i.e.,  $J \gg U$  [116]. In this chapter, we create dark solitons that are in fact close to the system's ground state. The idea is very natural. We generalize to the Bose-Hubbard Hamiltonian the methods of density and phase engineering as discussed in Section 4.4.1 for the DNLS. Here, all calculations are done using TEBD. We first relax the system in the presence of one or two external Gaussian beams to create one or two density notches. Next, we remove the external potential and imprint a desired phase. Finally, we evolve the system with only the lattice potential turned on. The evolution is characterized by a set of measures very similar to those presented in Section 4.1. As in the previous

chapter, we consider both standing solitons and soliton-soliton collisions, although emphasis is placed on the former.

## 5.1 Methods for Density and Phase Engineering

Density engineering in a system described by the Bose-Hubbard Hamiltonian is a rather straightforward task. To mold the desired density, one simply selects an appropriate external potential  $\epsilon_k$  to use in Equation (2.46) and then finds the ground state of the resulting Hamiltonian. Using TEBD, this ground state can be found by propagation in imaginary time as explained in Section 3.2.4. Of course, for sufficiently small systems, the ground state can be calculated via exact diagonalization.

On the other hand, phase engineering is more subtle. In mean-field theory, all atoms are assumed to be in the same wave function and hence in phase with one another. Thus, imprinting a phase on the many-body wave function is conceptually equivalent to doing so on a single-particle wave function. Quantum-field theory relaxes the assumption that all particles are in phase. However, we can still imprint a phase in the natural way so long as the condensate fraction is large enough. To do this, we can change the local lattice potential to  $\epsilon_k = -\theta_k \hbar / t_{\text{pulse}}$  for a short time  $t_{\text{pulse}}$  in real time to imprint a phase  $\theta_k$  at site  $k$ . In simulation, it suffices to apply the phase instantaneously which amounts to applying the on-site unitary operator  $\exp(i\hat{n}\theta_k)$ , where  $\hat{n}$  is the local number operator. The exact forms of the external potential  $\epsilon_k$  used for density engineering and of the imprinted phase  $\theta_k$  depend on the problem in question. The forms used for soliton engineering are given in the sections that follow.

## 5.2 Standing Solitons

We first concentrate on the case of an engineered standing soliton in the center of the lattice. A single Gaussian beam is used to engineer the density notch and a hyperbolic tangent phase profile is then imprinted across the notch. First, we present a characteristic simulation of engineered quantum soliton propagation and then calculate soliton decay times for different values of the effective interaction parameter.

### 5.2.1 Density and Phase Engineering of Standing Solitons

We can dig a single density notch centered at  $x = 0$  by performing imaginary time relaxation with an external Gaussian potential of the form

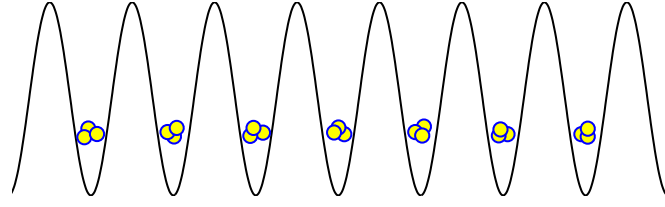
$$\epsilon_k = V_1 \exp\left(-\frac{x_k^2}{2\sigma_{V_1}^2}\right). \quad (5.1)$$

For the phase imprinting, we use a hyperbolic tangent phase profile of the form

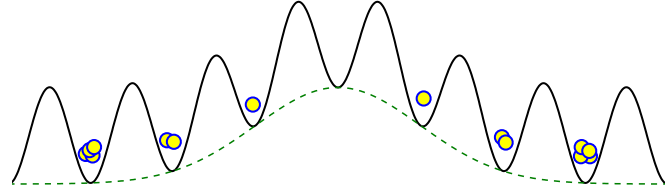
$$\theta_k = \frac{\Delta\theta_1}{2} \tanh\left(\frac{2x_k}{\sigma_{\theta_1}}\right). \quad (5.2)$$

For a true standing dark soliton, we would have to use a Dirac delta function for the potential in Equation (5.1) to effectively create two independent boxes so the wave function would heal perfectly to zero at the center of the lattice. Thus, for a Gaussian potential of finite amplitude and width, a certain fraction of the energy used to form the notch goes into the creation of phonons and a certain fraction goes into the creation of the soliton [54]. Also, standing solitons have a  $\pi$  phase drop across the notch in the form of a perfect step function; hence, ideally we should take  $\Delta\theta_1 = \pi$  and  $\sigma_{\theta_1} \rightarrow 0$ . Experimentally, the parameter  $\sigma_{\theta_1}$ , i.e., the width of the phase profile, represents diffraction-limited fall-off of the far-detuned laser beam used

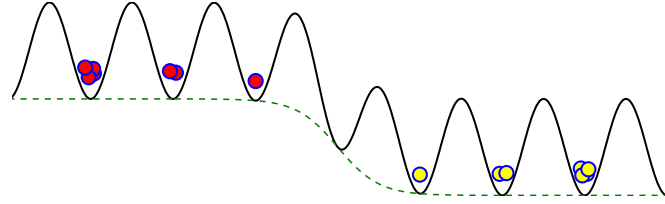




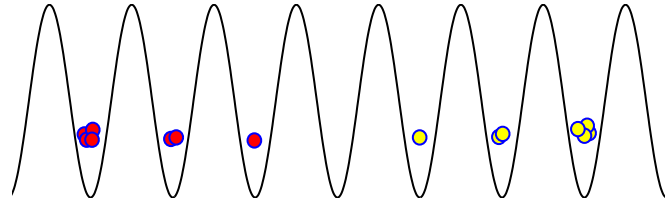
(a) Free lattice



(b) Density engineering



(c) Phase engineering



(d) Resulting state

Figure 5.1. *Schematic of density and phase engineering a standing soliton.* To engineering a standing soliton in a lattice, we (a) take a free lattice, (b) apply a tightly-focused blue-detuned Gaussian beam to dig a density notch, (c) turn off the Gaussian beam and raise half the lattice to imprint a phase, (d) lower the lattice resulting in (d). The lattice heights are the same in each panel, red indicates a  $\pi$  phase change on those atoms, and particle numbers should not be taken literally as the lattice is meant to extend past the sites shown.

to raise half the lattice [54]. If  $\sigma_{\theta 1}$  is on the order of the soliton healing length, the engineered soliton will drift to the left. We ignore this effect in simulation by taking a sufficiently small value of  $\sigma_{\theta 1}$ . Note, however, that stationary solitons can still be created with significant diffraction-limited fall-off by choosing a value of  $\Delta\theta$  slightly greater than  $\pi$  to create a second shallow soliton to carry away the momentum of the first [54].

Density and phase engineering using the forms (5.1) and (5.2) can be applied to either the DNLS or the Bose-Hubbard Hamiltonian for soliton creation. We consider both cases in this section. A schematic of the procedure used to quantum engineer a stationary dark soliton is depicted in Figure 5.1.

### 5.2.2 Characteristic Simulation

Let us now consider a single simulation of soliton engineering in both the mean-field and quantum many-body pictures. Like all simulations in Chapter 4, we select for the effective interaction parameter  $\nu U/J = 0.35$ . We choose to work on a lattice of  $M = 30$  sites with  $N = 30$  particles so that the filling factor  $\nu \equiv N/M = 1$ . This definition of the filling factor differs from that in Chapter 4 in which it was defined in terms of the norm of the DNLS solution used to create the initial state in the quantum picture. The relevant parameters used to engineering the soliton are  $V_1/J = 1$ ,  $\sigma_{V1}/a = 1$ ,  $\Delta\theta = \pi$ ,  $\sigma_{\theta 1}/a = 0.1$ , where  $a$  is the lattice constant. The reason that we select an even number of sites is that it allows us to set a reasonable amplitude  $V_1$  for the Gaussian potential. For an odd number of sites,  $V_1$  would have to be increased substantially in order for a node to be created at  $x = 0$ , a requirement for the dark soliton to be stationary. Not increasing  $V_1$  for an odd number of sites results in dynamical instability of the soliton since the wave function does not vanish

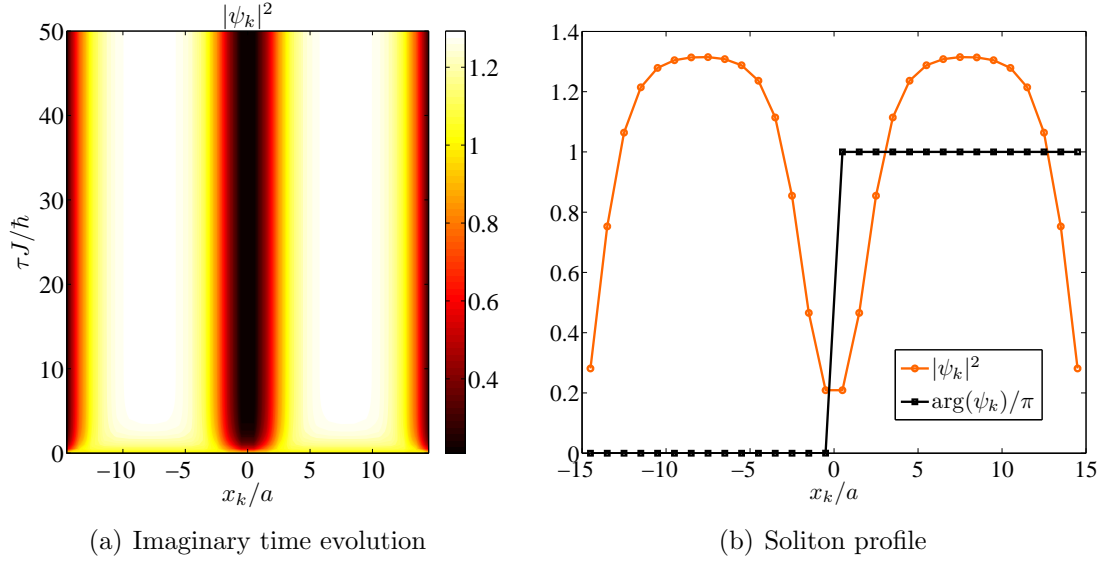


Figure 5.2. *Standing soliton engineering in DNLS.* (a) The DNLS is propagated forward in imaginary time with an external potential in the form of Equation (5.1) resulting in a single density notch in the center of the lattice. An instantaneous phase given by Equation (5.2) is then imprinted on the wave function resulting in the solution shown in (b).

at the origin, an effect we have observed. The solitons created with this method with an even number of sites are similar to the “*B* modes” analyzed in Reference [63].

Figure 5.2 shows imaginary time evolution in the DNLS with the potential (5.1) and the resulting DNLS condensate wave function after application of the phase imprint (5.2). The subsequent real time evolution (according to the DNLS) of the DNLS wave function in Figure 5.2(b) is displayed in Figure 5.3. We now wish to compare these results to a full quantum many-body calculation using TEBD.

To this end, we take the same parameters as used for the DNLS and perform imaginary time propagation in TEBD with the same Gaussian potential used to produce the density structure in Figure 5.2(b). Retaining  $\chi = 80$  basis sets and allowing up to  $d - 1 = 5$  particles per site, we are able to calculate a ground state

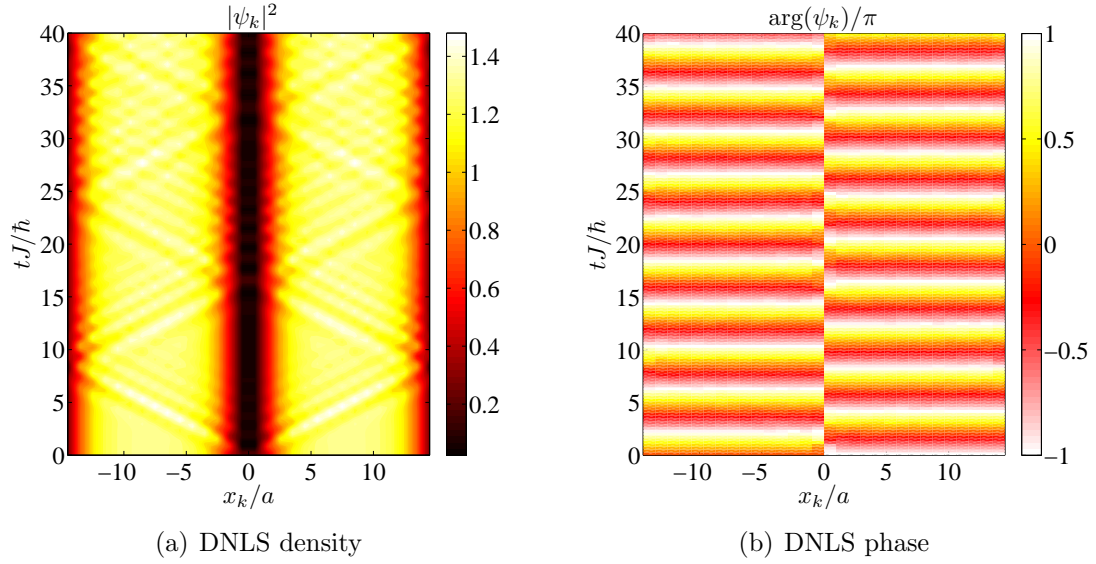


Figure 5.3. *Engineered standing soliton propagation in DNLS.* The density and phase engineered initial condition of Figure 5.2 is propagated forward in real time according to the DNLS. In (a), phonons are generated because we use a Gaussian potential of finite height ( $V_1 \neq \infty$ ) and finite width ( $\sigma_{V_1} \neq 0$ ) when density engineering the notch. As clearly seen in (b), a  $\pi$  phase drop across the notch persists throughout time evolution.

converged to  $10^{-6}$  on  $\max_{\ell} \left( \lambda_{\alpha_{\ell}}^{[\ell]} \right)$ , where  $\ell \in \{1, 2, \dots, M-1\}$  is a link index. The quantum depletion in this ground state is only  $D \approx 11\%$ . We then remove the Gaussian potential and model the application of an instantaneous phase imprint by applying to each site  $k$  the on-site unitary  $\exp(i\hat{n}\theta_k)$ , where  $\theta_k$  is the same narrow tanh phase profile shown in Figure 5.2(b). The resulting quantum dynamics are shown in Figures 5.4 and 5.5.

The evolution of the average particle number density and the three most highly occupied natural orbitals can be seen in Figure 5.4. As in the case of the mean-field soliton initial conditions presented in Section 4.3, we see that, in contrast to the DNLS dynamics of Figure 5.3, time evolution according to the Bose-Hubbard

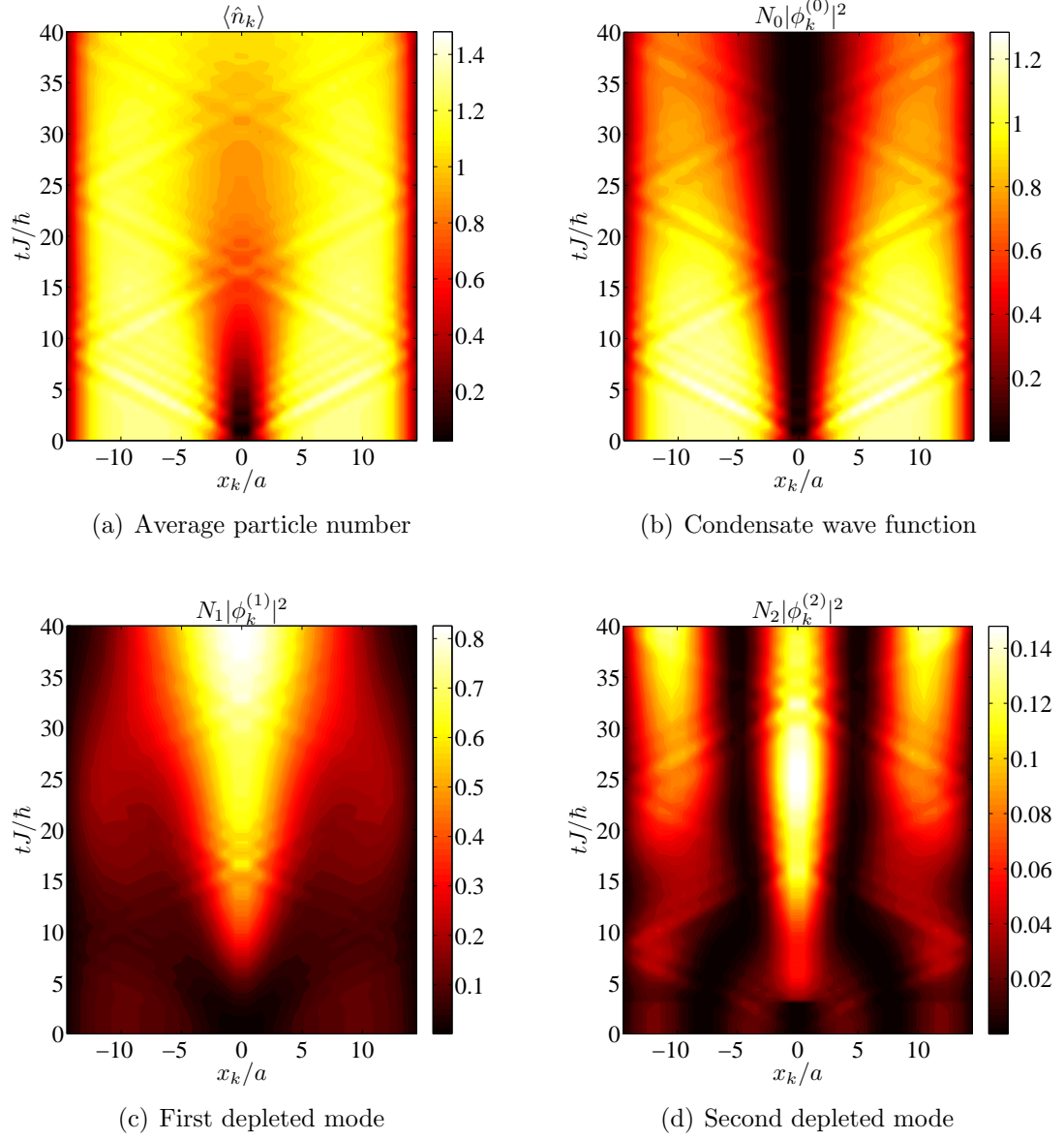


Figure 5.4. *Density and natural orbital dynamics for engineered standing quantum soliton.* The average particle density in (a) is a sum of all occupied natural orbitals. The three most highly occupied natural orbitals are shown in panels (b)–(d), including the condensate wave function in (b) which resembles a stationary dark soliton. The soliton fills in over time due mainly to depletion of atoms into mode  $\chi_1$  as shown in (c).

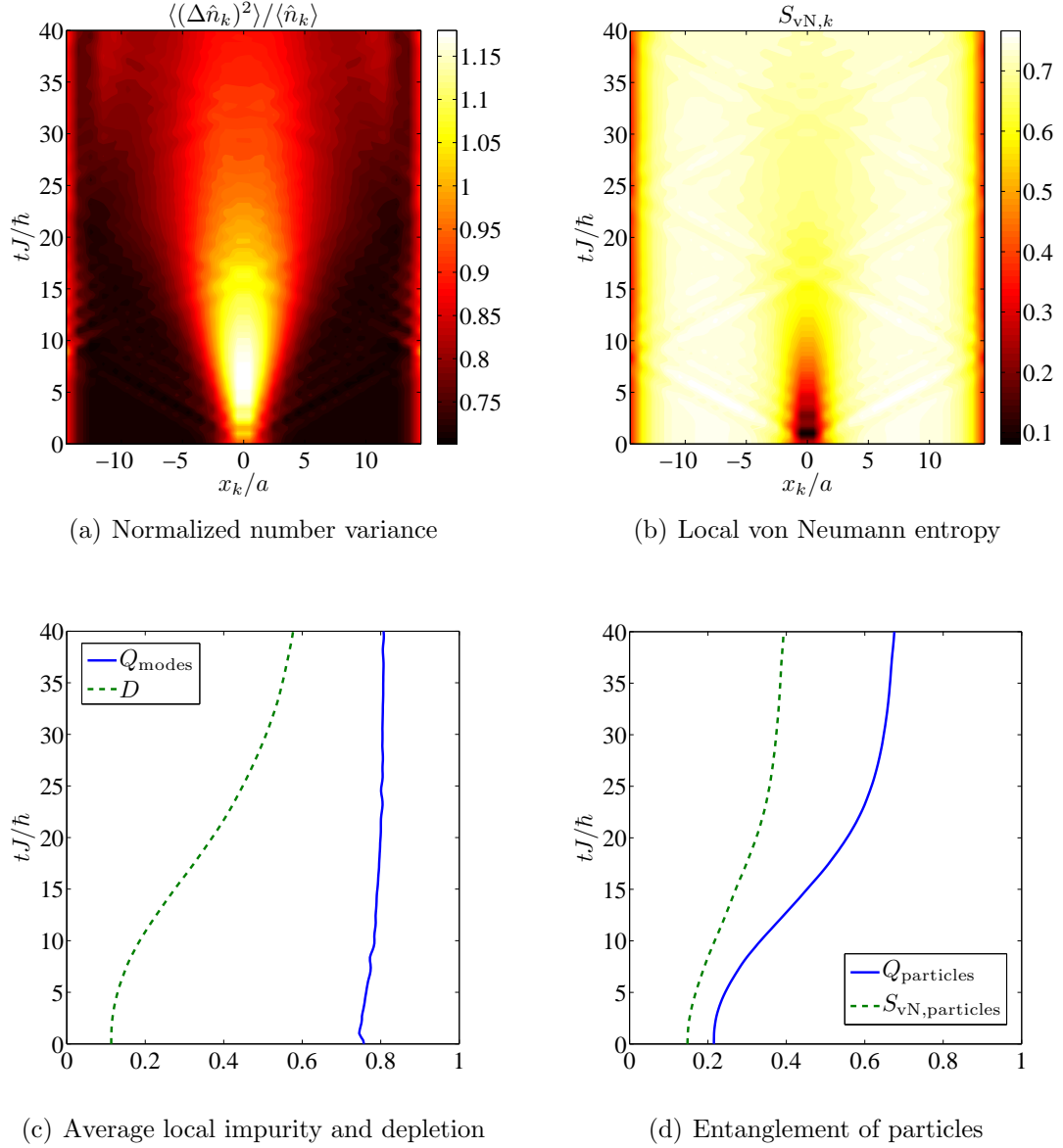


Figure 5.5. *Quantum measures for engineered standing quantum soliton.* (a) As in the quantum evolution of a mean-field soliton, the normalized particle number variance is greatest in the areas of space-time where the soliton is filling in. (b) On the other hand, unlike for a mean-field soliton, the local von Neumann entropy has finite value at the initial time. Soliton density engineering causes a decrease in entropy in the region of the notch. The average local impurity in (c) only changes slightly as the soliton fills. In (c) and (d), we see that both quantum depletion and particle entanglement grow in time.

Hamiltonian causes the soliton to fill in. This phenomena can be attributed to the same two-body scattering processes discussed in Section 4.3.2. The phase angles of the natural orbitals are not displayed, but we quote the symmetries of the lowest four modes as follows:  $\chi_0$  is an antisymmetric mode;  $\chi_1$  and  $\chi_2$  are both symmetric modes; and  $\chi_3$  (not shown) is an antisymmetric mode.

To characterize the quantum nature of the system, we consider normalized number variance, local von Neumann entropy, average local impurity, quantum depletion, single-particle impurity, and single-particle entropy. We show the time dependence of each of these measures in Figure 5.5. The general behavior of the normalized number variance [Figure 5.5(a)] is similar to that for mean-field soliton initial conditions as can be seen in Figure 4.6(a). In Figure 5.5(b), we see that soliton engineering causes the local von Neumann entropy to decrease in the region of the density notch. Time evolution causes this notch in entropy to dissipate. Unlike for mean-field initial conditions, we cannot define an order parameter based on the expectation value of the lowering operator. This is because such a quantity is inherently zero for a number-conserving Fock space. Also, in contrast to the results in Chapter 4, the average local impurity  $Q_{\text{modes}}$  now has finite value at  $t = 0$  and remains approximately constant over time. Panels (c) and (d) of Figure 5.5 depict this time dependence of  $Q_{\text{modes}}$  as well as growth in quantum depletion  $D$ , single-particle impurity  $Q_{\text{particles}}$ , and single-particle entropy  $S_{\text{vN,particles}}$ .

The simulation discussed above can be realized experimentally with the same parameters used to realize the simulation in Section 4.3.2. Those parameters can be found in Section 4.3.4, but we quote them here for completeness. The Bose-Hubbard parameter  $\nu U/J = 0.35$  at filling  $\nu = 1$  corresponds to  $^{87}\text{Rb}$  atoms with an  $s$ -wave scattering length tuned via Feshbach resonance to  $a_s = 1.0$  nm in an optical

lattice with longitudinal and transverse lattice heights  $V_0 = E_R$  and  $V_{0\perp} = 25 E_R$  created with lasers of wavelength  $\lambda = 850$  nm. The Gaussian beam used for density engineering then has height  $V_1 = J \approx 0.17 E_R$  and width  $\sigma_{V1} = a = 425$  nm. The width of the fall-off of tanh phase profile is  $\sigma_{\theta1} = 0.1 a = 42.5$  nm. Increasing the width of the phase profile to the order of the soliton healing length will cause the soliton to drift to the left, as we observed in simulations.

### 5.2.3 Soliton Lifetimes

Unlike in Section 4.3.3, we can no longer characterize growth time in quantum many-body effects by such measures as the order parameter norm and average local impurity. In fact, the initial state already exhibits highly nonclassical behavior, so it is no longer meaningful to discuss such a time scale. However, as demonstrated in the previous section, dark solitons engineered in optical lattices dissipate on an observable time scale due to quantum fluctuations. We characterize the time scale at which this instability occurs by (1) fitting the average particle number at the center lattice site to

$$\langle \hat{n}_{\text{mid}} \rangle \approx n_0 (1 - e^{-t/\tau_{\text{mid}}}), \quad (5.3)$$

as in Equation 4.28, (2) fitting the inner product of the time-evolving state with the initial state to

$$I \equiv |\langle \Psi(t) | \Psi(0) \rangle|^2 \approx e^{-t/\tau_{\text{inner}}}, \quad (5.4)$$

and (3) the occupation in the first depleted mode to

$$\frac{N_1}{N} \approx A + B \tanh \left( \frac{t - \tau_{\text{shift}}}{\tau_{N_1}} \right), \quad (5.5)$$



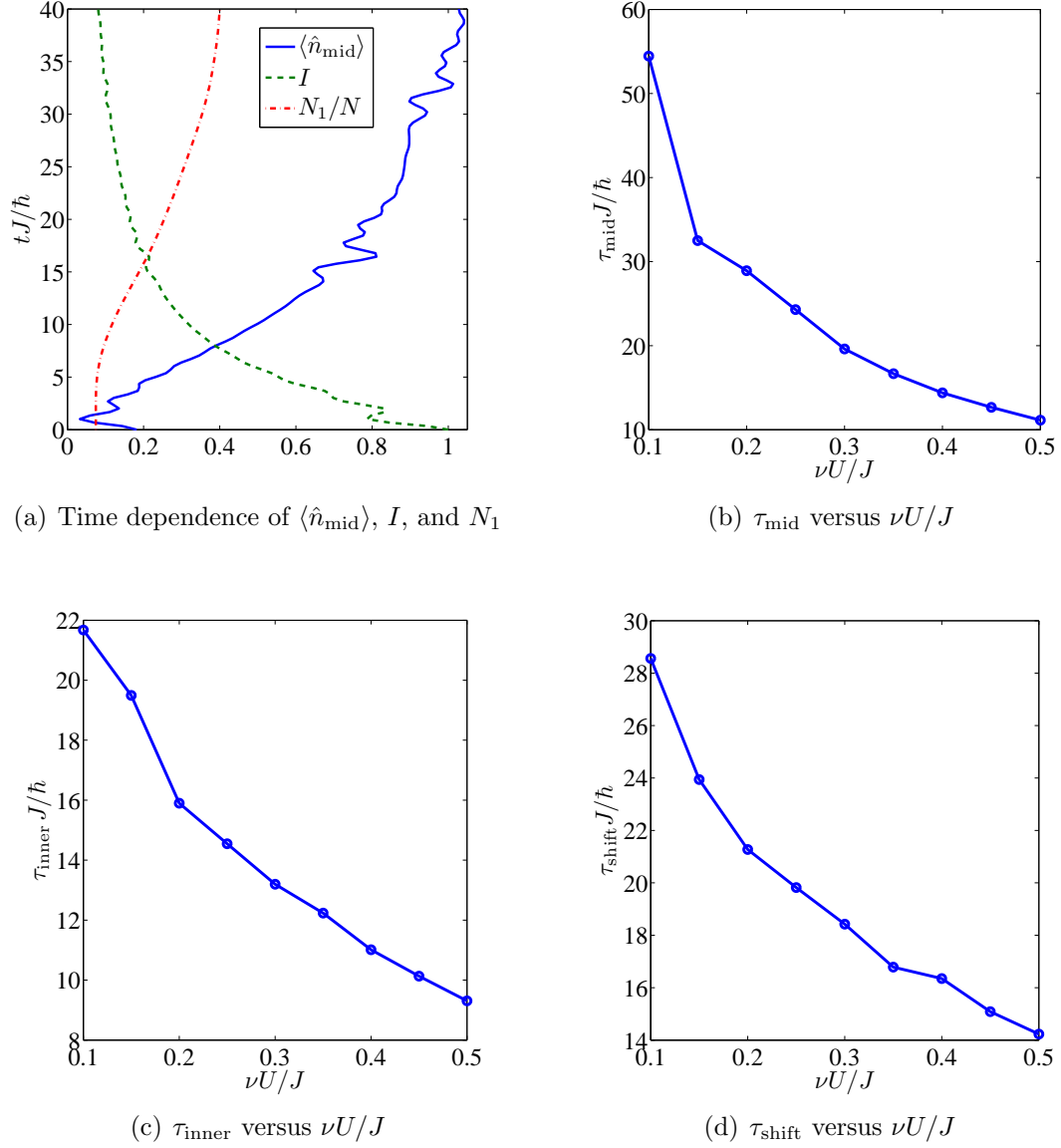


Figure 5.6. *Engineered dark soliton decay times.* (a) For the same simulation analyzed in Section 5.2.1, we plot versus time the average number in the middle lattice site, the inner product with the initial state, and occupation of the first depleted mode. Decay in  $I$ , the inner product of the state at time  $t$  with the state at time  $t = 0$ , signifies nonstationarity of the initial state. In (b)–(d), we plot the time scales  $\tau_{\text{mid}}$ ,  $\tau_{\text{inner}}$ , and  $\tau_{\text{shift}}$  as defined in Equations (5.3)–(5.5) versus the effective interaction strength  $\nu U/J$  at unit filling  $\nu = 1$ . The time scales all decrease as interactions are increased. The curves connecting data points in (b)–(d) serve as guides to the eye.

In Figure 5.6(a), we show the characteristic behavior of  $\langle \hat{n}_{\text{mid}} \rangle$ ,  $I$ , and  $N_1$  for the same simulation parameters used in Section 5.2.1, and in Figure 5.6(b)–(d), we plot the time scales  $\tau_{\text{mid}}$ ,  $\tau_{\text{inner}}$ , and  $\tau_{\text{shift}}$  for different values of the interaction parameter  $\nu U/J$  at fixed filling  $\nu = 1$ . We investigate the effects of filling factor on these time scales in our Reference [155] which is currently in preparation. As expected, increasing the interaction strength causes the soliton lifetime to decrease. This behavior was also observed in Section 4.3.3 for the case of mean-field soliton initial conditions.

### 5.3 Soliton-Soliton Collisions and Quantum-Induced Inelasticity

It is straightforward to apply the above density and phase engineering techniques to prepare an initial state in the Bose-Hubbard Hamiltonian that leads to a soliton-soliton collision. In Section 4.4, we looked at a soliton-soliton collision in the DNLS and analyzed soliton-soliton collisions in the Bose-Hubbard model by preparing the quantum system in an appropriate mean-field state. We showed that certain two-body scattering processes lead to depletion of atoms out of the condensate wave function and into natural orbitals of higher order. The first of which is an odd mode with vanishing density in the center of the lattice. If significant depletion into this mode occurs at a time scale comparable to the time of collision, there is an induced inelasticity in the collision. This point is demonstrated in Figure 4.15.

We now consider analogous simulations except that the initial conditions are prepared by performing density and phase engineering directly in the Bose-Hubbard Hamiltonian. For the external potential and phase profile, we use identical forms to those given in Equations (4.33)–(4.34). The results are generally similar to those in Section 4.4 except, of course, that the initial state itself exhibits quantum many-body behavior, i.e., finite depletion and finite entanglement. For brevity, we focus only

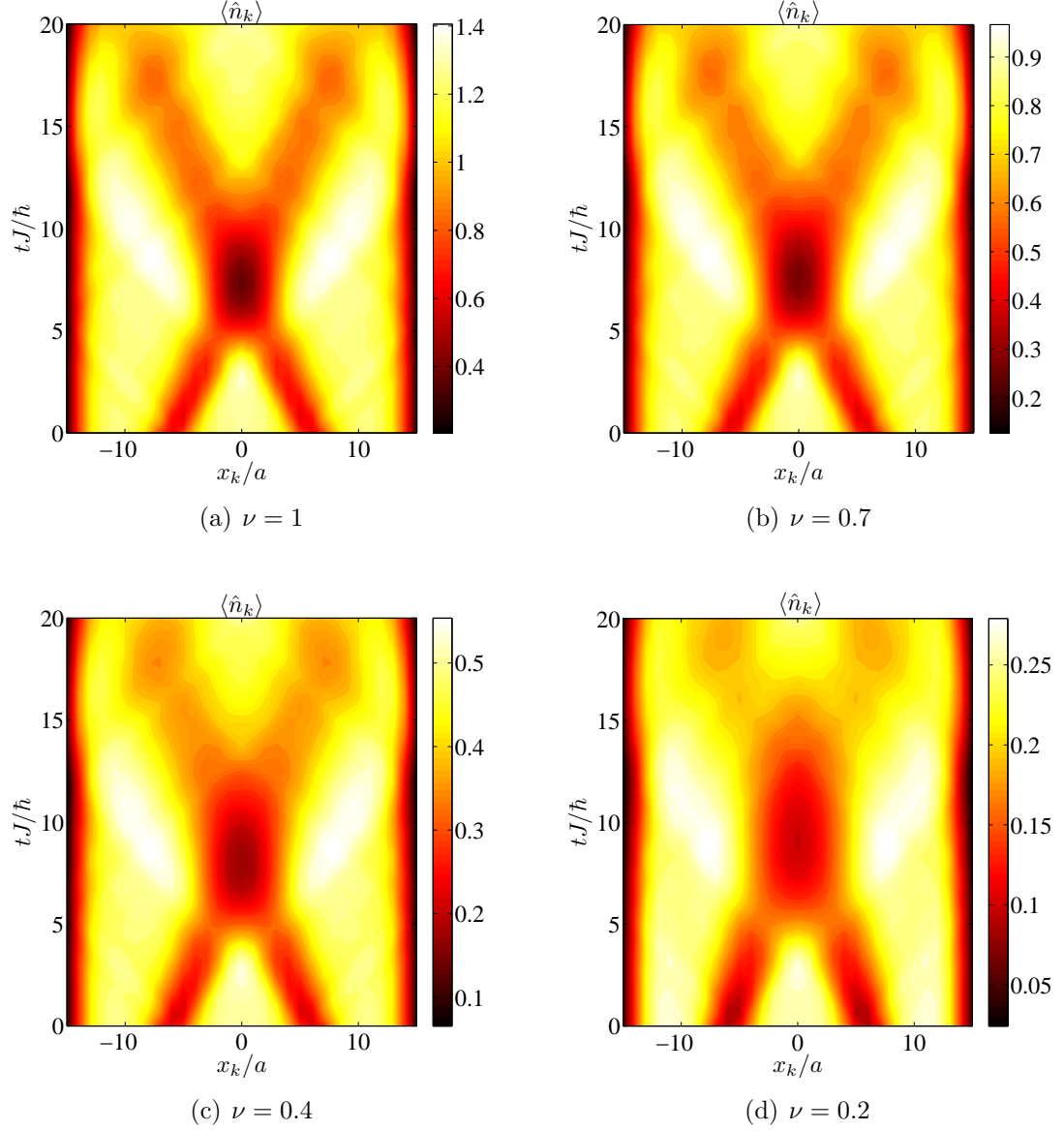


Figure 5.7. *Quantum-induced inelasticity for quantum engineered dark solitons.* A collision between two engineered dark quantum solitons is shown for fixed  $\nu U/J = 0.35$  at filling factors (a) 1, (b) 0.7, (c) 0.4, and (d) 0.2. The average particle number is plotted in each case. The collision elasticity decreases with decreased filling in a similar way to that observed in Figure 4.15.

the evolution of the average number distribution and show that quantum-induced inelasticity is not just an artifact of the mean-field initial conditions used throughout Chapter 4. For consistency, we select parameters values identical to those used in Section 4.4. To be precise, the effective interaction parameter is taken to be  $\nu U/J = 0.35$  on a lattice of  $M = 31$  sites. The two-soliton engineering parameters are  $V_2/J = 0.4$ ,  $\sigma_{V_2}/a = 1$ ,  $b/a = 6$ ,  $\Delta\theta_2 = 0.3\pi$ , and  $\sigma_{\theta_2}/a = 2$ . Relevant TEBD parameters are  $\chi = 80$  and  $d = 6$ . In Figure 5.7, we show a collision of two solitons at four separate filling factors:  $\nu = 1, 0.7, 0.4, 0.2$ . Up to a scale factor, the initial density is approximately the same in each case because we hold the *effective* nonlinearity fixed at  $\nu U/J = 0.35$ . As we lower the filling, the growth rate of quantum fluctuations increases. The mode into which most atoms deplete vanishes at  $x = 0$  and is similar at  $t = 0$  to the lowest-lying mode in the Bogoliubov spectrum for the ground state of the DNLS; it evolves in time into a mode with a sharp density notch at the center of the lattice. This behavior is similar to that shown in panels (b) and (c) of Figure 4.13. Tuning the time scale of this effect to near the time of collision causes the soliton-soliton interaction time to increase, hence decreasing the collision elasticity. This can clearly be seen by comparing the  $\nu = 1$  case to the  $\nu = 0.2$  case in Figure 5.7. Going to higher filling factors in this case would not be insightful because the collision is already much like the mean-field result at  $\nu = 1$ . Comparison to the associated DNLS simulation can be made by examining Figure 4.11.

## 5.4 Summary

In summary, we have demonstrated that the techniques of density and phase engineering for dark soliton creation [54, 55] can be generalized to ultracold bosons on a lattice described by the Bose-Hubbard Hamiltonian. When deep in the superfluid

phase of the ground state phase diagram, stationary dark solitons can be created with lifetimes on the order of tens of tunneling times. The lifetime of such quantum engineered solitons decreases as one tunes toward the Mott border. The basic mechanism responsible for soliton decay involves two-body scattering processes which deplete atoms out of the soliton condensate wave function into orbitals with nonvanishing density in the soliton's notch. Using the same density and phase engineering methods, we created initial conditions resembling two dark solitons moving toward one another at finite speed. For very low filling factors when the growth rate of quantum fluctuations is large, the collision becomes inelastic due to depletion processes which lead to occupation of modes with vanishing density at the position of the collision.

We purposely did not perform a time-independent Bogoliubov calculation in this chapter to analyze engineered standing dark solitons because the initial state is itself a dynamical state. However, one can still make comparisons to the Bogoliubov spectrum calculated in Section 4.3.5. The first depleted natural orbital in Figure 5.4(c) compares favorably at  $t = 0$  to the lowest-energy Bogoliubov excitation for the DNLS ground state, although at later times there is obviously large contributions from other Bogoliubov modes to the first depleted orbital, including the anomalous mode. Such a static Bogoliubov-based analysis once again gives us some insight but leaves out a lot of physics. A time-dependent Bogoliubov calculation could perhaps be done for this problem in a similar fashion to that presented in Reference [70] in the context of phase imprinting soliton generation in harmonic traps. However, with TEBD available to give us a quasi-exact answer, such a calculation should not be necessary.

## Chapter 6

### PRELIMINARY STUDY OF KIBBLE-ZUREK MECHANISM IN OPTICAL LATTICE OF SPIN-1 BOSONS

In this chapter, we perform a mean-field analysis of a symmetry-breaking quantum phase transition involving spin-1 bosons on a 1D optical lattice. These calculations will be used as a starting point for future analogous full quantum many-body simulations using TEBD. As with the quantum soliton problem studied in Chapters 4 and 5, the mean-field picture presents a simpler problem to solve. But, in that case, we showed that a more complete quantum description is necessary to accurately describe the quantum dynamics. We might expect a similar result in this study. The chapter is organized as follows. We first clearly formulate the problem and review its history. Next, discrete mean-field calculations are presented and comparisons are made to continuum mean-field results already in the literature. Finally, we give suggestions for future work and elucidate the advantages in using a full many-body description over its mean-field counterpart.

#### 6.1 Formulation of Problem and Methods Used

As described in Section 2.5.4, the Stamper-Kurn group at Berkeley conducted a seminal experiment [74] in which a ferromagnetic spin-1 condensate was prepared in the  $m_F = 0$  hyperfine level with a strong magnetic field. The magnetic field was then instantaneously quenched below a critical value that separates the  $m_F = 0$  polar phase from a ferromagnetic phase characterized by finite magnetization in directions

transverse to the magnetic field. Because the ferromagnetic phase exhibits rotational symmetry in the transverse plane, spontaneous symmetry breaking occurs when the system is quenched below the critical value. In the Berkeley experiment, the subsequent dynamics of the system involved the formation of spin textures, ferromagnetic domains, and topological spin vortices. Some recent theoretical works have investigated the effects of the quench *rate* on the dynamical phase transition [78, 79] and have revealed that scaling with the quench rate can be predicted by Kibble-Zurek theory [80, 81, 82, 83]. In this chapter, we focus on a 1D version of the phase transition when in the presence of an optical lattice. An analogous continuum study can be found in Reference [78] upon which we model our calculations.

We consider ferromagnetic atoms with total spin  $F = 1$  on a 1D lattice with box boundary conditions. This choice of boundary conditions is made because the future TEBD studies will most likely use box boundary conditions as well. Employing the single-band tight-binding approximation, the spin-1 Bose-Hubbard Hamiltonian as in Equation (2.83) becomes our governing model. Because the interactions are ferromagnetic, the spin-dependent interaction coefficient is negative, i.e.,  $U_2 < 0$ . Also, the addition of a magnetic field of strength  $B$  in the  $z$ -direction, which we choose to be along the longitudinal direction of the 1D lattice, gives rise to a constant external potential  $Q > 0$  on the  $m_F = \pm 1$  atoms, cf. Equation (2.99). This potential is due to the quadratic Zeeman effect; we ignore the linear Zeeman effect because it commutes with the Hamiltonian and thus only rotates the spins at the Larmor frequency [79]. Hence, the spin-dependent interaction term (proportional to  $U_2 < 0$ ) favors a ferromagnetic phase and competes with the quadratic Zeeman term (proportional to  $Q > 0$ ) which favors a polar phase characterized by all atoms in the  $m_F = 0$  hyperfine state.

For the present study, we use the spin-1 vector DNLS given in Equations (2.95)–(2.96) to study the mean-field behavior of the system in the single-band tight-binding limit. Specifically, we numerically simulate the vector DNLS using the fourth-order Runge-Kutta method in both real and imaginary time (see Section 3.1). To study the phase transition dynamically, we first calculate the ground state of a pure  $m_F = 0$  condensate; this will be the ground state of the full system for quadratic Zeeman strengths above a critical value  $Q_c$ . Generalizing the corresponding continuum result [78, 79], we expect a critical value  $Q_c \approx 2\nu|U_2|$ . It is apparent from Equations (2.95)–(2.96), that if at  $t = 0$ ,  $\psi_{\pm 1,k} = 0$ , then  $\psi_{\pm 1,k} = 0$  for  $t > 0$ , i.e., mean-field theory neglects quantum depletion out of a pure  $m_F = 0$  condensate due to two-particle spin-exchange scattering processes involving two colliding atoms in the  $m_F = 0$  state scattering into the  $m_F = \pm 1$  states. In order to mimic these quantum fluctuations in mean-field, we seed the initial  $m_F = \pm 1$  components with Gaussian white noise of width  $\sigma$ . That is, at each lattice site  $k$ , we use MATLAB’s `randn` function to generate random numbers with the probability distribution  $p(x) = \exp(-x^2/2\sigma^2)/(\sqrt{2\pi}\sigma)$  to assign to the real and imaginary parts of  $\psi_{\pm 1,k}$ . This seeding procedure was also used in References [78, 79] to model quantum fluctuations, although in the latter case the seeding was done in momentum space. In order to allow repetition of simulations, for each simulation we set the state of MATLAB’s random number generator to a specified state  $s \in \{1, 2, \dots, 2^{32} - 1\}$ . Also, before real time evolution, the total number of atoms in the system is normalized to

$$N = \sum_{k=1}^M \sum_{\alpha=-1}^1 |\psi_{\alpha,k}|^2. \quad (6.1)$$

Next, we numerically propagate the vector DNLS forward in real time. The quadratic



Zeeman strength is ramped linearly through the critical point:

$$Q(t) = Q_0 \left(1 - \frac{t}{\tau_Q}\right), \quad (6.2)$$

where  $Q_0 > Q_c$  and  $0 \leq t \leq \tau_Q$ . Thus, the rate of the downward quench is given by  $Q_0/\tau_Q$ . We can also calculate the corresponding equilibrium phase transition by using imaginary time propagation of the vector DNLS at each value of  $Q \in [0, Q_0]$ . Comparisons can then be made between the dynamical phase transition and its corresponding equilibrium prediction.

To characterize the system, we observe the local magnetization at site  $k \in \{1, 2, \dots, M\}$ :

$$\mathbf{f}_k = (f_{x,k}, f_{y,k}, f_{z,k})^T \equiv \sum_{\alpha, \beta=-1}^1 \psi_{\alpha,k}^* \mathbf{F}_{\alpha\beta} \psi_{\beta,k}, \quad (6.3)$$

where  $\mathbf{F}_{\alpha\beta}$  are elements of the spin-1 matrices given in Equation (2.86). From the local magnetization, we can calculate the local transverse magnetization given by

$$m_{T,k} \equiv f_{x,k}^2 + f_{y,k}^2 \quad (6.4)$$

and the total transverse magnetization given by

$$M_T \equiv \sum_{k=1}^M m_{T,k}. \quad (6.5)$$

It is also insightful to compute the total occupation numbers of the three spin components:

$$N_\alpha = \sum_{k=1}^M |\psi_{\alpha,k}|^2, \quad \alpha \in \{+1, 0, -1\}. \quad (6.6)$$

In the next two sections, we use these measures to analyze the characteristic behavior

of the system and make direct comparisons to the analogous continuum prediction presented in Reference [78].

## 6.2 Characteristic Simulation

In the following, we focus on a specific set of vector DNLS parameters in order to highlight the general behavior of the system. Namely, we choose  $M = 100$  sites at filling  $\nu \equiv N/M = 1$  with spin-independent interaction strength  $U_0/J = 3$  and spin-dependent interaction strength  $U_2/J = -0.5 < 0$ . Hence, from the continuum result, we should expect a critical value of  $Q_c \approx 2\nu|U_2| = J$ , cf. Equation (2.100). For the case of the dynamical phase transition, to ensure that at  $t = 0$  the system is in the polar phase, we select an initial quadratic Zeeman strength  $Q_0/J = 1.3 \gtrsim 1$  that is subsequently ramped linearly to  $Q = 0$  at a rate  $\tau_Q J/\hbar = 300$ . Before real time evolution, we seed the real and imaginary parts of the polar phase ground state order parameter at each site with Gaussian noise of width  $\sigma = 10^{-4}$  generated after setting the state of MATLAB's random number generator to  $s = 1$ . During evolution, we calculate the observables defined in the previous section.

In Figure 6.1(a), we depict the evolution of the transverse magnetization versus quadratic Zeeman strength both for the dynamical linear ramp of  $Q$  through the critical point and for the equilibrium prediction obtained by imaginary time relaxing the vector DNLS at each value of  $Q$  starting from a uniform state  $\psi_{\alpha,k} = \sqrt{N/3M}$ . The equilibrium prediction agrees well with the continuum result in that the transverse magnetization is nonzero for  $Q < Q_c \approx 2\nu|U_2| = J$ . We note that calculation of the ground state near the critical point converges slowly in imaginary time due to the phenomena of critical slowing down. For the equilibrium data in Figure 6.1, the imaginary time procedure was allowed to run for up to 300 tunneling times in step

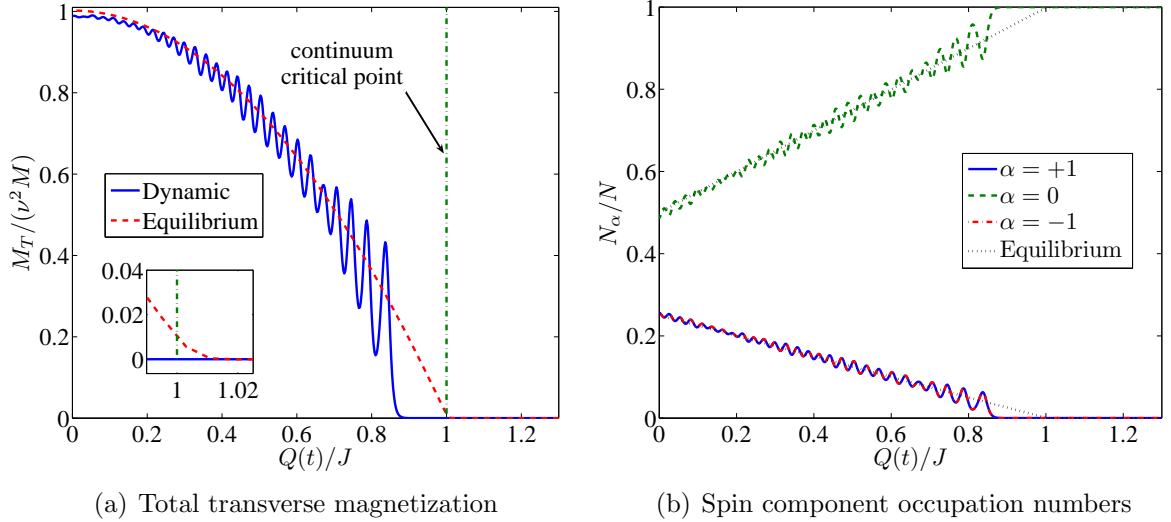


Figure 6.1. *Comparison of dynamic and equilibrium quantum phase transition.* For the parameters mentioned in the text, we compute (a) the total transverse magnetization and (b) occupation numbers of the three spin components as the quadratic Zeeman coefficient is swept through the critical point to zero. In each case, we consider both the dynamical and equilibrium phase transition. The inset in panel (a) is a magnification of the behavior near the critical point. We see that the critical point for our discrete box coincides with the continuum periodic boundary condition value up to about 1%; however, as we will see in Section 6.3, this discrepancy is important and cannot be neglected.

sizes  $\delta t = 0.001 \hbar/J$  to obtain convergence to  $\sim 1\%$  in  $M_T$  near the critical point; on the other hand, the equilibrium states far from the critical point typically converge after only  $\sim 20$  tunneling times. In Section 6.3, we show that small uncertainties in the critical point  $Q_c$  lead to relatively large uncertainties in the critical scaling properties of the system. This suggests that further analytical and numerical investigations are in order regarding whether finite size and/or discreteness cause fine-scale changes in the critical point. As for the former effect, we report that  $Q_c$  does increase past the  $2\nu|U_2|$  prediction as the system size is decreased, e.g., for  $M = 10$  sites with the same filling and interaction parameters as above, we find  $Q_c \approx 1.03 J = 1.03 (2\nu|U_2|)$ .

Due to the finite rate at which the critical point is crossed, the transverse magnetization begins growing at a value of  $Q$  past that predicted by the equilibrium curve. For the selected value of  $\tau_Q$ , the final state of the system is a slightly perturbed broken-symmetry ground state with  $M_T = \nu^2 M$ . As in [78], the oscillation amplitude of  $M_T$  decreases over time after the fast growth in magnetization that occurs at a distance  $\Delta Q_g$  after the critical point is crossed. As seen in Figure 6.1(b), oscillations are also observed in the occupation numbers  $N_\alpha$  of the three spin components when the phase transition occurs dynamically. Also, the equilibrium values for the  $N_\alpha$  are approximately the same as in the continuous case. That is, in the continuum we expect  $\frac{N_0}{N} = \frac{1}{2} \left( \frac{Q}{J} + 1 \right)$  and  $\frac{N_{\pm 1}}{N} = \frac{1}{4} \left( 1 - \frac{Q}{J} \right)$ , which are both in good agreement with the fine dotted black curves in 6.1(b).

Next, we consider the *local* behavior of the magnetization in the  $x$ - $y$  plane, i.e., in directions transverse to the magnetic field. The degeneracy of the ground state in the broken-symmetry phase means arbitrary but particular orientation of the transverse magnetization across the whole system. However, undergoing the phase transition dynamically will necessarily break this symmetry. We see in Figure 6.2 that spatial correlations appear in the transverse spin once the transverse magnetization begins growing at a time  $\Delta t_g$  after passing the critical point. As the system evolves further in time, the correlation length of the magnetization increases. For the case of  $M = 100$  sites considered here, the correlation length at the final time, which corresponds to  $Q = 0$ , is greater than the extent of the lattice. Thus, the lattice size would need to be increased to see entire spin textures.

At time  $t = 0$  when we are in the slightly perturbed (due to our Gaussian random seeding) polar phase, the longitudinal magnetization is approximately zero:  $f_{z,k} \approx 0$ . Because the the total longitudinal magnetization  $\sum_{k=1}^M f_{z,k}$  is conserved during time

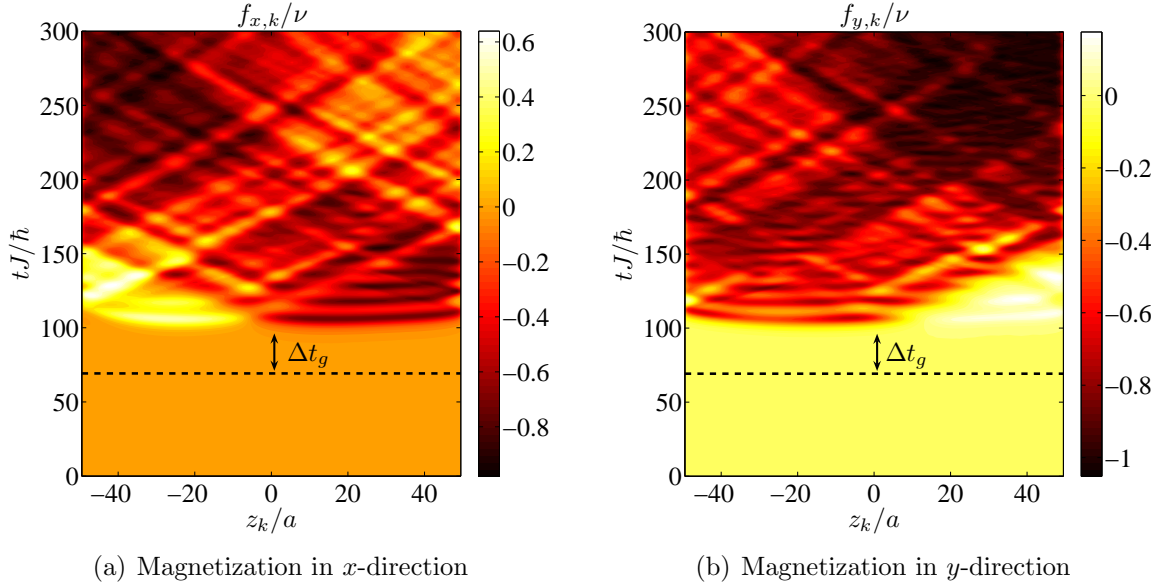


Figure 6.2. *Time evolution of transverse spin components.* For the dynamical phase transition, the local magnetization in the (a)  $x$  and (b)  $y$  directions is plotted versus space and time. The U(1) symmetry in spin space (and resulting rotational symmetry in the transverse plane) when in equilibrium in the broken-symmetry phase renders a corresponding equilibrium calculation irrelevant. Note that here we have defined the longitudinal direction to lie along the  $z$ -direction, hence  $z_k$  denotes the spatial position of site  $k$ . We see that there are spatial correlations in the transverse spins once nontrivial evolution begins, and the spin correlation length increases over time. The horizontal dashed lines indicate when the critical point has been crossed after which there is time a delay  $\Delta t_g$  before growth in transverse magnetization begins.

evolution, magnetic domains with fixed  $f_{z,k}$  sign form when the system enters the broken-symmetry phase. In Figure 6.3, we depict the local transverse magnetization [see Equation (6.4)] and the local longitudinal magnetization at the instant when  $Q(t)/J = 0.2 < 1$ . The center of the domains should occur where the local maximum of  $|f_{z,k}|$  line up with the local minima of the transverse magnetization  $m_{T,k}$ . The vertical dashed lines in Figure 6.3 lie approximately at the maxima of  $|f_{z,k}|$ , and it can be seen that in most cases there is a coincidence with a minima in  $m_{T,k}$ . Although

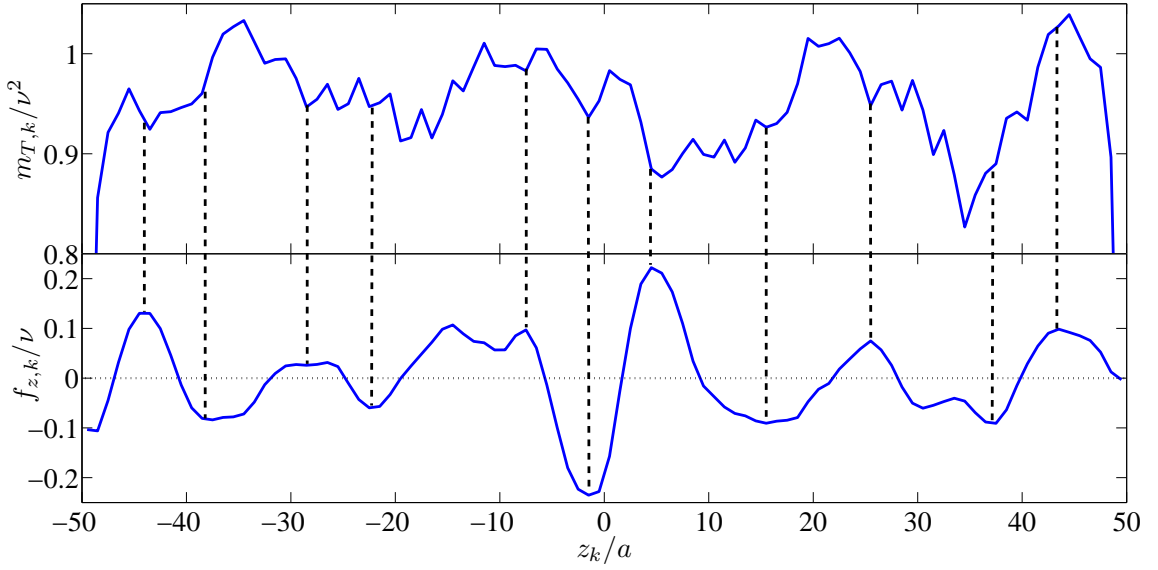


Figure 6.3. *Snapshot of formed magnetic domains.* For the instant  $Q(t)/J = 0.2$ , we plot the total local transverse magnetization on the top panel and the local longitudinal magnetization on the bottom panel. We see that magnetic domains, i.e., regions of constant  $f_{z,k}$  sign, have formed. The dashed vertical lines highlight coincidences between maxima in  $|f_{z,k}|$  and minima in  $m_{T,k}$ ; such coincidence are signatures of the magnetic domains. In both panels, we have, for visual purposes, connected discrete data points at each lattice site with straight lines.

we do not explore it here, the size of the formed magnetic domains after the system has dynamically entered the broken-symmetry phase should depend on the quench rate  $\tau_Q$  via a simple power law which is explainable by the Kibble-Zurek mechanism [78]. In the next section, we explore another scaling law predicted by Kibble-Zurek theory that relates the rate of the quench to the time at which nontrivial evolution begins.

### 6.3 Calculation of Time Scaling Exponent

It is clear from Figure 6.1 that there is a finite time after which the system has crossed the equilibrium critical point that unstable evolution begins. We denote this time  $\Delta t_g$ . If we let  $Q_g$  be the quadratic Zeeman strength at which  $M_T/(\nu^2 M) = 0.01$ , then by Equation (6.2) we can define

$$\Delta t_g \equiv \left( \frac{Q_c - Q_g}{Q_0} \right) \tau_Q, \quad (6.7)$$

where  $Q_c$  is the equilibrium critical value separating the polar phase from the broken-symmetry phase. Kibble-Zurek theory predicts a power law dependence of  $\Delta t_g$  with quench rate  $\tau_Q$  [78]:

$$\Delta t_g \propto \tau_Q^{1/3}. \quad (6.8)$$

We test this prediction in our system by running a number of simulations with identically seeded initial states but with different  $\tau_Q$ , calculating  $\Delta t_g$  for each run. We then perform a fit of the form

$$\frac{\Delta t_g J}{\hbar} = C \left( \frac{\tau_Q J}{\hbar} \right)^p \quad (6.9)$$

to the obtained data.

Using the continuum critical point  $Q_c = 2\nu|U_2| = J$  to compute  $\Delta t_g$ , our fit returns  $C = 6.12 \pm 0.21$ ,  $p = 0.273 \pm 0.005$ , giving an exponent  $p$  that differs by approximately 18% from the prediction in Equation (6.8). Figure 6.1 suggests a critical point slightly greater than  $2\nu|U_2|$ . The inset in Figure 6.1(a) suggests that we might take  $Q_c/J = 1.007$ , i.e.,  $Q_c = 1.007(2\nu|U_2|)$ , which yields  $C = 4.49 \pm 0.18$ ,  $p = 0.338 \pm 0.006$ , a result in much better agreement with (6.8). Figure 6.4(a) shows

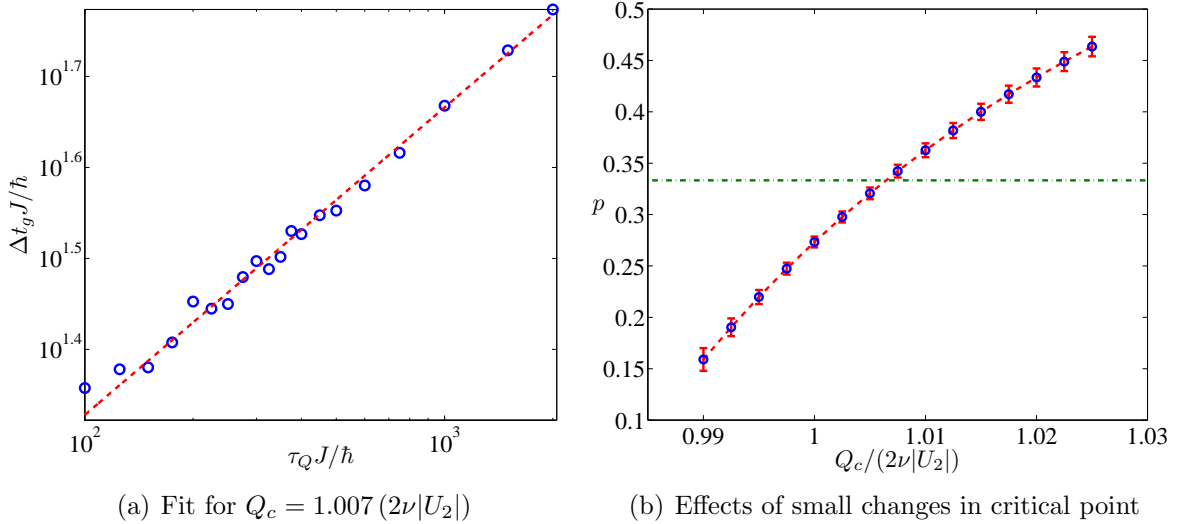


Figure 6.4. *Calculation of power law scaling exponent in time.* Defining the critical point to be  $Q_c = 1.007 J = 1.007 (2\nu|U_2|)$ , we show in (a) data of  $\Delta t_g$  versus quench rate  $\tau_Q$  for the filling and interaction parameters used in Section 6.2. The red dashed line is the obtained best-fit curve defined in the text. (b) The dependence on the scaling exponent  $p$  is very sensitive to fine-scale ( $\sim 1\%$ ) changes in the critical point. The horizontal green dashed-dotted line indicates the  $1/3$  prediction, and the red dashed curve serves as a guide to the eye. The error bars represent asymptotic standard deviations returned by `NonlinearRegress` command in *Mathematica*. Finite-size and/or discreteness effects which slightly alter the critical point, cf. the inset in Figure 6.1(a), should thus not be neglected when investigating scaling properties of the system with quench rate.

the data associated when taking  $Q_c = 1.007 (2\nu|U_2|)$  and the corresponding fit. In Figure 6.4(b), we show how the calculation of  $p$  depends on the selection of  $Q_c$ . We stress how sensitive  $p$  is on where we define the critical point. Similarly, the calculation should also depend strongly on how we define  $Q_g$ , the quadratic Zeeman strength at which growth in transverse magnetization begins during dynamical evolution. Here, as in [78], we have defined it as the point at which the normalized total transverse magnetization reaches 1%; however, this is just an arbitrary definition. In conclusion, we have observed in the spin-1 vector DNLS the  $1/3$  exponent predicted in [78]. But,



determination of this exponent is very sensitive to where the critical point lies and where one defines the instant at which unstable evolution begins. The former is not a consideration in analogous continuum periodic boundary condition studies because the critical point is obtainable analytically [79].

#### 6.4 Summary and Suggestions for Future Work

In this chapter, we have presented a discrete mean-field analysis of a quantum phase transition involving spin-1 bosons on a 1D optical lattice. This phase transition occurs due to a competition between ferromagnetic spin-dependent interactions and a quadratic Zeeman effect arising from the application of a spatially uniform magnetic field along the longitudinal direction of the lattice: the spin-dependent interactions favor a broken-symmetry phase, whereas the quadratic Zeeman effect favors a polar phase with all atoms in the  $m_F = 0$  hyperfine level. We considered a specific set of parameters and showed that the general qualitative behavior of the system is consistent with the results of a recent similar study performed by Damski and Zurek [78] which assumed a continuous 1D box with periodic boundary conditions.

In summary, if the quadratic Zeeman strength is decreased linearly through the critical point, then nontrivial evolution begins at a point in time after the equilibrium critical point has been passed. Oscillations appear in the total transverse magnetization, as well as in the occupation of the three allowed spin components, and the amplitudes of these oscillations decrease with time as the system tends to a slightly perturbed broken-symmetry phase at the final time when the magnetic field goes to zero. At the beginning of nontrivial evolution, spatial correlations appear in the transverse magnetization and the associated spin correlation length increases during time evolution. Also, longitudinal magnetic domains form after the system begins

unstable evolution. Finally, we showed that the scaling properties of the delay time at which unstable evolution begins are strongly dependent on the placement of the equilibrium critical point. Calculating the equilibrium behavior of the system near the critical point to high accuracy is relatively challenging numerically with imaginary time propagation; however, even at  $M = 100$  sites, we obtain converged results for the location of the critical point which indicate that it differs from the continuum periodic boundary condition result by less than 1%. This difference is greater for smaller systems, indicating that the discrepancy is likely due to the finite size of our 1D box. Using the calculated critical point for  $M = 100$ , we are able to obtain good agreement with the  $1/3$  power law behavior relating quench rate to delay time.

For future work, we suggest the following. The pure mean-field theory used above completely neglects the quantum fluctuations that are ultimately responsible for the observed dynamical phase transition. That is, a pure  $m_F = 0$  condensate will remain in the  $m_F = 0$  level for all time according to the spin-1 vector DNLS. This is hardly an accurate description of the physics though, because there exists a spin-conserving two-body collision process which depletes atoms out of the  $m_F = 0$  state into the  $m_F = \pm 1$  states. To emulate these quantum fluctuations in the mean field, we randomly seed the initial  $m_F = \pm 1$  components at each position as was done in previous continuum studies [84, 78, 79]. Subsequently, further growth in occupation of the  $m_F = \pm 1$  states is allowed. We propose the following questions concerning the validity of using such a mean-field theory for this problem. How important is the assumption that quantum fluctuations can be simulated in mean field simply via a random seeding procedure? Also, what happens when we relax the assumption that all atoms in a given spin component occupy the same spatial wave function? Both of these questions can be answered by performing a full quantum-many body

calculation of the dynamical phase transition. To this end, TEBD should serve as an ideal tool as it allows for quasi-exact simulation of quantum many-body dynamics on a lattice. In Appendix D, we include the module `spin1_module.f90` which builds the spin-1 Bose-Hubbard Hamiltonian in the appropriate TEBD form. This Hamiltonian could immediately be folded into the current non-number-conserving Fortran code but would be too inefficient to be effective without number and spin conservation. The reason for this inefficiency lies in the poor scaling of the algorithm with local Hilbert space dimension as discussed in Chapter 3.

Two other main advantages of using TEBD to simulate a spin-1 Kibble-Zurek mechanism on a lattice include (1) the ability to calculate entanglement dynamics during the phase transition and (2) the freedom to raise the lattice height and enter the strongly correlated regime. In the latter case, the mean-field vector DNLS description will inevitably break down. We also need to check whether the critical quadratic Zeeman strength changes in the quantum theory. Regardless, the above vector DNLS calculations should serve as a guide for the eventual full many-body TEBD calculations. At least initially, the procedure for simulating the phase transition in TEBD could mimic that which we have employed for the mean field. Specifically, we can calculate equilibrium properties of the system via imaginary time propagation for all relevant values of external magnetic field, and then simulate the phase transition dynamically by ramping down the quadratic Zeeman energy in real time. The latter can be accomplished by redefining and diagonalizing the Hamiltonian at each time step. This diagonalization process will further slow down the algorithm, making number and spin conservation in the spin-1 code even more necessary. This proposed numerical calculation will surely prove to be a challenge, but it will undoubtedly be accompanied by a wealth of interesting physics.

## Chapter 7

### CONCLUSIONS AND OUTLOOK

We have presented a quantum many-body treatment of the dynamics of dark solitons formed by ultracold bosonic atoms on one-dimensional optical lattices. Past studies of solitons in optical lattices have employed mean-field theories using both the continuum NLS [57, 58] and its discrete counterpart, the DNLS [59, 64]. These approaches are justified given that quantum fluctuations can be safely neglected. However, this assumption is only valid when we have (1) a hopping parameter much greater than the interaction parameter and (2) a system in the thermodynamic limit. The systems that we investigate are closer to those actually studied experimentally where one has an array of 1D lattices in which each lattice site contains a few atoms. In this thesis, we considered average filling factors up to one atom per site but will present results with higher filling factors in a future work [155]. We have clearly demonstrated that even far into the superfluid region of the Bose-Hubbard phase diagram, quantum fluctuations greatly affect dark soliton dynamics. For the case of harmonic trap geometries, previous studies have shown that quantum fluctuations cause standing dark solitons to fill in [65, 66, 67, 68, 70]. Here, we have obtained similar results for dark solitons in an optical lattice. We have also shown that, unlike with true dark solitons that exist as solutions of nonlinear partial differential equations, soliton-soliton collisions on a Bose-Hubbard lattice can be made inelastic by tuning the time scale of quantum fluctuations to occur near the time of collision. Thus, perhaps these structures should technically be termed *solitary waves*, although we continue to refer

to them as solitons.

We have considered two types of initial conditions for subsequent propagation of dark solitons according to the Bose-Hubbard Hamiltonian. In Chapter 4, we created quantum analogs to the dark solitons of the DNLS by selecting as initial quantum many-body states truncated Glauber coherent states with appropriate coherent state amplitudes. Although these states may not be easily obtained experimentally, they are pleasing from a theoretical standpoint as they exhibit negligible quantum depletion. That is, at time  $t = 0$  all bosons are made to occupy the same single-particle wave function. For our purposes, this wave function is either (1) a standing dark soliton positioned at the lattice center or (2) two dark solitons with equal and opposite phase drops with density notches displaced from the origin by a prescribed amount. Such states exhibit nearly perfect semiclassical behavior, e.g., zero quantum fluctuations, zero spatial entanglement, zero particle entanglement, and Poissonian number statistics. Hence, their behavior under the corresponding quantum equations of motion is an interesting theoretical question. In Chapter 4, it was shown that quantum evolution of mean-field soliton initial conditions differs greatly from the corresponding semiclassical evolution. Namely, certain allowed two-body scattering processes cause standing dark solitons to fill in within a time on the order of tens of tunneling times. A similar mechanism causes soliton-soliton collisions to appear inelastic. In our analysis, we have characterized the quantum dynamics with a complete set of measures including generalized quantum entropies and number fluctuations. As expected, quantum evolution causes a growth in quantum effects and the state evolves into one not describable by semiclassical theories. We have found that the growth time of quantum effects correlates with the soliton fill-in time.

Chapter 5 was devoted to the quantum engineering of solitons using density and

phase engineering techniques applied directly to the Bose-Hubbard Hamiltonian. This approach has the advantage that it emulates exactly how one would experimentally create dark solitons in optical lattices experimentally. With these initial conditions and for the parameter regimes considered, dark solitons once again decay on a time scale that is on the order of tens of tunneling times. Also, if the time scale of quantum effects is tuned appropriately, collisions may become inelastic. The qualitative behavior is similar to that displayed by the quantum evolution of purely mean-field solitons in Chapter 4. The main difference is that for quantum engineered dark solitons, the initial conditions themselves are already entangled.

As with any problem, there is more that can be learned. Comparison of our TEBD results to a time-dependent Bogoliubov calculation may prove insightful, as it would allow evaluation of the validity of the Bogoliubov method to describe dark soliton dissipation on a lattice. Also, the TEBD method, although very powerful, does not use an efficient basis for the kinds of states considered herein. We are forced to work in a basis of localized Wannier states in order for the TEBD algorithm to be applicable. One can generalize the Bose-Hubbard Hamiltonian to a Hamiltonian that contains destruction and creation operators in something other than a Wannier basis, e.g., delocalized Bloch wave functions. In such a basis, however, there is no way to order the modes so that only “nearest-neighbor” coupling occurs, hence TEBD is once again rendered inefficient. It is clear that for our problem the natural orbitals of the system are hardly localized on-site and are themselves time-dependent. It would thus be ideal to work with a basis that is time-adaptive to the current state. Methods which strive towards this goal are in a relatively early stage of development and collectively go by the name *time-dependent multiconfigurational Hartree-Fock theory* [112, 113, 114]. These methods were mentioned briefly at the end of Section 2.3.3.

Application of such theories to complicated systems such as lattice geometries could prove to be not only a better method for solving our soliton problem but could become another powerful tool for quasi-exact study of many-body phenomena, perhaps as a complement to TEBD. It may also be worthwhile to develop our own code to include finite temperature, both in mean field using the ZNG method [159] briefly discussed in Section 4.3.4 and in quantum field using the finite-temperature extension of TEBD [161]. Then, direct comparisons can be made between the effects of quantum and thermal fluctuations on dark solitons.

There are many variations on initial dark soliton-like initial conditions whose subsequent quantum many-body evolution can be explored with TEBD simulations. One example would be to create a pair of solitons with equal and opposite finite velocities via density engineering only but with no phase imprint. Another example would be to investigate the depletion of a single drifting dark soliton in the lattice not undergoing a collision. It may also be insightful to study the symmetries and dynamics of the natural orbitals when the system is initialized in a dark soliton state not placed in the center of the box. In this case, we should still expect the soliton to fill in, but the underlying natural orbitals would likely lose their even or odd symmetry. On a related note, it would be interesting to explore quantum-induced inelasticity for a pair of solitons colliding with different speeds. Another obvious extension of this work could involve the investigation of quantum fluctuations on bright solitons formed by attractive bosons in an optical lattice. In this case, the soliton is the system's ground state, so we might expect mean-field theory to work better than for the dark soliton. However, it would be interesting to see how quantum fluctuations affect the *dynamics* of bright solitons and collisions between two bright solitons. It should be straightforward to perform such studies within the framework of our current

TEBD code.

After the completion of the main chapters in this thesis, we calculated the *pair correlation function* during quantum evolution of a dark soliton. On the lattice, we define this quantity between sites  $i$  and  $j$  as  $g_{ij}^{(2)} \equiv \langle \hat{b}_i^\dagger \hat{b}_j^\dagger \hat{b}_j \hat{b}_i \rangle$ . This correlation function is related to the probability that when a particle is measured at site  $i$  another particle will be measured at site  $j$ , or vice versa. For visualization, we plot  $g_{\text{mid},k}^{(2)}$  over time, i.e., the pair correlation function from the initial location of the soliton out to site  $k$ . Initially, there is a notch in  $g_{\text{mid},k}^{(2)}$ , but this notch does not persist in time. This is one piece of evidence that the dark soliton is not simply diffusing in space, i.e., wandering to the left or right without dissipating. That is, the filling-in phenomena observed in the average local density is not just the result of averaging over many measurements of a wandering dark soliton. Note that this is consistent with the observation of population of higher-order natural orbitals that fill in the density notch. Another strong piece of evidence that the solitons are not spreading out is related to our quantum-induced inelasticity result: if solitons were spreading out, they would not appear to stick together on average over many density measurements. Hence, our study can confidently be classified as a full quantum entangled dynamical study of dark solitons.

In Chapter 6, we considered a dynamical quantum phase transition in a system of ferromagnetic spin-1 bosons trapped in a 1D lattice potential. This phase transition is driven by changing an external magnetic field that influences the energetics of the system through the quadratic Zeeman effect. Above a critical value of the quadratic Zeeman energy, continuous mean-field theory predicts a polar phase with zero net magnetization, while below the critical value, we expect a broken-symmetry ground state with rotational symmetry in the plane transverse to the magnetic field.



The dynamics of this phase transition are consistent with the Kibble-Zurek mechanism [77, 78, 79]. Using the recent continuum work of Damski and Zurek [78] as a guide, we showed that a discrete mean-field tight-binding theory on a lattice can describe this phase transition. To this end, we performed simulations of a spin-1 vector DNLS. We simulated the phase transition dynamically and made comparisons to the equilibrium prediction. The obtained results are consistent with those in Reference [78]. Using the transverse magnetization as an order parameter describing the equilibrium transition, our calculations indicate that for a finite and discrete system the critical point changes slightly from the corresponding prediction obtained in the continuum limit assuming periodic boundary conditions. However, we pointed out that this small discrepancy is important when calculating certain scaling properties of the system with quench rate. In the future, we plan to perform an analogous calculation in TEBD to fully characterize the role of quantum many-body effects on this dynamical phase transition. As highlighted in Section 6.4, there are many distinct advantages in using TEBD over a simple vector DNLS mean-field theory. On another note, a potential research question involving both solitons and spin-1 would be to investigate spin-exchange fluctuations on a dark soliton. That is, we could consider what happens when a dark soliton is formed by an  $m_F = 0$  condensate. Here, not only would the quantum fluctuations observed in Chapters 4 and 5 play a role, but there is also the depletion of the  $m_F = 0$  mode when two  $m_F = 0$  atoms collide resulting in two  $m_F = \pm 1$  atoms. Neglecting the former depletion processes, we might expect the soliton notch to be stable but with the soliton tails depleting to  $m_F = \pm 1$  states; this is due to finite density being necessary for spin-exchange processes. However, a full TEBD calculation would allow all depletion processes and potentially result in interesting spin dynamics during dissipation of the soliton.

## REFERENCES

- [1] S. N. Bose. Plancks gesetz und lichtquantenhypothese. *Zeitschrift für Physik*, 26:178–181, 1924.
- [2] A. Einstein. Quantentheorie des einatomigen idealen gases: Zweite abhandlung. *Sitzungsberichte der Preussischen Akademie der Wissenschaften*, page 3, 1924.
- [3] M. H. Anderson, J. R. Ensher, M. R. Matthews, C. E. Wieman, and E. A. Cornell. Observation of Bose-Einstein condensation in a dilute atomic vapor. *Science*, 269:198–201, 1995.
- [4] K. B. Davis, M.-O. Mewes, M. R. Andrews, N. J. van Druten, D. S. Durfee, D. M. Kurn, and W. Ketterle. Bose-Einstein condensation in a gas of sodium atoms. *Physical Review Letters*, 75:3969–3973, 1995.
- [5] C. C. Bradley, C. A. Sackett, J. J. Tollett, and R. G. Hulet. Evidence of Bose-Einstein condensation in an atomic gas with attractive interactions. *Physical Review Letters*, 75:1687–1690, 1995.
- [6] John Weiner, Vanderlei S. Bagnato, Sergio Zilio, and Paul S. Julienne. Experiments and theory in cold and ultracold collisions. *Reviews of Modern Physics*, 71:1–85, 1999.
- [7] M.-O. Mewes, M. R. Andrews, N. J. van Druten, D. S. Durfee, D. M. Kurn, and W. Ketterle. Observation of interference between two Bose condensates. *Science*, 275:637–641, 1997.
- [8] Immanuel Bloch, Theodor W. Hänsch, and Tilman Esslinger. Atom laser with a cw output coupler. *Physical Review Letters*, 82:3008–3011, 1999.
- [9] B. V. Hall, S. Whitlock, R. Anderson, P. Hannaford, and A. I. Sidorov. Condensate splitting in an asymmetric double well for atom chip based sensors. *Physical Review Letters*, 98:030402, 2007.
- [10] Gavin K. Brennen, Carlton M. Caves, Poul S. Jessen, and Ivan H. Deutsch. Quantum logic gates in optical lattices. *Physical Review Letters*, 82:1060–1063, 1999.
- [11] Oliver Penrose and Lars Onsager. Bose-Einstein condensation and liquid helium. *Physical Review*, 104:576–584, 1956.

- [12] Franco Dalfovo, Stefano Giorgini, Lev P. Pitaevskii, and Sandro Stringari. Theory of Bose-Einstein condensation in trapped gases. *Reviews of Modern Physics*, 71:463–512, 1999.
- [13] Yuri S. Kivshar and Govind P. Agrawal. *Optical Solitons: From Fibers to Photonic Crystals*. Academic Press, San Diego, 2003.
- [14] C. Sulem and P. L. Sulem. *Nonlinear Schrödinger Equations: Self-Focusing Instability and Wave Collapse*. Springer-Verlag, New York, 1999.
- [15] S. Burger, K. Bongs, S. Dettmer, W. Ertmer, K. Sengstock, A. Sanpera, G. V. Shlyapnikov, and M. Lewenstein. Dark solitons in Bose-Einstein condensates. *Physical Review Letters*, 83:5198–5201, 1999.
- [16] B. P. Anderson, P. C. Haljan, C. A. Regal, D. L. Feder, L. A. Collins, C. W. Clark, and E. A. Cornell. Watching dark solitons decay into vortex rings in a Bose-Einstein condensate. *Physical Review Letters*, 86:2926–2929, 2001.
- [17] D. L. Feder, M. S. Pindzola, L. A. Collins, B. L. Schneider, and C. W. Clark. Dark soliton states of Bose-Einstein condensates in anisotropic traps. *Physical Review A*, 62:053606, 2000.
- [18] N. N. Bogoliubov. Theory of superfluidity. *Journal of Physics (USSR)*, 11:23–32, 1947.
- [19] V. N. Popov. *Functional Integrals and Collective Excitations*. Cambridge University Press, 1987.
- [20] C. J. Pethick and H. Smith. *Bose-Einstein Condensation in Dilute Gases*. Cambridge University Press, 2002.
- [21] B. P. Anderson and M. A. Kasevich. Macroscopic quantum interference from quantum tunnel arrays. *Science*, 282:1686–1689, 1998.
- [22] Herman Feshbach. A unified theory of nuclear reactions II. *Annals of Physics*, 19:287–313, 1962.
- [23] D. Jaksch, C. Bruder, J. I. Cirac, C. W. Gardiner, and P. Zoller. Cold Bosonic atoms in optical lattices. *Physical Review Letters*, 81:3108–3111, 1998.
- [24] Matthew P. A. Fisher, Peter B. Weichman, G. Grinstein, and Daniel S. Fisher. Boson localization and the superfluid-insulator transition. *Physical Review B*, 40:546–570, 1989.

- [25] J. Hubbard. Electron correlations in narrow energy bands. *Proceedings of the Royal Society of London. Series A, Mathematical and Physical Sciences*, 276:238–257, 1963.
- [26] Elliott H. Lieb and F. Y. Wu. Absence of Mott transition in an exact solution of the short-range, one-band model in one dimension. *Physical Review Letters*, 20:1445–1448, 1968.
- [27] L. D. Carr and M. J. Holland. Quantum phase transitions in the Fermi–Bose Hubbard model. *Physical Review A*, 72:031604, 2005.
- [28] Fei Zhou. Mott states under the influence of fermion-boson conversion. *Physical Review B*, 72:220501, 2005.
- [29] L.-M. Duan. Effective Hamiltonian for Fermions in an optical lattice across a Feshbach resonance. *Physical Review Letters*, 95:243202, 2005.
- [30] Roberto B. Diener and Tin-Lun Ho. Fermions in optical lattices swept across Feshbach resonances. *Physical Review Letters*, 96:010402, 2006.
- [31] Arnaud Koetsier, D. B. M. Dickerscheid, and H. T. C. Stoof. BEC-BCS crossover in an optical lattice. *Physical Review A*, 74:033621, 2006.
- [32] Markus Greiner, Olaf Mandel, Tilman Esslinger, Theodor W. Hänsch, and Immanuel Bloch. Quantum phase transition from a superfluid to a Mott insulator in a gas of ultracold atoms. *Nature*, 415:39–44, 2002.
- [33] Markus Greiner, Olaf Mandel, Theodor W. Hänsch, and Immanuel Bloch. Collapse and revival of the matter wave field of a Bose-Einstein condensate. *Nature*, 419:51–54, 2002.
- [34] Qian Niu, Xian-Geng Zhao, G. A. Georgakis, and M. G. Raizen. Atomic Landau-Zener tunneling and Wannier-Stark ladders in optical potentials. *Physical Review Letters*, 76:4504–4507, 1996.
- [35] C. D. Fertig, K. M. O’Hara, J. H. Huckans, S. L. Rolston, W. D. Phillips, and J. V. Porto. Strongly inhibited transport of a degenerate 1D Bose gas in a lattice. *Physical Review Letters*, 94:120403, 2005.
- [36] Maxime Ben Dahan, Ekkehard Peik, Jakob Reichel, Yvan Castin, and Christophe Salomon. Bloch oscillations of atoms in an optical potential. *Physical Review Letters*, 76:4508–4511, 1996.

- [37] O. Morsch, J. H. Müller, M. Cristiani, D. Ciampini, and E. Arimondo. Bloch oscillations and mean-field effects of Bose-Einstein condensates in 1D optical lattices. *Physical Review Letters*, 87:140402, 2001.
- [38] Corinna Kollath, Andreas M. Läuchli, and Ehud Altman. Quench dynamics and nonequilibrium phase diagram of the Bose-Hubbard model. *Physical Review Letters*, 98:180601, 2007.
- [39] Marcos Rigol, Alejandro Muramatsu, and Maxim Olshanii. Hard-core bosons on optical superlattices: Dynamics and relaxation in the superfluid and insulating regimes. *Physical Review A*, 74:053616, 2006.
- [40] W. M. C. Foulkes, L. Mitas, R. J. Needs, and G. Rajagopal. Quantum Monte Carlo simulations of solids. *Reviews of Modern Physics*, 73:33–83, 2001.
- [41] U. Schöllwöck. The density-matrix renormalization group. *Reviews of Modern Physics*, 77:259–315, 2005.
- [42] Guifre Vidal. Efficient classical simulation of slightly entangled quantum computations. *Physical Review Letters*, 91:147902, 2003.
- [43] Guifre Vidal. Efficient simulation of one-dimensional quantum many-body systems. *Physical Review Letters*, 93:040502, 2004.
- [44] M. A. Nielsen and I. L. Chuang. *Quantum Computation and Quantum Information*. Cambridge University Press, 2000.
- [45] A. J. Daley, C. Kollath, U. Schollwöck, and G. Vidal. Time-dependent density-matrix renormalization-group using adaptive effective Hilbert spaces. *Journal of Statistical Mechanics*, page P04005, 2004.
- [46] Steven R. White and Adrian E. Feiguin. Real-time evolution using the density matrix renormalization group. *Physical Review Letters*, 93:076401, 2004.
- [47] Ulrich Schollwöck and Steven R. White. Methods for time dependence in DMRG. e-print cond-mat/0606018v1 (2006).
- [48] V. E. Zakharov and A. B. Shabat. Exact theory of two-dimensional self-focusing and one-dimensional self-modulation of waves in nonlinear media. *Zh. Eksp. Teor. Fiz.*, 61:118–134, 1971. [*Sov. Phys. JETP*, 34:62–69, 1972].
- [49] V. E. Zakharov and A. B. Shabat. Interaction between solitons in a stable medium. *Zh. Eksp. Teor. Fiz.*, 64:1627–1632, 1973. [*Sov. Phys. JETP*, 37:823–828, 1973].

- [50] J. Denschlag, J. E. Simsarian, D. L. Feder, Charles W. Clark, L. A. Collins, J. Cubizolles, L. Deng, E. W. Hagley, K. Helmerson, W. P. Reinhardt, S. L. Rolston, B. I. Schneider, and W. D. Phillips. Generating solitons by phase engineering of a Bose-Einstein condensate. *Science*, 287:97–101, 2000.
- [51] A. Weller, J. P. Ronzheimer, C. Gross, J. Esteve, M. K. Oberthaler, D. J. Frantzeskakis, G. Theocharis, and P. G. Kevrekidis. Experimental observation of oscillating and interacting matter wave dark solitons. e-print quant-ph/0803.4352v1 (2008).
- [52] Kevin E. Strecker, Guthrie B. Partridge, Andrew G. Truscott, and Randall H. Hulet. Formation and propagation of matter-wave soliton trains. *Nature*, 417:150–153, 2002.
- [53] L. Khaykovich, F. Schreck, G. Ferrari, T. Bourdel, J. Cubizolles, L. D. Carr, Y. Castin, and C. Salomon. Formation of a matter-wave bright soliton. *Science*, 296:1290–1293, 2002.
- [54] L. D. Carr, J. Brand, S. Burger, and A. Sanpera. Dark-soliton creation in Bose-Einstein condensates. *Physical Review A*, 63:051601, 2001.
- [55] S. Burger, L. D. Carr, P. Öhberg, K. Sengstock, and A. Sanpera. Generation and interaction of solitons in Bose-Einstein condensates. *Physical Review A*, 65:043611, 2002.
- [56] Jared C. Bronski, Lincoln D. Carr, Bernard Deconinck, and J. Nathan Kutz. Bose-Einstein condensates in standing waves: The cubic nonlinear Schrödinger equation with a periodic potential. *Physical Review Letters*, 86:1402–1405, 2001.
- [57] Pearl J. Y. Louis, Elena A. Ostrovskaya, Craig M. Savage, and Yuri S. Kivshar. Bose-Einstein condensates in optical lattices: Band-gap structure and solitons. *Physical Review A*, 67:013602, 2003.
- [58] Nikolaos K. Efremidis and Demetrios N. Christodoulides. Lattice solitons in Bose-Einstein condensates. *Physical Review A*, 67:063608, 2003.
- [59] Andrea Trombettoni and Augusto Smerzi. Discrete solitons and breathers with dilute Bose-Einstein condensates. *Physical Review Letters*, 86:2353–2356, 2001.
- [60] Luigi Amico and Vittorio Penna. Dynamical mean field theory of the Bose-Hubbard model. *Physical Review Letters*, 80:2189–2192, 1998.
- [61] M. J. Ablowitz and J. F. Ladik. Nonlinear differential-difference equations and Fourier analysis. *Journal of Mathematical Physics*, 17:1011–1018, 1976.

- [62] Yuri S. Kivshar, Wieslaw Królikowski, and Oksana A. Chubykalo. Dark solitons in discrete lattices. *Physical Review E*, 50:5020–5032, 1994.
- [63] Magnus Johansson and Yuri S. Kivshar. Discreteness-induced oscillatory instabilities of dark solitons. *Physical Review Letters*, 82:85–88, 1999.
- [64] P. G. Kevrekidis, R. Carretero-González, G. Theocharis, D. J. Frantzeskakis, and B. A. Malomed. Stability of dark solitons in a Bose-Einstein condensate trapped in an optical lattice. *Physical Review A*, 68:035602, 2003.
- [65] Jacek Dziarmaga, Zbyszek P. Karkuszewski, and Krzysztof Sacha. Quantum depletion of an excited condensate. *Physical Review A*, 66:043615, 2002.
- [66] Jacek Dziarmaga and Krzysztof Sacha. Depletion of the dark soliton: The anomalous mode of the Bogoliubov theory. *Physical Review A*, 66:043620, 2002.
- [67] Jacek Dziarmaga, Zbyszek P. Karkuszewski, and Krzysztof Sacha. Images of the dark soliton in a depleted condensate. *Journal of Physics B*, 36:1217–1229, 2003.
- [68] Jacek Dziarmaga and Krzysztof Sacha. Images of a Bose-Einstein condensate: Diagonal dynamical Bogoliubov vacuum. *Journal of Physics B*, 39:57–68, 2006.
- [69] J. Dziarmaga. Quantum dark soliton: Nonperturbative diffusion of phase and position. *Physical Review A*, 70:063616, 2004.
- [70] C. K. Law. Dynamic quantum depletion in phase-imprinted generation of dark solitons. *Physical Review A*, 68:015602, 2003.
- [71] A. C. Scott, J. C. Eilbeck, and H. Gilhoj. Quantum lattice solitons. *Physica D*, 78:194–213, 1994.
- [72] Y. Lai and H. A. Haus. Quantum theory of solitons in optical fibers. I. Time-dependent Hartree approximation. *Physical Review A*, 40:844–853, 1989.
- [73] Anthony J. Leggett. Bose-Einstein condensation in the alkali gases: Some fundamental concepts. *Rev. Mod. Phys.*, 73:307–356, 2001.
- [74] L. E. Sadler, J. M. Higbie, S. R. Leslie, M. Vengalattore, and D. M. Stamper-Kurn. Spontaneous symmetry breaking in a quenched ferromagnetic spinor Bose-Einstein condensate. *Nature*, 443:312–315, 2006.
- [75] J. Stenger, S. Inouye, D. M. Stamper-Kurn, H.-J. Meisner, A. P. Chikkatur, and W. Ketterle. Spin domains in ground-state Bose-Einstein condensates. *Nature*, 396:345–348, 1998.

- [76] H.-J. Miesner, D. M. Stamper-Kurn, J. Stenger, S. Inouye, A. P. Chikkatur, and W. Ketterle. Observation of metastable states in spinor Bose-Einstein condensates. *Physical Review Letters*, 82:2228–2231, 1999.
- [77] Austen Lamacraft. Quantum quenches in a spinor condensate. *Physical Review Letters*, 98:160404, 2007.
- [78] Bogdan Damski and Wojciech H. Zurek. Dynamics of a quantum phase transition in a ferromagnetic Bose-Einstein condensate. *Physical Review Letters*, 99:130402, 2007.
- [79] Hiroki Saito, Yuki Kawaguchi, and Masahito Ueda. Kibble-Zurek mechanism in a quenched ferromagnetic Bose-Einstein condensate. *Physical Review A*, 76:043613, 2007.
- [80] T. W. B. Kibble. Topology of cosmic domains and strings. *Journal of Physics A: Mathematical and Theoretical*, 9:1387–1398, 1976.
- [81] T. W. B. Kibble. Some implications of a cosmological phase transition. *Physics Reports*, 67:183–199, 1980.
- [82] W. H. Zurek. Cosmological experiments in superfluid helium? *Nature*, 317:505–508, 1985.
- [83] W. H. Zurek. Cosmological experiments in condensed matter systems. *Physics Reports*, 276:177–221, 1996.
- [84] Hiroki Saito, Yuki Kawaguchi, and Masahito Ueda. Topological defect formation in a quenched ferromagnetic Bose-Einstein condensates. *Physical Review A*, 75:013621, 2007.
- [85] Michael Uhlmann, Ralf Schützhold, and Uwe R. Fischer. Vortex quantum creation and winding number scaling in a quenched spinor Bose gas. *Physical Review Letters*, 99:120407, 2007.
- [86] Bogdan Damski and Wojciech H. Zurek. Dynamics of a symmetry-restoration quantum phase transition in a ferromagnetic Bose-Einstein condensate. e-print cond-mat/0711.3431v2 (2007).
- [87] Wojciech H. Zurek, Uwe Dorner, and Peter Zoller. Dynamics of a quantum phase transition. *Physical Review Letters*, 95:105701, 2005.
- [88] Bogdan Damski. The simplest quantum model supporting the Kibble-Zurek mechanism of topological defect production: Landau-Zener transitions from a new perspective. *Physical Review Letters*, 95:035701, 2005.



- [89] Daniel V. Schroeder. *An Introduction to Thermal Physics*. Addison Wesley Longman, 3rd edition, 2000.
- [90] A. Görlitz, J. M. Vogels, A. E. Leanhardt, C. Raman, T. L. Gustavson, J. R. Abo-Shaeer, A. P. Chikkatur, S. Gupta, S. Inouye, T. Rosenband, and W. Ketterle. Realization of Bose-Einstein condensates in lower dimensions. *Physical Review Letters*, 87:130402, 2001.
- [91] O. Penrose. The quantum mechanics of helium II. *Philosophical Magazine*, 42:1373–1377, 1951.
- [92] John von Neumann. *Mathematical Foundations of Quantum Mechanics*. Princeton University Press, 1955.
- [93] A. Einstein, B. Podolsky, and N. Rosen. Can quantum-mechanical description of physical reality be considered complete? *Physical Review*, 47:777–780, 1935.
- [94] C. N. Yang. Concept of off-diagonal long-range order and the quantum phases of liquid He and of superconductors. *Reviews of Modern Physics*, 34:694–704, 1962.
- [95] G. E. Astrakharchik, J. Boronat, J. Casulleras, and S. Giorgini. Superfluidity versus Bose-Einstein condensation in a Bose gas with disorder. *Physical Review A*, 66:023603, 2002.
- [96] Elliot H. Lieb, Robert Seiringer, Jan Philip Solovej, and Jakob Yngvason. *The Mathematics of the Bose Gas and its Condensation (The Oberwolfach Seminars)*. Birkhäuser Verlag, 2005.
- [97] R. Roth and K. Burnett. Phase diagram of bosonic atoms in two-color superlattices. *Physical Review A*, 68:023604, 2003.
- [98] D. Jaksch and P. Zoller. The cold atom Hubbard toolbox. *Annals of Physics*, 315:52–79, 2005.
- [99] D. R. Dounas-Frazer. Ultracold bosons in a multi-dimensional, tilted, double-well trap: Potential decoherence, tunneling resonances, and two-level phenomena. Master’s thesis, Colorado School of Mines, 2007.
- [100] A. M. Rey. *Ultracold bosonic atoms in optical lattices*. PhD thesis, University of Maryland, 2004.
- [101] L. D. Landau and E. M. Lifshitz. *Quantum Mechanics*. Butterworth-Heinemann, 3rd edition, 1977.

- [102] L. P. Pitaevskii. *Zh. Eksp. Teor. Fiz.*, 40:646, 1961. [*Sov. Phys. JETP*, 13:451, 1961].
- [103] E. P. Gross. Structure of a quantized vortex in boson systems. *Nuovo Cimento*, 20:454–477, 1961.
- [104] E. M. Wright, D. F. Walls, and J. C. Garrison. Collapses and revivals of Bose-Einstein condensates formed in small atomic samples. *Physical Review Letter*, 77:2158–2161, 1996.
- [105] L. D. Carr, Charles W. Clark, and W. P. Reinhardt. Stationary solutions of the one-dimensional nonlinear Schrödinger equation. i. Case of repulsive nonlinearity. *Physical Review A*, 62:063610, 2000.
- [106] L. D. Carr, Charles W. Clark, and W. P. Reinhardt. Stationary solutions of the one-dimensional nonlinear Schrödinger equation. ii. Case of attractive nonlinearity. *Physical Review A*, 62:063611, 2000.
- [107] L. D. Carr, M. J. Holland, and B. A. Malomed. Macroscopic quantum tunnelling of Bose-Einstein condensates in a finite potential well. *Journal of Physics B*, 38:3217–3231, 2005.
- [108] M. Olshanii. Atomic scattering in the presence of an external confinement and a gas of impenetrable bosons. *Physical Review Letters*, 81:938–941, 1998.
- [109] Eugene B. Kolomeisky, T. J. Newman, Joseph P. Straley, and Xiaoya Qi. Low-dimensional Bose liquids: Beyond the gross-pitaevskii approximation. *Physical Review Letters*, 85:1146–1149, 2000.
- [110] Michel Le Bellac. *Quantum Physics*. Cambridge University Press, 2006.
- [111] Ana Maria Rey, Guido Pupillo, Charles W. Clark, and Carl J. Williams. Ultra-cold atoms confined in an optical lattice plus parabolic potential: A closed-form approach. *Physical Review A*, 72:033616, 2005.
- [112] D. Masiello, S. B. McKagan, and W. P. Reinhardt. Multiconfigurational Hartree-Fock theory for identical bosons in a double well. *Physical Review A*, 72:063624, 2005.
- [113] David J. Masiello and William P. Reinhardt. Time-dependent quantum many-body theory of identical bosons in a double well: Early-time ballistic interferences of fragmented and number entangled states. *Physical Review A*, 76:043612, 2007.

- [114] Ofir E. Alon, Alexej I. Streltsov, and Lorenz S. Cederbaum. Multiconfigurational time-dependent Hartree method for bosons: Many-body dynamics of bosonic systems. *Physical Review A*, 77:033613, 2008.
- [115] Wei-Min Zhang, Da Hsuan Feng, and Robert Gilmore. Coherent states: Theory and some applications. *Reviews of Modern Physics*, 62:867–927, 1990.
- [116] W. Zwerger. Mott-Hubbard transition of cold atoms in optical lattices. *Journal of Optics B: Quantum and Semiclassical Optics*, 5:S9–S16, 2003.
- [117] D. van Oosten, P. van der Straten, and H. T. C. Stoof. Quantum phases in an optical lattice. *Physical Review A*, 63:053601, 2001.
- [118] A. M. Rey, K. Burnett, R. Roth, M. Edwards, C. J. Williams, and C. W. Clark. Bogoliubov approach to superfluidity of atoms in an optical lattice. *Journal of Physics B*, 36:825–841, 2003.
- [119] Kiyohito Iigaya, Satoru Konabe, Ippei Danshita, and Tetsuro Nikuni. Landau damping: Instability mechanism of superfluid Bose gases moving in optical lattices. *Physical Review A*, 74:053611, 2006.
- [120] L. J. Garay, J. R. Anglin, J. I. Cirac, and P. Zoller. Sonic black holes in dilute Bose-Einstein condensates. *Physical Review A*, 63:023611, 2001.
- [121] Hans Bethe. Zur theorie der metalle. eigenwerte und eigenfunktionen der linearen atomkette. *Zeitschrift für Physik*, 71:205, 1931.
- [122] M. Girardeau. Relationship between systems of impenetrable bosons and fermions in one dimension. *Journal of Mathematical Physics*, 1:516, 1960.
- [123] Toshiya Kinoshita, Trevor Wenger, and David S. Weiss. Observation of a one-dimensional Tonks-Girardeau gas. *Science*, 305:1125, 2004.
- [124] Marcos Rigol and Alejandro Muramatsu. Universal properties of hard-core bosons confined on one-dimensional lattices. *Physical Review A*, 70:031603, 2004.
- [125] Marcos Rigol, Vanja Dunjko, Vladimir Yurovsky, and Maxim Olshanii. Relaxation in a completely integrable many-body quantum system: An ab initio study of the dynamics of the highly excited states of 1D lattice hard-core bosons. *Physical Review Letters*, 98:050405, 2007.
- [126] V. E. Zakharov and L. D. Faddeev. Korteweg-de Vries equation, a completely integrable system. *Functional Analysis and Its Applications*, 5:280–287, 1971.

- [127] V. E. Zakharov, L. A. Takhtajan, and L. D. Faddeev. Complete description of solutions of the sine-Gordon equation. *Doklady AN SSSR*, 219:1334–1337, 1973.
- [128] E. P. Fitrakis, P. G. Kevrekidis, H. Susanto, and D. J. Frantzeskakis. Dark solitons in discrete lattices: Saturable versus cubic nonlinearities. *Physical Review E*, 75:066608, 2007.
- [129] I. E. Papacharalampous, P. G. Kevrekidis, B. A. Malomed, and D. J. Frantzeskakis. Soliton collisions in the discrete nonlinear schrödinger equation. *Physical Review E*, 68:046604, 2003.
- [130] Tin-Lun Ho. Spinor bose condensates in optical traps. *Physical Review Letters*, 81:742–745, 1998.
- [131] Shunji Tsuchiya, Susumu Kurihara, and Takashi Kimura. Superfluid-Mott insulator transition of spin-1 bosons in an optical lattice. *Physical Review A*, 70:043628, 2004.
- [132] Guang-Hong Chen and Yong-Shi Wu. Quantum phase transition in a multi-component Bose-Einstein condensate in optical lattices. *Physical Review A*, 67:013606, 2003.
- [133] Yuki Kawaguchi, Hiroki Saito, and Masahito Ueda. Can spinor dipolar effects be observed in Bose-Einstein condensates? *Physical Review Letters*, 98:110406, 2007.
- [134] J. Crank and P. Nicolson. A practical method for numerical evaluation of solutions of partial differential equations of the heat conduction type. *Proceedings of the Cambridge Philosophical Society*, 43:50–64, 1947.
- [135] Stig Larsson and Vidar Thomée. *Texts in Applied Mathematics: Partial Differential Equations with Numerical Methods*. Springer, 2005.
- [136] William H. Press, Brian P. Flannery, Saul A. Teukolsky, and William T. Vetterling. *Numerical Recipes in C*. Cambridge University Press, 1988.
- [137] Y.-Y. Shi, L.-M. Duan, and G. Vidal. Classical simulation of quantum many-body systems with a tree tensor network. *Physical Review A*, 74:022320, 2006.
- [138] I. Danshita, J. E. Williams, C. A. R. Sá de Melo, and C. W. Clark. Quantum phases of bosons in double-well optical lattices. *Physical Review A*, 76:043606, 2007.

- [139] Steven R. White. Density matrix formulation for quantum renormalization groups. *Physical Review Letters*, 69:2863–2866, 1992.
- [140] E. Schmidt. Zur theorie der linearen und nichtlinearen integralgleichungen. *Mathematische Annalen*, 63:433–476, 1906.
- [141] Stellan Östlund and Stefan Rommer. Thermodynamic limit of density matrix renormalization. *Physical Review Letters*, 75:3537–3540, 1995.
- [142] Masuo Suzuki. Fractal decomposition of exponential operators with applications to many-body theories and Monte Carlo simulations. *Physics Letters A*, 146:319–323, 1990.
- [143] A. J. Daley. *Manipulation and Simulation of Cold Atoms in Optical Lattices*. PhD thesis, Leopold-Franzens-Universität Innsbruck, 2005.
- [144] R. Franzosi. Nonclassical dynamics of Bose-Einstein condensates in an optical lattice in the superfluid regime. *Physical Review A*, 75:053610, 2007.
- [145] D. T. Pegg and S. M. Barnett. Unitary phase operator in quantum mechanics. *Europhysics Letters*, 6:483–487, 1988.
- [146] D. T. Pegg and S. M. Barnett. Phase properties of the single-mode electromagnetic field. *Physical Review A*, 39:1665–1675, 1989.
- [147] Jamie Williams. Size matters, but not that much. *The Quantum Collective Blog Archive*, April 2006.
- [148] David A. Meyer and Nolan R. Wallach. Global entanglement in multiparticle systems. *Journal of Mathematical Physics*, 43:4273, 2002.
- [149] Gavin K. Brennen. An observable measure of entanglement for pure states of multi-qubit systems. *Quantum Information and Computation*, 3:619, 2003.
- [150] Howard Barnum, Emanuel Knill, Gerardo Ortiz, and Lorenza Viola. Generalizations of entanglement based on coherent states and convex sets. *Physical Review A*, 68:032308, 2003.
- [151] Howard Barnum, Emanuel Knill, Gerardo Ortiz, Rolando Somma, and Lorenza Viola. A subsystem-independent generalization of entanglement. *Physical Review Letters*, 92:107902, 2004.
- [152] Xinhua Xi and Zhongxing Ye. Generalized quantum entropy. *Journal of Mathematical Physics*, 47:023502, 2006.

- [153] C. Tsallis. Possible generalization of Boltzmann-Gibbs statistics. *Journal of Statistical Physics*, 52:479–487, 1988.
- [154] A. Rényi. On measures of information and entropy. *Proceedings of the 4th Berkeley Symposium on Mathematics, Statistics and Probability*, pages 547–561, 1961.
- [155] R. V. Mishmash, L. D. Carr, I. Danshita, and C. W. Clark. Quantum many-body dynamics of dark solitons in optical lattices. *Physical Review A*, to be submitted, 2008.
- [156] A. Imamoglu, M. Lewenstein, and L. You. Inhibition of coherence in trapped Bose-Einstein condensates. *Physical Review Letters*, 78:2511–2514, 1997.
- [157] Wei Li, Ari K. Tuchman, Hui-Chun Chien, and Mark A. Kasevich. Extended coherence time with atom-number squeezed states. *Physical Review Letters*, 98:040402, 2007.
- [158] B. Jackson, N. P. Proukakis, and C. F. Barenghi. Dark-soliton dynamics in Bose-Einstein condensates at finite temperature. *Physical Review A*, 75:051601, 2007.
- [159] E. Zaremba, T. Nikuni, and Griffin A. Dynamics of trapped Bose gases at finite temperatures. *Journal of Low Temperature Physics*, 116:277, 1999.
- [160] Th. Busch and J. R. Anglin. Motion of dark solitons in trapped Bose-Einstein condensates. *Physical Review Letters*, 84:2298–2301, 2000.
- [161] Michael Zwolak and Guifré Vidal. Mixed-state dynamics in one-dimensional quantum lattice systems: A time-dependent superoperator renormalization algorithm. *Physical Review Letters*, 93:207205, 2004.
- [162] Daniel M. Greenberger, Michael A. Horne, and Anton Zeilinger. *Bell's theorem, Quantum Theory, and Conceptions of the Universe*. Kluwer Academics, Dordrecht, The Netherlands, 1989.

## APPENDIX A

### VIDAL DECOMPOSITION EXAMPLES

Vidal's decomposition on an arbitrary state in Fock space of the form

$$|\Psi\rangle = \sum_{i_1, i_2, \dots, i_M=1}^d c_{i_1 i_2 \dots i_M} |i_1\rangle \otimes |i_2\rangle \otimes \dots \otimes |i_M\rangle, \quad (\text{A.1})$$

reads

$$c_{i_1 i_2 \dots i_M} = \sum_{\alpha_1, \dots, \alpha_M}^{\chi} \Gamma_{\alpha_1}^{[1]i_1} \lambda_{\alpha_1}^{[1]} \Gamma_{\alpha_1 \alpha_2}^{[2]i_2} \lambda_{\alpha_2}^{[2]} \Gamma_{\alpha_2 \alpha_3}^{[3]i_3} \dots \Gamma_{\alpha_{M-1}}^{[M]i_M}. \quad (\text{A.2})$$

For an *arbitrary* state in Hilbert space for which all the coefficients  $c_{i_1 i_2 \dots i_M}$  are known, performing this decomposition is not generally useful because (1)  $\chi$  generally grows exponentially in size of the system  $M$  and (2) we usually do not have all the  $d^M$  coefficients at our disposal. Nonetheless, it is instructive to explicitly derive expressions for the  $\Gamma$ s and  $\lambda$ s in (A.2) for a few well-known low- $\chi$  states in order to get a feel for how one performs the decomposition. In this appendix, we focus on the product states, the GHZ state, and the W state. In Section 3.2.2, the procedure for decomposition of a general state is outlined.

#### A.1 Product States

When creating initial states for quantum soliton propagation in Chapter 4, we begin with a *product* of Glauber atom-number coherent states. Similarly, when using non-number conserving TEBD to calculate the ground state of a given Hamiltonian,

one often begins imaginary time propagation with a state that is an equal superposition of *all* allowed Fock states. Such a state is, of course, also a product state. It is thus essential to be able to perform the decomposition (A.2) for product states. Consider the vacuum state of a system of size  $M$ :

$$|\Psi\rangle = |0\rangle^{\otimes M}, \quad (\text{A.3})$$

which is the simplest product state of the  $M$  sites. (For simplicity, we refer to the subsystems associated with each index  $i_k$  as *sites*.) The Schmidt decomposition of any product state will involve only a *single* term so that with  $\chi = 1$  we have an exact representation of the state. Performing a splitting after site 1, we can write

$$|\Psi\rangle = \sum_{\alpha_1} \lambda_{\alpha_1}^{[1]} |\Phi_{\alpha_1}^{[1]}\rangle |\Phi_{\alpha_1}^{[2\cdots M]}\rangle = |0\rangle |0\rangle^{\otimes M-1}, \quad (\text{A.4})$$

and thus  $\lambda_{\alpha_1}^{[1]} = \delta_{\alpha_1,1}$  or, more generally,  $\lambda_{\alpha_\ell}^{[\ell]} = \delta_{\alpha_\ell,1}$ . The first  $\Gamma$  simply represents the coefficients associated with the individual Fock states  $|i_1\rangle$ . That is,  $|\Phi_{\alpha_1}^{[1]}\rangle = \sum_{i_1} \Gamma_{\alpha_1}^{[1]i_1} |i_1\rangle$ , so  $\Gamma_{\alpha_1}^{[1]i_1} = \delta_{\alpha_1,1} \delta_{i_1,0}$ .

We then proceed to expand the  $|\Phi_{\alpha_1}^{[2\cdots M]}\rangle$  in a local basis for the second site. That is,

$$|\Phi_{\alpha_1}^{[2\cdots M]}\rangle = \sum_{i_2} |i_2\rangle |\tau_{\alpha_1 i_2}^{[3\cdots M]}\rangle. \quad (\text{A.5})$$

For the present case, we can easily identify the vectors

$$|\tau_{\alpha_1 i_2}^{[3\cdots M]}\rangle = \delta_{\alpha_1,1} \delta_{i_2,0} |0\rangle^{M-2}. \quad (\text{A.6})$$



$\Gamma^{[2]}$  is then obtained by

$$|\tau_{\alpha_1 i_2}^{[3 \dots M]}\rangle = \sum_{\alpha_2} \Gamma_{\alpha_1 \alpha_2}^{[2] i_2} \lambda_{\alpha_2}^{[2]} |\Phi_{\alpha_2}^{[3 \dots M]}\rangle, \quad (\text{A.7})$$

where the Schmidt vectors  $|\Phi_{\alpha_2}^{[3 \dots M]}\rangle$  for the second bipartite splitting are trivially  $|0\rangle^{M-2}$ , and so  $\Gamma_{\alpha_1 \alpha_2}^{[2] i_2} = \delta_{\alpha_1,1} \delta_{\alpha_2,1} \delta_{i_2,0}$ . In general, we thus have  $\Gamma_{\alpha_{\ell-1} \alpha_{\ell}}^{[\ell] i_{\ell}} = \delta_{\alpha_{\ell-1},1} \delta_{\alpha_{\ell},1} \delta_{i_{\ell},0}$ .

This procedure can easily be applied to a general product state of the form

$$|\Psi\rangle = \bigotimes_{k=1}^M |\psi_k\rangle, \text{ where } |\psi_k\rangle = \sum_{i_k=1}^d c_{i_k}^{(k)} |i_k\rangle. \quad (\text{A.8})$$

Of course, we still have  $\chi = 1$ , so  $\lambda_{\alpha_{\ell}}^{[\ell]} = \delta_{\alpha_{\ell},1}$ . For the first bipartite splitting, we have

$$|\Psi\rangle = |\psi_1\rangle \bigotimes_{k=2}^M |\psi_k\rangle, \quad (\text{A.9})$$

so  $|\Phi_{\alpha_1}^{[1]}\rangle = \delta_{\alpha_1,1} |\psi_1\rangle$  and  $|\Phi_{\alpha_1}^{[2 \dots M]}\rangle = \delta_{\alpha_1,1} \bigotimes_{k=2}^M |\psi_k\rangle$ , and hence  $\Gamma_{\alpha_1}^{[1] i_1} = c_{i_1}^{(1)}$ . As before, we can expand  $|\Phi_{\alpha_1}^{[2 \dots M]}\rangle$  in the second site's local basis and find the vectors  $|\tau_{\alpha_1 i_2}^{[3 \dots M]}\rangle$  [see Equation (A.7)] to be

$$|\tau_{\alpha_1 i_2}^{[3 \dots M]}\rangle = \delta_{\alpha_1,1} c_{i_2}^{(2)} \bigotimes_{k=3}^M |\psi_k\rangle, \quad (\text{A.10})$$

from which we can identify  $\Gamma_{\alpha_1 \alpha_2}^{[2] i_2} = c_{i_2}^{(2)} \delta_{\alpha_1,1} \delta_{\alpha_2,1}$ . Or, more generally, we can write  $\Gamma_{\alpha_{\ell-1} \alpha_{\ell}}^{[\ell] i_{\ell}} = c_{i_{\ell}}^{(\ell)} \delta_{\alpha_{\ell-1},1} \delta_{\alpha_{\ell},1}$  for an arbitrary  $\Gamma$  and have thus obtained explicit expressions for the  $\Gamma$ s and  $\lambda$ s in (A.2) for a product state (A.8).

## A.2 GHZ State

Next, we consider the GHZ (Greenberger-Horne-Zeilinger) state [162] of  $M$  qubits (we now refer to the subsystems as *qubits* because they are assumed to be two-state systems) which is a maximally entangled state according to most entanglement measures:

$$|\Psi\rangle = \frac{1}{\sqrt{2}} (|0\rangle^{\otimes M} + |1\rangle^{\otimes M}). \quad (\text{A.11})$$

The Schmidt decomposition at an arbitrary link  $\ell$  will involve only  $\chi = 2$  terms:

$$|\Psi\rangle = \frac{1}{\sqrt{2}} (|0\rangle^{\otimes \ell} |0\rangle^{\otimes M-\ell} + |1\rangle^{\otimes \ell} |1\rangle^{\otimes M-\ell}). \quad (\text{A.12})$$

For the first splitting, we can easily identify  $\lambda_{\alpha_1}^{[1]} = \frac{\delta_{\alpha_1,1}}{\sqrt{2}}$  and  $\Gamma_{\alpha_1}^{[1]i_1} = \delta_{\alpha_1,1}\delta_{i_1,0} + \delta_{\alpha_1,2}\delta_{i_1,1}$ . In fact, the  $\lambda$ s can be written down immediately from the general Schmidt decomposition given in (A.12):

$$\lambda_{\alpha_\ell}^{[l]} = \frac{1}{\sqrt{2}} (\delta_{\alpha_\ell,1} + \delta_{\alpha_\ell,2}). \quad (\text{A.13})$$

We can then write the  $[2 \cdots M]$  part of the Schmidt vectors for the first splitting in the local basis for the second qubit

$$|\Phi_{\alpha_1}^{[2 \cdots M]}\rangle = \sum_{i_2} |i_2\rangle |\tau_{\alpha_1 i_2}^{[3 \cdots M]}\rangle = \delta_{\alpha_1,1} |0\rangle^{M-1} + \delta_{\alpha_1,2} |1\rangle^{M-1}, \quad (\text{A.14})$$

and hence,

$$|\tau_{\alpha_1 i_2}^{[3 \cdots M]}\rangle = \delta_{\alpha_1,1} \delta_{i_2,0} |0\rangle^{M-2} + \delta_{\alpha_1,2} \delta_{i_2,1} |1\rangle^{M-2}. \quad (\text{A.15})$$

The  $[3 \cdots M]$  part of the Schmidt vectors for the second splitting is given by

$$|\Phi_{\alpha_2}^{[3 \cdots M]}\rangle = \delta_{\alpha_2,1}|0\rangle^{M-2} + \delta_{\alpha_2,2}|1\rangle^{M-2}, \quad (\text{A.16})$$

from which we can use (A.7) with (A.15) to solve for the  $\Gamma_{\alpha_1\alpha_2}^{[2]i_2}$  yielding  $\Gamma_{\alpha_1\alpha_2}^{[2]i_2} = \delta_{\alpha_1,1}\delta_{\alpha_2,1}\delta_{i_2,0} + \delta_{\alpha_1,2}\delta_{\alpha_2,2}\delta_{i_2,1}$  which can be generalized immediately to yield

$$\Gamma_{\alpha_{\ell-1}\alpha_\ell}^{[\ell]i_\ell} = \delta_{\alpha_{\ell-1},1}\delta_{\alpha_\ell,1}\delta_{i_\ell,0} + \delta_{\alpha_{\ell-1},2}\delta_{\alpha_\ell,2}\delta_{i_\ell,1}. \quad (\text{A.17})$$

### A.3 W State

A less trivial example is the  $M$ -qubit W state defined by

$$|\Psi\rangle = \frac{1}{\sqrt{M}} \sum_{k=1}^M |0\rangle^{\otimes M-k} |1\rangle |0\rangle^{\otimes k-1}, \quad (\text{A.18})$$

which is an equal superposition of all states involving only a single qubit in the state  $|1\rangle$  and the remaining  $M-1$  qubits in the state  $|0\rangle$ . This state can always be written as a sum of two products:

$$\begin{aligned} |\Psi\rangle = & \sqrt{\frac{M-\ell}{M}} (|0\rangle^{\otimes \ell}) \otimes \frac{1}{\sqrt{M-\ell}} \left( \sum_{i=1}^{M-\ell} |0\rangle^{\otimes M-\ell-i} |1\rangle |0\rangle^{\otimes i-1} \right) \\ & + \sqrt{\frac{M}{\ell}} \left( \frac{1}{\sqrt{\ell}} \sum_{i=1}^{\ell} |0\rangle^{\otimes \ell-i} |1\rangle |0\rangle^{\otimes i-1} \right) \otimes (|0\rangle^{\otimes M-\ell}), \end{aligned} \quad (\text{A.19})$$

and thus has a Schmidt number  $\chi = 2$ . From Equation (A.19), we can identify the  $\lambda$ s and the first  $\Gamma$ :

$$\lambda_{\alpha_\ell}^{[\ell]} = \delta_{\alpha_\ell,1} \sqrt{\frac{M-\ell}{M}} + \delta_{\alpha_\ell,2} \sqrt{\frac{\ell}{M}}, \quad (\text{A.20})$$

$$\Gamma_{\alpha_1}^{[1]i_1} = \delta_{\alpha_1,1} \delta_{i_1,0} + \delta_{\alpha_1,2} \delta_{i_1,1}. \quad (\text{A.21})$$

For  $\ell > M/2$ ,  $\lambda_2^{[\ell]} > \lambda_1^{[\ell]}$ , so in practice the Schmidt vectors and coefficients should be reordered accordingly. For the sake of this discussion, we need not be concerned with this detail.

As before, we will write the  $[2 \cdots M]$  part of the Schmidt vectors for the  $\ell = 1$  splitting, i.e.,  $|\Phi_{\alpha_1}^{[2 \cdots M]}\rangle$ , in the local basis for the second qubit and find the vectors  $|\tau_{\alpha_1 i_2}^{[3 \cdots M]}\rangle$ . First, let us write down the actual Schmidt vectors for an arbitrary  $\ell$ :

$$|\Phi_{\alpha_\ell}^{[1 \cdots \ell]}\rangle = \delta_{\alpha_\ell,1} |0\rangle^{\otimes \ell} + \delta_{\alpha_\ell,2} \frac{1}{\sqrt{\ell}} \sum_{k=1}^{\ell} |0\rangle^{\otimes \ell-k} |1\rangle |0\rangle^{\otimes k-1}, \quad (\text{A.22})$$

$$|\Phi_{\alpha_\ell}^{[\ell+1 \cdots M]}\rangle = \delta_{\alpha_\ell,1} \frac{1}{\sqrt{M-\ell}} \sum_{k=1}^{M-\ell} |0\rangle^{\otimes M-\ell-k} |1\rangle |0\rangle^{\otimes k-1} + \delta_{\alpha_\ell,2} |0\rangle^{\otimes M-\ell}. \quad (\text{A.23})$$

Thus, for the first splitting we have

$$\begin{aligned} |\tau_{\alpha_1 i_2}^{[3 \cdots M]}\rangle &= \delta_{\alpha_1,1} \delta_{i_2,0} \sqrt{\frac{M-2}{M-1}} |\Phi_{\alpha_2=1}^{[3 \cdots M]}\rangle + \delta_{\alpha_1,1} \delta_{i_2,1} \frac{1}{\sqrt{M-1}} |\Phi_{\alpha_2=2}^{[3 \cdots M]}\rangle \\ &\quad + \delta_{\alpha_1,2} \delta_{i_2,0} |\Phi_{\alpha_2=2}^{[3 \cdots M]}\rangle \end{aligned} \quad (\text{A.24})$$

from which we can solve for the second  $\Gamma$  to be

$$\begin{aligned}\Gamma_{\alpha_1\alpha_2}^{[2]i_2} &= \delta_{\alpha_1,1}\delta_{\alpha_2,1}\delta_{i_2,0}\sqrt{\frac{M}{M-1}} + \delta_{\alpha_1,1}\delta_{\alpha_2,2}\delta_{i_2,1}\sqrt{\frac{M}{2(M-1)}} \\ &\quad + \delta_{\alpha_1,2}\delta_{\alpha_2,2}\delta_{i_2,0}\sqrt{\frac{M}{2}}.\end{aligned}\tag{A.25}$$

One can generalize this procedure for an arbitrary splitting and obtain

$$\begin{aligned}\Gamma_{\alpha_{\ell-1}\alpha_\ell}^{[\ell]i_\ell} &= \delta_{\alpha_{\ell-1},1}\delta_{\alpha_\ell,1}\delta_{i_\ell,0}\sqrt{\frac{M}{M-\ell+1}} + \delta_{\alpha_{\ell-1},1}\delta_{\alpha_\ell,2}\delta_{i_\ell,1}\sqrt{\frac{M}{\ell(M-\ell+1)}} \\ &\quad + \delta_{\alpha_{\ell-1},2}\delta_{\alpha_\ell,2}\delta_{i_\ell,0}\sqrt{\frac{M}{\ell}},\end{aligned}\tag{A.26}$$

which completes the decomposition.

## APPENDIX B

### ACCURACY AND CONVERGENCE OF TIME-EVOLVING BLOCK DECIMATION SIMULATIONS

In this appendix, we consider the main sources of error inherent in the TEBD algorithm. First, we examine the convergence of our results with respect to  $\chi$ , the number of basis sets retained for each two-site operation of the procedure; this is perhaps the most important numerical convergence parameter of the method. We show convergence plots for time-dependent simulations using TEBD of both mean-field dark solitons and quantum engineered dark solitons, as can be found in Chapters 4 and 5, respectively. In the second section, we discuss the other errors present in the routine, namely the errors associated with a Suzuki-Trotter expansion of the time evolution operator and with truncation of the local boson Hilbert space dimension. Convergence of our results with respect to  $\delta t$ , the Suzuki-Trotter time-step size, and  $d$ , the local Hilbert space dimension, will be summarized.

#### B.1 Error in Schmidt Truncation Procedure

As explained in Section 3.2.3, for each two-site operation performed during time evolution, we only retain the largest  $\chi$  eigenvectors of the reduced density matrices for the subsystems on each side of the link associated with the two-site operation. Due to the way in which we perform the two-site operation by calculating a singular value decomposition of a  $(\chi d) \times (\chi d)$  matrix, we discard the smallest  $\chi(d - 1)$  eigenvalues. In this section, we analyze convergence of our results with respect to  $\chi$ , thus assessing

the validity of truncating each Schmidt decomposition at the largest  $\chi$  Schmidt basis sets.

### B.1.1 Mean-Field Soliton Initial Conditions

In Figure B.1, we plot the time dependence of selected observables for different values of  $\chi$  for quantum evolution of a mean-field dark soliton. Other than  $\chi$ , the parameters used are identical to those used for the simulation in Section 4.3.2. Averages over local observables, such as the order parameter norm in Figure B.1(a) and the average local impurity in Figure B.1(b), converge quickly in  $\chi$ . Even at  $\chi$  as low as 20, we obtain physically sensible results. In Figure B.1(c), we plot the average number at the center site, i.e., the density at the soliton's center. It is clear from this figure that average local number is well-converged in  $\chi$ . On the other hand, quantum depletion as shown in B.1(d) is only converged to  $\lesssim 5\%$  at the final time for  $\chi = 50$ . The reason being that depletion is calculated via an eigendecomposition of the single-particle density matrix with elements  $\langle \hat{b}_j^\dagger \hat{b}_i \rangle$  that are nonlocal observables. This is a general result: because of the local nature of the matrix product decomposition of the state as defined in Equation (3.27), the more local an observable, the faster convergence occurs with respect to  $\chi$ . Thus, there is error on the quantitative value of the fragmentation time of the soliton, as signified by the peak in depletion, that is on the order of a few tunneling times. The qualitative picture, however, should remain unaffected. In Figure B.2, we take the  $\chi = 50$  simulation as the best result and plot the error of the observables displayed in Figure B.1 for the  $\chi \in \{40, 30, 20\}$  simulations relative to the  $\chi = 50$  simulation. In the relative error calculations, we normalize the difference between the two results to the average of the two results. These calculations can be used to make estimates in the percent error of the  $\chi = 50$

results.

The local Schmidt truncation error  $\tau_\ell^S$  is defined as the sum of discarded reduced density matrix eigenvalues for a given two-site operation at link  $\ell$ , cf. Equation (3.41). The total Schmidt truncation error  $\tau^S$  for a given time step is the sum of local Schmidt truncation errors associated with forward propagation of the entire system at that time step. Of course, this procedure requires  $\mathcal{O}(M)$  two-site operations. In Figure B.3(a), we plot the total Schmidt truncation error at each time. As expected, this value decreases with increased  $\chi$ . These simulations run for 4000 time steps because we use time steps of size  $\delta t = 0.01 \hbar/J$  for a total simulation time  $t_f = 40 \hbar/J$ . Thus, when integrated over time to the final time  $t_f$ , the total Schmidt truncation error is  $\mathcal{O}(10^{-2})$ . However, the *local* Schmidt truncation error at the final time can be estimated at  $10^{-2}/M \sim 10^{-3}$ , a very acceptable result. As a last check on our TEBD results we consider how well the method conserves total average number and total average energy, both conserved quantities according to the Bose-Hubbard Hamiltonian. In Figure B.3, we plot the relative error in these quantities at the final time as compared to the initial time. We see that both errors are  $\lesssim 1\%$ . The error in energy decreases as  $\chi$  is increased, while the error in total number does not depend strongly on  $\chi$  for the range of  $\chi$  considered here.

### B.1.2 Quantum Engineered Soliton Initial Conditions

We now consider convergence of our results with respect to  $\chi$  for the case of our quantum soliton engineering calculations as presented in Chapter 5. Here, we select the same parameters as the characteristic density and phase engineered dark soliton analyzed in Section 5.2.2. Recall that for that simulation we chose  $\chi = 80$ . In Figure B.4(a)–(c), we plot the number variance, von Neumann entropy, and average particle



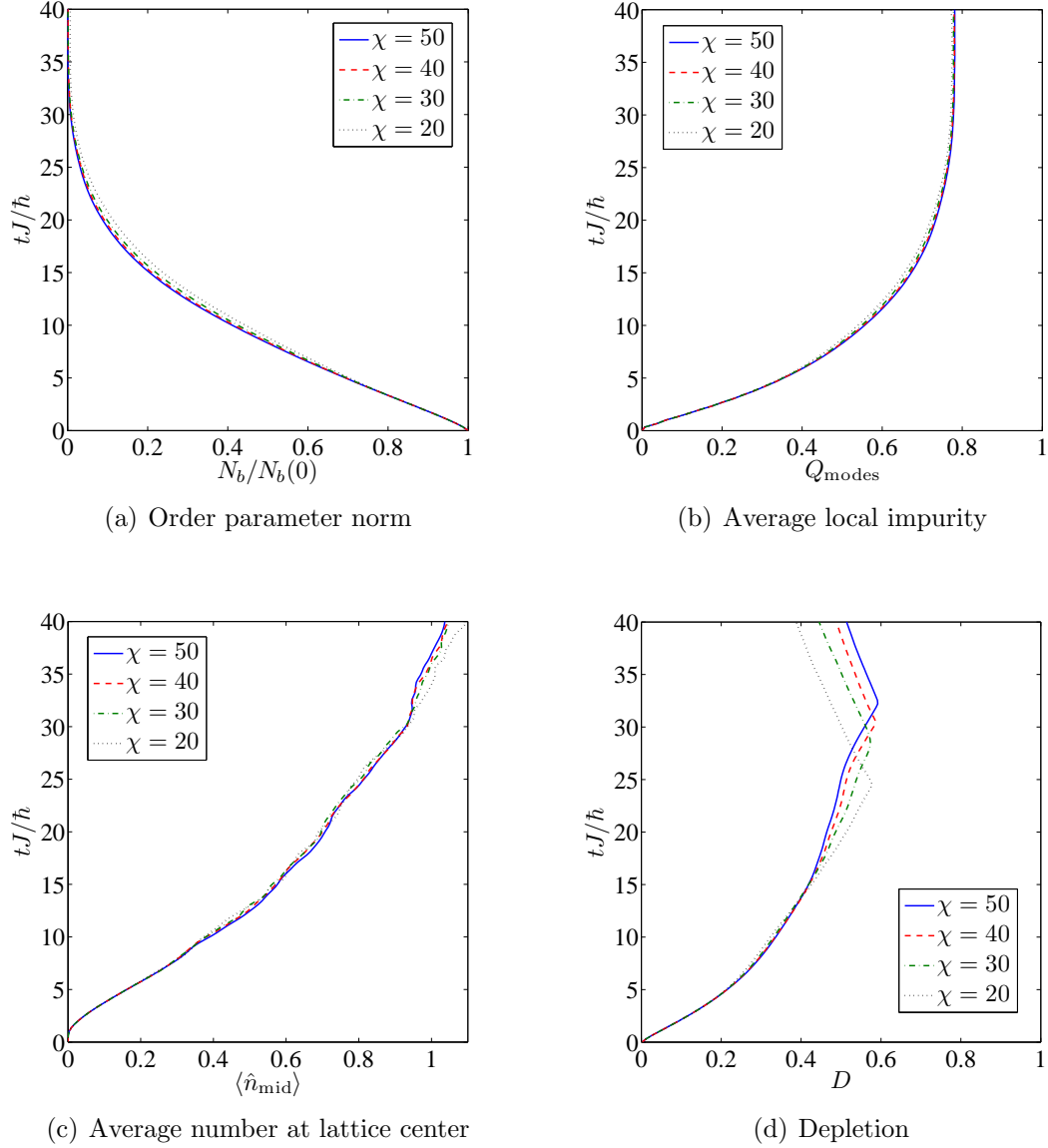


Figure B.1. *Dependence of observables on  $\chi$  for quantum evolution of a standing mean-field soliton.* For values of  $\chi \in \{50, 40, 30, 20\}$ , we plot over time the (a) order parameter norm, (b) average local impurity, (c) average particle occupation number at the center lattice site, and (d) quantum depletion. All other simulation parameters are the same as those used in the characteristic simulation of mean-field dark soliton quantum evolution presented in Section 4.3.2. The quantum depletion in (d) is less well-converged the other measures at late times due to its dependence on nonlocal observables.

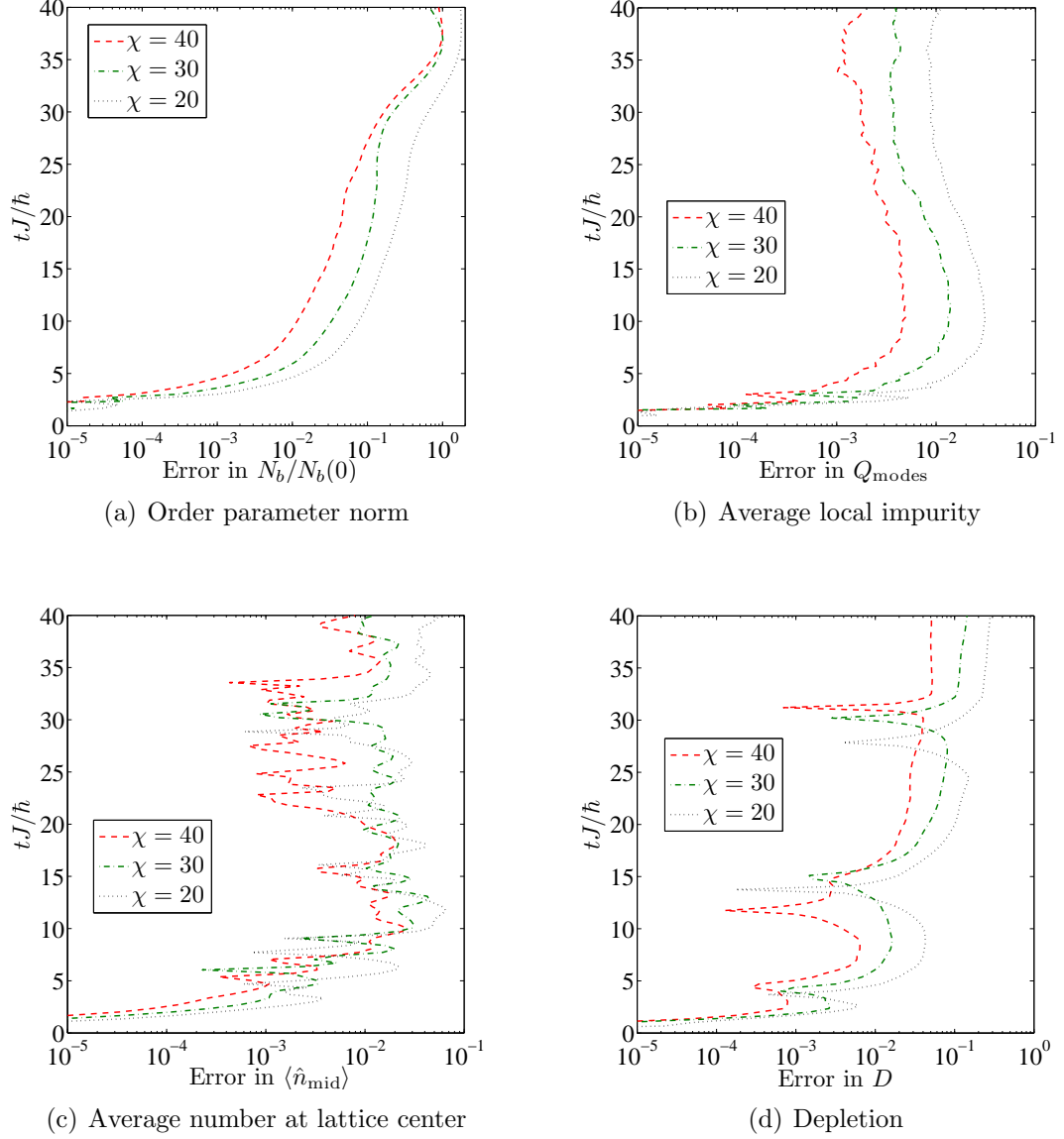


Figure B.2. *Relative error of observables with different  $\chi$  for quantum evolution of a standing mean-field soliton.* For the same measures as in Figure B.1, we plot the error of the  $\chi \in \{40, 30, 20\}$  results relative to the  $\chi = 50$  result. (a) The relative error in the order parameter norm at long times is large due to the quantity itself vanishing, hence small magnitude fluctuations are magnified. The errors in (b) average local impurity, (c) average number at lattice center, and (d) quantum depletion are all very acceptable.

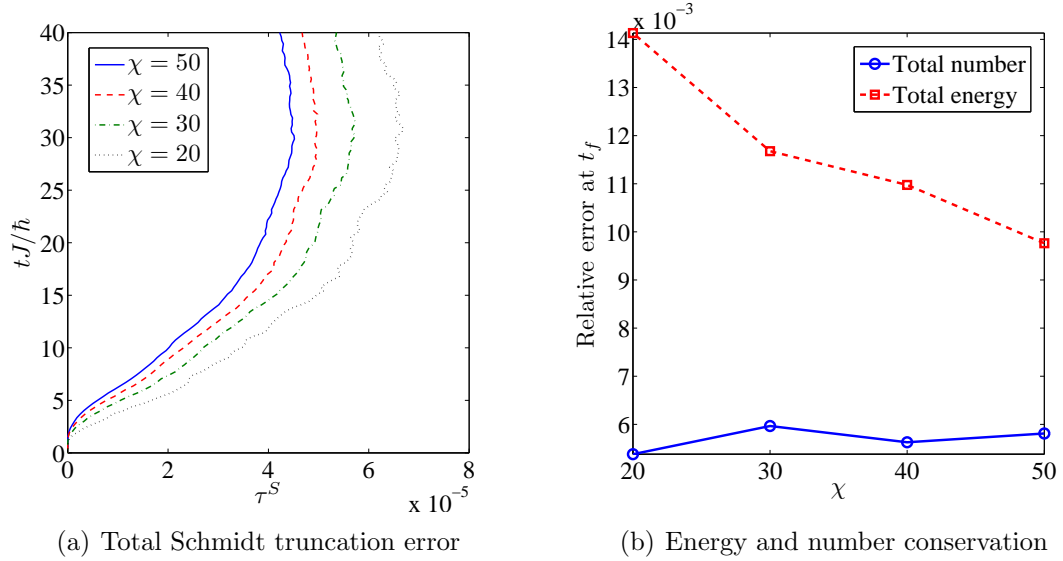


Figure B.3. *Truncation error and conservation of good quantum numbers for quantum evolution of a standing mean-field soliton.* (a) The total Schmidt truncation error for each TEBD time step is plotted over time for  $\chi \in \{50, 40, 30, 20\}$ . We see that for the values of  $\chi$  considered here this quantity stays  $\mathcal{O}(10^{-5})$ . Because for these simulations we choose  $M = 31$  sites, the Schmidt truncation error is only  $\mathcal{O}(10^{-6})$  for each time step. (b) As compared to their initial values, the relative error in average total particle number and average total energy at the final time are plotted versus the same values of  $\chi$  as in (a). We see that these errors are an acceptable  $\mathcal{O}(10^{-2})$ . The curves in (b) are a guide to the eye; actual data are points.

number all at the center site over time for different values of  $\chi$ . It is clear that local observables are converged at  $\chi = 80$ . Figure B.4(d) reveals that quantum depletion is also converged for  $\chi = 80$  despite it being nonlocal. For the same measures as in Figure B.4, Figure B.5 depicts the error in the  $\chi \in \{70, 60, 50\}$  data relative to the  $\chi = 80$  simulation. As expected, increasing  $\chi$  generally decreases the relative error of a given observable.

As in Section B.1.1, we now consider the Schmidt truncation error and conservation of total number and energy. In Figure B.6(a), we see that the total Schmidt truncation error at the final time is  $\lesssim 10^{-5}$  for  $\chi = 80$ ; thus, the integrated lo-

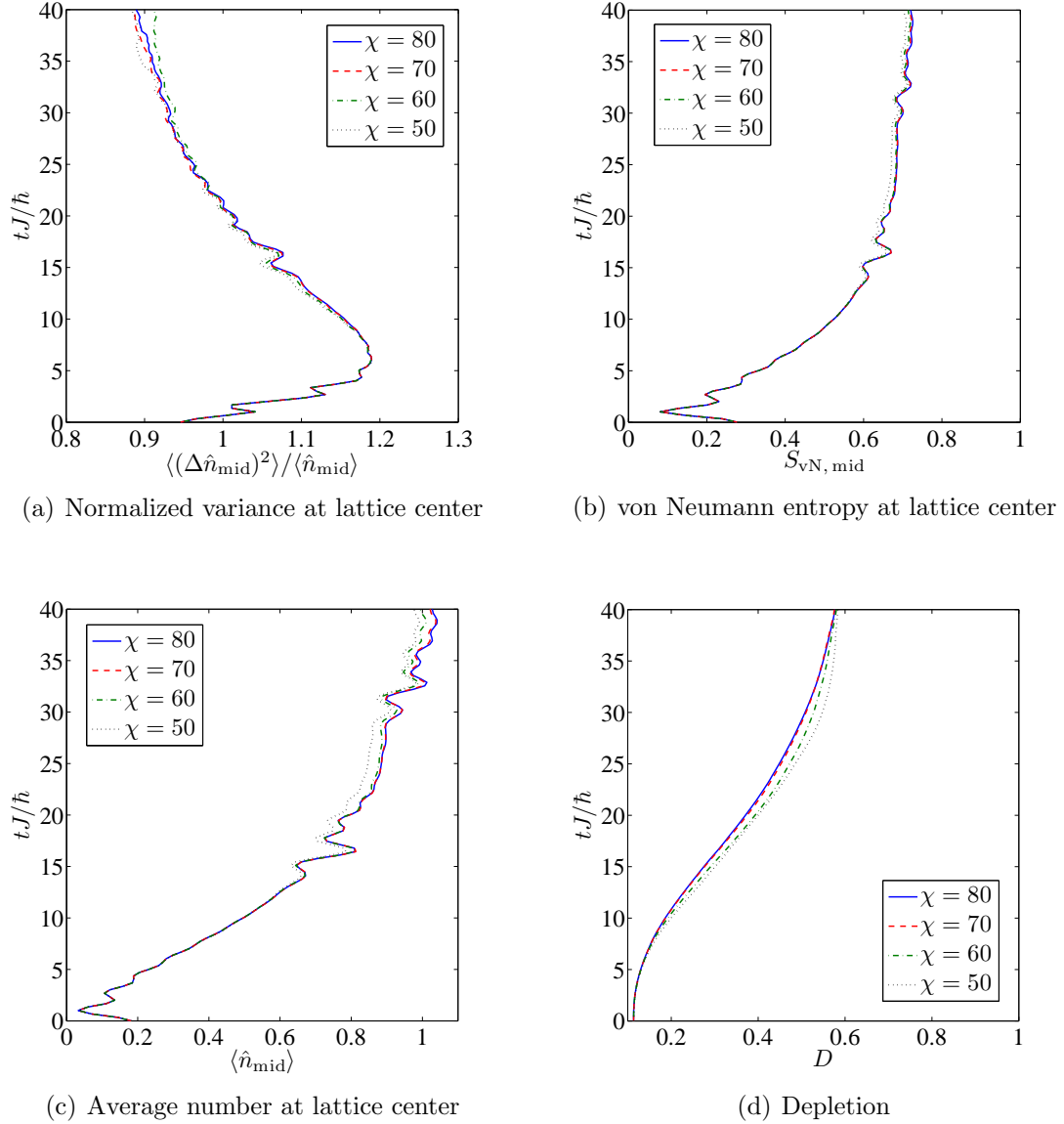


Figure B.4. *Dependence of observables on  $\chi$  for engineered standing quantum soliton.* For values of  $\chi \in \{80, 70, 60, 50\}$ , we plot over time the (a) normalized number variance, (b) local von Neumann entropy, and (c) average particle occupation number all at the center of the lattice. Because we use an even number of sites, we average the data associated with the sites immediately to the left and right of the lattice center. An analogous plot of quantum depletion is shown in (d). All other simulation parameters are the same as those used in the characteristic simulation of engineered dark quantum soliton propagation presented in Section 5.2.2. All results are acceptably well-converged with respect to  $\chi$ .

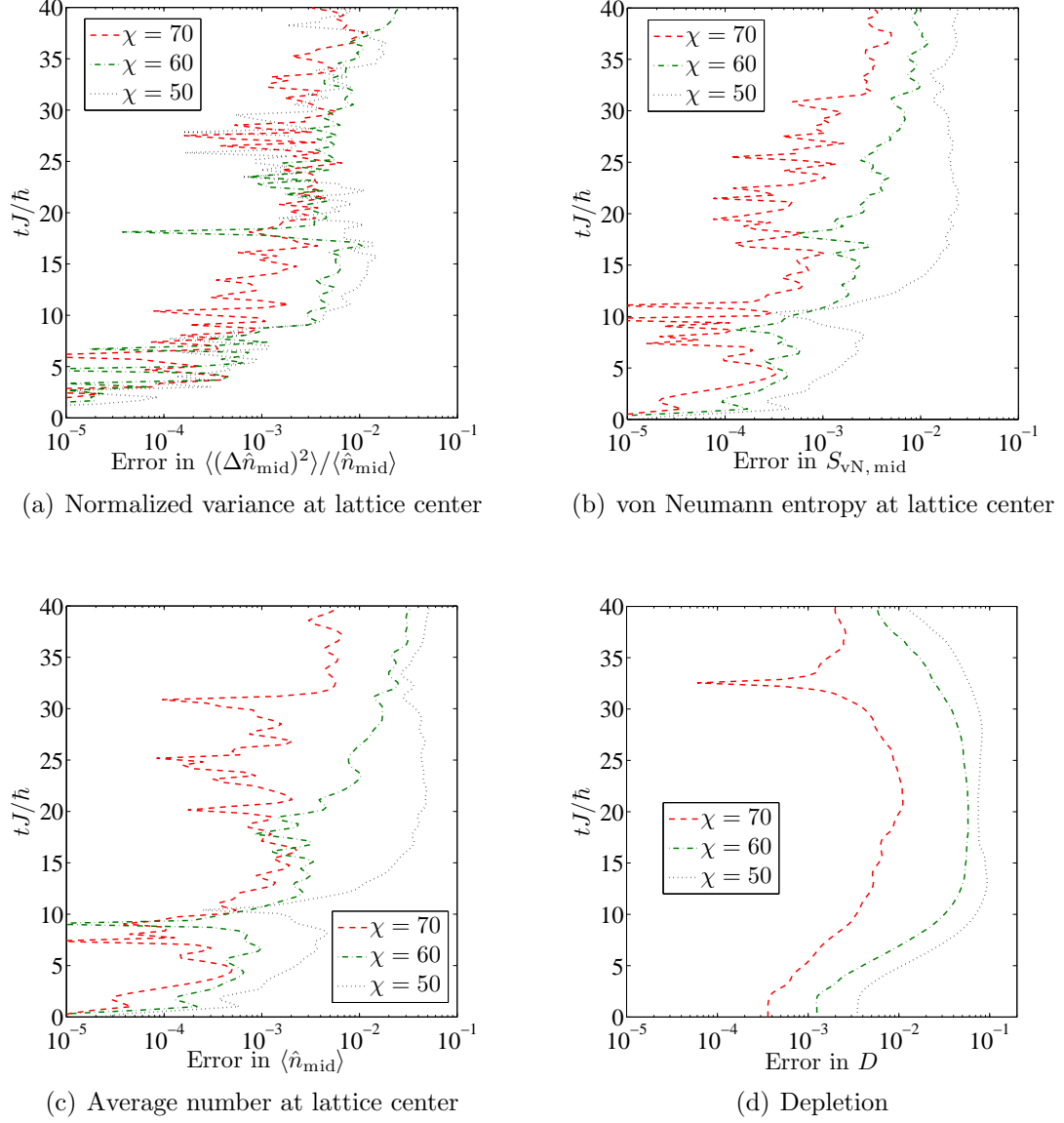


Figure B.5. *Relative error of observables with different  $\chi$  for engineered standing quantum soliton.* For the same measures as in Figure B.4, we plot the error of the  $\chi \in \{70, 60, 50\}$  results relative to the  $\chi = 80$  result. Although at a given time increasing  $\chi$  generally decreases the percent error, there are exceptions at certain times in the normalized number variance plot shown in (a). All results are clearly well-converged at  $\chi = 80$ .

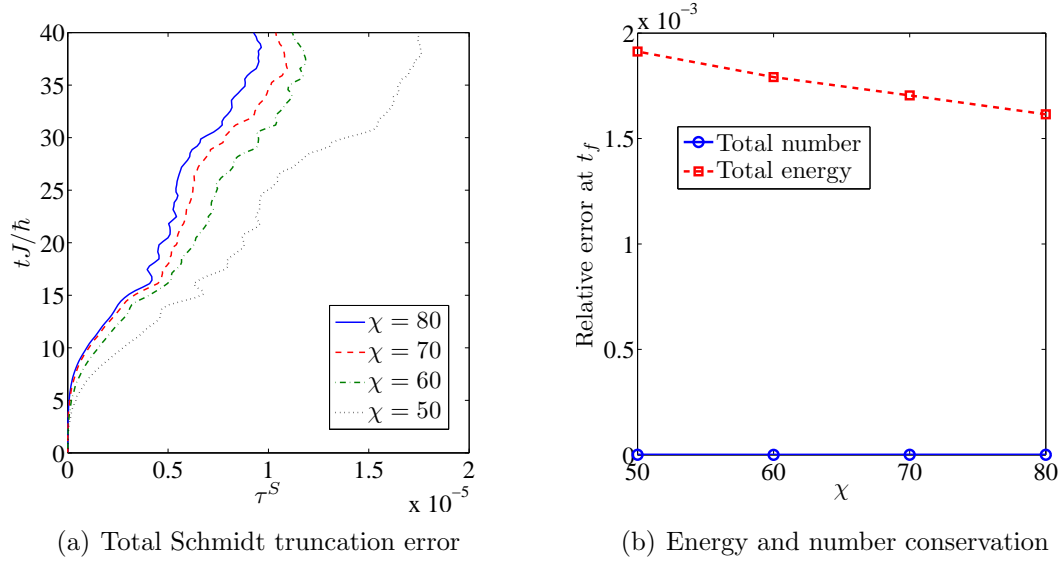


Figure B.6. *Truncation error and conservation of good quantum numbers for engineered standing quantum soliton.* (a) The total Schmidt truncation error for each TEBD time step is plotted over time for  $\chi \in \{80, 70, 60, 50\}$ . We see that for the values of  $\chi$  considered here this quantity stays  $\mathcal{O}(10^{-5})$ . Because for these simulations we choose  $M = 31$  sites, the Schmidt truncation error is only  $\mathcal{O}(10^{-6})$  for each time step. (b) As compared to their initial values, the relative error in average total particle number and average total energy at the final time are plotted versus the same values of  $\chi$  as in (a). Total number is conserved fundamentally due to our use of number-conserving methods. The energy is conserved to about 0.1%. Again, curves in (b) are a guide to the eye.

cal Schmidt truncation error over the 4000 time steps of the simulation is  $\mathcal{O}(10^{-2})$ . We see that increasing  $\chi$  from 20 to 80 results in only about a factor of two drop in Schmidt truncation error for these simulations. Figure B.6(b) shows the relative error in computed total number and average energy at the final time as compared to the initial time. Because we use number-conserving algorithms for these simulations, total number is conserved to machine precision, whereas the error in energy conservation is at an acceptable  $10^{-3}$ .

## B.2 Other Sources of Error

For all TEBD simulations in this thesis, we use a time step of size  $\delta t = 0.01 \hbar/J$ . Using the second-order Suzuki-Trotter expansion as in Equation (3.43), results in an error  $\mathcal{O}(\delta t^3)$  for each time step. Hence, by taking  $\delta t = 0.01 \hbar/J$  over 4000 time steps, we should expect an accumulated error of  $\mathcal{O}(10^{-3})$ . We tested the validity of using  $\delta t = 0.01 \hbar/J$  by going to  $\delta t = 0.005 \hbar/J$  and  $\delta t = 0.001 \hbar/J$  in the number-conserving code. The  $\delta t = 0.005 \hbar/J$  data agrees with the  $\delta t = 0.01 \hbar/J$  data to about 1% at long times. However, we do observe that decreasing the step size helps to hold the symmetry about the lattice center of the space-time surface plots displaying soliton evolution. As expected, this is especially true at long times. At short times, using a larger step size, e.g.,  $\delta t = 0.05 \hbar/J$ , may be justifiable.

The truncation of the local Hilbert space of a boson lattice system is not specific to TEBD. For instance, it is an approximation used in exact diagonalization studies as well. For the quantum evolution of mean-field soliton simulations in Chapter 4, we take the local dimension to be  $d = 7$ , allowing up to 6 bosons per site. For the  $\nu \leq 1$  filling factors considered, this leads to a coherent state truncation error of  $\Delta \lesssim 10^{-4}$ . Also, the normalized number variance remains on the order of unity throughout time evolution, thus indicating that 7 number states is plenty sufficient to describe the dynamics. However, we do find that decreasing  $d$  to 5 or 6 truncates the coherent state to such an extent that the soliton fill-in times decrease by a few tunneling times. For our quantum engineering soliton studies, we take  $d = 6$  in all simulations. In general, observables at  $d = 6$  are converged to about 1% compared to those obtained at  $d = 7$ . As with  $\chi$ , there is really no straightforward prescription in determining what local dimension is necessary for a given simulation. Instead, it is best to look for convergence of observables upon successively increasing  $d$ .

## APPENDIX C

### MEAN-FIELD SIMULATION CODE

This appendix contains the most important functions used for our discrete mean-field calculations in Chapters 4, 5, and 6. For specifics of the finite difference methods employed for time propagation of the DNLS for both scalar and spin-1 bosons, see Section 3.1. The real time propagation functions for the scalar and vector DNLS are shown below in Sections C.1 and C.2, respectively. In Section C.3, we show the code used to calculate Bogoliubov excitation spectrums as in Section 4.3.5. Discussion of Bogoliubov methods as applied to the DNLS is presented in Section 2.3.5. All mean-field code can be found in the thesis DVD under the folder `\DiscreteMeanField`.

#### C.1 scalarDNLS\_RTP.m

```
function [x, t, psi] = ...
    scalarDNLS_RTP(methodOpt, M, tf, dt, stores, printPeriod, ...
        psi0, Vext, hbar, J, U)

% [x, t, psi] = ...
%     scalarDNLS_RTP(methodOpt, M, tf, dt, stores, printPeriod, ...
%         psi0, Vext, hbar, J, U)
%
% Input parameters:
% methodOpt = type of method to use:
%             'expEuler' for explicit Euler,
%             'CN' for Crank-Nicolson.
%             'RK4' for 4th-order Runge-Kutta.
% M = number of lattice sites.
% tf = final time.
% dt = time step size.
% stores = number of time points to store for output.
```



```

% printPeriod = number of steps between status print.
% psi0 = initial wave function;
%     either M-dimensional vector or function handle.
% Vext = function handle for external potential.
% hbar = Planck's constant!
% J = hopping parameter.
% U = interaction parameter.
%
% Output variables:
% x = spatial grid.
% t = temporal grid with stores points.
% psi = solution with stores data points.

% Calculate temporal grids. T is the actual temporal grid with ~tf/dt
% points, whereas t is the truncated grid with stores points used for
% plotting.
Dt = tf/(stores - 1);
small_steps = ceil(Dt/dt);
dt = Dt/(small_steps - 1);
T = 0:dt:tf;
t = 0:Dt:tf;
Tpts = length(T);

% Calculate spatial grid.
x = ((-M + 1)/2:(M - 1)/2)';

% Allocate space for solution over time and set initial condition.
psi = zeros(M, stores);
psitemp = zeros(M, 1);
if ischar(psi0)
    psitemp = feval(psi0, x);
else
    psitemp = psi0;
end

% Define identity matrix and imaginary number i.
I = sparse(1:M, 1:M, 1, M, M);
i = sqrt(-1);

% Define kinetic energy part of Jacobian.
Hkin = sparse(1:M-1, 2:M, -J, M, M);
Hkin = Hkin + Hkin';

% Define external potential part of Jacobian.
if ischar(Vext)
    V = sparse(1:M, 1:M, feval(Vext, x), M, M);
else
    V = sparse(1:M, 1:M, Vext, M, M);
end

```

```

% Time iteration using method specified by input parameter methodOpt.
print_steps = ceil(printPeriod/dt);
storeInd = 1
display('Starting RTP!');
if strcmp(methodOpt, 'expEuler')
    for Tind = 1:Tpts
        if mod(Tind-1, small_steps-1) == 0
            psi(:, storeInd) = psitemp;
            storeInd = storeInd + 1;
        end
        if mod(Tind-1, print_steps) == 0
            disp(['time = ', num2str(T(Tind))]);
        end
        Hint = U * sparse(1:M, 1:M, abs(psitemp.^2), M, M);
        H = Hkin + V + Hint;
        psitemp = (I - i*dt*H/hbar) * psitemp;
    end
elseif strcmp(methodOpt, 'CN')
    for Tind = 1:Tpts
        if mod(Tind-1, small_steps-1) == 0
            psi(:, storeInd) = psitemp;
            storeInd = storeInd + 1;
        end
        if mod(Tind-1, print_steps) == 0
            disp(['time = ', num2str(T(Tind))]);
        end
        Hintleft = U * sparse(1:M, 1:M, abs(psitemp.^2), M, M);
        Hleft = Hkin + V + Hintleft;
        psihalf = (I - i*Hleft*dt/(2*hbar)) * psitemp;
        Hinthalf = U * sparse(1:M, 1:M, abs(psihalf.^2), M, M);
        Hhalf = Hkin + V + Hinthalf;
        Lop = I + i*Hhalf*dt/(2*hbar);
        Rop = I - i*Hhalf*dt/(2*hbar);
        psitemp = (Rop/Lop) * psitemp;
    end
elseif strcmp(methodOpt, 'RK4')
    for Tind = 1:Tpts
        if mod(Tind-1, small_steps-1) == 0
            psi(:, storeInd) = psitemp;
            storeInd = storeInd + 1;
        end
        if mod(Tind-1, print_steps) == 0
            disp(['time = ', num2str(T(Tind))]);
        end
        Hint = U * sparse(1:M, 1:M, abs(psitemp.^2), M, M);
        H = Hkin + V + Hint;
        F = H/(i*hbar);
        k1 = F * psitemp;
    end
end

```

```

        k2 = F * (psitemp + dt/2.0 * k1);
        k3 = F * (psitemp + dt/2.0 * k2);
        k4 = F * (psitemp + dt * k3);
        psitemp = psitemp + dt/6.0 * (k1 + 2*k2 + 2*k3 + k4);
    end
else
    error('methodOpt in scalarDNLS_RTP must be either expEuler, CN, or RK4');
end
display('RTP finished!');

```

## C.2 vectorDNLS\_RTP.m

```

function [x, t, psi, indsUp, inds0, indsDown] = ...
    vectorDNLS_RTP(methodOpt, M, tf, dt, stores, printPeriod, ...
        psiUp, psi0, psiDown, Vup, V0, Vdown, hbar, J, U0, U2)

% [x, t, psi, indsUp, inds0, indsDown] = ...
%     vectorDNLS_RTP(methodOpt, M, tf, dt, stores, printPeriod, ...
%     psiUp, psi0, psiDown, Vup, V0, Vdown, hbar, J, U0, U2)
%
% Input parameters:
% methodOpt = type of method to use:
%             'expEuler' for explicit Euler,
%             'CN' for Crank-Nicolson,
%             'RK4' for 4th-order Runge-Kutta.
% M = number of lattice sites.
% tf = final time.
% dt = time step size.
% stores = number of time points to store for output.
% printPeriod = number of steps between status print.
% psiUp = initial wave function for up component;
%         either M-dimensional vector or function handle.
% psi0 = initial wave function for 0 component;
%        either M-dimensional vector or function handle.
% psiDown = initial wave function for down component;
%          either M-dimensional vector or function handle.
% Vup = function handle for potential on up component.
% V0 = function handle for potential on 0 component.
% Vdown = function handle for potential on down component.
% hbar = Planck's constant!
% J = hopping parameter.
% U0 = spin-independent interaction parameter.
% U2 = spin-dependent interaction parameter.
%
% Output variables:
% x = spatial grid.

```

```

% t = temporal grid with stores points.
% psi = solution with stores data points.
% indsUp = row indices of up component.
% inds0 = row indices of 0 component.
% indsDown = row indices of down component.

% Calculate temporal grids. T is the actual temporal grid with ~tf/dt
% points, whereas t is the truncated grid with stores points used for
% plotting.
Dt = tf/(stores - 1);
small_steps = ceil(Dt/dt);
dt = Dt/(small_steps - 1);
T = 0:dt:tf;
t = 0:Dt:tf;
Tpts = length(T);

% Calculate spatial grid.
x = ((-M + 1)/2:(M - 1)/2)';

% Calculate indices of different spin components.
indsUp = 1:M;
inds0 = M+1:2*M;
indsDown = 2*M+1:3*M;

% Allocate space for solution over time and set initial conditions.
psi = zeros(3*M, stores);
psitemp = zeros(3*M, 1);
if ischar(psiUp)
    psitemp(indsUp) = feval(psiUp, x);
else
    psitemp(indsUp) = psiUp;
end
if ischar(psi0)
    psitemp(inds0) = feval(psi0, x);
else
    psitemp(inds0) = psi0;
end
if ischar(psiDown)
    psitemp(indsDown) = feval(psiDown, x);
else
    psitemp(indsDown) = psiDown;
end

% Define identity matrix and imaginary number i.
I = sparse(1:3*M, 1:3*M, 1, 3*M, 3*M);
i = sqrt(-1);

% Time iteration using method specified by input parameter methodOpt.
print_steps = ceil(printPeriod/dt);

```

```

storeInd = 1;
display('Starting RTP!');
if strcmp(methodOpt, 'expEuler')
    for Tind = 1:Tpts
        if mod(Tind-1, small_steps-1) == 0
            psi(:, storeInd) = psitemp;
            storeInd = storeInd + 1;
        end
        if mod(Tind-1, print_steps) == 0
            disp(['time = ', num2str(T(Tind)), ', Q = ', ...
                num2str(feval(Vdown, x, T(Tind)))]);
        end
        [Fz, Fminus] = ...
            calculateFs(psitemp(indsUp), psitemp(inds0), psitemp(indsDown));
        H = sparse([1:M-1, M+1:2*M-1, 2*M+1:3*M-1], ...
            [2:M, M+2:2*M, 2*M+2:3*M], -J, 3*M, 3*M) ...
            + sparse(1:2*M, M+1:3*M, ...
            U2/sqrt(2)*[Fminus; Fminus], 3*M, 3*M);
        H = H + H';
        H = H + sparse(1:3*M, 1:3*M, ...
            [feval(Vup, x, T(Tind)) + U0*(abs(psitemp(indsUp)).^2 + ...
            abs(psitemp(inds0)).^2 + abs(psitemp(indsDown)).^2) + U2*Fz; ...
            feval(V0, x, T(Tind)) + U0*(abs(psitemp(indsUp)).^2 + ...
            abs(psitemp(inds0)).^2 + abs(psitemp(indsDown)).^2); ...
            feval(Vdown, x, T(Tind)) + U0*(abs(psitemp(indsUp)).^2 + ...
            abs(psitemp(inds0)).^2 + abs(psitemp(indsDown)).^2) - U2*Fz], ...
            3*M, 3*M);
        psitemp = (I - i*dt*H/hbar) * psitemp;
    end
elseif strcmp(methodOpt, 'CN')
    for Tind = 1:Tpts
        if mod(Tind-1, small_steps-1) == 0
            psi(:, storeInd) = psitemp;
            storeInd = storeInd + 1;
        end
        if mod(Tind-1, print_steps) == 0
            disp(['time = ', num2str(T(Tind)), ', Q = ', ...
                num2str(feval(Vdown, x, T(Tind)))]);
        end
        [Fzleft, Fminusleft] = ...
            calculateFs(psitemp(indsUp), psitemp(inds0), psitemp(indsDown));
        Hleft = sparse([1:M-1, M+1:2*M-1, 2*M+1:3*M-1], ...
            [2:M, M+2:2*M, 2*M+2:3*M], -J, 3*M, 3*M) ...
            + sparse(1:2*M, M+1:3*M, ...
            U2/sqrt(2)*[Fminusleft; Fminusleft], 3*M, 3*M);
        Hleft = Hleft + Hleft';
        Hleft = Hleft + sparse(1:3*M, 1:3*M, ...
            [feval(Vup, x, T(Tind)) + U0*(abs(psitemp(indsUp)).^2 + ...
            abs(psitemp(inds0)).^2 + abs(psitemp(indsDown)).^2) + U2*Fzleft; ...

```

```

        feval(V0, x, T(Tind)) + U0*(abs(psitemp(indsUp)).^2 + ...
        abs(psitemp(inds0)).^2 + abs(psitemp(indsDown)).^2); ...
        feval(Vdown, x, T(Tind)) + U0*(abs(psitemp(indsUp)).^2 + ...
        abs(psitemp(inds0)).^2 + abs(psitemp(indsDown)).^2) ...
        - U2*Fzleft], 3*M, 3*M);
    psihalf = (I - i*Hleft*dt/(2*hbar)) * psitemp;
    [Fzmid, Fminusmid] = ...
        calculateFs(psihalf(indsUp), psihalf(inds0), psihalf(indsDown));
    Hhalf = sparse([1:M-1, M+1:2*M-1, 2*M+1:3*M-1], ...
        [2:M, M+2:2*M, 2*M+2:3*M], -J, 3*M, 3*M) ...
        + sparse(1:2*M, M+1:3*M, ...
        U2/sqrt(2)*[Fminusmid; Fminusmid], 3*M, 3*M);
    Hhalf = Hhalf + Hhalf';
    Hhalf = Hhalf + sparse(1:3*M, 1:3*M, ...
        [feval(Vup, x, (T(Tind)+T(Tind+1))/2) + ...
        U0*(abs(psihalf(indsUp)).^2 + abs(psihalf(inds0)).^2 + ...
        abs(psihalf(indsDown)).^2) + U2*Fzleft; ...
        feval(V0, x, (T(Tind)+T(Tind+1))/2) + ...
        U0*(abs(psihalf(indsUp)).^2 + abs(psihalf(inds0)).^2 + ...
        abs(psihalf(indsDown)).^2); ...
        feval(Vdown, x, (T(Tind)+T(Tind+1))/2) + ...
        U0*(abs(psihalf(indsUp)).^2 + abs(psihalf(inds0)).^2 + ...
        abs(psihalf(indsDown)).^2) - U2*Fzleft], ...
        3*M, 3*M);
    Lop = I + i*Hhalf*dt/(2*hbar);
    Rop = I - i*Hhalf*dt/(2*hbar);
    psitemp = (Rop/Lop) * psitemp;
end
elseif strcmp(methodOpt, 'RK4')
    for Tind = 1:Tpts
        if mod(Tind-1, small_steps-1) == 0
            psi(:, storeInd) = psitemp;
            storeInd = storeInd + 1;
        end
        if mod(Tind-1, print_steps) == 0
            disp(['time = ', num2str(T(Tind)), ', Q = ', ...
                num2str(feval(Vdown, x, T(Tind)))]);
        end
        [Fz, Fminus] = ...
            calculateFs(psitemp(indsUp), psitemp(inds0), psitemp(indsDown));
        H = sparse([1:M-1, M+1:2*M-1, 2*M+1:3*M-1], ...
            [2:M, M+2:2*M, 2*M+2:3*M], -J, 3*M, 3*M) ...
            + sparse(1:2*M, M+1:3*M, ...
            U2/sqrt(2)*[Fminus; Fminus], 3*M, 3*M);
        H = H + H';
        H = H + sparse(1:3*M, 1:3*M, ...
            [feval(Vup, x, T(Tind)) + U0*(abs(psitemp(indsUp)).^2 + ...
            abs(psitemp(inds0)).^2 + abs(psitemp(indsDown)).^2) + U2*Fz; ...
            feval(V0, x, T(Tind)) + U0*(abs(psitemp(indsUp)).^2 + ...

```

```

        abs(psitemp(inds0)).^2 + abs(psitemp(indsDown)).^2); ...
        feval(Vdown, x, T(Tind)) + U0*(abs(psitemp(indsUp)).^2 + ...
        abs(psitemp(inds0)).^2 + abs(psitemp(indsDown)).^2) - U2*Fz], ...
        3*M, 3*M);
    F = H/(i*hbar);
    k1 = F * psitemp;
    k2 = F * (psitemp + dt/2.0 * k1);
    k3 = F * (psitemp + dt/2.0 * k2);
    k4 = F * (psitemp + dt * k3);
    psitemp = psitemp + dt/6.0 * (k1 + 2*k2 + 2*k3 + k4);
end
else
    error('methodOpt in vectorDNLS_RTP must be either expEuler, CN, or RK4');
end
display('RTP finished!');

```

### C.3 BogModes.m

```

function [u, v, evals] = BogModes(psi, mu, J, U, epsilon)

% [u, v, evals] = BogModes(psi, mu, J, U, epsilon)
%
% Input parameters:
% psi = DNLS solution.
% mu = chemical potential of DNLS solution.
% J = hopping parameter.
% U = interaction parameter.
% epsilon = external potential
%
% Output variables:
% u = u's in Bogoliubov equations.
% v = v's in Bogoliubov equations.
% evals = frequencies of collective excitations.

% Calculate matrix G to diagonalize.
M = length(psi);
G = sparse(1:M, 1:M, -mu + 2*U*abs(psi).^2 + epsilon, 2*M, 2*M) ...
    + sparse(M+1:2*M, M+1:2*M, mu - 2*U*abs(psi).^2 - epsilon, 2*M, 2*M) ...
    + sparse(1:M-1, 2:M, -J, 2*M, 2*M) ...
    + sparse(M+1:2*M-1, M+2:2*M, J, 2*M, 2*M) ...
    + sparse(1:M-1, 2:M, -J, 2*M, 2*M).' ...
    + sparse(M+1:2*M-1, M+2:2*M, J, 2*M, 2*M).' ...
    + sparse(1:M, M+1:2*M, U*psi.^2, 2*M, 2*M) ...
    + sparse(M+1:2*M, 1:M, -U*conj(psi).^2, 2*M, 2*M);

% Diagonalize G, select only those modes with positive norm, and normalize

```

```

% solution accordingly.
[vecs, evals] = eig(full(G)); diag(evals);
[evals, sortInds] = sort(diag(evals), 'ascend');
vecs = vecs(:, sortInds);
norms = sum(abs(vecs(1:M, :)).^2 - abs(vecs(M+1:2*M, :)).^2, 1);
posInds = find(norms > 10^-8);
evals = evals(posInds);
vecs = vecs(:, posInds);
for i = 1:size(vecs, 2)
    vecs(:, i) = vecs(:, i) ./ sqrt(norms(posInds(i)));
end

% Store final solution.
u = vecs(1:M, :);
v = vecs(M+1:2*M, :);

```



## APPENDIX D

### TIME-EVOLVING BLOCK DECIMATION CODE

In this appendix, we present the current version of our TEBD code. For brevity in display, we only show in Section D.1 the module used for generation of the spin-1 Bose-Hubbard Hamiltonian; this module will be used in a future work investigating the Kibble-Zurek mechanism in a system of spin-1 bosons on an optical lattice. The entire code used to produce the results in this thesis can be found in a nicely formatted pdf file entitled `sourceCode.pdf` in the included thesis DVD under the folder `\AppendixD`.

#### D.1 `spin1_module.f90`

```
MODULE spin1_module

    USE system_parameters
    USE MPDtools_module

    IMPLICIT NONE

    ! Declare spin-1 operators.
    TYPE(matrix) :: aup_op
    TYPE(matrix) :: adagup_op
    TYPE(matrix) :: a0_op
    TYPE(matrix) :: adag0_op
    TYPE(matrix) :: adown_op
    TYPE(matrix) :: adagdown_op
    TYPE(matrix) :: nup_op
    TYPE(matrix) :: n0_op
    TYPE(matrix) :: ndown_op
    TYPE(matrix) :: nupn0_op
    TYPE(matrix) :: n0ndown_op
    TYPE(matrix) :: nupndown_op
    TYPE(matrix) :: nupsq_op
```

```

TYPE(matrix) :: ndownsq_op
TYPE(matrix) :: adagupadagdowna0sq_op
TYPE(matrix) :: adag0sqaupadown_op
TYPE(matrix) :: Ssq_op
TYPE(matrix) :: ntot_op
TYPE(matrix) :: ntotsq_op
TYPE(matrix) :: Ssqxone_op
TYPE(matrix) :: onexSsq_op
TYPE(matrix) :: ntotxone_op
TYPE(matrix) :: onexntot_op
TYPE(matrix) :: ntotsqxone_op
TYPE(matrix) :: onexntotsq_op
TYPE(matrix) :: nupxone_op
TYPE(matrix) :: onexnup_op
TYPE(matrix) :: ndownxone_op
TYPE(matrix) :: onexndown_op
TYPE(matrix) :: adagupxaup_op
TYPE(matrix) :: adag0xa0_op
TYPE(matrix) :: adagdownxadown_op
TYPE(matrix) :: tup_op
TYPE(matrix) :: t0_op
TYPE(matrix) :: tdown_op
TYPE(matrix) :: ttot_op

```

#### CONTAINS

```

! Function to calculate physical site local dimension for spin-1 system.
FUNCTION spin1LocalDim(maxFill)
  INTEGER, INTENT(IN) :: maxFill
  INTEGER :: spin1LocalDim
  spin1LocalDim = ((maxFill + 3)*(maxFill + 2)*(maxFill + 1))/6
END FUNCTION spin1LocalDim

! Subroutine that returns list of on-site states for a Hilbert space truncated at &
nmax maximum particles per site.
SUBROUTINE onsiteStateList(list, nmax)
  INTEGER, INTENT(IN) :: nmax
  COMPLEX(KIND=8), INTENT(OUT) :: list(:, :)
  INTEGER i, j, n(3), counter, k
  list = 0.0_8
  counter = 0
! Loop over all nmax, beginning with nMax=0.

  DO k = 1, nmax+1, 1
    counter = counter+1
    n = 0.0_8
! Put all particles in the m=1 spin state.
    n(1) = k-1
! Counter keeps track of the proper indexing.

```

```

list(counter, :) = n(:)

! Loop over the number in the m=0 spin state
DO i = 1, k-1, 1
  counter = counter+1
  n(1) = n(1)-1
! Begin by placing all particles that are not in the m=1 state in the m=0 state.
  n(2) = k-1-n(1)
  n(3) = 0
  list(counter, :) = n(:)

  DO j = 1, k-1-n(1), 1
    counter = counter+1
! Move particles out of the m=0 state into the m=-1 state.
    n(2) = n(2)-1
    n(3) = n(3)+1
    list(counter, :) = n(:)
  END DO
END DO
END DO

END SUBROUTINE onsiteStateList

! Kronecker delta function defined for two vectors vec1 and vec2.
FUNCTION kronDelta(vec1, vec2, dim)
  COMPLEX(KIND=8), INTENT(IN) :: vec1(:), vec2(:)
  INTEGER, INTENT(IN) :: dim
  INTEGER :: kronDelta
  INTEGER :: dim1, dim2, i, j
  INTEGER, DIMENSION(dim) :: booles
  dim1 = SIZE(vec1)
  dim2 = SIZE(vec2)
  IF (dim1 /= dim .OR. dim2 /= dim) THEN
    STOP "Dimensions of input vectors in function kronDelta &
      must be the same."
  END IF
  DO i = 1, dim
    IF (vec1(i) == vec2(i)) THEN
      booles(i) = 1
    ELSE
      booles(i) = 0
    END IF
  END DO
  kronDelta = 1
  DO j = 1, dim
    kronDelta = kronDelta * booles(j)
  END DO
END FUNCTION kronDelta

```

! Subroutine to create matrix representations of operators pertinent to spin-1 & Bose-Hubbard Hamiltonian.

```

SUBROUTINE CreateSpin1ops()
  INTEGER :: i, j, d, dsq, spinSize
  TYPE(matrix) :: stateList, newState
  COMPLEX(KIND=8) :: preFactor
  d = localSize
  dsq = d*d
  spinSize = 3
  ALLOCATE(aup_op%m(d, d))
  ALLOCATE(adagup_op%m(d, d))
  ALLOCATE(a0_op%m(d, d))
  ALLOCATE(adag0_op%m(d, d))
  ALLOCATE(adown_op%m(d, d))
  ALLOCATE(adagdown_op%m(d, d))
  ALLOCATE(nup_op%m(d, d))
  ALLOCATE(n0_op%m(d, d))
  ALLOCATE(ndown_op%m(d, d))
  ALLOCATE(nupn0_op%m(d, d))
  ALLOCATE(n0ndown_op%m(d, d))
  ALLOCATE(nupndown_op%m(d, d))
  ALLOCATE(nupsq_op%m(d, d))
  ALLOCATE(ndownsq_op%m(d, d))
  ALLOCATE(adagupadagdowna0sq_op%m(d, d))
  ALLOCATE(adag0sqaupadown_op%m(d, d))
  ALLOCATE(Ssq_op%m(d, d))
  ALLOCATE(ntot_op%m(d, d))
  ALLOCATE(ntotsq_op%m(d, d))
  ALLOCATE(Ssqxone_op%m(dsq, dsq))
  ALLOCATE(onexSsq_op%m(dsq, dsq))
  ALLOCATE(ntotxone_op%m(dsq, dsq))
  ALLOCATE(onexntot_op%m(dsq, dsq))
  ALLOCATE(ntotsqxone_op%m(dsq, dsq))
  ALLOCATE(onexntotsq_op%m(dsq, dsq))
  ALLOCATE(nupxone_op%m(dsq, dsq))
  ALLOCATE(onexnup_op%m(dsq, dsq))
  ALLOCATE(ndownxone_op%m(dsq, dsq))
  ALLOCATE(onexndown_op%m(dsq, dsq))
  ALLOCATE(adagupxaup_op%m(dsq, dsq))
  ALLOCATE(adag0xa0_op%m(dsq, dsq))
  ALLOCATE(adagdownxadown_op%m(dsq, dsq))
  ALLOCATE(tup_op%m(dsq, dsq))
  ALLOCATE(t0_op%m(dsq, dsq))
  ALLOCATE(tdown_op%m(dsq, dsq))
  ALLOCATE(ttot_op%m(dsq, dsq))
  aup_op%m = CMPLX(0.0, KIND=8)
  a0_op%m = CMPLX(0.0, KIND=8)
  adown_op%m = CMPLX(0.0, KIND=8)
  ALLOCATE(stateList%m(d, spinSize))

```

```

ALLOCATE(newState%m(1, spinSize))
CALL onsiteStateList(stateList%m, maxFilling)
DO j = 1, d
    newState%m(1, :) = stateList%m(j, :)
    preFactor = SQRT(newState%m(1, 1))
    newState%m(1, 1) = newState%m(1, 1) - 1.0_8
    DO i = 1, d
        aup_op%m(i, j) = &
            preFactor*kronDelta(stateList%m(i, :), &
                newState%m(1, :), spinSize)
    END DO
END DO
adagup_op%m = TRANSPOSE(aup_op%m)
DO j = 1, d
    newState%m(1, :) = stateList%m(j, :)
    preFactor = SQRT(newState%m(1, 2))
    newState%m(1, 2) = newState%m(1, 2) - 1.0_8
    DO i = 1, d
        a0_op%m(i, j) = &
            preFactor*kronDelta(stateList%m(i, :), &
                newState%m(1, :), spinSize)
    END DO
END DO
adag0_op%m = TRANSPOSE(a0_op%m)
DO j = 1, d
    newState%m(1, :) = stateList%m(j, :)
    preFactor = SQRT(newState%m(1, 3))
    newState%m(1, 3) = newState%m(1, 3) - 1.0_8
    DO i = 1, d
        adown_op%m(i, j) = &
            preFactor*kronDelta(stateList%m(i, :), &
                newState%m(1, :), spinSize)
    END DO
END DO
adagdown_op%m = TRANSPOSE(adown_op%m)
nup_op%m = MATMUL(adagup_op%m, aup_op%m)
n0_op%m = MATMUL(adag0_op%m, a0_op%m)
ndown_op%m = MATMUL(adagdown_op%m, adown_op%m)
nupn0_op%m = MATMUL(nup_op%m, n0_op%m)
n0ndown_op%m = MATMUL(n0_op%m, ndown_op%m)
nupndown_op%m = MATMUL(nup_op%m, ndown_op%m)
nupsq_op%m = MATMUL(nup_op%m, nup_op%m)
ndownsq_op%m = MATMUL(ndown_op%m, ndown_op%m)
adagupadagdowna0sq_op%m = &
    MATMUL(MATMUL(MATMUL(adagup_op%m, adagdown_op%m), &
        a0_op%m), a0_op%m)
adag0sqaupadown_op%m = &
    MATMUL(MATMUL(MATMUL(adag0_op%m, adag0_op%m), &
        aup_op%m), adown_op%m)

```

```

Ssq_op%m = 2.0_8*nupn0_op%m + 2.0_8*n0ndown_op%m + nup_op%m + &
          2*n0_op%m + ndown_op%m + &
          nupsq_op%m - 2.0_8*nupndown_op%m + ndownsq_op%m + &
          2*adagupadagdowna0sq_op%m + 2*adag0sqaupadown_op%m
ntot_op%m = nup_op%m + n0_op%m + ndown_op%m
ntotsq_op%m = MATMUL(ntot_op%m, ntot_op%m)
CALL TensorProduct(Ssqxone_op%m, Ssq_op%m, one_op%m)
CALL TensorProduct(onexSsq_op%m, one_op%m, Ssq_op%m)
CALL TensorProduct(ntotxone_op%m, ntot_op%m, one_op%m)
CALL TensorProduct(onexntot_op%m, one_op%m, ntot_op%m)
CALL TensorProduct(ntotsqxone_op%m, ntotsq_op%m, one_op%m)
CALL TensorProduct(onexntotsq_op%m, one_op%m, ntotsq_op%m)
CALL TensorProduct(nupxone_op%m, nup_op%m, one_op%m)
CALL TensorProduct(onexnup_op%m, one_op%m, nup_op%m)
CALL TensorProduct(ndownxone_op%m, ndown_op%m, one_op%m)
CALL TensorProduct(onexndown_op%m, one_op%m, ndown_op%m)
CALL TensorProduct(adagupxaup_op%m, adagup_op%m, aup_op%m)
CALL TensorProduct(adag0xa0_op%m, adag0_op%m, a0_op%m)
CALL TensorProduct(adagdownxadown_op%m, adagdown_op%m, adown_op%m)
tup_op%m = adagupxaup_op%m + Transpose(adagupxaup_op%m)
t0_op%m = adag0xa0_op%m + Transpose(adag0xa0_op%m)
tdown_op%m = adagdownxadown_op%m + Transpose(adagdownxadown_op%m)
ttot_op%m = tup_op%m + t0_op%m + tdown_op%m
DEALLOCATE(stateList%m)
DEALLOCATE(newState%m)
PRINT *, "Spin-1 operators created!"
END SUBROUTINE CreateSpin1ops

! Subroutine to deallocate spin-1 operators.
SUBROUTINE DestroySpin1ops()
  DEALLOCATE(aup_op%m, adagup_op%m, a0_op%m, adag0_op%m, &
            adown_op%m, adagdown_op%m, nup_op%m, n0_op%m, ndown_op%m)
  DEALLOCATE(nupn0_op%m, n0ndown_op%m, nupndown_op%m, &
            nupsq_op%m, ndownsq_op%m, &
            adagupadagdowna0sq_op%m, adag0sqaupadown_op%m)
  DEALLOCATE(Ssq_op%m, ntot_op%m, ntotsq_op%m)
  DEALLOCATE(Ssqxone_op%m, onexSsq_op%m, &
            ntotxone_op%m, onexntot_op%m, &
            ntotsqxone_op%m, onexntotsq_op%m)
  DEALLOCATE(nupxone_op%m, onexnup_op%m, &
            ndownxone_op%m, onexndown_op%m)
  DEALLOCATE(adagupxaup_op%m, adag0xa0_op%m, adagdownxadown_op%m, &
            tup_op%m, t0_op%m, tdown_op%m, ttot_op%m)
  PRINT *, "Spin-1 operators destroyed!"
END SUBROUTINE DestroySpin1ops

! TEBD form of spin-1 Bose-Hubbard Hamiltonian with quadratic Zeeman strength VB.
! J, U0, U2 are the usual spin-1 Bose-Hubbard parameters and mu0 is the &
chemical potential.

```

! This subroutine needs to be modified if an arbitrary external potential on the & three components is desired.

```

SUBROUTINE HamiltonianSpin1(H, J, U0, U2, mu0, VB)
  TYPE(matrix), POINTER :: H(:)
  REAL(KIND=8), INTENT(IN) :: J, U0, U2, mu0, VB
  INTEGER :: i, n
  n = systemSize
  DO i = 1, (n-1)
    H(i)%m = ((-1.0_8*mu0 - U0/2.0_8 - U2)*ntotxone_op%m + &
      U0/2.0_8*ntotsqxone_op%m)/2.0_8 + &
      ((-1.0_8*mu0 - U0/2.0_8 - U2)*onexntot_op%m + &
      U0/2.0_8*onexntotsq_op%m)/2.0_8 + &
      (U2/2.0_8*Ssqxone_op%m)/2.0_8 + &
      (U2/2.0_8*onexSsq_op%m)/2.0_8 + &
      VB*(nupxone_op%m + ndownxone_op%m)/2.0_8 + &
      VB*(onexnup_op%m + onexndown_op%m)/2.0_8 + &
      J*ttot_op%m
  END DO
  H(1)%m = H(1)%m + ((-1.0_8*mu0 - U0/2.0_8 - U2)*ntotxone_op%m + &
    U0/2.0_8*ntotsqxone_op%m)/2.0_8 + &
    (U2/2.0_8*Ssqxone_op%m)/2.0_8 + &
    VB*(nupxone_op%m + ndownxone_op%m)/2.0_8
  H(n-1)%m = H(n-1)%m + ((-1.0_8*mu0 - U0/2.0_8 - U2)*onexntot_op%m + &
    U0/2.0_8*onexntotsq_op%m)/2.0_8 + &
    (U2/2.0_8*onexSsq_op%m)/2.0_8 + &
    VB*(onexnup_op%m + onexndown_op%m)/2.0_8
END SUBROUTINE HamiltonianSpin1

```

END MODULE spin1\_module